

University of Southampton Research Repository

Copyright © and Moral Rights for this thesis and, where applicable, any accompanying data are retained by the author and/or other copyright owners. A copy can be downloaded for personal non-commercial research or study, without prior permission or charge. This thesis and the accompanying data cannot be reproduced or quoted extensively from without first obtaining permission in writing from the copyright holder/s. The content of the thesis and accompanying research data (where applicable) must not be changed in any way or sold commercially in any format or medium without the formal permission of the copyright holder/s.

When referring to this thesis and any accompanying data, full bibliographic details must be given, e.g.

Thesis: Author (Year of Submission) "Full thesis title", University of Southampton, name of the University Faculty or School or Department, PhD Thesis, pagination.

Data: Author (Year) Title. URI [dataset]

University of Southampton

Faculty of Engineering and Physical Sciences

School of Engineering

Application-led, online analysis for the continuous production of Metal-Organic Frameworks (MOFs)

by

Molly Jane Clark

ORCID ID 0000-0002-0604-6961

Thesis for the degree of Doctor of Philosophy

July 2024

University of Southampton

Abstract

Faculty of Engineering and Physical Sciences

School of Engineering

Doctor of Philosophy

Application-led, online analysis for the continuous production of Metal-Organic Frameworks (MOFs)

by

Molly Jane Clark

Metal-organic frameworks (MOFs) are a class of hybrid functional materials.¹ Modular in nature and highly tuneable, they have been used in a wide range of applications such as adsorption,² gas separation,³ and catalysis.⁴ Generally, MOFs are solvothermally made in batch-type processes and their analysis and property assessment requires considerable time and chemist intervention. Successful flow synthesis of MOFs with improved space-time yield, enhanced uniformity and quality of crystals have been published in recent years and developed in this work.⁵⁻⁷ However, there is currently no means for the inline characterisation of the MOF product, such that optimisation of in-flow MOF synthesis is complex and labour intensive.

This work investigates a qualitatively distinct approach. Using in-line UV-Vis during continuous production, an application-led focus is implemented whereby the amount of synthesised MOF is assessed based on its performance against a target application. The final system contains a synthetic, application and separation element with a final in-line UV-Vis spectrometer which produces real-time data on the process fluid. The chosen system used was HKUST-1 and the target application was adsorption of organic dye methylene blue.

The work presented in this thesis describes an established set-up that can quantifiably assess HKUST-1s ability to adsorb methylene blue during continuous synthesis. Not only does this prove the concept of 'application-led' analysis for the first time, but it helps to bridge the gap within future MOF production. By producing MOFs in flow while gathering in-situ analytical data on their adsorption ability this setup can act as a quality assurance tool for high throughput experimentation.

Table of Contents

Abstract	i
Table of Contents.....	i
Publications and Presentations	vii
Research Thesis: Declaration of Authorship	ix
Acknowledgements	xi
Definitions and Abbreviations.....	xv
Chapter 1 Introduction	17
1.1 Metal organic frameworks	17
1.1.1 Structure and Geometry	17
1.1.2 MOF synthesis: Solvothermal	18
1.1.3 Scale Up Methods	19
Chapter 2 Literature Review: Flow synthesis and In-line analysis for Metal Organic Frameworks	21
2.1 Continuous flow synthesis	21
2.1.1 General setup of a flow reactor	21
2.1.2 Benefits of flow processing	22
2.1.3 Analysis methods	25
2.1.4 Self-optimisation	27
2.2 Flow synthesis of MOFs.....	28
2.2.1 Microfluidics and segmented flow	29
2.2.2 Alternative continuous setups	32
2.3 Candidate techniques for In-line/On-line MOF analysis	35
2.3.1 Adapting standard ex-situ MOF analysis techniques for in-situ analysis.....	36
2.3.2 Alternatives to standard ex-situ techniques	46
2.3.3 Indirect in-situ analysis.....	48
2.3.4 Modifications and applications	49
2.3.5 Flow synthesis	49
2.4 Summary and the research problem	51

Table of Contents

2.5	Aims of the thesis.....	53
Chapter 3	The methodology and thesis structure	54
3.1	Initial approaches and considerations	54
3.1.1	Applications-led testing	54
3.1.2	Metal-Organic Frameworks: Considerations	55
3.1.3	The final envisioned set-up.....	56
3.1.4	The cross-flow filtration device	57
3.2	Thesis structure.....	57
Chapter 4	Synthesis of Metal Organic Frameworks	61
4.1	Candidate MOFs.....	61
4.1.1	HKUST-1	61
4.1.2	ZIF-8.....	62
4.2	Experimental methods.....	63
4.2.1	Materials and methods.....	63
4.2.2	HKUST-1 batch synthesis ¹³⁵	64
4.2.3	ZIF-8 batch synthesis ¹⁵⁷	64
4.2.4	Stability tests.....	64
4.2.5	Flow synthesis of HKUST-1.....	64
4.3	Results and Discussion	67
4.3.1	Batch synthesis and characterisation of HKUST-1.....	67
4.3.2	Batch synthesis and characterisation of ZIF-8	69
4.3.3	Framework stability	71
4.3.4	Flow Synthesis of HKUST-1	75
4.4	Conclusions	88
Chapter 5	Analysis: Organic dye adsorption by Metal Organic Frameworks ...	90
5.1	Organic dye adsorption by candidate MOFs	90
5.1.1	Adsorption as a MOF application	90
5.1.2	Adsorption	91
5.1.3	Possible adsorption mechanisms.....	92

5.1.4	Organic dyes	93
5.1.5	Adsorption analysis	94
5.2	Experimental methods	95
5.2.1	Materials and methods	95
5.2.2	Stock dye solutions and preliminary dye screening.....	95
5.2.3	Calibration curves.....	96
5.2.4	Control experiments for batch adsorption: pH stability and reagent effect ...	96
5.2.5	Adsorption kinetics of redispersed HKUST-1 towards methylene blue.....	96
5.2.6	Adsorption kinetics of dispersed HKUST-1.....	96
5.2.7	Adsorption kinetics of dispersed HKUST-1: observing dilution effects	96
5.2.8	Control experiments for flow adsorption	97
5.2.9	Adsorptive kinetics of dispersed HKUST-1 (in flow).....	97
5.3	Results and Discussion	98
5.3.1	Screening of organic dyes for adsorption by HKUST-1	98
5.3.2	Methyl Blue	100
5.3.3	Methylene Blue	101
5.3.4	Batch adsorption: Adsorptive kinetics of redispersed HKUST-1	103
5.3.5	Batch adsorption: Adsorptive kinetics of dispersed HKUST-1	104
5.3.6	Batch adsorption: Effect of the amount of dispersed HKUST-1 on adsorption 105	
5.3.7	Flow adsorption: control experiment, silica capillary vs PTFE tubing.....	107
5.3.8	Flow adsorption: effect of dispersed HKUST-1 density on adsorption.....	107
5.4	Conclusions.....	109
Chapter 6	Separation: Hardware development and testing	111
6.1	Functionality of the envisioned analyser device.....	111
6.1.1	Separation	111
6.2	Experimental methods	114
6.2.1	Designing of the chips	114
6.2.2	Membrane filter testing	114
6.2.3	Fabrication methods	115
6.2.4	Device testing methods.....	116

Table of Contents

6.2.5	Testing of dye removal using 3D printed filtration devices.....	117
6.3	Results and Discussion	118
6.3.1	Designing and testing of microfluidic channels	118
6.3.2	Fabrication of a full cross-flow filtration device	127
6.3.3	Functionality	134
6.3.4	Commercial device.....	137
6.4	Conclusion.....	146
Chapter 7	Integrated in-line analysis of Metal Organic Frameworks.....	149
7.1	Integration of the system	149
7.2	Experimental methods.....	149
7.2.1	The optimised integrated system set-up.....	149
7.2.2	In-situ spectrometer	150
7.3	Results and Discussion	152
7.3.1	Initial single system integration.....	152
7.3.2	A single system utilising a co-current separation arrangement.....	154
7.3.3	In-situ spectrometry: OceanOptics in-situ spectrometer.....	157
7.4	Conclusions	163
Chapter 8	Application of ‘print-pause-print’ for new 3D printed chemical processing technology	165
8.1	Introduction	166
8.1.2	MXenes	166
8.2	Experimental methods.....	167
8.2.1	Materials and methods.....	167
8.2.2	Filtration devices.....	168
8.2.3	Semi-continuous reaction for MXene synthesis.....	170
8.3	Results and Discussion	173
8.3.1	Cross-flow filtration device	173
8.3.2	Syringe filter.....	176
8.3.3	Reactionware: Semi-continuous etching of MAX phase	178

8.4	Conclusions.....	183
Chapter 9	Conclusions and future outlook.....	184
9.1	Summary	184
9.2	Future work	185
Chapter 10	Appendix.....	187
10.1	MATLAB code for (R,G,B) value extraction	187
List of References.....		189

Publications and Presentations

Clark M J, Garg T, Rankin K, Bradshaw D, Nightingale A M, 2023, 3D printed filtration and separation devices with integrated membranes and no post-printing assembly. *React. Chem. Eng.*, 2024, **9**, 251-259

(Submitted) Clark M J, Oakley A, Zhelev N, Carravetta M, Byrne T, Nightingale A M, Bimbo N, MXene synthesis in a semi-continuous 3D-printer PVDF flow reactor., 2024

(Drafted) Clark M J, Bradshaw D, Nightingale A M, An ‘application-led’ online analysis technique and set-up to monitor the continuous production of HKUST-1

(Drafted review paper) Clark M J, Bradshaw D, Nightingale A M, MOF monitoring- in-situ analysis of metal-organic frameworks

PorMat 2022 – Poster prize awarded

MOF2022

PorMat 2023 – Poster prize awarded

PorMat 2024

Research Thesis: Declaration of Authorship

Print name: MOLLY JANE CLARK

Title of thesis: Application-led, online analysis for the continuous production of Metal-Organic Frameworks (MOFs)

I declare that this thesis and the work presented in it are my own and has been generated by me as the result of my own original research.

I confirm that:

1. This work was done wholly or mainly while in candidature for a research degree at this University;
2. Where any part of this thesis has previously been submitted for a degree or any other qualification at this University or any other institution, this has been clearly stated;
3. Where I have consulted the published work of others, this is always clearly attributed;
4. Where I have quoted from the work of others, the source is always given. With the exception of such quotations, this thesis is entirely my own work;
5. I have acknowledged all main sources of help;
6. Where the thesis is based on work done by myself jointly with others, I have made clear exactly what was done by others and what I have contributed myself;
7. Parts of this work have been published as:-

Clark M J, Garg T, Rankin K, Bradshaw D, Nightingale A M, 2023, 3D printed filtration and separation devices with integrated membranes and no post-printing assembly. *React. Chem. Eng.*, 2024,**9**, 251-259

Signature:Date:

Acknowledgements

Completing this PhD and my studies is a significant milestone in my life, and it would not have been possible without the support, guidance, and encouragement of many people. I am deeply grateful to everyone who has helped me along this journey- professionally and non-professionally.

I extend my deepest gratitude to my supervisors. To Dr Adrian Nightingale, for your unwavering support, invaluable guidance, and endless patience. Your insight and expertise have been instrumental as I moved into the field of engineering and in shaping this work into what it is. To Dr Darren Bradshaw your encouragement, support and care have been vital in keeping me both sane and focussed throughout my university experience. Without you I would not have followed this path. Thank you both for believing in me and pushing me to achieve my best, you have been the best advisors and mentors I could have asked for.

A heartfelt thank you to my fellow PhD candidates old and new and the many project/masters students I have worked alongside. There are too many to mention but you all know who you are. Your friendships and our discussions (intellectual and not-so!) have made my research experience so special and made this journey enjoyable and unforgettable. Thank you all for keeping me sane (almost). Each of you are amazing and it has been a pleasure to work with you all. Special thanks to Tom who was a joy to work alongside with all our laughs and chats over the lab bench. Thank you for putting up with me and always being up for a drinks trip whether it be a Pret or a Pint. To India, whose friendship and support through the highs and lows has been utterly invaluable. Thank you for being my ranting partner, wine Friday partner, yoga partner and laughing partner. Finally to Niamh, you were an amazing addition to the group in the final year, you brought so many laughs and always a great pair of earrings. I can't wait to visit Southampton and see everyone soon.

To Louise, thank you for putting up with me the last 8 years. You have lived with me from undergrad to masters to PhD. Your support, brutal honesty, advice and amazing sense of humour have been a joy and you'll always be such a special friend. There are so many other people I could thank, that I am fortunate enough to call my friends who have been with me throughout my journey. I know I will be happy to tell each of them that I have FINALLY finished studying.

To my Mum and Dad, your unconditional love, support, and sacrifices have allowed me to pursue this PhD. Thank you for being the best role models, always believing in me, encouraging me to strive for excellence and helping me through every challenge. To my Aunt June, thank you for

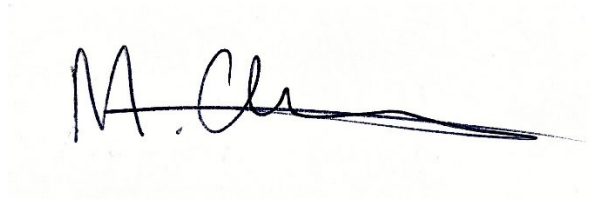
Acknowledgements

being one of my biggest supports in everything I do. Your company and sense of humour is second to none and I cant wait to celebrate over a bag of jelly babies and a bottle of wine with you.

You have all shaped me into the person I am today, and for that, I am eternally grateful. I count myself very lucky to have you all.

Finally, to my faithful best friend and little girl, Scruffy, thank you for being my source of comfort and happiness. You were always a constant reminder of the simple pleasures in life, and your unconditional love and loyalty provided solace during stressful times both inside and outside of my studies. This thesis is dedicated to you, I wish you could have been here to the end.

Thank you.

A handwritten signature in black ink, appearing to read 'M. Ch', followed by a long, horizontal, slightly wavy line that extends to the right.

If we knew what it was we were doing, it would not be called research, would it?

- **Albert Einstein**

Definitions and Abbreviations

API	Active Pharmaceutical Ingredient
BET	Brunauer-Emmett-Teller
CFD	Computational Fluid Dynamics
CVD.....	Chemical Vapour Deposition
DoE	Design of Experiments
EDS	Energy Dispersive X-Ray Spectroscopy
FDM.....	Fused Deposition Modelling
FTIR	Fourier-Transform X-Ray Spectroscopy
HKUST-1	Hong Kong University of Science and Technology
MOF.....	Metal Organic Framework
NMR	Nuclear Magnetic Resonance
PAT	Process Analytical Technology
PPP	Print Pause Print
PXRD.....	Powder X-Ray Diffraction
RGB.....	Red, Green, Blue
SBU	Secondary Building Unit
SCXRD.....	Single Crystal X-Ray Diffraction
SEM	Scanning Electron Microscopy
STY.....	Space Time Yield
TGA.....	Thermogravimetric Analysis
TMA.....	Trimethylamine
UV-Vis.....	Ultra-Violet Visible
VDW	Van Der Waals
ZIF.....	Zeolitic Imidazolate Framework

Chapter 1 Introduction

1.1 Metal organic frameworks

Metal-organic frameworks (MOFs) represent a sophisticated class of ordered, porous materials characterised by the periodic coordination of rigid metal nodes, typically comprising of metal ions or clusters known commonly as secondary building units (SBUs), and multitopic organic linkers into open crystalline frameworks.¹ This field has seen unparalleled interest since it was first termed by Yaghi *et. al.* in 1995⁵ when the successful design and synthesis of a layered material featuring cobalt centres octahedrally coordinated by 1,3,5-benzenetricarboxylate linkers was described for selective binding of aromatic guest materials. The terminology officially adopted for MOFs by IUPAC in 2013 categorised them as a dynamic, sub-class of coordination networks, which may extend into one, two or three dimensions through repeating units and need not necessarily to be crystalline.⁶ With typical attributes such as permanent porosity, high specific surface areas (several thousand m^2g^{-1}), robust thermal decomposition temperatures ($>250\text{ }^\circ\text{C}$) and diverse geometries,⁷ MOFs have emerged as compelling materials for various applications in gas storage,⁸ catalysis,⁹ CO_2 and chemical adsorption,^{10,11} hydrocarbon separation and storage,¹² drug delivery, and sensing.^{13,14} Their dynamicity make them responsive to external stimuli such as temperature and pressure, leading to structural alterations and hence changes in properties.⁷ Furthermore, the modular nature of MOFs allows for meticulous selection of both inorganic and organic moieties to achieve a high level of rational design that enables control over properties such as porosity, functionality, density, crystal size and conductivity to suit desired applications.^{1,8}

1.1.1 Structure and Geometry

The synthesis of MOFs is governed by both thermodynamic and kinetic factors, each playing a crucial role in dictating the formation and properties of the materials. Thermodynamic considerations dictate the stability and energetics of MOF formation, while kinetic factors influence the rate and mechanism of assembly, including nucleation and crystal growth processes.¹⁵ The principles of coordination chemistry play a fundamental role in MOF synthesis, governing the coordination-driven self-assembly of metal ions or clusters with organic ligands.

MOFs are typically constructed through the formation of strong coordination bonds between the metal nodes and the coordinating atoms of ligands, such as oxygen, nitrogen or sulfur.¹

Additionally, weaker, yet important, interactions such as hydrogen bonds, π - π interactions and Van Der Waals (VDWs) forces, contribute to the molecular arrangement and adopted topologies

within MOFs.⁷ The coordination of metal ions with several ligands leads to polynuclear clusters, commonly known as secondary building units (SBUs) which serve as building blocks for MOF structures.¹⁶ These can vary in complexity, sometimes involving multiple metal ions which give rise to a large number of coordination geometries when constructed together. The geometry and functionality of organic linkers play a crucial role in determining the structure and properties of MOFs. Linkers with different denticity (e.g. bi-, tri-, multi-), geometries (e.g. linear, trigonal planar, tetrahedral) and functional groups (e.g. carboxylates, imidazoles, thiols, pyridines) interact with metal ions possessing different coordination numbers, oxidation states and sizes leading to diverse MOF architectures with varied pore sizes, volumes, shapes and functionalities.¹⁶ The geometry and connectivity of these components determine the MOFs topological structure, ranging from simple frameworks (e.g. cubic, tetragonal) to more complex arrangements (e.g. zeolitic, interpenetrated).¹ Finally, the stoichiometry and metal:ligand ratio influence the composition and properties of MOFs, control of this ratio further allows for the tuning of framework properties. Figure 1.1 shows an example of a benchmark MOF, called HKUST-1.

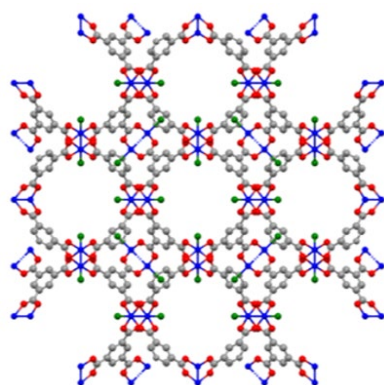


Figure 1.1: Image of copper-based MOF, HKUST-1 generated on Mercury. Grey, carbon; red, oxygen; royal blue, copper. Hydrogens have been omitted for clarity and the green ellipsoid represents exchangeable water at the axial position.

1.1.2 MOF synthesis: Solvothermal

Solvo- or hydrothermal synthesis is the most basic and facile practise for MOF synthesis, affording thousands of known structures and enabling new synthesis. In this method, reagents are dissolved and combined in a solvent medium within closed vessels, such as Teflon-lined autoclaves, operating under autogenous pressure at temperatures exceeding the boiling point of the solvent.¹⁷ Typically, reactions are carried out in high boiling point, polar solvents or their mixtures (dimethylformamide (DMF), diethylformamide (DEF), acetonitrile (MeCN), ethanol (EtOH), water (H₂O) etc.), at elevated temperatures for extended periods of time ranging from hours to days. Higher temperatures serve to facilitate bond formations, while slow, controlled cooling rates have been shown to affect crystal growth.¹⁸ This method is an example of a batch-

type process where reactions are carried out independently of one another in cycles where each cycle produces a batch of product.

Alternative and well-regarded synthetic approaches for MOFs include microwave-assisted,¹⁹ electrochemical,²⁰ mechanochemical²¹ and chemical vapour deposition (CVD)²² methods. These methods tend to require specialist equipment and skill in practise. Despite existing methods giving the general chemist the means to produce high quality MOF crystals, traditional synthetic routes impose major challenges in terms of long crystallisation periods, poor reproducibility²³ and difficult in manufacturing on the kilo to tonne scale.¹⁷

MOF coordination relies upon nucleation at the vessel surface. A simple upscale in reaction vessel volume significantly reduces the surface to volume ratio²³ and hence, the reaction efficiency with respect to the yield and/or product quality.²⁴ Therefore, a method to conveniently expand the reaction scale whilst maintaining or improving vessel proportions is extremely attractive to applied MOF chemistry. Researchers have worked to develop versatile, scaled up methods with several reported examples in mechanochemical synthesis,²⁵ spray-drying assisted methods¹⁷ and flow chemistry.^{26,27,28}

1.1.3 Scale Up Methods

Mechanosynthesis is a well-known technique whereby MOF precursors are milled without the need for solvent to promote chemical reaction. The solvent-free conditions mean a fast and efficient synthesis can occur with low solubility precursors and good reproducibility compared to other methods.²⁹ Until recently, mechanochemical synthesis has been a batch processing technique meaning production rate is low however, twin screw extrusion is a relatively new method whereby reactants are transported through an interlocked screw configuration using continuous, positive displacement conveying which moves material along the barrel of the system by trapping it within intermeshing screw channels. This serves as a reliable and precise method for continuous MOF production³⁰ however it has a high energy usage, significant space requirements and requires regular upkeep and cleaning to ensure product quality and assurance.

Spray drying methods use the rapid evaporation of reaction mixtures to produce highly dispersed powders. It is a simple and continuous processing method that has been applied for many MOFs including high nuclearity SBU frameworks, multimetallic frameworks and MOF composites.¹⁷ Despite this, the initial set-up is expensive and thermal efficiency is low meaning high energy usage and poor environmental implications. Furthermore, it is a messy process and equipment

cleaning is extensive and time-consuming but necessary to prevent unwanted materials or the build-up of impurities and unreacted material.

Flow processing is a versatile technique that continuously produces product by flowing reagent solutions together. It has excellent heat and mass transfer properties and hence, high production rates and reactors can be constructed from basic and inexpensive materials. Furthermore, downstream processes such as purification and analysis can be integrated, and optimisation algorithms may be used to give an autonomous system from synthesis to analysis.^{31,32} A basic flow setup offers the ability for unlimited scale up through longer operation or increased flow rates, removes the batch-to-batch variability and enables the incorporation of quality control procedures *via* in-line or on-line analysis. Hence, it is a great strategy for production that has been chosen as the focus for this project in particular the possibility of in-line analysis of flow-synthesised MOFs with a view in developing more production-friendly, quality-assured methods for making MOFs defined by highly crystalline products showing good monodispersity, uniform morphology and characterisation data matching that previously reported and deposited within the Cambridge crystallographic database (ccdc).

Chapter 2 Literature Review: Flow synthesis and In-line analysis for Metal Organic Frameworks

In this chapter I will start by reviewing the current literature surrounding flow synthesis for MOFs. I will then assess and discuss current in-line analysis techniques which provide insight *via* real time data into synthetic flow setups.

2.1 Continuous flow synthesis

Continuous flow processing is crucial to the pharma sector,^{33,34} being well established in the petrochemical and fine chemical industry as standard, becoming more common for low volume, high value chemical production now also.³⁵ More recently, rapid development has been seen in the continuous synthesis of inorganic, functional materials such as nanoparticles,³⁶ quantum dots^{37,38} and MOFs.³⁹ Benefitting greatly from its steady state operation, precise variable control and broader green implications, flow chemistry is of keen interest within many branches of chemistry.

2.1.1 General setup of a flow reactor

The inherent modularity of flow reactors means they may be set-up in various ways with multiple, dependent steps and cycles; however, this may be generalised. Figure 2.1 shows the general set-up for a simple, two-feed flow reactor with an integrated analysis and feedback algorithm. It is worth noting that this is a one-step reaction, but flow syntheses can have multiple reaction work up and analysis stages.

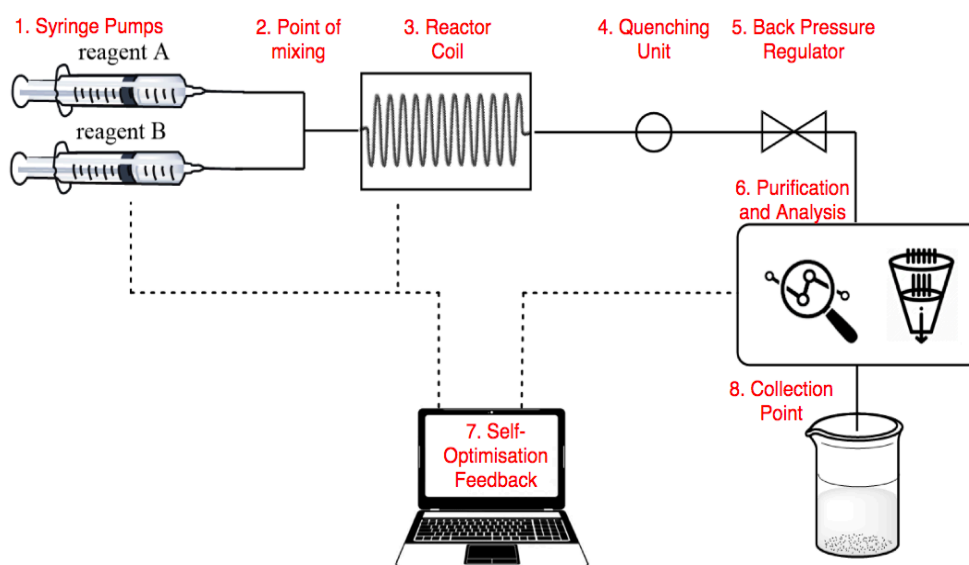


Figure 2.1: The general setup for a flow reactor. Adapted from Chem. Rev.2017, 117, 11796–11893.

The components are as follows: 1. Reagent delivery- for common lab-scale continuous processing, syringe or peristaltic pumps are used for controlled delivery of reagents at specified flow rates; 2. Point of mixing- these are commonly Y- or T- shaped junction points. Active and passive mixing of the fluids is complex with a lot of influencing factors including but not limited to the physical design of the reactor and flow pattern e.g. single or multiphase flow, size of the channels etc;⁴⁰ 3. Reactor coil- this may be submersed in an oil bath, ultrasonicated, submitted to a form of irradiation or placed under pressure for the reaction to occur. The length of this coil, along with the associated flow rate, dictates the reaction time and may easily be lengthened or shortened as required, this is commonly referred to as the residence time; 4- Quenching unit, an appropriate procedure is sometimes needed to terminate the reaction upon leaving the reactor unit thus, avoiding unreliable results and possible side reactions; 5- Back pressure regulator, this component allow reactions to be performed under elevated pressures by providing a constant upstream pressure. High pressure conditions mean reactions may occur in solvents at temperatures exceeding their boiling point which is key in many methodologies; 6- Optional steps involve the integration of in-line analysis and purification platforms to produce real-time data or higher quality product; 7- Self-optimisation algorithms form closed loops for autonomous and precise multivariate control of reaction parameters (e.g. reagent concentrations, flow rates, temperature, pressure etc.); 8- A collection point for the end product.

2.1.2 Benefits of flow processing

In contrast to a batch process, a flow set-up involves a reaction typically occurring in a pipe with an impressive number of advantages.

Firstly, small diameter flow systems (100s of microns) offer high surface area to volume ratios, surpassing those of batch-type reactors. This gives faster heat transfer rates with uniform reaction environments. As a result, reactions can occur over shorter time periods and new synthetic pathways can be promoted. Competitive space-time yield (STY) values are reported for systems under flow due to continuous and consistent production as well as superior mass transfer efficiency.³¹ This value is a measure of the amount of product produced per unit volume of the reactor in a 24 hr period measured in $\text{kgm}^{-3}\text{day}^{-1}$. A greater STY value means producing more product in the same amount of time, increasing a reaction's economic and environmental viability.

Another key benefit of flow chemistry is that it enables precise multivariate control over the reaction parameters which, when combined with in-line or on-line monitoring, allows reaction

optimisation 'on-the-fly'.⁴¹ Stable reagents and solvents that will not degrade or foul the channels are key to achieve this to maintain optimal and consistent function and prolong lifetime of the flow reactor.³⁶ Many reaction parameters may be adjusted (e.g. concentrations, flow rates, pressure, temperature) easily and the subsequent effect can be closely monitored. A good example of this is the tuneable synthesis of silver nanoparticles, through simple adjustment of the initial silver precursor concentration varying nanoparticle sizes (5-10 nm) may be synthesised on command.⁴² This has also been demonstrated during the continuous synthesis of UiO-66 by Taddei *et. al.*⁴³

Furthermore, reduced volumes, easy automation and excellent heat and mass transport intensification properties of the reactors mean highly reactive reagents, harsh conditions or toxic and harmful chemicals can be used safely.⁴¹ For example, during the organometallic synthesis of rimonabant and efaproxiral, multiple steps were necessary to successfully use highly pyrophoric chemical, trimethylammonium (TMA) in THF at high temperatures for direct amide formation. To do this in a batch-style process, low volumes and a glove box or Schlenk-line apparatus is necessary to reduce risk and avoid contact of TMA with oxygen.⁴⁴ By using continuous synthesis, higher space time yields were seen along with less manual handling and reduced risk, demonstrating its advantage.

A big advantage to the use of flow processing is set-up modulation. Integration of downstream processes such as purification or analysis is possible.¹⁷ It is generally rare for a product to be isolated directly from its reaction mixture without further purification such as solvent exchange, immobilisation or activation. Moreover, analytical devices and in-line spectroscopic techniques can also be implemented to produce real time data for reaction monitoring. Partnering the precise variable control with self-optimisation algorithms, a flow reactor may be fully automated and optimised based on satisfaction coefficients embedded in the algorithm dictating the optimal result.

Finally, scale up of many orders of magnitude without fundamentally changing the process is more straightforward. Flow reactors offer a 'smart dimensioning' element whereby their performance and efficiency are unaffected by changes to the reactor coil length or integration of further steps such as analysis. This was demonstrated by Rubio-Martinez *et. al.* for the scalable continuous processing of benchmark MOF, Al-fumarate.³¹

However, flow processing isn't without problems. Channel fouling is a significant obstacle whereby material can cling to the inner walls of the flow reactor potentially clogging the channels

and affecting the flow and heat transfer rates. This has been well documented in the continuous synthesis of gold nanoparticles (Au-NPs).⁴⁵ In efforts to prevent this, segmented flow has been used whereby an immiscible oil is used to favourably wet the inner walls and carry discrete aqueous droplets of the reaction mixture.⁴⁵ This has been successfully applied, however, increased concentrations have also been shown to cause considerable fouling.⁴⁵

A second method using sodium citrate as a surfactant to prevent agglomeration has also been demonstrated by Bianchi *et. al.* who presented a novel, scalable, photochemical flow process to synthesise small spherical Au-NPs, avoiding fouling during scale up with lithium phenyl-2,4,6-trimethylbenzoylphosphinate and sodium citrate as the initiator and stabilising species that prevents fouling. From scale up, they were successfully able to produce a daily output of 65 gday⁻¹.⁴⁶ A critical consideration when designing and operating a flow system is the dimensions as small changes can have profound effects. For example, the volumetric flow rate (Q) holds a proportional relationship with the quartic radius of the tube (R⁴) as stated within the Hagen-Poiseuille law which relates the length of the reactor, volumetric flow rate and reactor radii. (Equation 1) Nonetheless, the various benefits of flow processing interlink to make an overall very desirable setup. In the next section, the different type of analysis methods that may be implemented within continuous processes are discussed.

Equation 1: The Hagen-Poiseuille Law. Where p=pressure, μ = dynamic viscosity, L= length of the reactor, Q= volumetric flow rate, R= radii of the reactor.

$$Q = \frac{\Delta p R^4 \pi}{8 \mu L}$$

2.1.3 Analysis methods

Miniaturised analysis of reaction mixtures may be carried out several ways in continuous flow including 'off-line', 'on-line' and 'in-line' analysis. (Figure 2.2) Firstly, and most commonly, is off-line analysis where the reaction and data collection stages are separate, and samples require manual collection and preparation for analysis. Of the methods, it is the most inefficient and labour-intensive but sufficient for laboratory-scale work. On-line analytical techniques remove the need for manual intervention by automatically sampling the reaction mixture at regular periods and delivering it for direct analysis. If the analytical method can collect data as the reaction progresses without affecting the reaction mixture, it may be integrated in-line within a flow process system.⁴¹

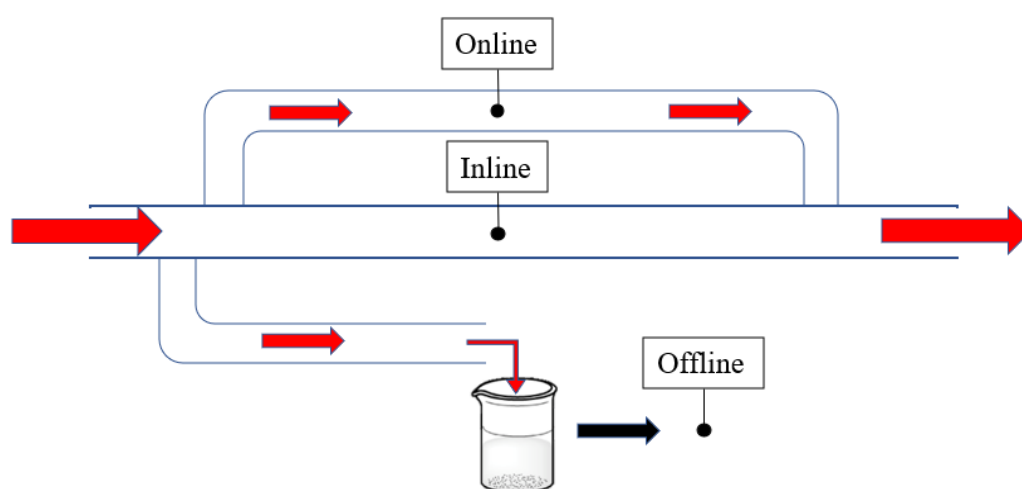


Figure 2.2: Diagram highlighting the differences in on-line, in-line and off-line analysis within a flow set-up. Red arrows represent the direction of flow.

In-line analysis defines the use of analytical techniques to give real time or in-situ data directly from the reaction vessel. This is possible within batch or continuous set-ups and is widely used within organic chemistry and the pharmaceutical industry in particular,^{47,48,49} and has also been applied to materials synthesis, such as colloidal quantum dots⁵⁰ and optoelectronic polymers.⁵¹ By probing intermediate reaction stages, in-line data can give information on reaction intermediates, pathways, and kinetics. This can be used to develop and hone techniques for synthesis of MOFs and help to deepen our understanding of their self-construction mechanism and what is happening within the reaction vessel from reactant to product. Moreover, when used in a flow reactor, parameters can be readily tuned for fast optimisation and exploration of the parameter space. It also makes for a powerful quality assurance tool for production, ensuring that product meets defined criteria without the need for manually intensive off-line analysis. Numerous techniques have been used for in-line analysis such as nuclear magnetic resonance (NMR),^{52,53}

infrared (IR),^{54,55} Raman,³⁴ UV-Vis,^{56,57} and fluorescence spectroscopies.⁵⁸ Off-line analysis is used to do all of this also but is a bit slower in practice due to the need for sampling.

2.1.3.1 In-line analytical techniques

There are many techniques that have been successfully applied for in-line analysis and monitoring. When selecting a technique, several criteria need to be addressed. Primarily it needs to give pertinent data on the material being studied (e.g. IR spectroscopy for functional group modification in organic molecules, fluorescence spectroscopy for colloidal quantum dots gives information on size and size distribution). The more information that can be obtained from that data the better (e.g. a single IR spectrum can give information on multiple different reagents, products and intermediates).⁵⁹ There is also a practical requirement; the technique must be accessible when considering expense, availability, and ease of use. Several techniques can be used in parallel to obtain complementary and confirmatory data for fuller insights into the reaction or product and off-line analysis is often used also. Due to the flexibility of flow anatomy, analytical devices and hence data may be collected at any point or at numerous locations along the set-up. Moreover, process analytical technology (PAT) such as logic and digital feedback loops may be implemented for self-optimisation, working towards autonomous and intelligent systems.

Bart *et. al.* successfully developed a high-resolution microfluidic probe using in-situ NMR spectroscopy to monitor the rapid amine-catalysed acetylation of benzyl alcohol in batch. Fine analysis of the data showed 70 % conversion within the first 3 minutes of reaction. This was further developed for monitoring the reaction of acetyl chloride with benzyl alcohol using hazardous and difficult to handle compound, triethylamine. From the data, intermediate species and reaction mechanisms were identified and proposed.⁶⁰ In another example, UV-Vis spectroscopy was used as a fast-working PAT tool for monitoring RAFT polymerisation of monomer units. Spectra were obtained every 10 s and used to assess the amount of conversion, showing efficient polymerisation screening with significantly reduced time scales.⁶¹ Furthermore, Raman spectroscopy has been used to monitor complex catalytic reactions in the selective oxidation of benzyl alcohol, catalysed by Au-Pd on a TiO₂ support. The response of the carbonyl band (C=O) was monitored to distinguish the effects of individual parameters leading to the elucidation of optimal conditions for a 95.5 % yield.⁶²

It is possible to not only integrate these sorts of devices at any point in a multistep flow synthesis, but also have multiple points of analysis. A good demonstration of both these points was recently shown by Sagmeister *et. al.*³⁴ who presented an integrated multistep synthesis of pharmaceutical, mesalazine on a single platform with four complimentary analytical techniques. The in-line techniques used (NMR, UV-Vis and IR spectroscopies) facilitated reaction monitoring at each stage of the synthesis (Figure 2.3) and were placed to capitalise on individual advantages in the data obtained. The first stage of synthesis was nitration, it was monitored by NMR spectroscopy to give compositional information on the regioisomer products in the mixture. UV-Vis spectroscopy was used after hydrolysis and finally, IR spectroscopy to give key spectroscopic data about the nitro-group reduction. Finally, an on-line UHPLC quantification taken every seven minutes was used to get a detailed reaction composition of the end mixture. The system worked well at steady state producing 1.6 gh^{-1} with potential for scale up and responded well to changes in various parameters and moreover, demonstrated how in-line and on-line analyses can be combined with flow chemistry to give controlled, quality assured production.

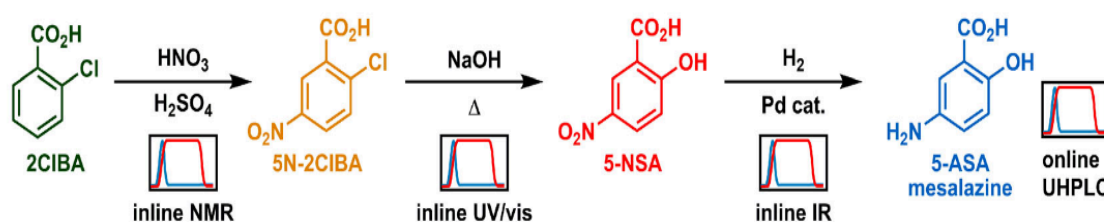


Figure 2.3: The multistep synthesis and advanced PAT used under continuous flow for API drug, mesalazine.³³

2.1.4 Self-optimisation

Self-optimisation is a process by which flow reactors are combined with process analytics and optimisation algorithms including local or global search strategies.³² These algorithms use experimental data to decide logical experimental conditions in search of optimal reaction conditions. Advances in automation within chemistry have naturally led to the increased use of algorithms which permit closed loops and digital feedback control in flow systems. This approach enables rapid and efficient exploration of the reaction parameter space, making them well suited for optimisation problems and predicting chemical reactivity and outcomes.

Traditionally, optimal conditions are determined through a rational Design of Experiments (DoE) by making logical adjustments to different variables of a reaction to isolate and identify the effects on the product.⁶³ This is a complex and generally inefficient process, with the likelihood of determining complete and optimised conditions slim. As outlined, in-line monitoring permits real

time or in-situ data generation and, when combined with self-optimisation algorithms, data is subsequently read and structured as part of a closed feedback loop. High volumes of relevant data are extracted and collated into a knowledge-base which may be employed by the algorithm to facilitate process control and achieve its user-defined output (e.g. product optimisation for yield, crystallinity or crystal size).⁴¹

In an early report, self-optimisation was used to tune the properties of fluorescent CdSe nanoparticles by integrating an in-line spectrometer and employing a global search algorithm.³⁶ More recently, similar methods have been applied to seamlessly synthesise lead-halide perovskite quantum dots (LHP QDs) with tuneable optical properties in a high-throughput manner.³⁸ Integrating a custom-flow cell to obtain photoluminescence data, (Figure 2.4B) they demonstrated an AI-guided approach to extensively explore and document the parameter space with 10-fold multivariate control. In less than 40 minutes, the optimal conditions for 10 distinctly emitting LHP QDs were realised. (Figure 2.4A) For the case of all self-optimisation reactors, they depend on having appropriate in-line/on-line analysis methods that can autonomously give metrics on product quality and/or quantity.

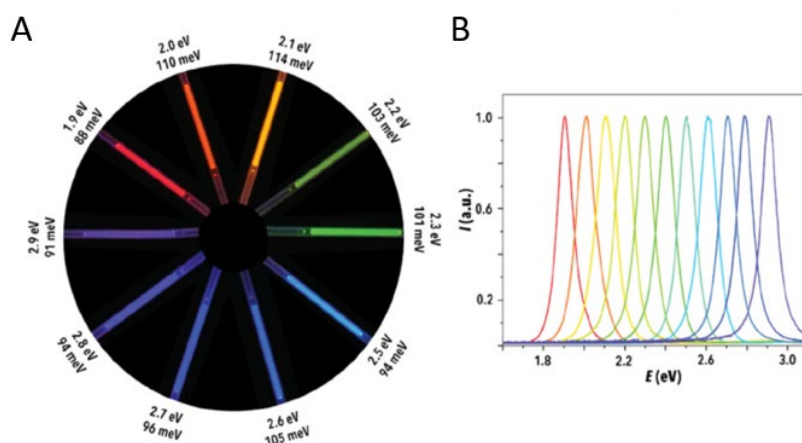


Figure 2.4: A) UV-illuminated, optimised LHP QD synthesised using self-optimisation algorithms; B) Photoluminescence spectra collected in-line of the 10 optimised CsPbX₃ (X= Cl, Br, I) QDs.³⁸

2.2 Flow synthesis of MOFs

Recent literature suggests that continuous flow processing presents a promising approach for both the synthesis and scalable production of MOF structures. Pure, high-quality framework can be reliably produced and tuned accordingly *via* a diverse array of set-ups that are readily scaled up. Continuous processing has demonstrated its applicability for many well-established and lesser known MOFs with several reviews having been written.^{17,23,27,64} Furthermore, this method has

facilitated the synthesis of novel MOFs and the development of innovative methods, exploiting the unique transport properties inherent to flow systems and highlighting its advantages. This short review will explore microfluidics as the predominant method for continuous synthesis of MOFs due to its relevance with the work discussed in this thesis, with notable studies highlighting the advantages of flow based approaches to traditional batch processing. Additionally, alternative forms of continuous reactor will be briefly discussed along with recent advances in the field including the synthesis of MOF biocomposites and the integration of downstream processes. This review seeks to provide insights into the development and application of continuous processing for MOF fabrication, highlighting its role in driving progress within the field.

2.2.1 Microfluidics and segmented flow

Microfluidic (MF) flow processing uses microscale flow reactors (cross-sectional dimensions of 10s-100s of microns) and can be readily constructed from simple materials.⁶⁵ These systems offer precise control over fluid dynamics, characterised by well-defined flow patterns,²⁷ favourable separation efficiencies and enhanced transport properties due to the small volumes involved. The use of microfluidic platforms within the field of MOF synthesis has gained prominence recently.

Often, an immiscible carrier fluid is used to introduce segmented flow within the system, a strategy aimed at mitigating clogging while simultaneously promoting internal mixing.²³ Faustini *et. al.* utilised segmented flow in a novel approach to prepare benchmark MOFs: HKUST-1, MOF-5, UiO-66 and IRMOF-3.⁶⁶ In this case, premixed precursor solutions were infused, as uniform droplets, in silicone oil to act as nanolitre-sized reactors. (Figure 2.5A) HKUST-1 was detected in less than a minute, highlighting the intensified transfer properties seen in flow, specifically MFs. They demonstrated, through precise multivariate control, that increased precursor concentrations and longer residence times yielded lower Brunauer-Emmett-Teller (BET) surface areas with the highest being recorded after 3 minutes at 90°C. Furthermore, after a residence time of 12 minutes, a 68 % yield was obtained. In a batch solvothermal synthesis, a STY value.

In the same report 65 % yield wasn't recorded until 24 hr; an improvement on both the experimental conditions and, versatility and development of the method was demonstrated, showing how non-conventional synthesis and seamless integration of flow processing is possible. Tricky Ru₃BTC₂ structures were successfully isolated and a two-step integration platform for the synthesis of three core-shell MOF composites was shown.⁶⁶ Notably, this included well-documented magnetic material, Fe₃O₄@ZIF-8, which is useful for facile separation and

immobilisation through switchable, external magnetization, for example.⁶⁶

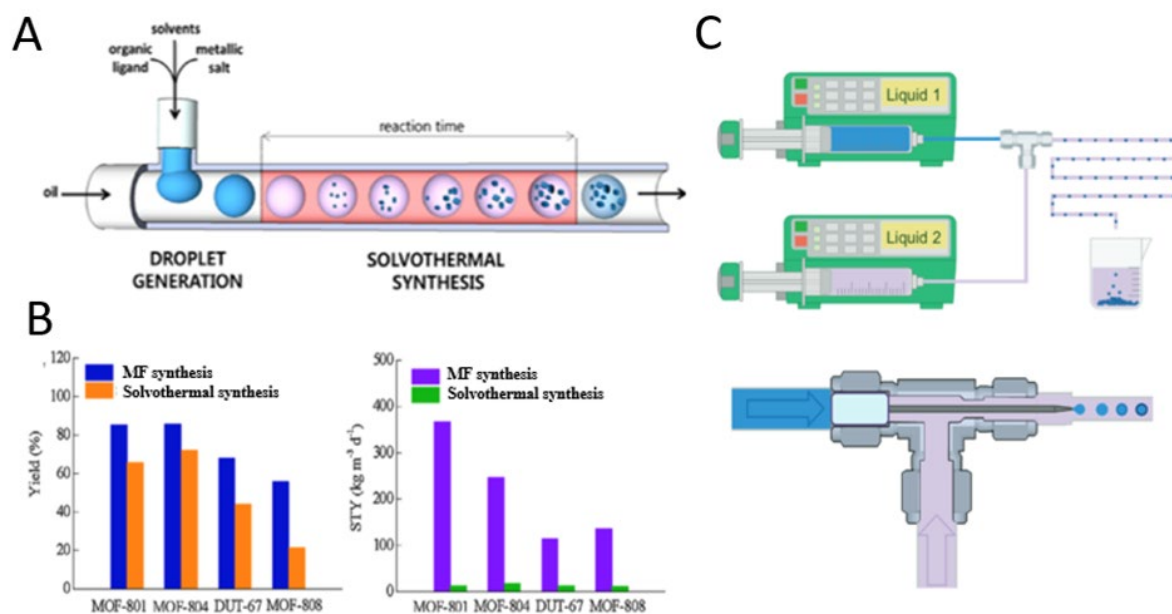


Figure 2.5: A) Synthetic diagram showing the formation of nanolitre sized droplets of precursor solutions (blue) to be carried in oil, acting as microreactors for solvothermal synthesis.⁶⁶ B) Bar charts comparing the yield microfluidic and solvothermal methods for a series of frameworks with respect to percentage yield and STY values.⁷¹ C) Process overview showing the two immiscible liquids supplied through syringe pumps to the T-junction and a close up of the junction. The formation of aqueous droplets (blue) in the continuous organic phase (pink) occurs at the junction and hollow capsules of HKUST-1 (dark blue) subsequently form due to self-crystallisation at the liquid-liquid interface.⁷²

In a separate study this method was applied for scalable synthesis of Zr-based MOF composite UiO-66@MgFe₂O₄.⁶⁷ Upscale of the reaction was demonstrated, moving from milli to gram scale synthesis with production rates of 0.27 to 12.87 ghr⁻¹. Furthermore, the STY values were 24 times that recorded for batch synthesis. Highlighting two major advantages inherent to flow processing.

Microfluidic reactors have further been applied in this way for most significant MOF structures including ZIF-8,⁶⁸ the MIL-88 family⁶⁹ (M= Fe, Cr, Sc) and CPO-27 (Ni).⁷⁰ Individual works have developed a series of MOFs such as the MOF-801, -808, -804 family with STY values and % yields outperforming those previously reported in all cases and crystallinity being matched or improved upon.⁷¹ (Figure 2.5B)

In a recent study, continuous flow was employed for the accelerated synthesis of $[\text{Ni}_2\text{Cl}_2(\text{BTDD})]$ (H_2BTDD = bis(1H-1,2,3-triazolo- [4,5-b], [4',5'-i] dibenzo-[1,4]-dioxin) for atmospheric water capture.⁶³ Dramatic improvements to the STY and optimisation of synthesis conditions were achieved through manual exploration of the synthesis space utilising a DoE approach and multivariate control techniques. (Figure 2.6) Furthermore, computational fluid dynamics (CFD) was used to strategically plan for a target production rate of 1 kg per month. The modularity and flexibility inherent to flow reactors were instrumental in enabling such planning and versatility for large scale production.

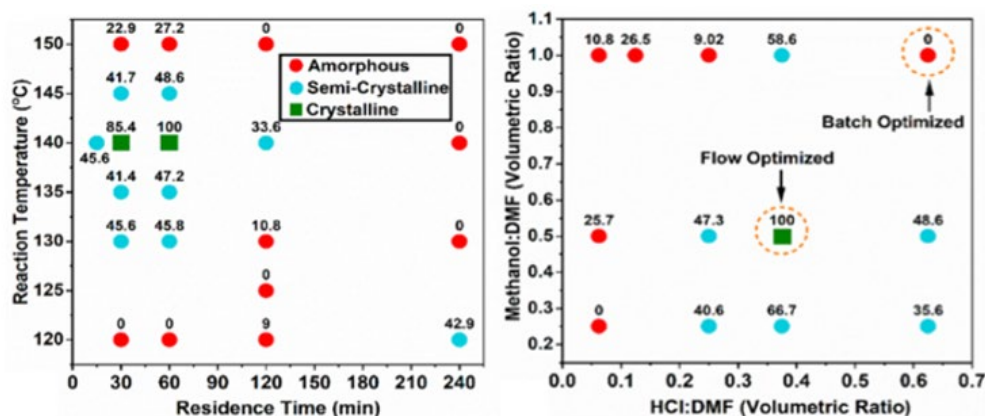


Figure 2.6: Maps of the parameter space investigated for the flow synthesis of $\text{Ni}_2\text{Cl}_2(\text{BTDD})$, varying the reaction temperature and residence time (left) then the volumetric ratios of MeOH/DMF and HCl/DMF solvent mixtures at a fixed temperature, residence time and metal/linker ratio (140 °C, 1 hr, 2.2:1, respectively) (right). Label numbers represent the relative % crystallinity, quantified using PXRD peak intensities.⁶³

MF can also be harnessed to make templated MOF structures that would be difficult in batch methods. In an early example of the continuous synthesis of MOFs, segmented flow was employed to exploit the interface of the droplet sphere formed between immiscible fluids as a template for synthesis.⁷² Two syringe pumps containing a) metal-ion containing aqueous solution and b) linker containing organic phase supplied a microfluidic reactor through a T-junction. (Figure 2.5C) Due to liquid immiscibility, the organic phase can favourably wet the vessel lining and discrete, aqueous droplets form to be carried in flow. A self-completing crystallisation at the liquid-liquid interface produced hollow capsules of Cu-based MOF, HKUST-1 ($[\text{Cu}_3(\text{BTC})_2(\text{H}_2\text{O})_3]$ where BTC = 1,3,5-benzenetricarboxylate) with uniform thickness, minimal permeability and no further purification required. These hollow spheres are useful MOF constructs; they may be used to encapsulate species for applications in controlled drug delivery as an example. In batch reports, synthesis of such structures can require hard templates for removal post synthesis⁷³ which can afford permeable or incomplete crystallisation.

Finally, MFs has been shown to promote new chemical reactivity for framework synthesis. Novel cerium-based framework, $[\text{Ce}_5(\text{BDC})_{7.5}(\text{DMF})_4]$ (DMF= N,N-dimethylformamide) was synthesised as sub-micrometre agglomerates in an ultrafast manner (<30 s). Solvothermal batch synthesis later performed needed 12 hrs at 150 °C for micrometre sized crystals to form showing another improvement on the STY values of batch vs flow processing.⁷⁴

2.2.2 Alternative continuous setups

Continuous processing is not limited to microfluidic dimensions. Other reactor types reported for MOF synthesis include plug-flow reactors (PFR) and continuously stirred tank reactors (CSTR). It is worth noting, both these types of reactors may be constructed with microfluidic dimensions.

2.2.2.1 Plug flow reactors

A plug flow reactor is an idealised model whereby segments, or ‘plugs’ of precursor solutions move as discrete entities down a tubular reactor with no mixing or back flow. (Figure 2.7)

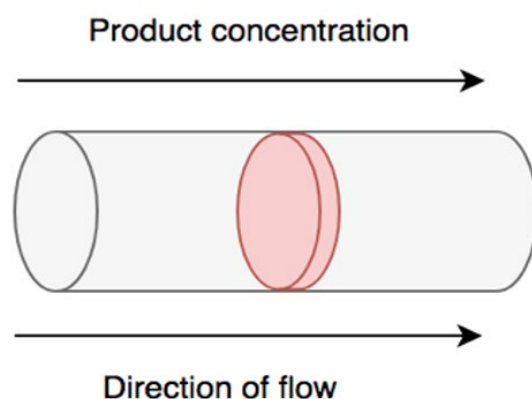


Figure 2.7: A simplified diagram for a PFR model, showing a single discrete plug flowing axially.

As precursors react, the composition of the slugs varies to increase the concentration of the desired products. This model is described as idealised as it not realistic with the discrete segments exhibiting Taylor dispersion. (Figure 2.8) In this movement, the shear flow of parallel streamlines along the capillary move at different velocities when assuming Laminar flow. Laminar flow is a smooth and regular flow of fluid particles in parallel layers. The cross-sectional velocity differences and radial diffusion of the slugs causes an axial dispersion of molecules for back mixing and can be combatted by inducing cross channel mixing.

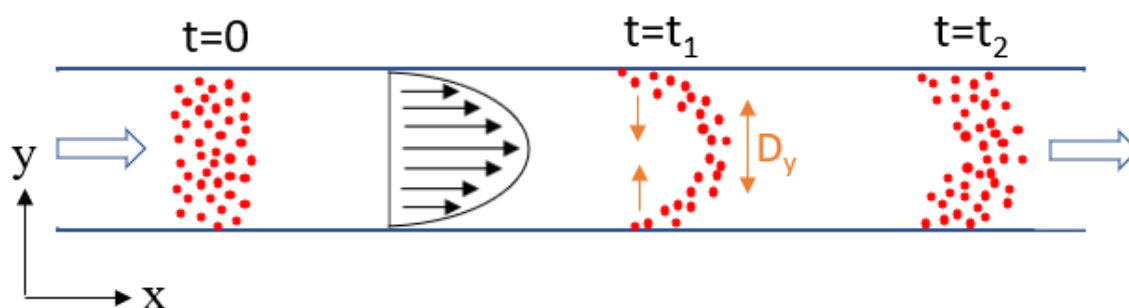


Figure 2.8: Diagram showing Taylor dispersion. Discrete 'plugs' enter the reactor (t_0) they are subjected to a range of velocities (u , black arrows) with the central small molecules travelling at maximum velocity (u_{\max}) and those close to the tubular walls experiencing the lowest velocity (u_{\min}) this causes a distortion of the plugs (t_1) with diffusion gradients (orange arrows) being formed. Molecules diffuse along these gradients (D_y) to give enhanced diffusion of the plugs downstream (t_2).

Gimeno-Fabra *et al.* presented the first continuous plug-flow reactor for prototypical MOFs: HKUST-1 and CPO-27 using counter current mixing.⁷⁵ A precursor-solvent solution was injected upstream to meet a downstream flow of superheated water at a mixing point upon which nucleation can occur. Control of the concentrations and temperatures meant the MOF crystal size could be tuned; in the case of CPO-27 this was by a whole order of magnitude (nano to micro scale). Surface areas of $1030 \text{ m}^2\text{g}^{-1}$ and $1950 \text{ m}^2\text{g}^{-1}$ were reported for CPO-27 and HKUST-1, respectively which have not been improved on for HKUST-1. Interestingly, the reported STY for CPO-27 ($1501 \text{ kgm}^{-3}\text{day}^{-1}$) using this setup was much higher than for MF synthesis ($806 \text{ kgm}^{-3}\text{day}^{-1}$) but a similar surface area of $1085 \text{ m}^2\text{g}^{-1}$. A possible reason for this unexpected difference being the microfluidic system used a water only solvent system and reduced temperatures (90 vs 300°C). This demonstrates the green and energy saving implications of microfluidic dimensions in flow as well as its ability to promote new chemical reactivity. It is also a good example of where microfluidics dimensions have been used and not necessarily given the better STY value highlighting the competing sustainability factors whereby the flow process would need to be run for a longer time period to achieve the same product yield.

In 2014, Rubio Martinez *et. al.* highlighted the versatility of PFRs synthesising MOFs: NOTT-400, UiO-66 and HKUST-1 in times of 10, 10 and 15 mins, respectively.⁷⁶ (Figure 2.9A) All times and temperatures reported vast improvement from their usual 24 hr batch-reaction times. Through using a logical DoE approach, manual optimisation was achieved, and a diagram was constructed from data collected for flow HKUST-1 to show the influence of 9 individual parameters on the production quality which, in this case, was defined as the product of the calculated BET surface area (SA_{BET}) and percentage yield (Yield%). (Figure 2.9B)

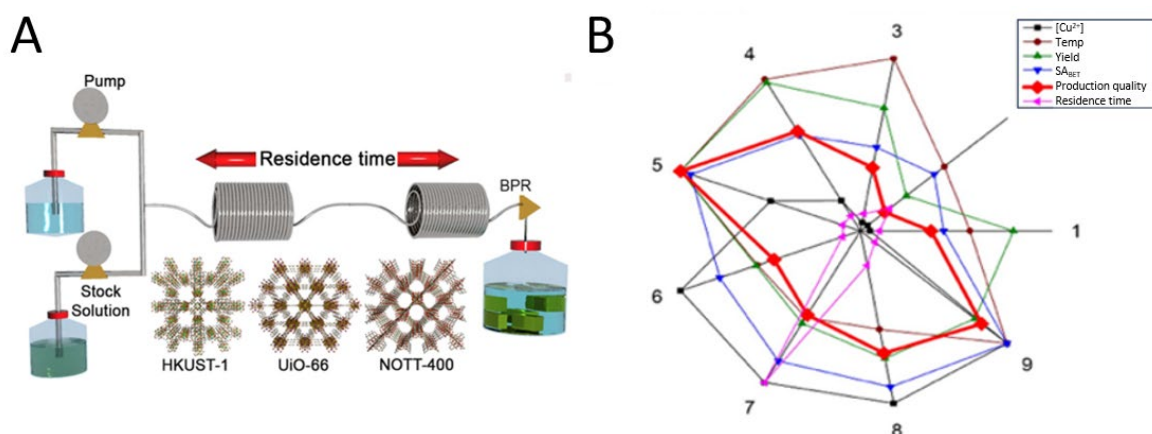


Figure 2.9: A) A versatile PFR schematic used in the synthesis of HKUST-1, UiO-66 and NOTT-400, differing by the relative residence time.⁷⁶ B) An overview of the influence of reaction parameters on the HKUST-1 product based on the experimental conditions laid out. In this case, production quality was defined as the product of the calculated BET values and percentage yield.⁷⁶

2.2.2.2 Continuously stirred tank reactors (CSTR)

Another alternative flow set-up is continuously stirred tank reactors (CSTR) which use tanks for reaction under stirring with a continuous stream of incoming and outgoing material and uniform, steady state composition. (Figure 2.10)

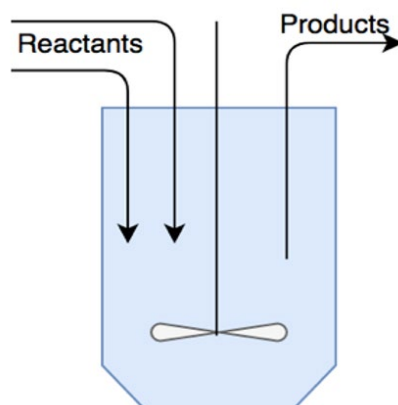


Figure 2.10: A simplified diagram for CSTR. Black arrows represent the movement of fluid and the grey turbine shape represents a stirrer.

Finally, classic MOF, MOF-5 crystals (13-40 μm) were synthesised in a continuous stirred tank reactor after 2 hours with a maximum STY of $1000 \text{ kgm}^{-3}\text{day}^{-1}$. (Figure 2.11) The residence time was adjusted accordingly to understand and optimise the reaction with respect to the STY value. The method showed high yields (82 %), scalability and reasonable optimisation.⁷⁷

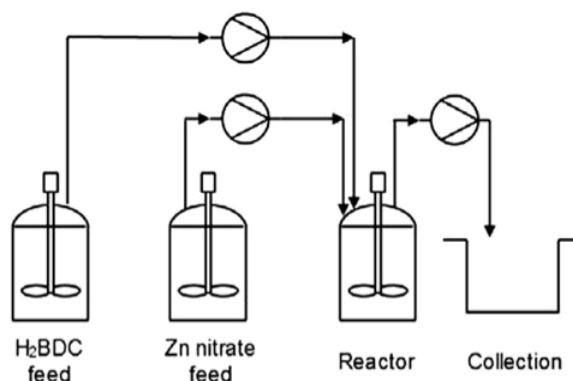


Figure 2.11: A) Schematic for a CSTR for the synthesis of MOF-5 in less than 2 hours.⁷⁷

2.2.2.3 Disadvantages to alternative flow set-ups

Despite PFR and CSTR set-ups providing proven potential in the continuous synthesis of MOFs and the fact they may be constructed on microfluidic scales. They have inherent disadvantages as to why they were not chosen for use in this PhD research. Plug flow reactors struggle with scalability issues; through altering either the cross-sectional diameter or length of the tubular reactor, the internal mixing and residence times or flow rates required are inherently affected. On the other hand, CSTRs struggle with residence time distributions, where maintaining a consistent residence time for the whole volume as it is transferred from each section of the set-up is difficult to control and leads to variation.

2.3 Candidate techniques for In-line/On-line MOF analysis

One of the advantages of flow reactors is the potential for automation, and the use of in-line/on-line analysis to self-optimize reactions or get quality-assured production. While there have been numerous papers describing continuous MOF synthesis, there have been very few that exploit this advantage. Here I look in more detail at candidate analysis techniques.

Not all standard MOF techniques can be implemented in-situ due to their destructive/invasive nature or a lack of facilitating instrument technology. As such, researchers have explored alternative analytical techniques, such as 'indirect' tracking of solvent species or combined in- and ex-situ studies, to monitor MOF crystallisation.

This section seeks to highlight the potential of in-situ monitoring when applied to MOF synthesis. In contrast to previous reviews,^{78,79,80} which focused on how in-situ techniques can elucidate and give understanding of the fundamental dynamic processes occurring during nucleation and growth, the motivation is to evaluate previously reported in-situ techniques and ascertain their applicability to specialist studies but also as routine tools to optimise new processes or syntheses, or be used as quality control systems for production. This will be discussed in terms of two criteria – accessibility and usefulness. In this context I will discuss the advantages and disadvantages of previously reported analytical techniques and suggest how these can be improved or adapted to continuous synthesis in the future. This literature review has been prepared for submission to a journal, aiming to contribute to the advancement of in-situ monitoring in MOF synthesis. It should be noted that all in-situ analysis methods discussed refer to batch-style reactions unless stated otherwise.

2.3.1 Adapting standard ex-situ MOF analysis techniques for in-situ analysis

2.3.1.1 X-ray

As hybrid, crystalline materials, one of the most obvious and important ways of determining MOF quality is by characterising its structure and crystallinity. X-ray based techniques typically record the angular scattering from a material's crystal planes and provide structural information on the short-range order of a species such as crystallite size, shape, crystallinity, and internal stress or strain. Moreover, spectra can be acquired continuously as a means for in-situ analysis to determine quantitative kinetic data such as rate constants and activation energies.⁸¹ This has successfully been used to observe perovskite formation, degradation⁸² and phase transitions.⁸³

XRD is a standard technique for MOF characterisation that has also been used extensively for in-situ monitoring of MOFs during batch synthesis. Most benchmark MOFs such as ZIF-8,^{84–86} UiO-66,^{87,88} CPO-27,⁸⁹ HKUST-1⁹⁰ and the MIL-family^{91–93} have been studied using in-situ, time-resolved X-ray analysis. However, data cannot be obtained from sub-nanometre crystallites and amorphous species using standard XRD instruments, hence limiting its ability to probe the earliest stages of MOF nucleation.⁷⁸ Consequently, in-situ studies using XRD to probe reaction progress have used high-energy short-wavelength X-rays found at synchrotron light sources. It is interesting to note that, to my knowledge, all previously reported in-situ XRD analysis reports have used synchrotron X-ray sources. While these XRD sources cannot be accessed routinely, they have provided a range of insightful data on MOF crystallisation over many time scales from pre-nucleation to crystalline product.

One example where XRD has been used to monitor MOF growth in a time-resolved manner is the report by Wu *et. al.*⁹⁴ who observed the solvothermal crystallisation of a new MOF, $[\text{Yb}_2(\text{BDC})_3(\text{DMF})_2] \cdot \text{H}_2\text{O}$ using energy dispersive X-ray diffraction (EDXRD), identifying an exchange in coordinated solvent as the reaction progresses. In-situ studies were carried out on a beamline using a bespoke polyether ether ketone (PEEK) reaction cell with a 5 mL volume and internal thermocouple for temperature monitoring. The tube was heated within a Oxford-Diamond in-situ Cell (ODISC) and 2D diffraction patterns were collected every minute.

Figure 2.12A shows a 3D contour for how the XRD pattern evolved over time during a 120 °C synthesis. Pawley refinement and full pattern integration gave quantitative data on the total crystallinity and unit cell parameters, plotted in Figure 2.12B. MOF crystals were first detected after 30 mins and kinetic analysis of the total crystallinity curve indicated crystallisation as the rate determining step over nucleation.

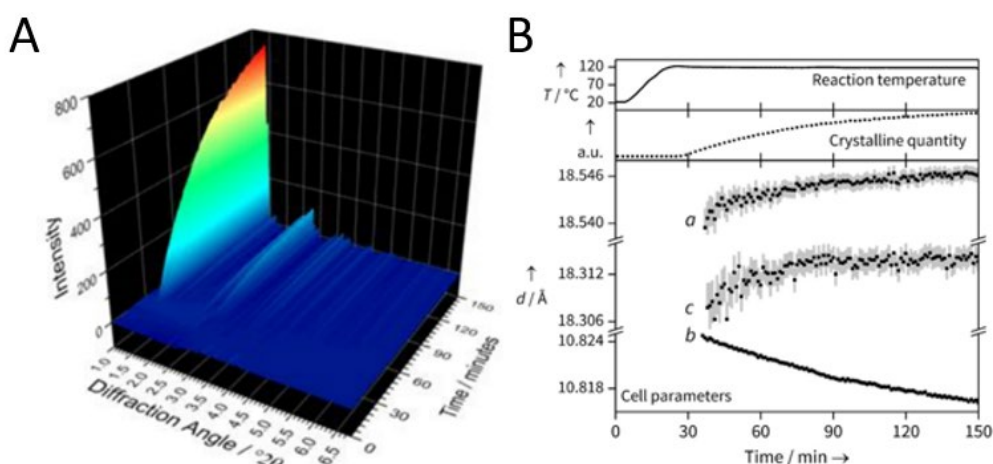


Figure 2.12: A) 3D contour map of the low angle Bragg scattering measured during the synthesis of $[\text{Yb}_2(\text{BDC})_3(\text{DMF})_2] \cdot \text{H}_2\text{O}$ at 120 °C and B) the data extracted *via* full pattern integration including the totally crystal quantity, calculated lattice cell parameters and the internal temperature readings. Figure adapted from Wu *et. al.*, (2016).⁹⁴

Temporal trends of the lattice parameters revealed a simultaneous expansion/contraction mechanism of the 1D diamond channels of the framework as cell parameter *a*, mirrored by cell parameter *c*, steadily increased in length and cell parameter *b* decreased. (Figure 2.12B) Rietveld analysis and supporting ex-situ data (combined thermogravimetric analysis, differential scanning calorimetry and mass spectrometry (TGA-DSC-MS)) on quenched samples indicated how the diffraction patterns were sensitive to the coordinated solvent with DMF and H_2O primarily holding their electron density on the (200) and (110) plane, respectively. The coordinated ratio of water to DMF was quantified against the integrated XRD peak areas over time and revealed how water,

initially coordinated to Yb^{3+} in solution, is replaced by DMF as the reaction progresses. Thus a consistent model for the evolution of lattice parameters in which solvent exchange occurs during crystal formation was constructed.

The work represents a previously unexplored approach to mechanistic analysis and a significant broadening and advancement in obtainable in-situ XRD data. By measuring and comparing lattice parameter values, the pore behaviour was modelled during formation identifying both the mechanism of formation and solvent exchange on the MOF product. This highlights the importance of solvent effects and shows how coordination at different crystal planes affects crystal growth.

Synchrotron light sources have also been used for other X-ray based analytical techniques to gain insight into MOF nucleation and growth. Small-angle X-ray spectroscopy (SAXS) and wide-angle X-ray spectroscopy (WAXS) have commonly been used to monitor the size and morphology of MOFs and their crystal properties, respectively.^{81,95,96} SAXS data is subject to a range of theoretical corrections and a 1-100 nm particle detection range. In contrast, WAXS can observe much smaller distances on the interatomic scale to provide structural information and, due to a non-reliance upon Bragg scattering, it can be used to probe amorphous material. Importantly, this means it may be used to monitor nucleation and growth from the earliest stages in any crystalline state (amorphous to crystalline). SAXS/WAXS data has previously revealed intermediate amorphous species and followed amorphous-to-crystalline transformations in frameworks such as UiO-66,⁹⁷ ZIF-71⁹⁸ and ZIF-8 biocomposites.⁹⁹

SAXS is commonly employed for in-situ monitoring relative to other X-ray based techniques because of its versatility and breadth of obtainable knowledge (e.g. crystal size, morphology and properties).⁹⁸ It is worth noting that complementary or ex-situ monitoring is often needed to rationalise and resolve data. Similarly, some forms of X-ray absorption spectroscopy (XAS) including extended X-ray absorption fine structure (EXAFS) and X-ray absorption near edge structure (XANES) have been used to provide structural information on amorphous phase species during MOF formation by characterising local chemical environments with oxidation states.^{100,101} It is limited by scattering events experienced when small clusters are present but has been used to study some of the earliest stages of MOF formation.

More recently, X-ray pair distribution function (XPDF) measurements have been used to acquire temporal structural information on high electron density, amorphous single cluster species to monitor MOF nucleation and subsequent coordination.¹⁰² This technique detects wide angular

range scattering off nanomaterials and represents a measure of the probability of finding a certain interatomic distance, $G(r)$ within a species. In-situ XPDF was used for the first time to study the formation of Hf- based UiO-family frameworks.¹⁰² XPDF is particularly sensitive to heavier elements such as Zr and Hf and can distinguish clearly between isolated Zr atoms, Zr_4 clusters, Zr_6 clusters and Zr_{12} clusters typical to the UiO framework as seen in ex-situ studies. In-situ monitoring was performed in a steel sample holder with a slit for the X-ray beamline. A series of experiments were designed to isolate each stage of the formation such that their comparison could isolate their effects. Clusters were successfully differentiated using simulated XPDF studies, proving the methods success. Behaviour of the system was monitored by tracking the change in area of specific key peaks in the XPDF demonstrating the evolution of Hf clusters over the time scale from solution phase to full crystalline framework. This includes the formation of Hf_{12} double clusters from Hf_6 single clusters which requires the presence of water whilst it was observed that formic acid is crucial for the formation of single clusters. Furthermore, an elevated temperature was shown to be necessary for the double clusters to form. A mechanism for formation of **hcp** UiO-66(Hf) was proposed, (Figure 2.13) advancing our understanding and presenting a previously unexplored route to in-situ analysis of MOF formation for a family of particularly promising candidates in many applications.

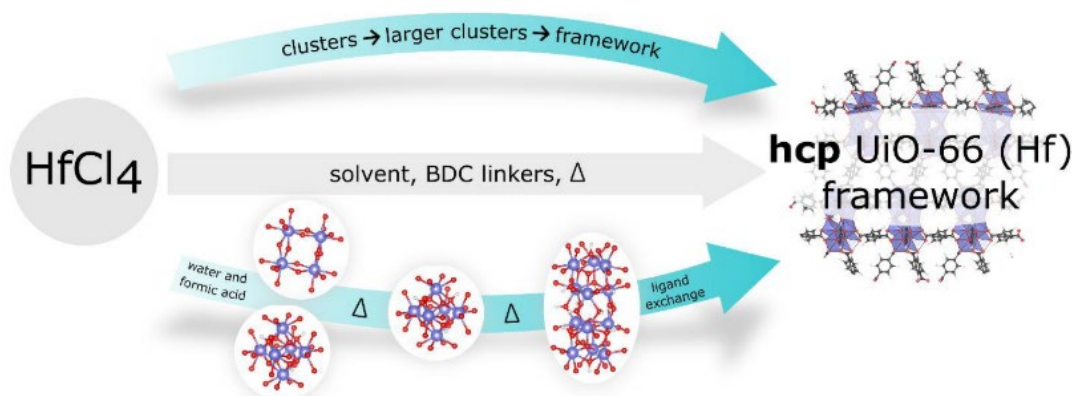


Figure 2.13: The proposed mechanism of formation for **hcp** UiO-66(Hf) in solvothermal conditions.¹⁰²

While in-situ XRD provides a rich source of quantitative structural and kinetic data, the limited facility numbers and high costs associated mean that it is limited to fundamental studies. The low power of X-ray sources in standard XRD equipment found in universities and research institutes mean that such data cannot be routinely obtained there and hence researchers wanting to monitor MOF synthesis in-situ need to look to other techniques. Furthermore, operation at the beamline is complex, generally requiring specially designed flow cells to have sufficient transparency for X-ray yet minimised effect on the reaction environment as well as specialist knowledge. Continued efforts are being made to improve sealed reaction vessels for in-situ

scattering measurements both at the beamline and on standard XRD instrumentation, to be more representative of solvothermal experiments conducted in a lab-based setting. This has noticeably seen improvements during the mechanochemical synthesis of MOFs.^{103,104}

If one does not have access to these facilities, what other options are available? As well as XRD, the most common standard techniques used to characterise MOFs ex-situ are BET sorption isotherms, TGA analysis, electron microscopy, IR spectroscopy and occasionally, NMR. Of these, electron microscopy, NMR, and IR can be used to analyse MOF synthesis in-situ.

2.3.1.2 Electron microscopy

Microscopy methods such as liquid cell transmission electron microscopy (LCTEM),¹⁰⁵ scanning electron microscopy (SEM)¹⁰⁶ and atomic force microscopy (AFM)¹⁰⁷ can give information on crystal morphology and in certain-situations can be used to monitor the crystallisation process. LCTEM can provide direct imagery of real time nucleation and growth. For example, a recent contribution used a novel, combination of regular and cryo TEM to establish three distinct nucleation steps of ZIF-8 previously unaccounted for in current nucleation models.¹⁰⁵ A liquid-liquid phase separation of the reaction solution into solute rich and solute poor regions was seen over the image series, followed by a condensation and subsequent crystallisation of the open-framework within the solute rich areas. (Figure 2.14)

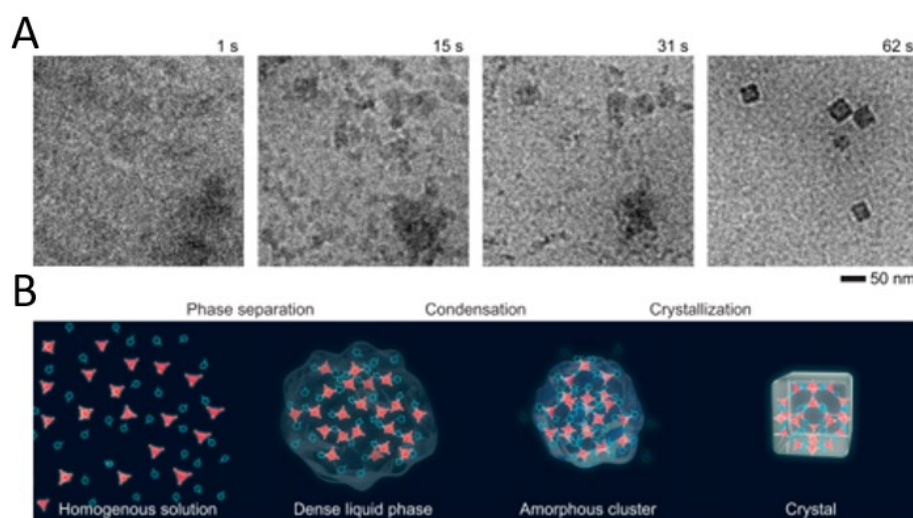


Figure 2.14: A) Image series of in-situ LCTEM studies performed during the formation of ZIF-8 highlighting a three-step nucleation process. B) Diagrams for the nucleation stages identified using the LCTEM images.¹⁰⁵

The broad significance of this approach is that it provides direct imaging of crystallisation through which beam-sensitive materials may transform. Findings also contrast previous classical models indirectly based upon zeolite formation and highlight how crystallisation of prototypical MOFs such as ZIF-8 are still not fully understood.

While in-situ electron microscopy can give useful insight into MOF formation, the breadth of data is reduced compared to XRD, providing limited structural information. Moreover, with the highly specific reaction conditions such as nanoscale reaction volumes, required for in-situ electron microscopy to be possible there is a question about how representative the results are for typical synthetic methods. Additionally, while electron microscopy is more easily accessed than synchrotron based XRD, specialist training is necessary with relatively high capital and running costs. Consequently, electron microscopy is ill-suited as a routine lab-based monitoring method and certainly not suitable for in-line analysis.

2.3.1.3 Vibrational spectroscopy

Raman and IR spectroscopy are fundamental techniques, used to measure the frequencies that radiation is scattered or absorbed by a sample upon bond excitation. These methods offer highly specific structural insights and can be applied to most solid and liquid samples without consumption. Considered complementary, the Raman effect is weak, yielding strong peaks for vibrational modes of functional groups with weak, readily polarised dipoles, conversely IR shows strong signals for strong dipoles. As such, their efficacy is limited by spatial symmetry and chemical composition of the sample under investigation.

As monitoring tools, fibre optic based probes have been developed for in-situ analysis. The temporal evolution of chosen vibrational modes can give direct information as to the chemical proceedings and possible species within a reaction. Previously, they have been important in observing chemical reaction and formation steps as well as confirming identities of species. In the case of MOFs, it is dependent on the system being monitored and its relative chemical composition on whether Raman and IR spectroscopy can be successfully employed for MOF monitoring. e.g. strong electronic transitions, monitoring unreacted linker, probing stretching frequencies of metal-linker coordination. This can be the evolution of a M-L bond or indirectly, through the degradation of solvent such as DMF to formic acid as a framework modulator has also been seen in NMR.¹⁰⁸ In practice, monitoring probes and apparatus are commercially available for purchase and have been successfully applied in MOF formation elucidation.

In-situ IR monitoring apparatus was first used for MOF formation in 2017 to observe the crystallisation process of Zr-fumarate with commercially available IR monitoring equipment.¹⁰⁹ MOF formation was discussed indirectly, monitoring the decomposition of reaction solvent, DMF to formic acid which subsequently modulates the reaction. The findings and methodologies developed underpinned the foundations for their further work probing defect formation in Zr-fumarate frameworks.¹¹⁰ In 2018, H. Embrechts similarly used a commercially purchased solvothermal reactor with in-situ connections to IR, Raman and turbidity probes to monitor and define the formation mechanism for MIL-53(Al).¹⁰⁸ These methods were also used to describe the role of pre-nucleation building units (PNBUs) in the determination of MIL-53(Al) formation.¹¹¹

In 2020, H. Embrechts used parallel measurements of in-situ IR, Raman and turbidity to study the controlled formation mechanism of topological MOF isomers, MIL-68(Al) and MIL-53(Al).¹¹² The methodology used commercially purchased solvothermal reactors, benchtop analysers and monitoring probes. Turbidity measures the opacity of the reaction mixture which is directly proportional to the amount of solid formed. MIL-68(Al) was initially identified as the kinetically favoured product of formic acid modulated synthesis performed at low temperatures in DMF. It also acts as an intermediate species, converting to thermodynamically stable MIL-53(Al) during longer reaction times. In-situ data followed the integrated area of characteristic Raman bands of the carboxylate group, $\delta(\text{COO}^-)$ of the intermediate PNBUs species and selected carbon-carbon and carbon-hydrogen bonds, $(\nu_{\text{CC}} + \delta\text{CH})$ of the MOF product to rationalise this. (Figure 2.15)

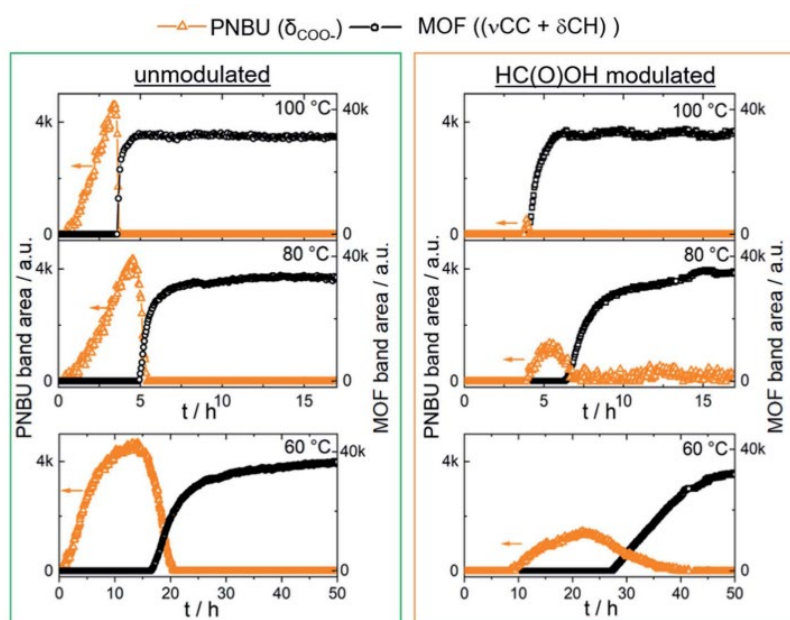


Figure 2.15: Evolution graphs of the characteristic Raman band areas of the PNBUs and MOF product during synthesis in DMF with and without modulation. Figure adapted from H. Embrechts *et al.* (2020).¹¹²

In the presence of formic acid, the evolution of characteristic Raman band areas showed a significant delay (5 to 10 hr) and rate reduction for PNBu formation and accumulation across all the temperatures tested. (Figure 2.15, orange) Aggregation and hence loss of these units into the extended framework meant an increase in crystalline MOF product. (Figure 2.15, black) The activation energies for PNBu formation could be calculated from the Raman spectra for modulated and unmodulated synthesis as $77 \pm 3 \text{ kJmol}^{-1}$ and $66 \pm 3 \text{ kJmol}^{-1}$, respectively to support this observation. In contrast, activation was unaffected for MOF formation (90 kJmol^{-1}) indicating that formic acid influences PNBu formation to steer the reaction to MIL-68(Al) rather than MOF crystallisation. Complementary in-situ FTIR data was used to explain this. An expected [Al-HC(O)O] band was absent during coordination indicated a mechanism of modulation away from common competitive interference with the organic linker for metal sites. Instead, IR showed a hydrogen bond is formed between formic acid and the carboxylate group of the linker. This interaction rationalises MIL-68(Al) formation in the presence of formic acid; free H₂BDC is used as a molecular template for construction during MIL-53(Al) coordination, this is unavailable in the presence of formic acid hence the isomer forms with DMF in its pores, slowing nucleation and growth.

Accessibility of these techniques in general is an improvement compared to synchrotron facilities required in x-ray scattering analysis, being found as benchtop instrumentation and widely available for purchase as highly sensitive probes. Also, as techniques they are standard practise in terms of operation and interpretation of the obtained spectra. Moreover, IR and Raman produce a good source of kinetic and structural information on the reaction species demonstrated from early nucleation and much richer wealth of knowledge compared to microscopy. It is expected for these techniques to become more prevalent for in-situ monitoring studies and novel strategies to be formulated for indirectly monitoring MOF formation e.g., through tracking of solvent species or modulators themselves.

2.3.1.4 NMR

NMR spectroscopy produces valuable information on the local chemical environments within a structure, making it desirable to implement for in-situ monitoring. Notably, various post-synthetic behaviours and interactions common to MOFs have been monitored and discussed using NMR^{113,114} however, it has had limited use in observing MOF formation with only several reports in the last few years.^{100,106,115}

A high-field spectrometer is essential, precluding bench-top instruments, and several spectra are often needed to provide a clear picture, adding complexity during analysis. Furthermore, NMR

active nuclei must be present within the reaction media and give indicative information as to the reaction progress e.g., a change in environment over time that is directly related to crystallisation. NMR has been demonstrated for monitoring MOF formation *via* observation of the metal,¹⁰⁶ ligand¹¹⁵ and solvent¹⁰⁰ coordination environments.

In a recent study, a combined liquid-state and solid-state in-situ characterisation NMR ('CLASSIC') technique was exploited using a high-field spectrometer to monitor the formation of nickel-phosphonate framework, MFM-500(Ni).¹¹⁵ (Figure 2.16) Both ^1H and ^{31}P NMR spectra may be studied due to the MOFs composition. A 20 μL reaction solution placed on the NMR rotor was heated to various fixed temperatures and a three measurement cycle of NMR spectra was routinely obtained from the sample over a 4-36 hr period. ^1H NMR spectra showed well defined shifts in resonances during MOF formation at all the temperatures studied. These were compared against control solutions which used different temperatures, solvent mixtures or just the linker for example to understand the resonance shifts. At greater temperatures, peaks showed better resolution and shifted to higher ppm indicating a better disaggregation of the linker. An initial shift of aromatic proton environments to lower ppm suggested aggregation of the linker within solution (as confirmed by control experiments) and was consistent with anticipated shifts from deprotonation of the phosphonic acid groups of the BTPPA linker also. Subsequent shift to higher ppm was then observed, in line with metal-linker coordination occurring. An upfield shift (6.5 to 4.5 ppm) of a broad peak was also noted; ascribed to a change in solvent mixture as water was liberated from the Ni(II) coordination sphere during linker coordination. Large scale reactions for the corresponding temperatures with matching concentrations and ratios were performed and ex-situ $^{31}\text{P}\{^1\text{H}\}$ and ^1H NMR was recorded *via* periodically extracted aliquots. In all cases, results showed good agreement to in-situ measurements, reaction time scales were maintained, and phase-pure MFM-500(Ni) was isolated as confirmed by PXRD.

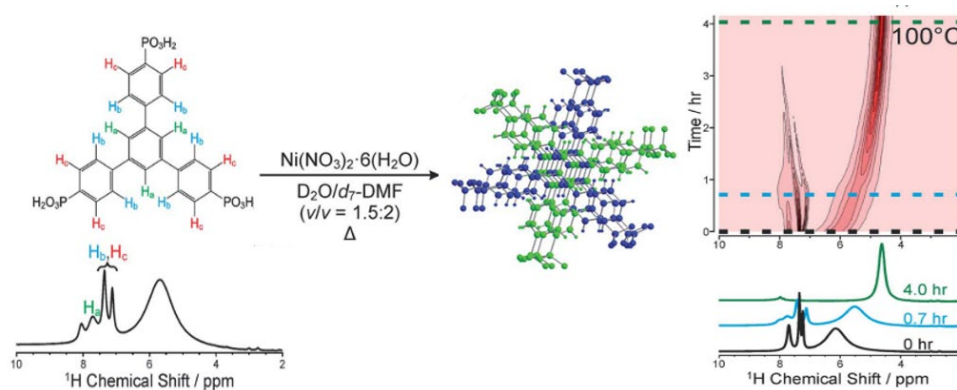


Figure 2.16: Schematic for the adapted synthesis of MFM-500(Ni) showing the proton assignment and ^1H NMR spectra of the organic linker, 1,3,5-benzene-tri-p-phenyl phosphonic acid (BTPPA) and the change in intensity of these peaks during a 100 °C synthesis.¹¹⁵

Furthermore, time dependent changes in peak ratios from ^1H NMR were quantified and used to determine activation parameters on the nucleation and growth process. The activation energies for nucleation and growth were calculated as $61.4 \pm 9.7 \text{ kJmol}^{-1}$ and $72.9 \pm 8.6 \text{ kJmol}^{-1}$, respectively indicating growth as the rate determining step.

NMR is a technique with a lot of potential, limited by the instruments available and ease of analysis. Obtainable data is vast including complex structural information on chemical environments and kinetic parameters through adapting methods used in other studies. NMR can be used to observe all aspects of synthesis including the reagents, products, and solvents in parallel. Much like LCTEM, however there are questions as to the accuracy of these methods due to the small reaction volumes and need for ex-situ controls to produce concrete conclusions. However, the future of in-situ monitoring is expected to utilise this technique further as benchtop spectrometers get more powerful and newer, innovative methods for in-situ monitoring are developed.

Applying standard MOF characterisation techniques for in-situ analysis has become more prevalent in recent years. X-ray based techniques dominate early literature in one-off studies and have naturally provided the most information thus far. Obtainable spectra are highly informative across many time scales of MOF formation from the earliest stage to crystal product and is a readily developed method at synchrotron facilities for a range of materials. However, its inaccessibility is limiting. The cost and specialism for use is high and facility numbers low. As traction for the field of in-situ monitoring has increased, efforts to improve instrumentation and develop novel monitoring strategies have been focussed on. As a result, trends in literature for in-situ monitoring of MOF formation have shifted to other standard techniques. The availability of probes and benchtop analysers, despite high initial upfront costs, have facilitated the use of IR and Raman spectroscopy resulting in a wealth of structural and kinetic information, alike to XRD, but obtainable with a much higher level of accessibility. NMR spectroscopy as a standard technique has been reported the least, it has shown promise in monitoring post synthetic behaviours yet facilitating instrumentation is still lacking and limits its access. However, the potential is vast in particular for frameworks containing NMR active nuclei diverging from classical ^{13}C and ^1H spectra e.g. ^{27}Al and ^{31}P . Current benchtop NMR instruments show poor resolution and liquid phase probes are expensive. It is expected in the next few years for more research to focus on NMR as a monitoring tool for MOF frameworks with an improvement in facilitating technology required.

2.3.2 Alternatives to standard ex-situ techniques

Thus far I have discussed standard (ex-situ) MOF analysis techniques that have been adapted for in-situ analysis. Another approach is to apply techniques that are not typically used for MOF analysis but make more sense in a reaction-monitoring scenario. One such technique that is highly suitable for in-situ monitoring is light scattering. Static light scattering (SLS) measures the scattering intensity of particles in suspension as a function of the scattering angle. The intensity and spatial arrangement of light scattered by small particles is directly dependent on their size and shape. Statistical analysis of scattering curves yields values for the radius of gyration (R_g) which is directly proportional to the particle radius and average particle mass values (M_w). Similarly dynamic light scattering (DLS), which uses a single fixed detector, can determine particle size by measuring the fluctuating intensity of scattered light resulting from Brownian motion.

Recently, time resolved SLS has been used to study MOF nucleation and growth, often in conjunction with other complementary techniques. Several groups have explored in-situ light scattering for MOF analysis using a home-built instrument based on a design by Becker *et. al.* first proposed in 1991.¹¹⁶

One example of the usefulness of this technique was shown by Cravillon *et. al.*¹¹⁷ who used it to help screen and rationalise the effect of several modulators on the size and shape of a zeolite-type framework, ZIF-8. During the unmodulated synthesis of ZIF-8 NPs, particles were first detected after 130 s with an associated radius of gyration, R_g of 20 nm. (Figure 2.17a) Analysis concluded that NP formation in the absence of a modulator provided a slow nucleation with a comparatively fast growth as shown by the steady increase in molecular weight over time yet constant size shown in Figure 2.17a. After 800 s, the radius began to increase indicating agglomeration of primary NPs. At this point nucleation vs agglomeration can no longer be differentiated using this technique. Complementary ex-situ SEM of droplets taken from the synthesis confirmed formation observations ($t < 800$ s) and agglomeration ($t > 800$ s). Data collected in the presence of different modulating linkers, sodium formate and 1-methylimidazole showed significant differences. (Figure 2.17b and c, respectively) Primary detection was later in both cases ($t = 350$ s and 500 s) for a greater particle size ($R_g = 50$ nm). A change in growth mechanism was seen between 480 and 600 s for both modulated syntheses as indicated by a disruption in the linear increase of R_g over time, (Figure 2.17b and c, red circle) They inferred that in the case of formate modulation, initial particle aggregation was followed by a particle-monomer addition growth past $t = 480$ s. SLS data from 1-methylimidazole modulated synthesis of ZIF-8 microcrystals

showed a simultaneous aggregation/particle-monomer addition growth which became dominated by the latter in later stages of crystal growth.

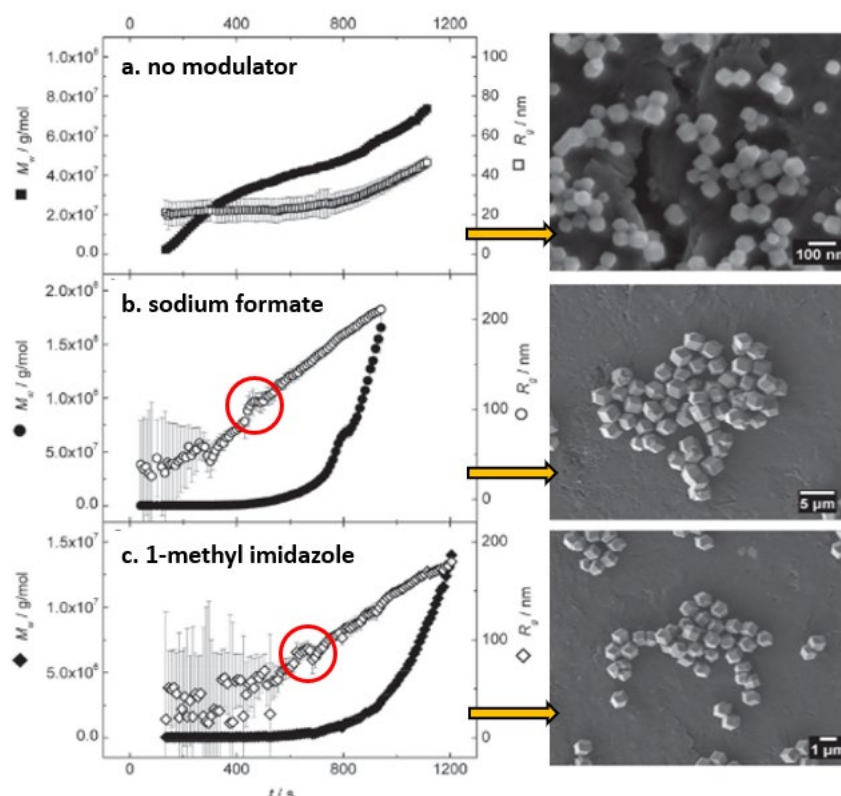


Figure 2.17: Left: The temporal evolution of the weight-averaged particle mass, M_w , and radius of gyration, R_g , for the formation of ZIF-8 a) nanocrystal without a modulating ligand; b) microcrystals in the presence of sodium formate and c) 1-methylimidazole.

Right: SEM images of crystals collected from the adjacent procedures.¹¹⁷

The versatility of this approach is shown by the wide range of different MOF materials that it has been applied to including MOF-5,¹¹⁸ HKUST-1,¹¹⁹ and ZIF-71.^{98,117,120} Despite its relative low cost and the availability of commercial systems, light scattering has seen limited uptake in recent years. The instruments time resolution (2 s) and high limit of detection (30 nm) are significant relative to the rate and scale of nucleation and hence means the earliest stages of nucleation cannot be observed. By comparison, LCTEM can be collected at 20 frames per second and show a particle size through direct imagery, not a calculated hydrodynamic ratio. Arguably, the light scattering stage is of great interest but with the development of in-situ monitoring and relevant instruments and technologies, SLS as an option has been outcompeted with more accessible and data rich approaches available.

2.3.3 Indirect in-situ analysis

All the techniques discussed thus far have concerned the direct characterisation of the product, intermediates, reagents, or solvent, however monitoring does not have to be limited to specific species within the reaction vessel. Bulk measurements such as pH and turbidity can also yield useful data. While not giving any indication of product quality, these parameters give insights into reaction kinetics^{108,121,122} in a similar fashion to the in-situ NMR and Raman studies mentioned earlier^{100,109} which tracked solvents or associated modulators to indirectly monitor crystallisation. Importantly the implementation of such monitoring apparatus is much cheaper and easier than the techniques that have been discussed thus far.

It is known that pH data is qualitatively important within MOF formation kinetics.⁹⁸ Nucleation is dependent and highly sensitive to pH;¹²³ dictating linker deprotonation and, in some cases, the in-situ decomposition of common solvents such as DMF to modulating species. As a result, pH has regularly been used to control crystal sizes and growth¹²⁴ and has been used in conjunction with high-powered XRD using low-cost Raspberry-Pi apparatus to confirm concentrations of metastable species and hence, has indirectly provided structural information.¹²⁵ Turbidity is dependent on both the number and size of particles and hence provides an indication of the overall amount of framework that has precipitated. If recorded over time it can give insight into synthesis times and rates.¹⁰⁸ Neither technique provides information on structure or properties of a material but are highly accessible offering a low entry point for in-situ monitoring, especially as these can easily be obtained from homebuilt “open” hardware.

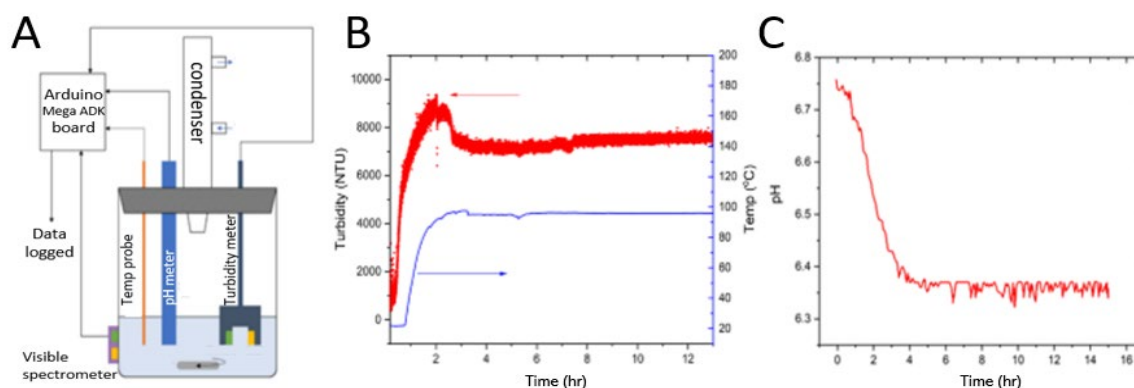


Figure 2.18: A) Schematic diagram of the bespoke set-up. B) Turbidity, temperature and C) pH data collected using the *in-situ* monitoring set-up.¹²²

This approach was used by Yeung and co-workers in 2020 who aimed to use in-situ monitoring to optimise the synthesis of Ni-based MOF, STA-16.¹²² The reaction was monitored using a bespoke instrument comprised of an Arduino microcontroller combined with off-the-shelf sensors for pH, temperature, turbidity, and a 6-channel visible light spectrometer (Figure 2.18A) which in total

cost less than £100.¹²² Turbidity and pH data was complementary with changes stabilising after 5 hr to indicate a reaction completion time. (Figure 2.18B and C) Ex-situ PXRD and N₂ physisorption data confirmed a well-defined STA-16 framework with a minimal reduction in pore volume compared to a 72 hr reaction time. Samples produced after 5 hr had smaller crystallite sizes (69 to 87 nm, respectively) but yield was unaffected. They went on to demonstrate the methodology for prototypical MOF, ZIF-8.

This approach of using simple microcontrollers and sensors to take bulk readings of the system features high accessibility, low cost and facile set-up. The simplified set-up produces cruder data and can often need complementary or confirmatory data alongside it to draw conclusions; adding complexity to data analysis. Despite its simplicity, the kinetic information obtained is insightful and there is scope for further analysis or development of the apparatus to provide greater knowledge as to the reaction crystallisation and optimisation.

2.3.4 Modifications and applications

In-situ monitoring has not been limited to the crystallisation of MOFs. As techniques and methodologies have developed, several works have looked to monitor post-synthetic engineering of frameworks including solvent-assisted ligand exchange (SALE)¹²⁶ and post-synthetic functionalisation of organic linkers.¹²⁷ Furthermore, it has been used to monitor MOFs during their applications.^{101,128–131}

2.3.5 Flow synthesis

All reports discussed in this case study so far were performed under static batch style conditions with few reports of in-situ analysis during flow synthesis.^{43,132–134} Of those, the earliest is from 2017 highlighting the prevalence of flow chemistry as a research area and branch of in-situ MOF monitoring. Introducing flow elements to procedures can benefit from continuous production and complex parameter control facilitating scale up, optimisation and quality assurance within synthesis.

Taddei *et. al.* used synchrotron radiation for the in-situ analysis of UiO-66 crystallisation in flow in 2017.⁴³ This high resolution X-ray study allowed real time reaction monitoring by shooting a beam of high energy X-rays at a section of the transparent tubing and helped to identify two stages of crystallisation. To assess findings, off-line experiments were done; these agreed with in-situ observations and confirmed the method to be reliable.

In a recent example, in-situ WAXS was used to investigate the crystallisation of multicomponent MOF series, UMCM-1 ($\text{Zn}_4\text{O}(\text{bdc})(\text{btb})_{4/3}$) and MUF-77 ($\text{Zn}_4\text{O}(\text{hmtt})_{4/3}(\text{bpdc})_{1/2}(\text{bdc})_{1/2}$) during continuous synthesis.¹³⁴ Diffraction data was obtained using beamline X-rays targeted at various points along a steady state flow reactor where distance from the start represents different residence times. (Figure 2.19) This novel method of synthesis and data collection alleviates some of the non-homogeneity and vessel concerns inherent to batch style synthesis. X-ray analysis revealed a directed growth mechanism for UMCM-1 and a contrasting, non-preferential growth for MUF-77. Yields were comparable to batch synthesis after 10 minutes for both samples; showing high phase purity and similar physical properties to those previously prepared. In addition, growth kinetic parameters were calculated for optimisation and future scale up outlooks.

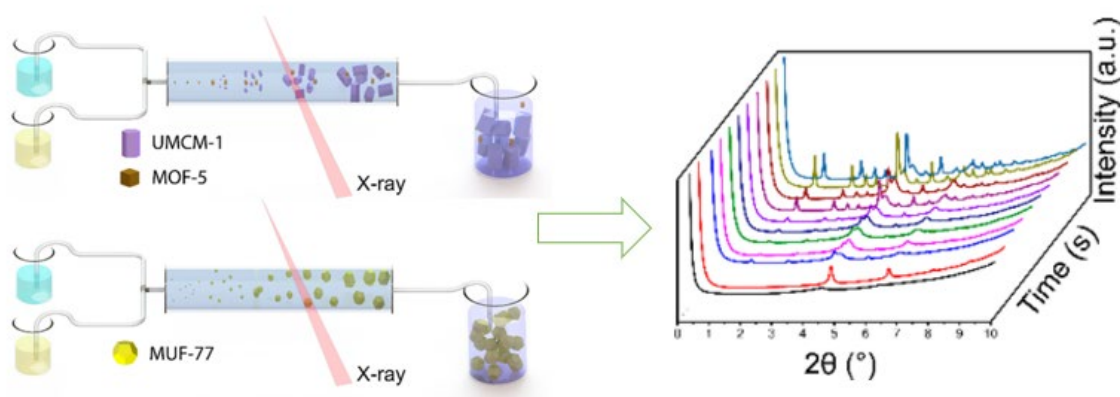


Figure 2.19: Diagram showing the X-ray in-situ analysis of UMCM-1 and MUF-77.¹³⁵

In summary, current literature discussing in-line analysis of MOFs during continuous synthesis use synchrotron facilities which are highly inaccessible, expensive and require specialist training for operation. This area represents a significant gap for exploration within research to combine the inherent advantages to both flow synthesis and in-situ monitoring. A table is given below summarising each technique and its associated advantages and disadvantages.

2.4 Summary and the research problem

Metal-organic frameworks are class of hybrid functional materials shown to have a wide range of applications such as adsorption,² gas separation,³ and catalysis.⁴ Despite this, the use of MOFs in industry has still not been widely achieved. Generally, MOFs are solvothermally made in batch-type processes and their analysis and property assessment requires considerable time and manual intervention. However, these processes are time consuming, requiring elevated temperatures and specialist equipment making their energy efficiency and reproducibility poor. Furthermore, they are not easily scalable. This has prompted a shift in focus to other methods. Several papers describing successful flow synthesis of MOFs with improved space-time yield, good uniformity and enhanced quality of crystals have been published in recent years. However, there is yet to be an efficient and versatile method reporting the analysis of these frameworks in line on a facile, lab-scale basis.

A basic set of MOF characterisation data would usually contain a powder x-ray diffraction (PXRD) pattern, sorption isotherms, thermogravimetric analysis (TGA), scanning electron microscopy (SEM) and ideally, a full structural refinement from single crystal x-ray diffraction (SCXRD) if the material is newly reported/discovered. None of these can currently be implemented for in-line analysis practically.

When considering the current spectroscopic techniques available for in-situ analysis (e.g., XRD, LCTEM, NMR, IR, Raman) in a lab-based setting, few of them would be useful for the in-line characterisation of MOFs during continuous production. A summary of these techniques with their associated advantages, disadvantages and measurements times is shown in Table 2.1.

NMR is a highly precise and fast technique used to identify chemical environments and elucidate organic structures. However, to use NMR for MOF analysis, samples must be prepared using deuterated solvents and strong acids causing destruction of the framework. This is impractical to implement in a flow reactor and would not allow for in-line analysis, as desired. Moreover, NMR could not be solely used to characterise the MOF as it provides little detail as to the framework's integrity and so further analysis would be required. Finally, current benchtop spectrometer doesn't possess strong enough magnets to provide necessary data to analysis the frameworks as they are made.

Vibrational spectroscopy (e.g., Raman and infrared) monitoring is promising. As a method, it can confirm the presence of specific bonding frequencies present within the sample but not exclusive

to the framework e.g., any unreacted reagents present and the beam being scattering from the heterogenous dispersion flowing through the line of detection. This was pre-empted to cause several layers of complexity and possible secondary ex-situ data. Despite its potential, I wanted to look at other approaches in this work.

Table 2.1: Summary of the advantages and disadvantages associated with in-situ analytical techniques for MOFs that have been described in current literature.

Technique	Measurement timescale	Advantages	Disadvantages
X-ray based e.g. EDXRD, SAXS/WAXS, EXAFS, XANES, XAS, XPDF	0.02 s ^{<94}	<ul style="list-style-type: none"> • Standard MOF characterisation technique. • Can probe all time scales of crystallisation. • Good structural and crystal symmetry information. 	<ul style="list-style-type: none"> • Requires synchrotron irradiation which is specialist, expensive and facilities are in low numbers. • Samples may be sensitive to the X-ray beam.
Electron microscopy e.g. SEM, TEM, AFM	0.6 s ¹⁰⁵	<ul style="list-style-type: none"> • Direct imaging of the crystals. • Can be used to monitor crystallisation processes. • Relatively fast data acquisition. 	<ul style="list-style-type: none"> • Site specific • Small, non-representative volumes of reaction mixture. • Limited structural information. • Expensive equipment
Vibrational spectroscopy e.g. Raman, IR	3-5 min ^{111, 112}	<ul style="list-style-type: none"> • Provide structural insights. • Kinetic information may also be obtained. • Relatively inexpensive probes available. 	<ul style="list-style-type: none"> • Efficacy is limited by the spatial symmetry and chemical composition of the samples.
NMR	Several mins ¹¹⁵	<ul style="list-style-type: none"> • Gives complex structural and kinetic information. • May be used to monitor all aspects of synthesis e.g. reagents products, solvents, modulators. 	<ul style="list-style-type: none"> • Small, non-representative volumes of reaction mixture. • Need ex-situ complementary characterisation data.
Light scattering e.g. SLS, DLS	2 s ¹¹⁷	<ul style="list-style-type: none"> • Provide good kinetic information. • Gives pertinent data on growth mechanisms. • Low set up cost. 	<ul style="list-style-type: none"> • High limit of detection for crystals (30 nm).
Indirect in-situ analysis e.g. pH and turbidity probes	<0.5 s (turbidity) 20-30 s (pH) ¹²²	<ul style="list-style-type: none"> • Relatively inexpensive probes available. • Good kinetic information collected. • Easy set up. 	<ul style="list-style-type: none"> • Requires complementary data to make accurate conclusions. • No structural information collected.

In conclusion, the in-line analytical techniques that could be applied for MOF analysis are highly limited. This limits in flow MOF synthesis to off-line analysis a time-consuming process which is costly and open to error due to the significant handling and time resolution between synthesis, purification and subsequent analysis. This project broadly aims to investigate a qualitatively distinct approach to this issue to help bridge the gap between lab and industrial scale production of MOF materials.

2.5 Aims of the thesis

The primary aim of this project was to investigate a qualitatively distinct approach to in-line MOF analysis by developing a platform for indirect analysis of MOFs as they are made in continuous processes. The focus was application-led, whereby the product quality may be quantified not on the physical properties, but on the performance of the material against a targeted application. In-line UV-Vis spectroscopy was used to monitor the efficiency of a framework at its target application by producing real time data which can be used to draw conclusions about the synthesised framework.

In the first instance, MOF candidates were selected against a set of pre-determined criteria which included being well characterised, easily synthesised with previous reports of successful continuous procedures and having a known application which may be quantified using an in-line monitoring technique which has simple integration and high sensitivity. This was investigated thoroughly for implementing within a complete and optimised process from MOF synthesis to subsequent analysis. Within the analytical part of the set-up, pre-existing and novel hardware was repurposed and developed, respectively for potentially integration within the analytical part of the set-up. Upon success, real time data was collected and analysed to indirectly assess the quality of the reaction stage of the set-up.

Chapter 3 The methodology and thesis structure

3.1 Initial approaches and considerations

In this section I will be discussing the initial approaches to achieve the aims and objectives stated in 2.5. A distinct methodology to develop an integrated set-up utilising applications-led analysis will be discussed, including the key considerations that form a start point for this project from both a chemical and hardware aspect. Furthermore, the envisioned device and set-up for analysis will be outlined.

3.1.1 Applications-led testing

In-line analysers will be developed and implemented as part of a synthetic flow system for MOFs. Their focus will be applications-led, whereby the product quality may be quantified not on their physical properties, but on its performance against a targeted application such as adsorption. In-line spectroscopic techniques will be used to monitor the efficiency of the framework at its target application by producing real time data.

3.1.1.1 Potential applications: considerations

Metal organic frameworks are a diverse class of functional materials with a broad list of potential applications. Upon considering which one should lead the focus for the first developed system, several considerations were to be made. Ideally, the application should be simple e.g. through addition of a species or exposure to external stimuli, readily quantified by an existing in-line spectroscopic technique and non-destructive to the framework for in-line application. In the case of a destructive or framework altering application, online testing would be required.

A possible application displayed by MOFs that could be implemented in-line for analysis is catalysis. MOFs and their composites may be used to promote catalytic reactions via photocatalysis; facile addition of a reactive species in the flow reactor setup along with external stimuli can be used to promote the reaction in flow. The efficiency of the catalysis may be assessed using many current in-line techniques. For examples, using Raman spectroscopy to monitor and quantify the formation or depletion of an active bond in the catalysed species or similarly, IR may be used.

A second application of MOFs is within sensing. This can be the sensing of ions, gases, or even solvents. This is particularly prevalent where luminescent MOFs are utilised as sensor monitoring can be performed using fluorescence spectroscopy.

Another example application is in water remediation. MOFs are known to be able adsorptive materials with fast kinetics and high selectivity often without the need for further stimuli. Many benchmark MOFs have been shown to have an adsorptive capacity towards a species, or several, including organic dyes, ions or DNA fragments. The simplicity of the method (e.g. addition of the adsorptive species) along with its potential to be used for numerous frameworks is attractive to this project. UV-Vis, fluorescence or IR could all be used to quantify this mechanism.

From the applications and techniques presented; the adsorption of organic dyes and its analysis using UV-Vis offers a facile and quick method for MOF analysis. While this was the chosen system to test, the other approaches discussed are equally viable and could be used in future work. Organic dyes are commonly used to model a materials adsorptive property and are readily sourced. Furthermore, UV-Vis is a sensitive and versatile technique that provides quantitative data on a sample's ability to absorb light. It is highly robust and has been implemented widely within flow synthesis and offers future opportunity for analysis of several MOF materials.

3.1.2 Metal-Organic Frameworks: Considerations

Based on considerations thus far, a viable MOF candidate to showcase the applications-led analysis approach needed to be chosen which must satisfy several criteria: Firstly, it's flow synthesis had to be previously reported in literature. Secondly, it should have been proven as a candidate for adsorption of organic molecules.

The first MOF structure initially chosen for investigation (Chapter 4 and Chapter 5) is extensively researched HKUST-1. This framework meets both the outlined criteria with several reports for the continuous synthesis of HKUST-1^{75,76,135} and on the adsorptive removal of organic dyes.^{136,137} Similarly, ZIF-8 has also had its continuous synthesis demonstrated and been shown as an able adsorbent for organic dyes making it the second potential MOF candidate for the final set-up.

Both MOF candidates were taken forward for initial experimentation to screen their previously reported flow synthesis^{68,138,139} and their organic dye adsorption abilities^{140–142} before determining the most appropriate chemical system to focus on.

3.1.3 The final envisioned set-up

The envisioned set-up for combined flow synthesis and integrated analysis is shown in Figure 3.1. Precursor solutions for MOF candidates are pumped using a syringe pump (Figure 3.1.1) to a T-junction (Figure 3.1.2). Synthesis will occur in the reactor coil (Figure 3.1.3) using elevated temperatures and possibly pressures. Upon leaving the reactor coil, an organic dye solution will be added into the stream (Figure 3.1.4) for adsorption to occur along a length of tubing with a pre-determined residence time (Figure 3.1.5). The dye and MOF mixture will then enter the in-line analyser for diffusion across the membrane (Figure 3.1.6) into the bottom stream which is being supplied from a fourth syringe (Figure 3.1.8) at the same rate. The bottom cavity outlet point takes the filtrate for UV-Vis analysis (Figure 3.1.7) to generate real time data for online reaction monitoring and feedback control (Figure 3.1.9). The MOF@dye and remaining dye leave the analyser for collection (Figure 3.1.10).

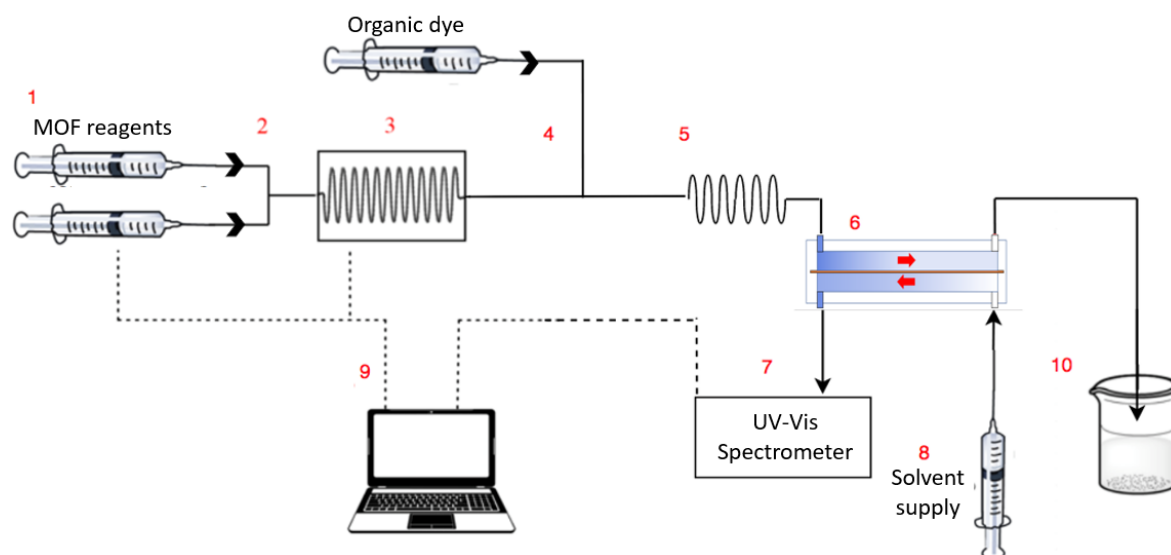


Figure 3.1: The end, integrated flow setup including the synthesis, dye addition and adsorption, separation, UV-Vis analysis and collection. Where 1- syringe pump loaded with reagents; 2-T-junction; 3-reactor coil; 4- syringe pump infusing the organic dye; 5- adsorption coil; 6- in-line filtration component; 7-UV-Vis spectrometer; 8- fourth syringe pump infusion carrier solvent; 9- PC for online reaction monitoring and feedback control; 10-collection of the MOF@dye stream.

3.1.4 The cross-flow filtration device

A cross sectional image of the envisioned appearance and functionality of the proposed cross-flow filtration device is shown in Figure 3.2.

A design of channels spans the chip above and below a membrane filter, working as a cross-flow filtration system with inlet and outlet points either side. The MOF will undergo a predetermined adsorption process prior to entering the analyser. The process fluid, containing the MOF@dye and remaining dye, will then flow through the inlet and across the chip. Diffusion of the unadsorbed dye will diffuse across the membrane into the channels below where a solvent stream or 'carrier' fluid with an equal rate of flow will be carried in the opposite direction. This cross-flow arrangement is necessary for full diffusion of the unadsorbed dye due to a constant concentration gradient being maintained throughout the entirety of the system. To ensure this, initial calculations for the diffusion time of the organic dye molecules will be used to dictate the dimension of the system. Furthermore, following set up, the UV-Vis spectrum of the process stream outlet will be measured ex-situ to ensure no dye is remaining. The second stream will be carried out of the device and analysed via UV-Vis to generate data relating to the amount of dye removed from solution.

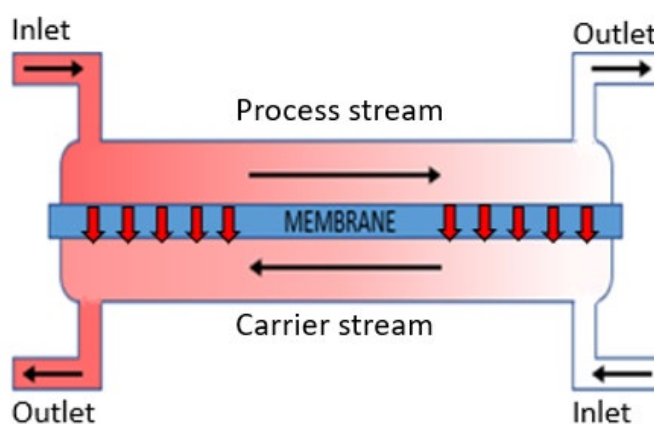


Figure 3.2: A cross-sectional diagram for the envisioned cross-flow filtration device. Red gradient shading indicates the crude concentration of dye within the flowing streams; red arrows indicate the direction of diffusion for the dye molecules from the process to the carrier stream and black arrows represent the expected direction for fluid flow.

3.2 Thesis structure

This thesis is composed of five results chapters detailing the experimental work done over the course of this PhD funding, including research from three journal articles at different stages of publication (not chapter exclusive), before drawing conclusions and discussing the future outlook within this field. Chapters 4 to 6 break down the individual sections of the final envisioned

Chapter 3

platform, as shown in Figure 3.1 and primary aim for this work before drawing it all together in chapter 7 which describes testing of a fully integrated flow synthesis and analysis system. Chapter 8 features further work, not directly related to the central PhD project, that exploited the findings from chapter 6. Each chapter contains an introduction, aims, experimental section, results and discussion and concluding statements. A complete bibliography for the entirety of the thesis is given at the end.

Chapter 4 details the synthesis of selected MOFs: HKUST-1 and ZIF-8 in batch and in flow. Batch synthesis methods are performed to provide comparison characterisation data. Several parameters are explored for the continuous production of these MOFs to produce an optimal synthesis procedure for the set-up including, time, concentration, temperature and molar ratio. The work discussed here was mostly being done at the same time as the work discussed in chapter 5.

Chapter 5 establishes the application element to the final set-up, the adsorption of organic dyes. Several controls in batch and flow are discussed and the adsorptive kinetics of HKUST-1 for the chosen dye are investigated to produce a facile system that is easily applied in-line and has the potential for quick and easy analysis.

Chapter 6 looks at the separation of free, unadsorbed dye from the process stream so that it can be quantified away from the MOF and hence the amount of dye adsorbed to the MOF determined. Designs and fabrication methods are explored including 3D printing culminating in the development of a promising new technique using fused deposition modelling (FDM). A commercial device was also developed for the continuous separation of free dye.

Chapter 7 brings together the three previous chapters; integrated the full set-up into a single continuous set-up working from synthesis, adsorption and through to separation. An in-situ spectrometer is integrated and real time UV-Vis data is collected continuously which synthesis parameters are systematically adjusted to produce temporal graphs with quantifiable, stepwise changes in spectra that indicate changes in dye removal aligning with changes in the synthesised product within the system.

Finally, chapter 8 presents three distinct devices fabricated by FDM printing and utilising a print-pause-print technique with their functions clearly demonstrated. This includes a dead-end syringe filter, a piece of reactionware for semi-continuous MXene synthesis and the refinement of the

cross-flow filtration device first introduced in chapter 6. This chapter's work was performed in parallel with that of chapter 6.

Chapter 4 Synthesis of Metal Organic Frameworks

In this chapter, I will discuss the selection and synthesis of MOF candidates HKUST-1 and ZIF-8 within batch and continuous set-ups. The aim of this work was to determine candidate MOFs that could be analysed using an ‘application-led’ approach and establish a flow synthesis procedure applicable to the final overall process. The work described in this chapter was performed in parallel with that described in chapter 5 where the results collected steered the focus and hence progression this chapter took.

4.1 Candidate MOFs

A viable MOF candidate needed to be chosen to showcase the ‘application-led’ analysis approach of this work (dye adsorption, analysed using UV-Vis). Several key criteria were satisfied by the chosen MOFs: Firstly, it had to be well-characterised for easy-benchmarking with previously reported flow syntheses. Secondly, it should be known to readily adsorb organic molecules. With these criteria in mind, two benchmark MOFs were chosen for investigation: HKUST-1 and ZIF-8.

4.1.1 HKUST-1

The first MOF structure chosen for investigation was extensively researched HKUST-1. HKUST-1 is a Cu-based MOF, first synthesised in 1999¹⁴³ and the first framework to be commercialised under the name Basolite® C300, prepared *via* an electrochemical process taking 3-12 hr.⁷⁵

The HKUST-1 framework ($[\text{Cu}_3(\text{BTC})_2(\text{H}_2\text{O})_3]_n$, where BTC= benzene-1,3,5-tricarboxylate) is made of dimeric copper nodes connected by BTC^{2-} linkers and has bimodal porosity. The final lattice is cubic (*fcc*) and is typically described with a **tbo** topology. (Figure 4.1A) The Cu_2 paddlewheel unit, or SBU, consists of a copper(II) dimer bridged by four tritopic BTC molecules and a single water molecule axially coordinated to each centre where Cu(II) ions are presenting a pseudo-octahedral geometry. (Figure 4.1B) During thermal activation or heating, these water molecules are removed to give coordinatively unsaturated metal sites (Cu^{2+}) available to other molecules. The conversion

to the dehydrated state can be visually observed by the characteristic colour change from turquoise to dark blue/purple post activation.¹⁴⁴

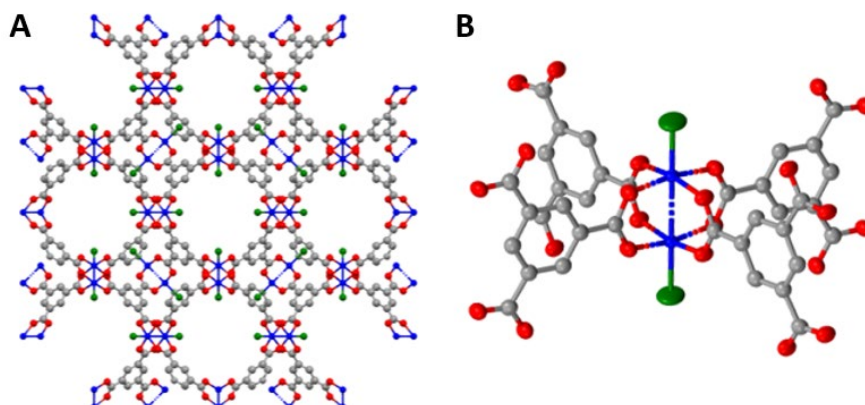


Figure 4.1: A) Structure of cubic HKUST-1 and B) the dimeric copper paddlewheel secondary building unit structure. Grey, carbon; red, oxygen; royal blue, copper. Hydrogens have been omitted for clarity and the green ellipsoid represents exchangeable water at the axial position. Images generated using Mercury.

The bimodal porosity, high surface area and high density of open metal sites within the framework give HKUST-1 strong sorption properties, previously being investigated for paraffin/olefin separation,¹⁴⁵ CO₂ capture,¹⁴⁶ water remediation¹⁴⁷ and water harvesting applications.^{148,149} However, alike to many MOFs, it's long-term and aqueous stability is poor due to the strong interactions between the open metal sites and water causing structural changes as hydrolysis occurs.¹⁵⁰ This issue is addressed with stability experiments and the use of ethanol solvent in this chapter.

4.1.2 ZIF-8

The second MOF chosen was ZIF-8 (Zn(mIm)₂, where mIm= 2-methylimidazolate). ZIF-8 is a Zn-based framework that features tetrahedrally connected Zn²⁺ and 2-methyl imidazole organic linkers. The framework displays a **sod**-topology featuring cages (11.6 Å) comprised of interconnected six-membered imidazole rings with an accessible diameter of 3.4 Å. (Figure 4.2)

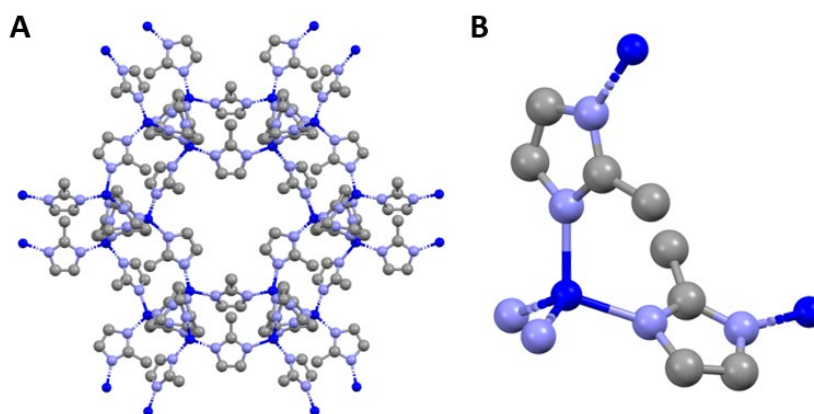


Figure 4.2: A) Structure of ZIF-8 and B) the $\text{Zn}(\text{mlm})_2$ secondary building block showing how Zn^{2+} tetrahedrally coordinates. Grey, carbon; blue, nitrogen; royal blue, zinc. Hydrogens have been omitted for clarity. Images generated using Mercury.

ZIF-8 displays excellent thermal and chemical stability, retaining its structure in various solvents and alkaline to neutral pH. It has been shown to have many adsorption-based applications, including gas separation,^{151,152} organic dye adsorption^{14,141,153,154} and hydrocarbon separation.^{155,156}

4.2 Experimental methods

4.2.1 Materials and methods

All chemicals and reagents were purchased from chemical suppliers with no further purification necessary before use.

$\text{Cu}(\text{NO}_3)_2 \cdot 2.5\text{H}_2\text{O}$ (98 %), trimesic acid (95 %), $\text{Zn}(\text{NO}_3)_2 \cdot 6\text{H}_2\text{O}$ (98 %), 2-methyl imidazole (98 %), were all purchased from Sigma Aldrich. Ethanol solvent (<99 %, wet) was purchased from Sigma Aldrich. Tubing was obtained from RS components (PTFE, $\varnothing = 1$ mm). Silica capillary was purchased from CM scientific. Syringes (20 mL, BD Plastipak Luer Lock) were purchased from RS components. For all flow syntheses syringe pumps (Harvard apparatus) controlled *via* computer software (LabView) were used to provide accurate infusion of the reagents. IDEX flangeless $\frac{1}{4}$ -28" fittings were purchased from Cole-Palmer.

Powder X-Ray Diffraction (PXRD) patterns were collected on a Bruker D2 Phaser using Cu K α radiation source ($\lambda = 1.5418 \text{ \AA}$). SEM Imagery and energy dispersive spectroscopy (EDS) was collected on a JEOL JSM7200F. Infrared spectroscopy was recorded on a Thermo Fischer, Nicolet iS5 iD7 ATR. TGA thermograms were collected on a Netzsch TG209 libra in Air at 50 mL/min flow rate and temperature range of 30-900 °C.

4.2.2 HKUST-1 batch synthesis¹³⁵

The HKUST-1 batch synthesis procedure was taken from previous reports.¹³⁵ $\text{Cu}(\text{NO}_3)_2 \cdot 2.5\text{H}_2\text{O}$ (0.385 g, 1.66 mmol) and H_3BTC (0.185 g, 0.88 mmol) were dissolved separately in ethanol to make a total solvent volume of 10 mL. The metal solution was added to the ligand solution to form a blue precipitate immediately then heated in an oil bath (79 °C) for 4 hrs. The precipitate is likely small crystallites of the MOF solid in the early stages of formation and growth. The solid was collected and washed with ethanol (10 mL) then soaked overnight in ethanol (10 mL) before being dried in air (25 °C).

4.2.3 ZIF-8 batch synthesis¹⁵⁷

The ZIF-8 batch synthesis procedure was taken from previous reports.¹⁵⁷ $\text{Zn}(\text{NO}_3)_2 \cdot 6\text{H}_2\text{O}$ (0.397 g, 1.33 mmol) and 2-methyl imidazole (1.08 g, 13.15 mmol) were dissolved separately in DI water to make a total solvent volume of 30 mL. The solutions were combined at room temperature for 48 hr without stirring. A white precipitate formed almost instantly which was collected post reaction using centrifugation (rpm 8000) was washed in ethanol (2x 10 mL) and left to dry in air (RTP).

4.2.4 Stability tests

The pH of DI water was adjusted used 0.2 M HCl and 0.2 M NaOH. Synthesised HKUST-1 (50 mg) was then immersed in the pH adjusted DI water (pH= 3; 7; 10; 20 mL) and stirred for 120 mins. The solid was isolated using centrifugation (10000 rpm, 1min) and dried in the oven (70 °C). This was repeated with ethanol without pH adjustment.

4.2.5 Flow synthesis of HKUST-1

In a general procedure, the metal and linker solutions were individually loaded into 20 mL syringes (BD Plastipak, Luer Lock) with exiting tubing (PTFE, \varnothing = 1 mm, 10 cm) leading to a connecting T-junction followed by fused silica capillary tubing (\varnothing = 0.7 mm, 10 m) as the synthesis vessel for the framework. All connectors used were IDEX flangeless ¼-28" fittings. Residence times, corresponding to reaction time, were set by adjusting the flow rate. The exiting fluid was collected in a centrifuge tube then centrifuged (10000 rpm, 1min) in a microfuge.

4.2.5.1 Concentrations and synthesis time

Stock solutions of $\text{Cu}(\text{NO}_3)_2 \cdot 2.5\text{H}_2\text{O}$ (0.06 M) and trimesic acid (0.12 M) were made in ethanol. For example, $\text{Cu}(\text{NO}_3)_2 \cdot 2.5\text{H}_2\text{O}$ (0.06 M, 3.488 g, 250 mL) and trimesic acid (0.12 M, 6.304 g, 250 mL). All lower concentrations were produced using sequential dilution with ethanol.

Using the general procedure (4.2.5) and stock solutions of copper nitrate hemi pentahydrate and trimesic acid, reagent concentrations ([0.0075:0.015 M], [0.03:0.06 M] and [0.06:0.12 M]) and different synthesis times ($t = 2, 5, 10, 20$ minutes) were investigated for their effect on the synthesised framework. For each molar condition, all the synthesis times mentioned were looked at with mass flow rates calculated and PXRD taken.

4.2.5.2 Molar ratios

Using the general procedure (4.2.5) and stock solutions of copper nitrate hemi pentahydrate and trimesic acid, the M:L concentration [0.03:0.06 M] was tested for different molar ratios (M:L= 1:8, 1:4, 1:2, 1:1, 1:0.5) at different reaction times ($t = 10, 20, 30, 40$ and 50 min). In each case the ratio was manipulated using the flow rates of the individual reagent streams while maintaining the overall synthesis flow rate. A summary of the experiments performed are given in Table 4.1.

Table 4.1: Summary of the experiments performed to investigate the three parameters: reagent concentration, molar ratio and synthesis time where $a = [0.0075:0.015]$ M, $b = [0.03:0.06]$ M and $c = [0.06:0.12]$ M.

	Time / min						
Molar ratios / M:L	2	5	10	20	30	40	50
1:8			b	b	b	b	b
1:4			b	b	b	b	b
1:2	a, b, c	a, b, c	a, b, c	a, b, c	b	b	b
1:1			b	b	b	b	B
1:0.5			b	b	b	b	b

4.2.5.3 Sample calculations for EDS measurements

Sample calculation to calculate the M:L ratio from elemental wt% generated using EDS after a 2 minute reaction time considering the copper to oxygen ratio.

$$\begin{array}{rcl}
 \frac{Cu}{O} & & \\
 \frac{23.8}{63.55} & & \frac{25.2}{15.99} \\
 = 0.37 & & = 1.575 \\
 \frac{0.37}{0.37} & & \frac{1.575}{0.37} \\
 = 1 & & = 4.25 \\
 \times 3 & & \times 3 \\
 3 & & 12.75
 \end{array}$$

Given there are 6 oxygens per trimesic acid. The copper to trimesic acid calculated ratio is:

$$3 : 2.1$$

4.3 Results and Discussion

4.3.1 Batch synthesis and characterisation of HKUST-1

HKUST-1 was successfully synthesised using a solvothermal method adapted from previous reports¹³⁵ as confirmed by PXRD, FTIR and TGA data. New batches of HKUST-1 were synthesised regularly using this method with some batch-to-batch variation as expected. Variations were identified in the obtained yield and the Bragg peak width and intensities at $\theta = 6.92^\circ$ and 11.83° .

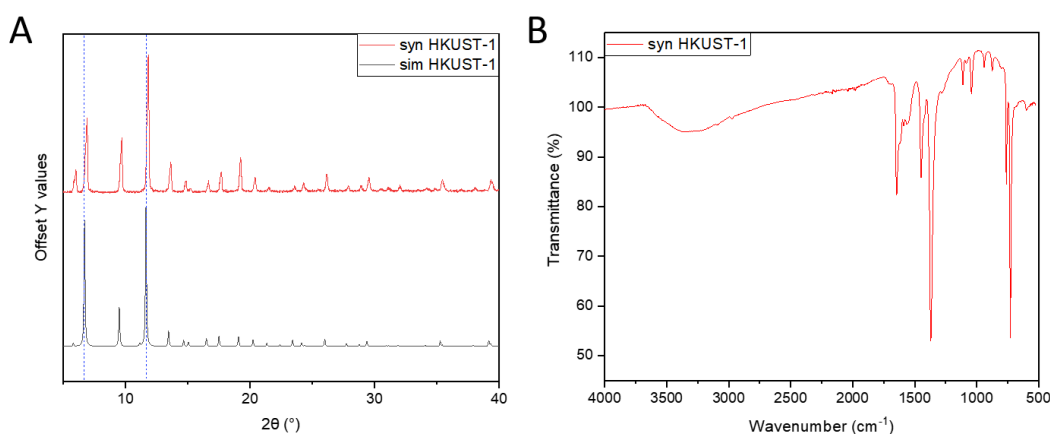


Figure 4.3: Characterisation data for representative batch synthesised HKUST-1. A) PXRD pattern where blue dashed lines show the small shift in 2θ values for the two most prominent peaks and B) FTIR spectra.

The collected PXRD data is shown in Figure 4.3A. The pattern was in good agreement with the simulated data (ccdc deposit number 943009) aside a 0.2° shift to higher values. This is commonly seen in MOFs and usually indicates the presence of guest molecules within the framework pores, affecting the d-spacing and hence the peak positions for the framework.¹⁵⁸ Another possible explanation for the presence of this shift could be in the method of collection e.g. Mo or Cu sources within the instrument. Characteristic peaks were observed at $2\theta = 6.02^\circ$, 6.92° , 9.70° , 11.83° , 13.61° , 19.23° with no new or depleted peaks and the relative intensities of the main peaks agreeing with the simulated single crystal data. Moreover, the peaks are intense and narrow suggesting highly crystalline material.

FTIR data also compared well to that reported for HKUST-1.¹⁵⁸ (Figure 4.3B) The presence of metal-ligand (Cu-O) coordination can be seen with a strong absorbance at 728 cm^{-1} indicating the successful coordination of Copper to the organic linker. Vibrational modes for the carboxylate groups are observed with C-O stretching (1373 cm^{-1}) and C=O stretching (1645 cm^{-1} and 1543 cm^{-1}) indicating the presence of the organic linker, trimesic acid. Moreover, aromatic C=C stretching

from the benzene ring at 1448 cm^{-1} also confirms this.^{159–161} The broad peak seen in the $3500\text{--}3000\text{ cm}^{-1}$ range represents O-H stretching of water coordinated at the open Cu^{2+} site absorbed from the atmosphere.^{147,149}

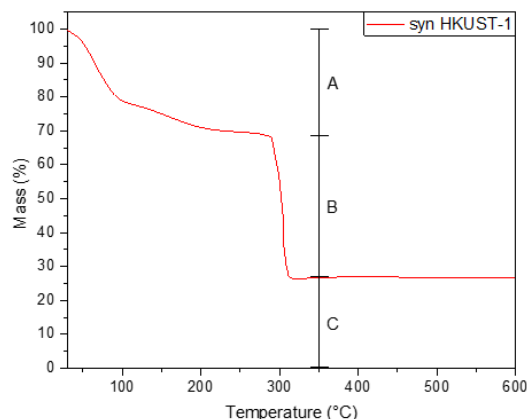


Figure 4.4: Thermogravimetric data for batch-synthesised HKUST-1. Where A= initial loss of solvent/guest molecules; B= organic linker loss and C= remaining metal oxide.

Thermogravimetric data can be seen in Figure 4.4. The framework showed good thermal stability up to $300\text{ }^{\circ}\text{C}$, agreeing with literature.¹⁶² An initial mass loss (Figure 4.4A) from $50\text{--}160\text{ }^{\circ}\text{C}$ represented 32.1 % of the total mass and indicates loss of water, solvent molecules and any impurities or smaller crystallites present within the framework. The remaining solid is the total HKUST-1 present within the sample. The second and largest stage of loss (Figure 4.4B) occurs at $300\text{ }^{\circ}\text{C}$ as the organic ligand is degraded. This accounted for 40.9 % of the total mass and 60.23 % of the remaining mass, hence the framework. The remaining solid is CuO (Figure 4.4C) making up 39.77 % of the framework. These relative ratios are in good agreement with the chemical formula of HKUST-1, $[\text{Cu}_3(\text{BTC})_2(\text{H}_2\text{O})_3]$ which indicate a metal:linker ratio of 3:2 and those reported in literature¹⁶² confirming the correct chemical composition.

SEM images (Figure 4.5) show a sample of HKUST-1 obtained *via* this batch-style method. The particles are non-uniform in size and shape with no distinguishable morphology present. An average particle size was calculated using ImageJ software as $0.99^{+3.41}_{-0.82}\text{ }\mu\text{m}$ (50+ crystals measured) highlighting the large range in crystal sizes.

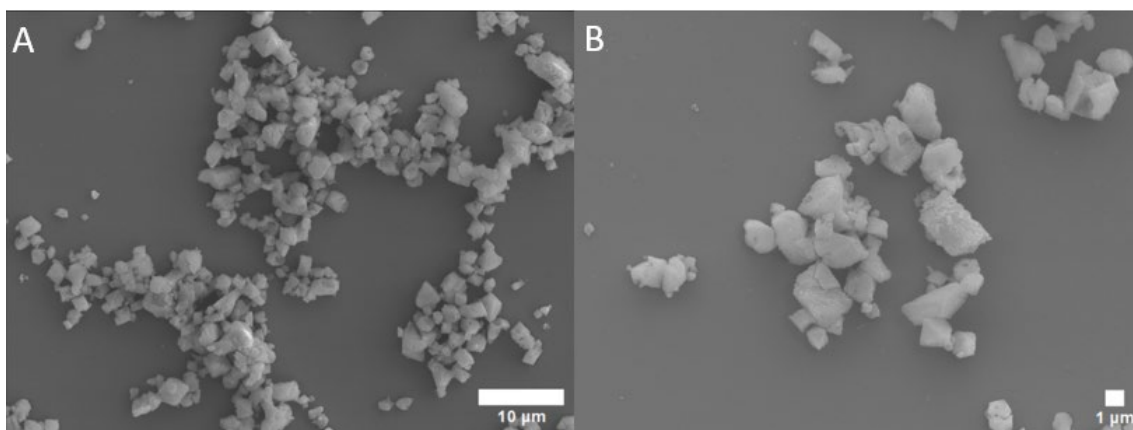


Figure 4.5: SEM images for as-synthesised HKUST-1 using a batch-style solvothermal approach.

It is known that solvothermal synthesis cannot effectively control the nucleation and growth of HKUST-1 with nucleation processes extending far into the crystal growth mechanisms of the framework formation, so random, non-uniform growth is expected and has been previously reported.¹⁶³

4.3.2 Batch synthesis and characterisation of ZIF-8

ZIF-8 was successfully synthesised in batch using a previously reported method¹⁶⁴ and confirmed by PXRD, FTIR and TGA data. PXRD pattern showed good agreement with the simulated crystal data with peaks at $2\theta = 7.50^\circ$, 10.42° , 12.80° and 18.25° (Figure 4.6A). No new or depleted peaks were observed and the relative intensities of the main peaks agreed with the simulated crystal data. Peaks were broader than expected, possibly due to sub-micrometer sized crystals or non-uniform growth.

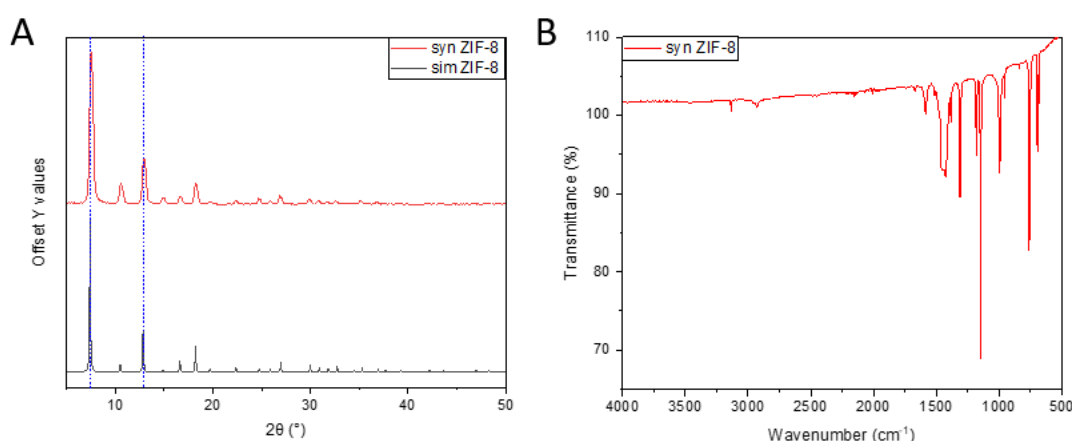


Figure 4.6: Characterisation data for batch synthesised ZIF-8. A) PXRD pattern where blue dashed lines show the small shift in 2θ values for the two most prominent peaks and B) FTIR spectra.

Successful synthesis was further confirmed using FTIR spectra. (Figure 4.6B) Peaks at 3136 cm^{-1} and 2932 cm^{-1} are assigned to the aromatic and aliphatic stretching vibrations of C-H bonds in the imidazolate linker. This is also the same for the stretch at 1590 cm^{-1} which is attributed to the C=N stretching vibration. A weak signal at 1669 cm^{-1} is seen, for the C=C stretching mode of the linker. Finally, the C-N stretching mode is visible at 1150 cm^{-1} as a very strong peak. A Zn-N stretching vibration is expected around 425 cm^{-1} , however this is out of the range of the spectra. These results match well with those reported for ZIF-8.⁷³

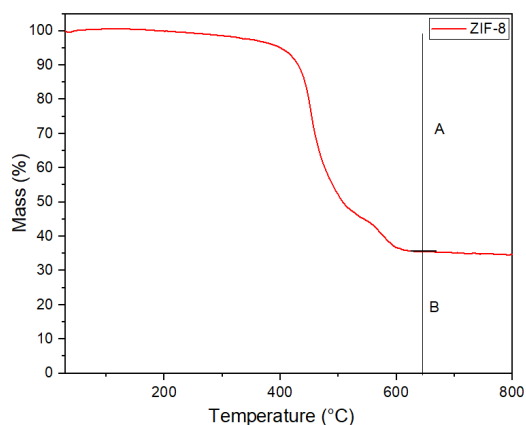


Figure 4.7: Thermogravimetric data for batch-synthesised ZIF-8. Where A= loss of organic linker and B= remaining metal oxide.

TGA data for ZIF-8 is shown in Figure 4.7. The framework showed high thermal stability ($450\text{ }^{\circ}\text{C}$), a common property of zeolite frameworks, and a single loss of mass (Figure 4.7A) accounting for 65 % of the total. This degradation represents the loss of the organic linker to leave ZnO (35 %). (Figure 4.7B) The thermogram shows no guest molecules, including water were present in the framework as no mass loss was seen at lower temperatures, this agrees with the FTIR where no broad stretch was seen for O-H bonds in the $2500\text{--}3500\text{ cm}^{-1}$ range. (Figure 4.6B) The thermogram is in agreement with reported literature¹⁶⁵ and the expected stoichiometric ratios of metal:linker (1:2) according to the frameworks structural formula of $[\text{Zn}(\text{mlm})_2]$.

SEM images (Figure 4.8) for ZIF-8 show a well dispersed, oval morphology with some agglomeration seen which is expected from the methodology used.¹⁶⁴ The crystals show poor uniformity with an average crystal length calculated as $4.54 \pm_{-4.18}^{+9.57}\text{ }\mu\text{m}$ (50+ crystals measured) but a phase pure sample which is consistent with the XRD data. (Figure 4.6A)

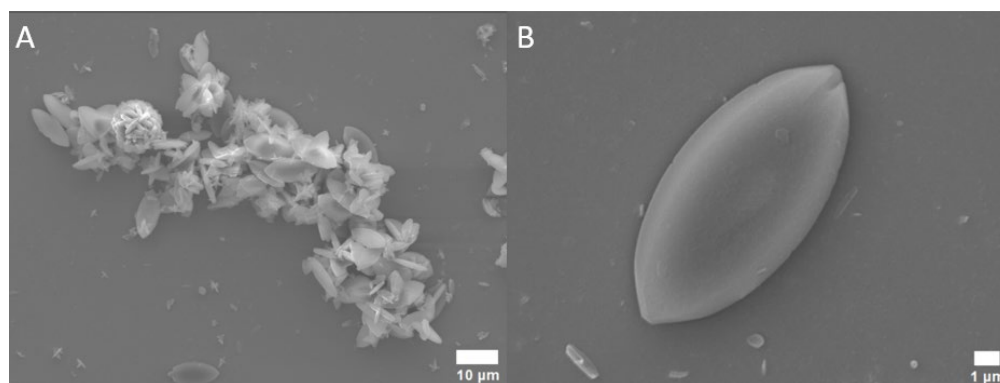


Figure 4.8: SEM images for as-synthesised ZIF-8 using a batch-style solvothermal approach.

From this point, no more ZIF-8 content will be discussed in this chapter. As stated at the start of this chapter, in parallel to this work being undertaken, the work in chapter 5 was also being done. Findings from chapter 5 determined that HKUST-1 was the better candidate MOF to initially focus on during this PhD research and the focus was turned entirely to HKUST-1. As a result, flow synthesis work of ZIF-8 was not carried out and due to time constraints, was not returned to later.

4.3.3 Framework stability

For application-led analysis I was expecting to take MOF products continuously produced, adding in organic dye and solvent and then subsequently analysing the continuous stream. For this to be accurate the product should not be affected by the test itself. Therefore, the stability of the HKUST-1 was assessed in both water and ethanol.

4.3.3.1 Water

The aqueous stability of the framework was assessed. HKUST-1 was dispersed in pH-adjusted water solutions (3, 7, 10) for 2 hours and the recovered framework was physically compared and characterised against the parent material.

A significant physical change could be clearly seen in the material after dispersion in water (pH 7) where it appeared less dense in structure after 120 min and therefore more open. (Figure 4.9A) PXRD of the recovered framework confirmed a phase change in all three pH-adjusted solutions to the same product with no initial peaks remaining and an overall lowered crystallinity, indicated by the reduction in peak intensities. (Figure 4.9B) The presence of precursors and degradation products e.g. $\text{Cu}(\text{OH})_2$ were ruled out using PXRD spectra, confirming a new phase had formed. The pH was tracked at set time periods over the 120 minutes and was found to converge to pH 3.8-4.1 in all cases, irrespective of the starting pH, indicating loss of the acidic linker, trimesic acid had occurred (Figure 4.10). The HKUST-1 phase isolated from the pH 10 solution was the

most crystalline, evidenced by the low background noise and more-defined peaks with full change to the new phase observed after 60 minutes. As the starting pH was decreased, the material became less crystalline, with the acidic solution (pH 3) affording a largely amorphous product.

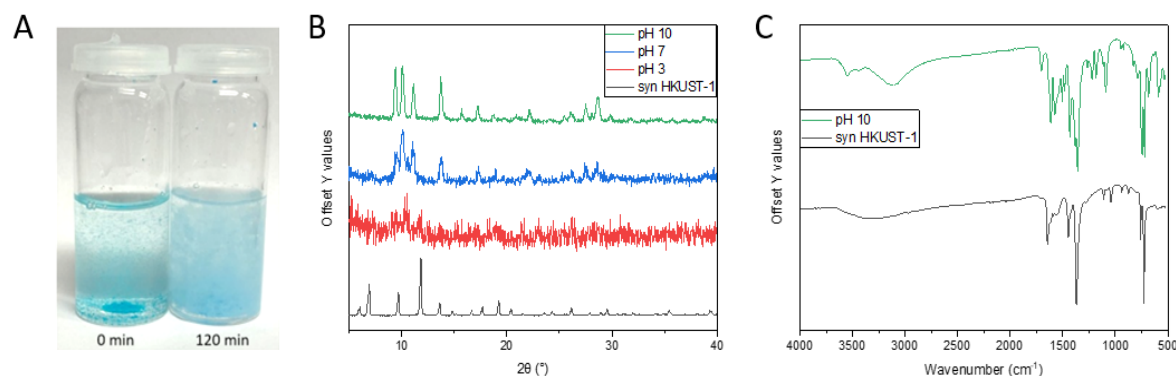


Figure 4.9: Images of dispersed HKUST-1 in water (pH 7) at 0 and 120 min showing the physical change in appearance, B) PXRD patterns of recovered HKUST-1 after immersion in pH adjusted water (pH 3-10) during aqueous stability testing and C) FTIR spectra for the new isolated product after immersion in alkali (pH 10) water.

Following soaking at pH 10 for 60 minutes, PXRD and FTIR data was collected and compared to the framework before soaking. The Bragg reflections (Figure 4.9B, green) at $2\theta = 9.3^\circ$, 10.1° and 11.2° of the crystalline phase match those reported by Majano *et. al.* in their studies of HKUST-1 stability.¹⁶⁶ They described the solid as a mixed phase, partial degradation product of 1) a layered hybrid structure of $[\text{Cu}_2\text{OH}(\text{BTC})(\text{H}_2\text{O})]$ and 2) a 1D, Cu:BTC coordination polymer, formed by hydrolysis at the open metal sites. Despite efforts, they were unable to elucidate a full crystal structure of the hybrid material but did demonstrate the reversibility of the process using ethanol. Later, the decomposition process was elucidated through a series of simulations which identified three different stages of hydrolysis; the first being reversible and affected up to 65 % of Cu sites within the framework structure.¹⁶⁷

FTIR spectra are shown in Figure 4.9C. In the O-H stretching region ($3500\text{--}2500\text{ cm}^{-1}$) multiple environments have appeared including free hydroxyl sites, which is evidence of carboxylic acid groups reforming on the linkers upon hydrolysis of the Cu-O bond. Furthermore, numerous C=O stretches ($1500\text{--}1800\text{ cm}^{-1}$) appeared and peaks at 1693 cm^{-1} and 1600 cm^{-1} from the intact framework have a lowered intensity indicating a loss or change in the bonding environment. Finally, the C-H and C=C stretch (1454 cm^{-1} and 1397 cm^{-1} , respectively) of the linker shifted and several changes in the fingerprint region can be seen indicating partially removed molecules of

trimesic acid consistent with the observed phase transformation in the PXRD data. These findings indicate HKUST-1 has poor aqueous stability.

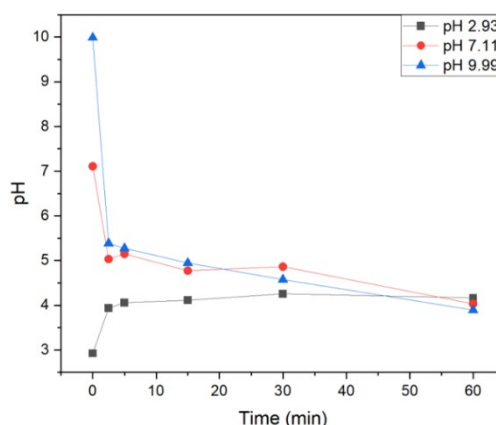


Figure 4.10: A temporal graph showing the change in solution pH during aqueous stability tests of HKUST-1 at varying initial pH showing how it converges to 3.8-4.1 in all cases. This data represents a single experimental run and has no error bars.

To confirm the instability of HKUST-1 in water and confirm the leaching of trimesic acid in pH > 7 the soaked framework could be isolated, dried and weighed to look for a change in mass or assessed via NMR to observe chemical environments. At pH 3 it is suspected that the amorphous solid (Figure 4.9C, red) is potentially being protonated by free protons, causing an increase in the reaction mixture pH. Due to the pH stabilising around 4.1 in each separate experiment it is predicted that this value represents the isoelectric point of the synthesised framework whereby the net surface charge is 0.

4.3.3.2 Ethanol

The stability of HKUST-1 was investigated in ethanol (>99 %) using the same procedure. PXRD data (Figure 4.11A) showed no change in the framework with all Bragg peaks retained and no new ones appearing but a difference in the relative ratio of their intensities. Furthermore, crystallinity remained unaffected and no amorphous material formed which is clear by the flat background. Supporting FTIR data (Figure 4.11B) confirmed that no new functional group environments had formed and relative peak intensities were the same. It was concluded from these results that HKUST-1 showed good ethanolic stability after 2 hours of exposure.

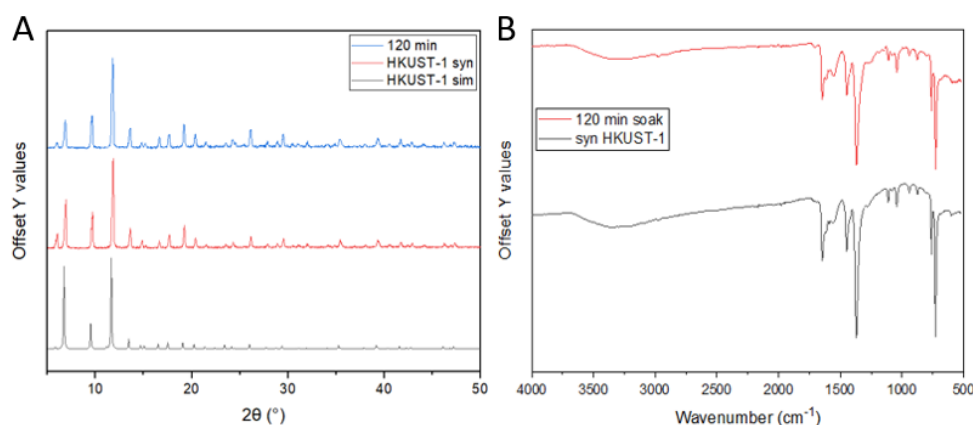


Figure 4.11: A) PXRD patterns and B) FTIR spectra for the recovered HKUST-1 framework after 120 min immersion in ethanol compared to the as-synthesised and simulated data.

In one report, the structural stability of HKUST-1 in ethanol compared to water was highlighted and chemically rationalised.¹⁵⁰ The PXRD spectra of the recovered material showed no change after soaking suggesting a much stronger stability in ethanol and thus, solvent-dependent structural integrity of the framework. Water shows enhanced mobility within the framework as it has full access to all pore sites unlike ethanol which has a collision diameter (4.3 Å) greater than the smallest pore (4 Å). Furthermore, water is a stronger H-bond donor due to its enhanced Bronsted Lowry acidity ($pK_a(\text{H}_2\text{O}) = 14$; $pK_a(\text{EtOH}) = 15.9$) hence destabilising the Cu-O bond toward hydrolysis.¹⁵⁰ On the other hand, ethanol's weakened interaction with the Cu sites provide stability and protection hence, resisting change.

A change or degradation of HKUST-1 is undesirable when considering the broader aims of this research. If the framework's stability is compromised during continuous production, then a device aiming to improve and optimise synthesis cannot be implemented in-line. Therefore, using water within the system is not a viable option but pure ethanol is.

4.3.4 Flow Synthesis of HKUST-1

Following the successful batch-synthesis and characterisation of HKUST-1 and the determination of its ethanolic stability, the objective was to transfer synthesis from batch to continuous. Initially a set-up was formulated based on previously reported methods for HKUST-1 flow synthesis as shown in Figure 4.12.⁷⁶

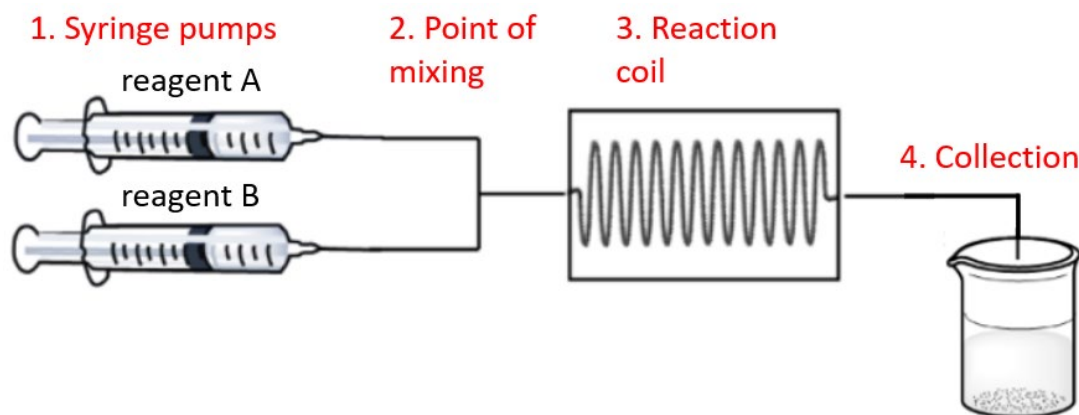


Figure 4.12: Diagram showing the experimental set-up for the flow synthesis of HKUST-1. Adapted from Rubio-Martinez *et. al.*⁷¹

Two syringe pumps with syringes containing the reagent solutions (Figure 4.12.1) were combined at a T-junction for interdiffusion mixing along the PTFE tubing (Figure 4.12.2, $\varnothing=1$ mm, 10 cm) and directed simultaneously into the reaction coil (Figure 4.12.3) which was immersed in a water bath (80 °C) for homogenous heating. The residence time within the reaction coil and hence reaction time was adjusted using the flow rate set at the syringe pumps and the crude product collected in a vial (Figure 4.12.4) and analysed ex-situ accordingly. Several aspects of the set-up and parameters needed to be adjusted including: reaction coil material, times, temperatures and molar ratios.

The reagent concentrations were [0.03:0.06 M] (M:L, where M= $\text{Cu}(\text{NO}_3)_2 \cdot 2.5\text{H}_2\text{O}$ and L= H_3BTC)⁷⁵ due to previously determined synthetic results and the solvent was ethanol (<99 %) based on stability work discussed in 4.3.3. Notably, unlike the set-up reported,⁷⁶ the Vapourtec R4/R2+ reactor with perfluoroalcoyl (PFA) tubing was not used or the back pressure regulator. The aim was to run several procedures to achieve reaction times of 2, 5, 10 and 20 mins.

In the first instance, a large pressure build up was observed *via* irregular areas of deep blue (representing nucleated HKUST-1 framework) along the tubing length (Figure 4.13A) and surges of flow rate could be seen at the tubing exit at a 2 min residence time. Furthermore, evidence of fouling was visible along the length of the tubing as blue particulate coated the lumen.

(Figure 4.13B) Notably, this was concentrated near the start where HKUST-1 would first be nucleating.

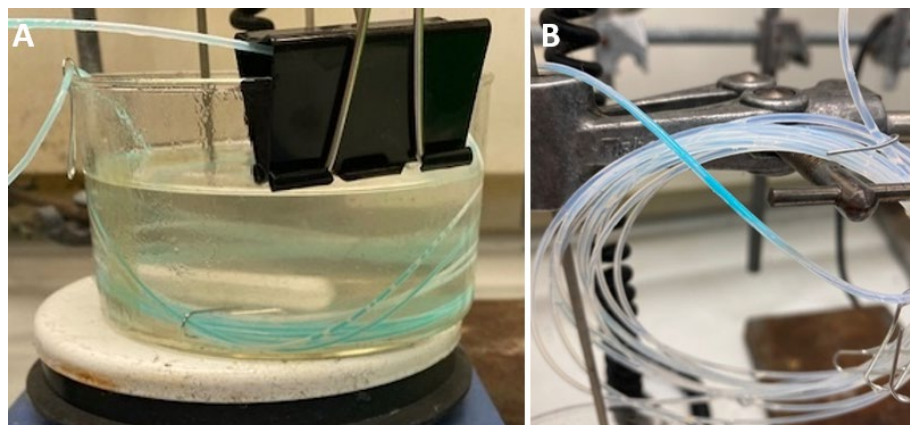


Figure 4.13: Images of issues experienced during preliminary flow synthesis including A) stochastic areas of HKUST-1 through the length of the reaction coil and B) fouling of the inner lumen of the reaction.

Despite using a fluoropolymer tubing alike to what was reported, fouling of the tubing was not expected. However, in literature, HKUST-1 has previously been used to form mixed-matrix membranes (MMM) with other fluoropolymers such as polyvinylidene difluoride (PVDF) indicating that the type of fluoropolymer used has an influence on the interactions.¹⁶⁸ MMMs require strong interactions between the polymer and framework to prevent the formation of interstitial voids in the membrane hence it is expected for the HKUST-1 framework to potentially adhere strongly to the PTFE tubing, causing fouling of the channel. Also, due to the system being purely ethanolic, the use of an 80 °C water bath was not appropriate as ethanol has a boiling point of 78 °C hence it was boiling and gassing within the reaction coil, causing surges of flow rate.

Due to the unavailability of a BPR, to resolve these issues the water bath temperature was lowered to 65 °C in line with the successful continuous synthesis utilising a CSTR in an ethanolic system reported by McKinstry *et. al.*¹³⁵ and a fused silica capillary with an internal diameter of 0.7 mm was used as the reactor coil. The capillary was chosen to transition the surface chemistry of the tubing from a hydrophobic to hydrophilic nature. Previously this has been a success at minimizing the inherent fouling seen during the flow synthesis of gold nanoparticles.⁴⁵ These changes were successful and used in subsequent flow syntheses

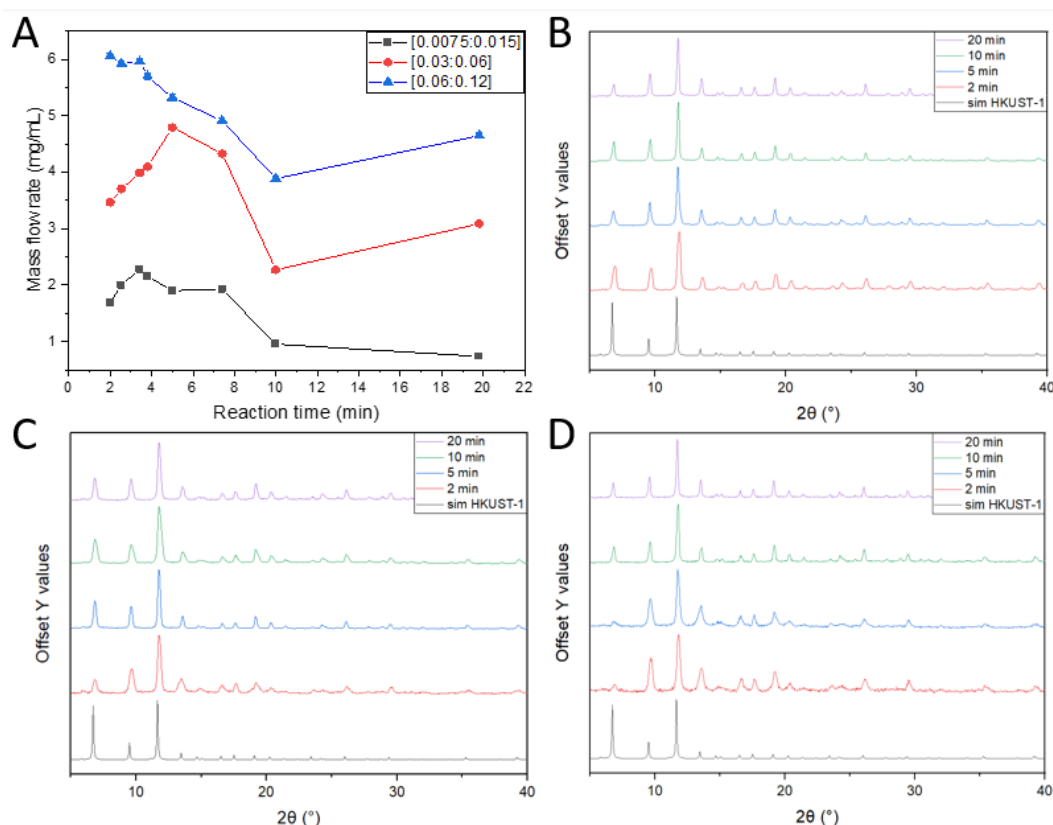


Figure 4.14: A) Mass flow rates, defined as the amount of synthesised framework per unit volume, for different reagent concentrations in a 1:2 molar ratio against reaction time for HKUST-1 flow synthesis. Each data point represents 3 experimental runs with error bars included. PXRD patterns for the crude collected product for each reagent concentration tested B) [0.0075:0.015 M], C) [0.03:0.06 M] and D) [0.06:0.12 M] at different reaction times (t= 2, 5, 10 and 20 min).

A 1:2 molar concentration ratio was used through the flow synthesis experiments in line with previous reports¹³⁵ meaning the Cu^{2+} acts as the limiting reagent and would ideally be completely consumed in the reaction. Several concentrations were evaluated to look at the mass flow rate in each case ([0.0075:0.015 M], [0.03:0.06 M] and [0.06:0.12 M]) The results of these can be seen in Figure 4.14 for the reaction times tested (t=0-20 min).

As the concentrations increased, mass flow rate, defined as the amount of product isolated per unit volume, and hence yield increased when compared to other batch experiments.

(Figure 4.14A) In all cases, no observable trend with residence time could be identified and when the synthesis time was increased from 2 to 20 minutes, an overall slight decrease in mass flow rate was observed which is within experimental error bars and highlights the variability of MOF synthesis which is highly dependent on surface to volume ratios and slight differences through the capillary e.g. due to crystallite deposition, despite consistent cleaning each day. It was observed that when a [0.06:0.12 M] ratio was used, a build up in pressure/potential clogging occurred as calculated flow rates were lower than what was set which, when run for a prolonged period, was accentuated. Due to the expense and large lead time of fused silica capillary, a larger diameter reaction coil was not purchased to overcome this and it was determined that this set of experimental conditions was not possible for the set up.

PXRD of the collected products were taken. (Figure 4.14B-D) Both the crude (non-washed) and washed product were analysed for each residence time, Figure 4.14 shows the normalised PXRD patterns for the crude HKUST-1 isolated from the reactor. When considering the broader use of this data relative to the aim of this work, the crude product is more representative of what would be flowing in-line to the fabricated devices for analysis and hence will be discussed.

The diffraction data (Figure 4.14B-D) shows that in all cases, continuous flow synthesis produced phase pure HKUST-1, with Bragg peaks matching those seen in the simulated single crystal data. Directional growth is also evident; relative peak intensities compared to the simulated data differ with the peak at 6.92° being present but not significant and the peak at 11.83° seemingly more prominent. This could be a consequence of the shear stress expected within the capillary due to laminar flow.

Rate of formation is rapid; after 2 minutes, patterns matching the simulated crystal data with sharp and narrow peaks, high intensity and minimal noise to the baseline are seen for the principle reflections indicating a highly crystalline solid and no observable metastable intermediate under the conditions tested. This agrees with previous in-situ studies monitoring HKUST-1 formation using EDXRD⁹⁰ as well as my own observations from batch experiments where precipitate is immediately formed upon contact of the two reagent solutions even at room temperature indicating rapid crystallisation kinetics. As the reaction time is increased to 20 minutes, peaks become more defined for all concentrations. At a higher concentration ([0.06:0.012 M]) a lowered crystallinity was observed specifically at the lower reaction times (2 and 5 minutes). This is possibly due to excess levels of reagents coordinating at a fast rate than

in the previous tests and causing the formation of less ordered crystals with higher levels of defects.

No unreacted reagent is present within the isolated products despite the linker being added to excess (1:2 molar ratio) and the analysed samples being crude, unwashed products. This is likely due to the unreacted, soluble reagents being decanted off post centrifugation. It is important to note this would not be the case in-line as the product would still be dispersed within the reaction mixture as it passes through the system hence, a consideration for the work later reported in this thesis.

Within the integrated device, the continuously synthesised framework was to be fed into an in-line filtration/separation device with an incorporated membrane filter to separate the free, unadsorbed dye from the stream. Therefore, a key consideration in determining the most appropriate continuous synthesis conditions was the size of the synthesised crystals. (This will be discussed thoroughly and made clearer later in this thesis, 6.3.1.1) If crystals were too small, they would pass through the membrane (pore size= 200 nm) into the filtrate and cause turbidity hence impeding in-situ measurements. Moreover, crystals could cause blockages across the breadth of the membrane surface, limiting diffusion and the lifetime of the device. Therefore, a continuous synthesis was required for uniform, monodisperse growth of HKUST-1 above the 200 nm threshold.

SEM images were taken of the crude samples collected for each PXRD pattern plotted in Figure 4.14B-D. They were used to confirm crystallinity, morphology and average size of the crystals to determine an appropriate methodology for continuous production. Imaging software, ImageJ, was used to calculate the average particle size and energy dispersive spectroscopy (EDS) analysis was used to assess the chemical composition of the crystals through elemental percentages.

Figure 4.15 shows the SEM images collected for a [0.0075:0.015 M] ratio at each synthesis time; these represent the best crystals imaged across the concentrations tested based on morphology and monodispersity that could be considered for the optimal HKUST-1 set-up. Interestingly, they also show an evolution in crystal growth through different definable morphologies some of which have not been previously seen in HKUST-1 to the best of my knowledge. All other images collected showed non-uniform crystal growth with no definable morphology alike to those of the batch-synthesised HKUST-1 shown in Figure 4.5.

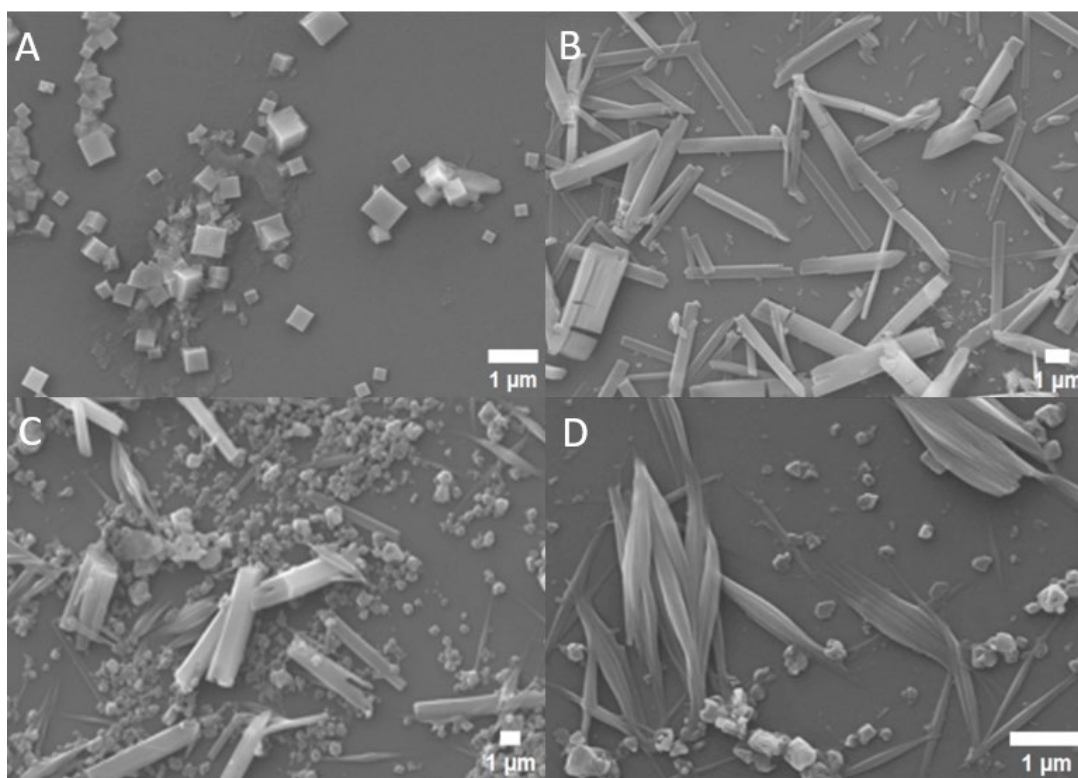


Figure 4.15: SEM images showing HKUST-1 produced *via* continuous synthesis using a [M:L] ratio of [0.0075:0.015] after reaction times of A) 2 min; B) 5min; C) 10 min and D) 20 min.

A range of morphologies were identified for the different synthesis times used and in some cases a variety of morphologies. Typical crystal morphology of formed HKUST-1 is octahedral.¹⁶¹ After 2 minutes of continuous synthesis, monodisperse cubic crystals with non-uniformity and a small degree of agglomeration was observed. (Figure 4.15A) The average particle size was calculated as 0.33 μm with an upper and lower limit of 0.71 and 0.15 μm , respectively. The lower limit of these crystals is below the pore size threshold and therefore could pass through the membrane causing filtrate turbidity and blockages of the filtration surface.

After 5 minutes of continuous synthesis, a plate-like morphology was seen with no evidence of the cubic morphology. (Figure 4.15B) The plate-like crystals showed good dispersity with an average size of $4.42 \pm 2.5 \mu\text{m}$ but poor uniformity in terms of length and width. Alike to the 2 minute reaction time, no impurities were identified, agreeing with PXRD. Despite poor

uniformity, the crystals seen and described here are above the 0.2 μm threshold for the membrane pore size and represent a good synthetic methodology to use for in-line analysis. To my knowledge, evidence of this morphology has not been reported for HKUST-1, it is suggested that this is the visual representation of the directional growth seen in the PXRD (Figure 4.14B) and discussed earlier.

After 10 minutes, a mixture of plate and fibre-like crystals was seen along with a third non-descript shape of crystal with no clear crystal planes, alike to those isolated during the batch style synthesis. (Figure 4.15C) The fibre-like crystals showed a degree of agglomeration and an average size of $2.15 \pm 1.48 \mu\text{m}$. Meanwhile, the amorphous crystals indicated rapid nucleation and agreed with the unnormalized PXRD data which showed a reduced overall peak intensity, used to infer crystallinity. These amorphous crystals ranged in size from 0.18 – 0.97 μm , a six-fold difference, highlighting their non-uniformity. Finally, the plate-like crystals are bigger ($5.41^{+1.08}_{-0.71} \mu\text{m}$) than those obtained at shorter reaction times with a more three-dimensional appearance and less defined crystal edges, with fragmentation at the crystal ends.

The final reaction time of 20 minutes showed a mixture of fibre-like and amorphous particles. (Figure 4.15D) The fibre crystals had increased in size from the shorter reaction time (10 mins) to an average size of 2.53 μm with an upper and lower limit of 3.69 and 1.56 μm , respectively.

EDS analysis of the SEM images collected following a continuous synthesis with a [0.0075:0.015 M] M:L concentration ratio was conducted to confirm the chemical composition of the isolated crude HKUST-1 at each reaction time. Elemental compositions were given in wt% and the relative Cu:BTC molar ratio was subsequently calculated. This is summarised in Table 4.2 with sample calculations given in the experimental section. (4.2.5.3)

Table 4.2: Summary of the elemental compositions of HKUST-1 found by EDS analysis of the SEM images and the calculated Cu:BTC molar ratios.

Reaction time / min	Elemental composition / wt%		Calculated Cu:BTC ratio
	Cu	O	
2	23.8	25.2	3:2.1
5	21.0	30.6	3:2.2
10	18.7	30.0	3:2.8
20	17.9	27.4	3:3.1

HKUST-1 has the chemical formula $[\text{Cu}_3(\text{BTC})_2(\text{H}_2\text{O})_3]$. Therefore, it is expected that for every three copper atoms, two BTC linkers are coordinated; this is equivalent to 18 carbons. Elemental analysis indicated that ratio increased with time. A 3:2 ratio was calculated for all reaction times except 20 minutes with a slightly elevated BTC ratio being calculated for the crude HKUST-1 product. The higher ratio of organic linker to metal could be due to BTC being added to excess as a part of the initial infused reagent solution meaning the crystal surface could bear more BTC than copper as the metal sites are saturated causing higher elemental compositions to be seen. Furthermore, this data represents analysis of the crude product. PXRD (Figure 4.14B) confirmed that a phase pure solid was isolated however without washing stages, excess unreacted organic linker may be more present on the surface of the crystals. Furthermore, EDS is a site specific technique; despite this data being averaged across several sites, it is not representative of the entire sample or the bulk.

From the syntheses using a 65 °C temperature, it was determined the most appropriate HKUST-1 was a 5 minute continuous synthesis with M:L reagent concentrations of [0.0075:0.015 M]. These parameters gave pure HKUST-1, shown to be uniform, monodisperse crystals with plate-like morphology above the threshold for the membrane pore size and a structural formula of 3:2.2 for the copper to linker ratio.

Continuous synthesis work up to this point has used elevated temperatures (65 °C), however, upon simple mixing of the two reagent solutions, precipitate was seen rapidly evolving. Therefore, the necessity for high temperatures was considered and a room temperature set-up was proposed. When comparing temperature systems (65 °C and room temperature) it would be more appropriate to use a room temperature system due to safety, convenience, and green chemistry principles. The use of a water bath (>2 L) while operating electrical equipment e.g., syringe pumps, mixing plates and computers produces a significant risk of electrocution, damage as well as potential wider safety concerns in the case of a spillage. Also, the silica capillary was packaged on a 40 cm diameter polystyrene spool. Removal of the silica capillary to submerge it within the water bath caused breakage of the capillary due to its fragile nature which meant a recalculation of flow rates each time and inconsistencies between experiments as well as presenting a second safety concern of glass fragments. Meanwhile, leaving the capillary on the spool required it being weighted down as polystyrene is buoyant within a water bath big enough to accommodate the spool, this was highly impractical. Due to the reasons stated and in order to maximise yield, the set-up was repeated at room temperature with a [0.03:0.06 M] concentration ratio.

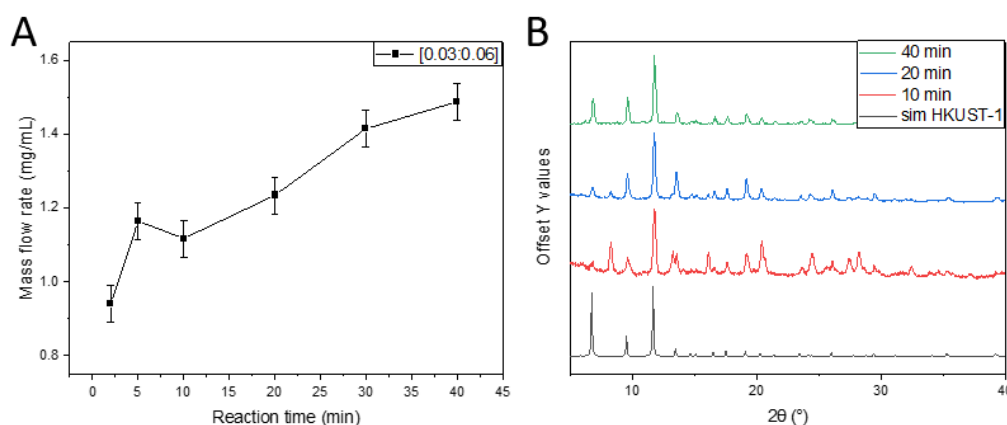


Figure 4.16: A) Mass flow rate and B) PXRD patterns for the continuous synthesis of HKUST-1 at room temperature using a [0.03:0.06 M] concentration ratio. Error bars represent the standard deviation.

In the investigation of room temperature synthesis, the analysis of mass flow rates revealed a positive trend over the varying synthesis durations, (Figure 4.16A) with the durations doubled compared to previous studies. (Figure 4.14A) An increase in mass flow rate from 0.94 to 1.23 ± 0.05 mg/mL occurred between 2 and 20 minutes with a small decrease seen between 5 and 10 minutes that is within the error bar range, then a further marginal increase to 1.49 mg/mL following a synthesis duration of 40 minutes. This is less than the mass flow rate yielded when a temperature of 65 °C was employed (3.087 mg/mL after 20 minutes). Moreover, PXRD patterns showed marked disparities for the differing reaction times. (Figure 4.16B vs Figure 4.14C) Specifically, while a 2-minute synthesis yielded phase-pure, highly crystalline HKUST-1 when a 65 °C temperature was employed, similar success wasn't achieved until 40-minutes for a room temperature synthesis, characterised by diminished noise and absence of new peaks. After 10 minutes, spectra showed HKUST-1 to be present but with an irregular baseline, broad peaks and certain peaks deviating from simulated data at 8.21 and 13.25 °, indicative of amorphous material and a potential mixed phase with a second crystalline solid forming (this is addressed on Page. 84). Additional peaks reduced in intensity after a 20 minute synthesis and by a 40 minute reaction duration, phase-pure, crystalline HKUST-1, devoid of new or depleted peaks was successfully isolated.

SEM images for the isolated HKUST-1 product following a 40 minute room temperature synthesis were collected. (Figure 4.17) Crystals show non-uniform growth with the majority exhibiting no definable morphology. Nevertheless, distinct octahedral morphology consistent with typical HKUST-1¹⁶² is evident in the isolated crystals, as illustrated in Figure 4.17B. Some degree of particle agglomeration is observed with particle sizes ranging from 80 to 700 nm; the lower limit of which falls below the previously discussed pore size. Furthermore, EDS analysis of the SEM images yielded a Cu²⁺: BTC ratio of 3:2.2 aligning with the structural formula of HKUST-1 and

further evidence of a successful synthesis. On comparison to crystals obtained *via* batch solvothermal synthesis, (Figure 4.17) these show clearer crystal planes and a lesser amorphous character, along with the expected octahedral morphology of pure HKUST-1.

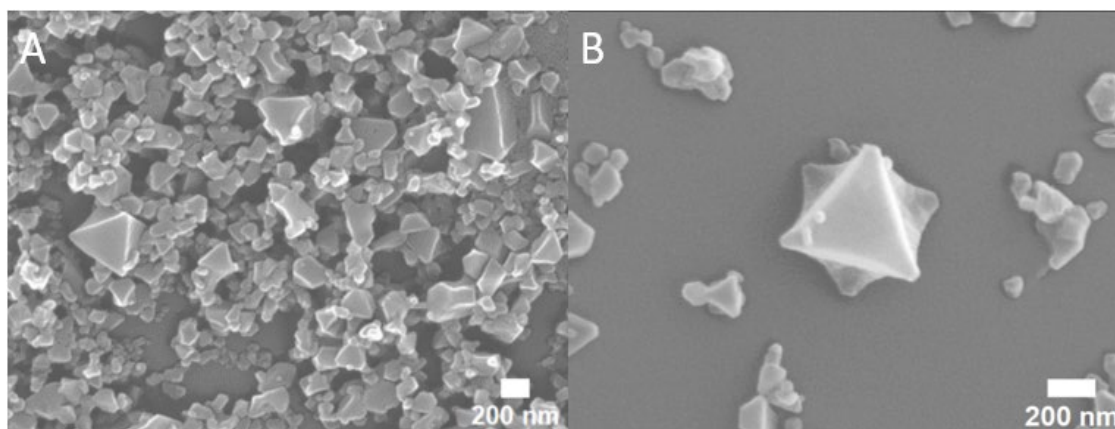


Figure 4.17: SEM images for continuously synthesised HKUST-1 after a 40 minute synthesis at room temperature.

All flow experiments carried out so far have produced crystals with visibly improved crystallinity in the collected characterisation data when compared to the batch-style synthesis but with a mixture of morphologies and a large range of particle sizes. This highlights the inherent benefits of flow synthesis in providing uniform reaction environments for improved reactions over shorter period of time. It also further shows how the synthesis of HKUST-1 is difficult to control without the use of higher boiling point solvents (e.g. DMF) and the presence of modulators due to its rapid nucleation which extends far in to the crystal growth.¹⁶²

Continuing with the room temperature synthesis, the effect of molar ratios on the mass flow rate (Figure 4.18) and isolated product were investigated. The molar ratios were manipulated using flow rates where the reagent stock solutions ([0.03:0.06 M]) and total synthesis flow rate were kept the same for each synthetic duration and molar ratios were set based on the flow rates of the individual reagents e.g. For a 40 minute synthesis ($Q_{\text{syn}} = 96.21 \mu\text{L}/\text{min}$) a 1:8 molar ratio would be set as $Q_{\text{Cu}^{2+}} = 19.24 \mu\text{L}/\text{min}$, $Q_{\text{BTC}} = 76.97 \mu\text{L}/\text{min}$ and a 1:1 molar ratio would be set as $Q_{\text{Cu}^{2+}} = 64.14 \mu\text{L}/\text{min}$, $Q_{\text{BTC}} = 32.07 \mu\text{L}/\text{min}$.

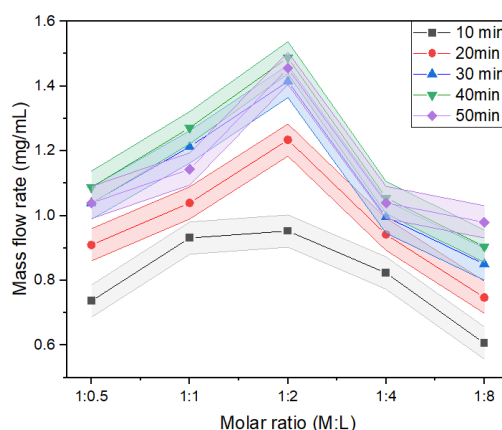


Figure 4.18: Mass flow rate vs molar ratio (M:L) at different reaction times from 10 to 50 minutes.

The range of error is represented by colour filled areas. Error bars represent the standard deviation.

As reaction duration was increased, the mass flow rate increased for each molar ratio until after a 30 minute synthesis. From 30 to 50 minutes, all mass flow rates fall within the same error range shown by the overlapping colour fill areas in Figure 4.18. Interestingly in all durations tested an increase in mass flow rate is seen up to a 1:2 molar ratio followed by a decrease at 1:4 and 1:8 ratios. This is expected because initially the linker concentration is limiting to HKUST-1 formation, before becoming in high excess by a 1:4 ratio which could be impeding coordination and preventing formation which has been previously seen when McKinstry *et. al.* reported on the effects of different solvent conditions on MOF-5.¹⁶⁹

Supporting PXRD patterns are given for reaction durations of 20 and 40 minutes. (Figure 4.19) In both cases, when a 1:4 and 1:8 molar ratio was employed a noisier baseline with new peaks deviating from the HKUST-1 simulated pattern can be seen, more so for a 20 minute synthesis duration. In the case of a 20 minute synthesis it would appear a new crystalline solid has formed at a 1:8 molar ratio due to the lack of main HKUST-1 peak at 6.92 ° and new peaks at 8.21, 13.25, 15.97, 20.15 and several from 24.38-28.48 °. This becomes a mixed phase with HKUST-1 at 1:4 ratio which is still evident at 1:2 to a lesser degree.

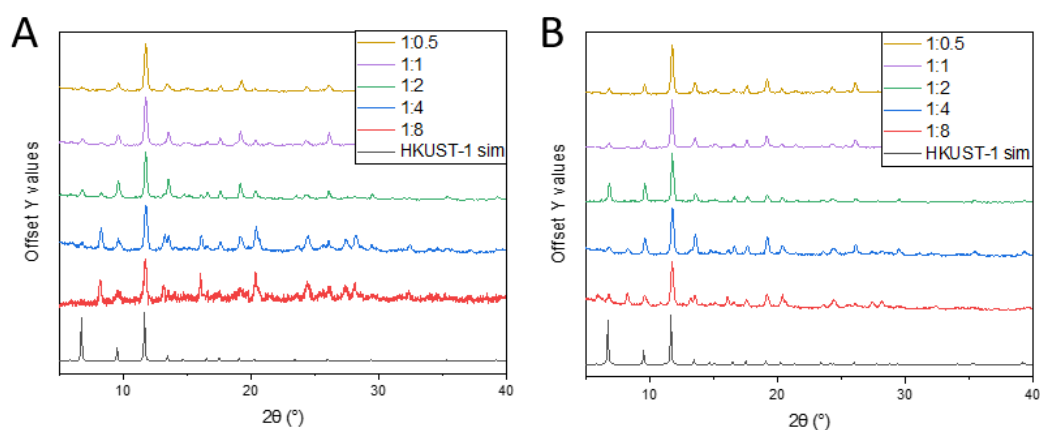


Figure 4.19: PXRD data sets for a) 20 minute and b) 40 minute continuous synthesis of HKUST-1 at different molar ratios (M:L= 1:8, 1:4, 1:2, 1:1 and 1:0.5) manipulated using flow rates.

Similarly, for a 40 minute synthesis, the mixed phase trend of crystalline solids is also seen for a 1:8 and 1:4 molar ratio but with HKUST-1 appearing more prevalent overall than at 20 minutes. When a 1:2 ratio is employed pure-phase HKUST-1 is isolated. At a 1:1 and 1:0.5 molar ratio a highly diminished main peak at 6.92 ° is seen for both synthesis durations but no other deviations from the HKUST-1 simulated pattern or evidence of a mixed phase. At these molar ratios the organic linker is no longer in excess as it has fallen below the HKUST-1 structural formula (1:1.5) and is therefore expected to be fully incorporated within the framework from the reaction mixture. The lowering of this peak could be due to a lack of available organic linker partnered with a directional growth previously discussed causing one crystal plane to prevail over another.

Electron diffraction was performed (with the help of Dr Dan Rainer, NCS, University of Southampton) on samples to further confirm the presence of HKUST-1 and identify the second crystalline solid forming by elucidating the crystal structure of selected crystals seen within prepared specimens. Initial sample analysis examined the isolated product obtained following a 40 minute, room-temperature synthesis at a 1:2 molar ratio. The presence of HKUST-1 was confirmed, with crystal structures successfully determined for individual crystals and .cif files being generated showing HKUST-1's anticipated cubic unit cell ($a=b=c=25.9$ Å, Fm3m symmetry). Subsequently, a second sample was analysed, obtained from a 20 minute reaction duration at room temperature with a 1:8 molar ratio. No HKUST-1 was detected among the crystals examined, consistent with predictions based on PXRD. (Figure 4.19A, red) However, it is important to acknowledge the inherent subjectiveness and site-specific nature of electron diffraction similar to all imaging techniques, therefore the data obtained only represents a small fraction of crystals within the sample meaning the presence of HKUST-1 cannot be excluded and vice versa for the second crystal phase in the first sample discussed. All crystals analysed within this sample

exhibited the same crystal structure which was successfully determined. The structure and corresponding .cif file matched a crystal previously reported¹⁶⁶ and deposited in the ccdc database (UVITAW) where they describe the solvent mediated reconstruction of HKUST-1 in ethanol, this crystal structure is shown in Figure 4.20.

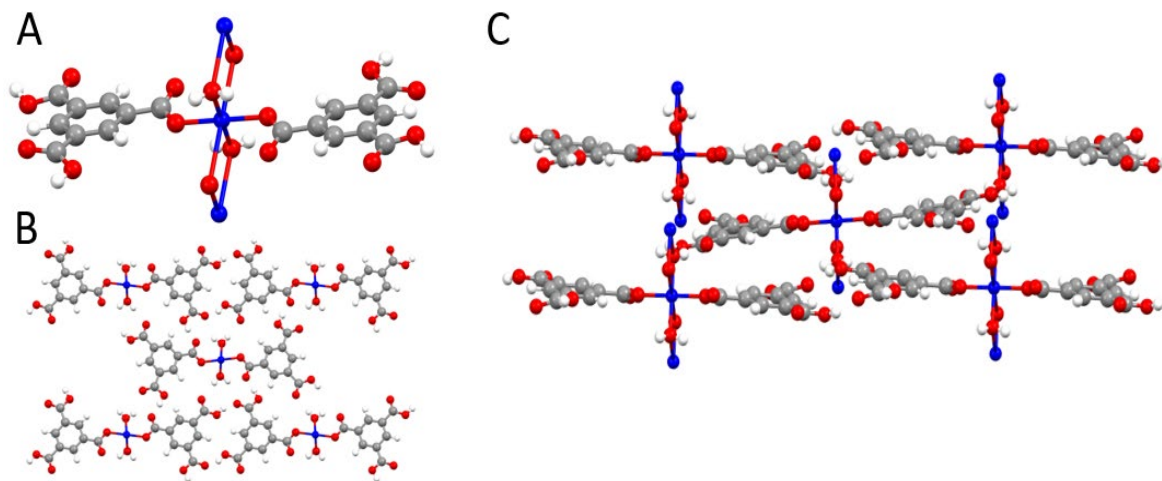


Figure 4.20: Images produced using Mercury for the second crystal structure detected from a 20 minute, RT synthesis with a 1:8 molar ratio. A) the unit cell, B) visualised down the a-axis and C) showing the packing of unit cells in a layered structure with M:L ratio of 1:0.5.

The structure of the second crystalline solid shows a layered structure where copper atoms have octahedral geometry with two axial water ligands and four coordinated organic linkers. The unit cell (Figure 4.20A) orients itself into a layered structure (Figure 4.20C) on the basis of VDWs forces between the aromatic region of the trimesic acid linker. This positioning provides a gateway into a HKUST-1 structure indicating this to be a potential intermediate as substantiated by the findings of Majano *et. al.*¹⁶⁶ who discussed the reconstruction of collapsed HKUST-1 in ethanol at room temperature which draws large comparison with the set-up described here for HKUST-1 synthesis. Differences between how this product was obtained and how it has been achieved previously is that in past work they used degraded product from the hydrolysis of pre-formed HKUST-1 rather than reagent solutions to produce and investigate the solid discussed and their study was done in batch-style conditions under stirring.

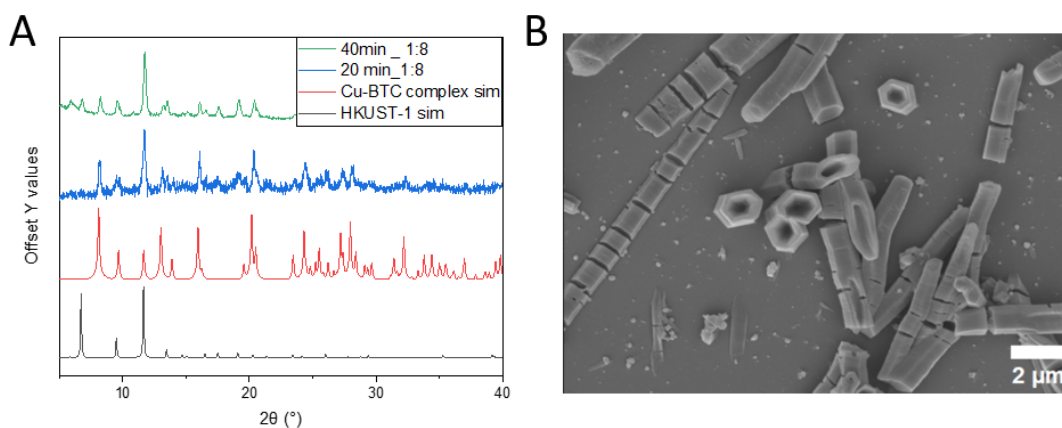


Figure 4.21: A) PXRD pattern comparison of two collected samples against the simulated crystal data for the Cu-BTC complex and HKUST-1 and B) SEM images of the Cu-BTC sample (PXRD pattern represented in green) showing crystals of the second crystal solid identified using electron diffraction.

PXRD data is shown comparing the simulated patterns for the two isolated crystals (Cu-BTC complex and HKUST-1) against the second sample analysed *via* electron diffraction (Figure 4.21A, blue) and a mixed phase sample showing both HKUST-1 and the Cu-BTC complex as present. (Figure 4.21A, green) For both comparisons the peaks align well. SEM images for the sample showing Cu-BTC complex made during a 20 minute, room temperature with a 1:8 molar ratio indicate an unusual morphology of hollow hexagonal prisms alike to that seen in honeycomb cells produced by bees. Previously, SEM images of this phase have been reported and partially agreed with those reported here showing shard like crystals but with more fractured structures and no hexagonal prisms.¹⁶⁶ In this case, the crystals were formed from the degradation of HKUST-1 crystals and not directly synthesised like discussed here. The presence of the Cu-BTC complex is significant as it will inevitably possess different adsorption abilities for organic dyes. The amount of the complex relative to the amount of HKUST-1 will therefore have an effect on the amount of dye adsorbed when it is added in-line for ‘application-led’ analysis.

4.4 Conclusions

Thus far, the flow synthesis of HKUST-1 has been investigated extensively with relation to concentration, temperature, and synthesis time with characterisation data in the form of PXRD, SEM and EDS being shown. From experiments performed at 65 °C it was determined that successful synthesis was independent of the concentration used. Characterisation of the crystals obtained from a [0.0075:0.015 M] M:L concentration ratio showed high levels of crystallinity in PXRD patterns and the SEM images collected after just 2 minutes. Furthermore, crystals showed good monodispersity and uniform, plate-like morphology after a 5 minute synthesis with particle

sizes above the required threshold (200 nm) discussed. Despite the evident success, employing a 65 °C temperature *via* submersion into a water bath presented several challenges, significantly safety with respect to if spillage occurred and difficulty working with fused silica capillary spools with a water bath. Furthermore, the low mass flow rates calculated for this concentration ratio added another layer of impracticality; often requiring collection periods double the synthesis time to produce a measurable quantity of solid with the weighing equipment available. Due to these reasons and the knowledge that simple mixing of the two reagents at room temperature could provide HKUST-1, the experiment set-up was repeated at room temperature. The mid concentration ratio ([0.03:0.06 M]) tested was employed to maximise mass flow rate and due to lab observations showing that the highest concentrations to exhibit clogging and pressure build up *via* visible deposits within the capillary and calculated flow rates being lower than those set at higher reaction times. During the room temperature synthesis, PXRD showed that a synthesis time x20 longer than that used at 65 °C was required to produce a crystalline, phase-pure HKUST-1 of the same quality. Considering green principles, the reduction in temperature would be expected to be more impactful with relation to sustainability but the longer times are a conflicting element to the benefits of this temperature reduction. SEM images showed non-uniform crystal growth with evidence of octahedral crystals throughout the sample, an anticipated shape for typical HKUST-1 synthesis and low degree of amorphous character. EDS substantiated a successful synthesis by showing a Cu^{2+} :BTC ratio of 3:2.2 which matches that expected from the structural formula of HKUST-1. Despite the crystal size range (80 to 700 nm) extending below the membrane pore size and set threshold, later work discussed in this thesis will show that this did not present any issues when the system became fully integrated. Further investigative work at room temperature looked at the effect of reagent molar ratio on the resultant product. As the molar ratio was increased, mass flow rate also increased until a 1:4 and 1:8 M:L ratio was employed when it steadily decreased. Upon analysing the PXRD of samples collected during the 20 and 40 minute experimental run, it could be seen that during the increase (1:0.5 to 1:2) HKUST-1 forms, due to the steady evolution of the main peak found at 6.92 °. For the molar ratios surpassing this, a mixed phase system begins to form preferentially. This is more prevalent in the lower reaction duration. Electron diffraction was used to identify this second crystal phase as Cu-BTC complex (M:L= 1:0.5), previously reported and deposited within the ccdc.

After consulting all the data presented in this chapter it was determined that a 40 minute room temperature synthesis using a 1:2 molar ratio was the optimal conditions for producing HKUST-1 which is used in subsequent chapters to build a process for in-line analysis of the chemical product.

Chapter 5 Analysis: Organic dye adsorption by Metal Organic Frameworks

In the previous chapter, criteria were set out for a candidate MOF to be used within an application-led continuous synthetic system. HKUST-1 was chosen as an appropriate candidate for the in-line analytical system based on the first part of the criteria, a flow procedure was established and optimised for efficient and reliable synthesis of crystalline HKUST-1. In this chapter an application for the system will be evaluated for the implementation of an application-led in-line analyser, whereby the synthetic output may be quantified not on physical property, but the performance of the material against a targeted application. The selected application was the adsorption of organic dyes, a common application for MOFs which can be easily implemented in-line *via* simple infusion of the dye and can be readily analysed in-line using analytical techniques which can provide useful informative data on the synthesised framework, are rapid, sensitive and previously demonstrated in-situ.

5.1 Organic dye adsorption by candidate MOFs

5.1.1 Adsorption as a MOF application

Metal organic frameworks are known to show good adsorption abilities with fast kinetics and high selectivity often without the need for further stimuli attributed to their high surface area and porosity, tunable pore size and functionality and ability to form strong interactions with other atoms, ions and molecules.

Many benchmark MOFs have demonstrated diverse adsorption applications including gas storage^{8,12} and separation, catalysis,⁹ chemical sensing,¹¹ water remediation and drug delivery.¹⁰ When considering an appropriate adsorption application to implement in-line it should, ideally, be simple e.g. through addition of a species or exposure to external stimuli, readily quantified by an existing in-line spectroscopic technique that is sensitive and fast and non-destructive to the framework.

From the adsorptive applications and techniques presented; the adsorption of organic dyes and its analysis using UV-Vis offers a facile and quick method for testing a MOFs ability to remove organic molecules from solvent media- such as in water remediation applications. Organic dyes are commonly used to model a materials adsorptive property, are readily sourced and implementing them within a continuous system is achievable. Furthermore, UV-Vis is a sensitive

and versatile technique that provides quantitative data on a sample's ability to absorb light and offers future opportunity for analysis of several MOF materials including those stated above.

5.1.2 Adsorption

Adsorption is a surface process involving the adhesion of atoms, ions or molecules onto the surface of an adsorbent. It differs from absorption which generally involves the passing of atoms into the bulk material either *via* dissolution or diffusion.

Adsorption can generally be classified into physisorption and chemisorption. Physisorption involves molecular interactions between adsorbate and adsorbent e.g. electrostatics, H-bonding, Van Der Waals, π - π interactions whereas chemisorption involves irreversible covalent bonding.¹⁷⁰ (Figure 5.1)

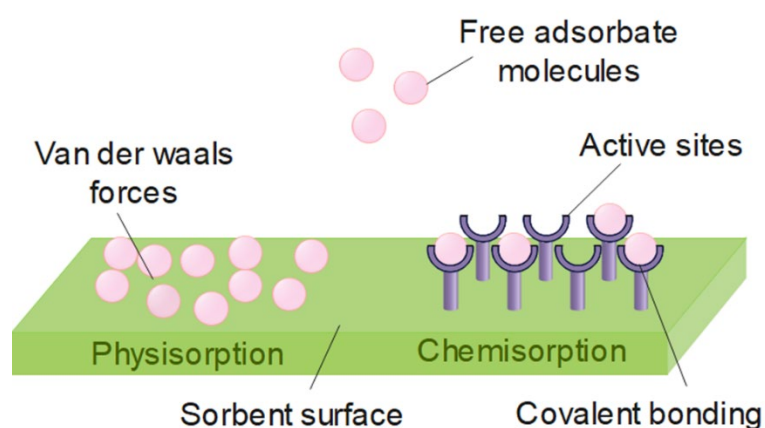


Figure 5.1: Diagram showing the different types of adsorption: physisorption and chemisorption and the forces involved between the adsorbate and sorbent.

The amount of adsorbate taken up from solution per unit volume can be quantified using Equation 1. This is termed the adsorption capacity, measured in mg/g. A higher value indicates a better adsorbing material and vice versa; optimising this value is significant to improve adsorption.

Equation 2: Equation to calculate a material's adsorption capacity at time= t. Adsorption capacity (Q_t); volume (V); initial adsorbate concentration (C_0); adsorbate concentration at t (C_t); mass of adsorbent (m).

$$Q_t = \frac{V(C_0 - C_t)}{m}$$

5.1.3 Possible adsorption mechanisms

The adsorption of organics onto MOF surfaces can occur through one or more distinct physisorption type mechanisms. Open and active metal sites may act as adsorption sites whilst functionalised pores are able to improve adsorption capacity through specific, non-covalent host-guest interactions such as electrostatics,^{171–173} hydrogen bonding,^{174,175} π - π interactions^{176,177} and acid-base interactions.¹⁷⁸ (Figure 5.2)

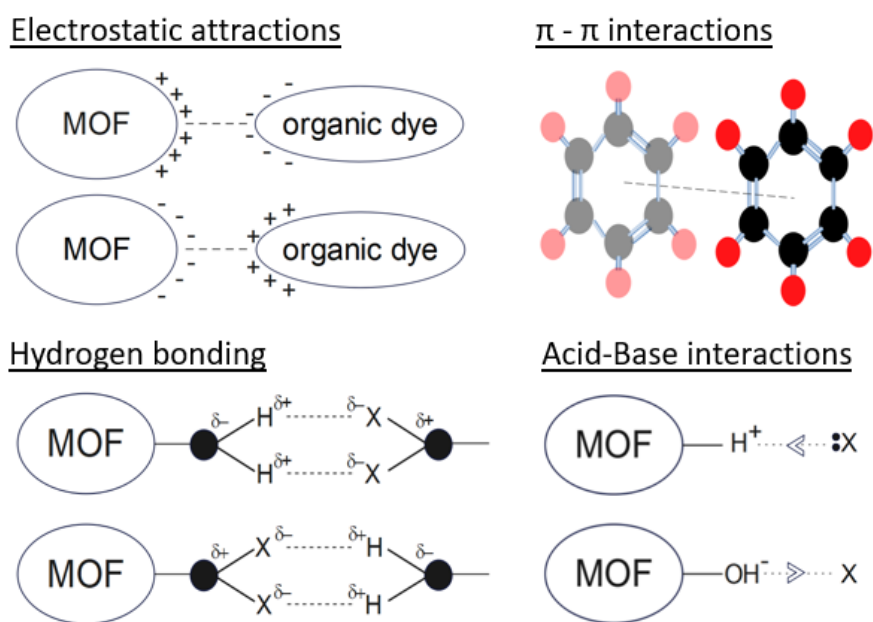


Figure 5.2: Schematics to show the different type of adsorption mechanisms expected between metal-organic frameworks and organic dyes including electrostatics, π - π interactions acid-base interactions and hydrogen bonding (in order of relative bond strengths). Adapted from Hasan *et.al.*¹⁷⁷

Electrostatic interactions occur between oppositely charged species and are considered the strongest of the forces mentioned. The net surface charge or zeta potential of a MOF may be cationic or anionic and interact with charged absorbates as electrostatic interactions. π - π stacking refers to the non-covalent, interaction between aromatic rings when they orient into attractive arrangements that enable orbital overlap. They are so named due to how the rings orient parallel to one another to disperse and enhance the interaction across the molecules. Organic dyes are highly conjugated molecules containing aromatic rings while the organic linkers incorporated into the framework of MOFs broadly contain aromatic rings also, making π - π stacking a prevalent interaction that promotes adsorption.^{176,177} Hydrogen bonding involves dipole dipole interactions between hydrogen atoms bonded to strongly electronegative atoms (e.g. N, O, F) and another electronegative atom and finally, acid-base interaction involve interactions between acidic protons and electron pairs or basic hydroxyls and electron poor atoms.

5.1.4 Organic dyes

Organic dyes are large organic compounds that form coloured soluble dyes. They are highly conjugated π -systems generally containing aromatic rings that absorb light in the ultraviolet/visible spectrum (400 - 700 nm). Some examples of typical cationic (methylene blue (MB), rhodamine B (RhB)) and anionic (methyl orange (MO), methyl blue) dyes can be found in Figure 5.3.

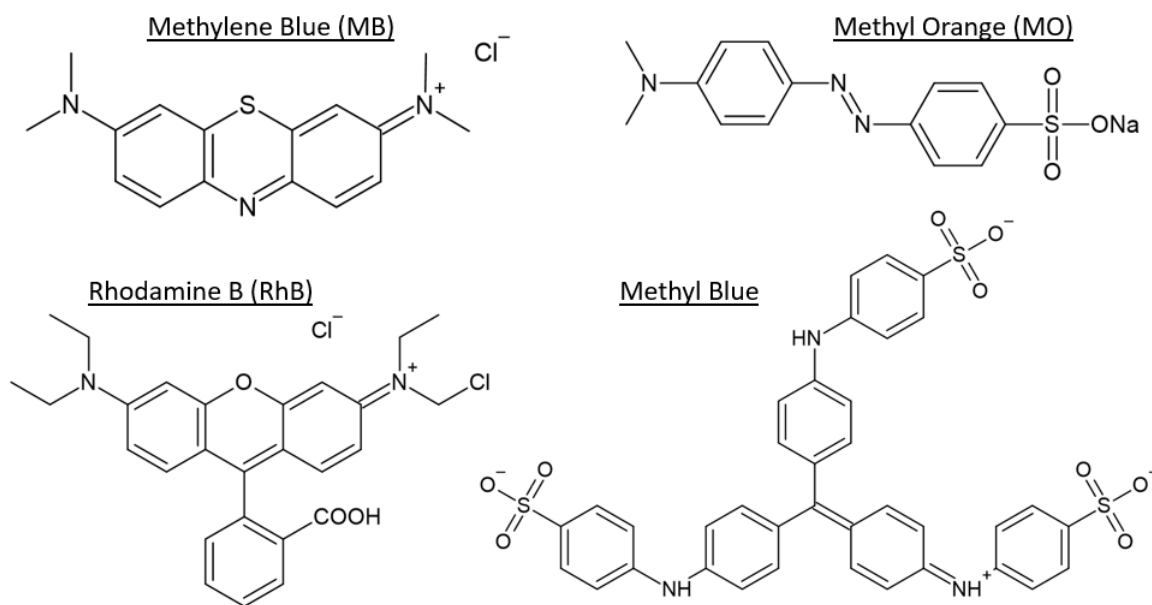


Figure 5.3: Structures of some common organic dyes including: methylene blue (MB), methyl orange (MO), rhodamine B (RhB) and methyl blue. Structures were produced on ChemDraw.

The first study reporting MOFs as adsorbents for organic dyes was published in 2010 by Haque *et al.*¹⁷⁹ They employed Cr-based MIL-101 and MIL-53 (MIL= Material of Institute Lavoisier) to efficiently adsorb anionic methyl orange (MO) from wastewater. The calculated adsorption capacity was greater than that measured for activated carbon, with MIL-101 exhibiting the best performance (e.g. at starting concentrations of 40 ppm after 500 minutes 8 mg/g, 51 mg/g and 83 mg/g of MO was adsorbed for AC, MIL-53 and MIL-101 respectively). It was discussed that the sulfate ion of the dye interacted electrostatically with the cationic framework. Also from the MIL family, MIL-100(Fe) and MIL-100(Cr) were used to absorb MB and MO from solution with the Fe-based framework showing better adsorption capacity for both dyes and the Cr-based framework showing selective adsorption for MB. In aqueous environments both adsorbents showed negatively charged surface areas leading to rapid and efficient adsorption through electrostatic attraction whilst the study also inferred that the central metal also had great effect on the adsorption capacities calculated as they were isorecticular MOFs with only the central metal ion differing meaning that changes in the adsorption capacity for the organic dyes was likely due to

the central metal ion. Furthermore, Lin *et. al.*, employed HKUST-1 in the adsorption of methylene blue, analysing the kinetics and thermodynamics associated with the mechanism.¹⁸⁰ They showed that when the surface became negatively charged in solution pH > 4, adsorbed dye was enhanced compared to lower pH when the framework was positively charged. Other common MOFs such as MIL-53,^{179,181} ZIF-8,^{14,142,182,183} UiO-66^{184,185} and MOF-235¹⁸⁶ have all been identified and applied for adsorptive dye removal in aqueous environments.

5.1.5 Adsorption analysis

To quantitatively analyse the adsorption of dyes, Ultraviolet-Visible (UV-Vis) spectroscopy is a valuable tool. UV-Vis spectroscopy measures the amount of light absorbed (absorbance) or transmitted (transmittance) by a sample at specific wavelengths or across a range. Absorbance, is related to concentration of the absorbing species according to the Beer-Lambert law, given in Equation 2.

Equation 3: The Beer Lambert law which relates the concentration of a species to its absorbance (A). Where ϵ = molar absorptivity ($M^{-1}cm^{-1}$); c = concentration (M); l = path length (cm).

$$A = \epsilon cl$$

The UV region spans wavelengths from 200-400 nm while the visible region covers the 400-700 nm region. Different dyes absorb light at characteristic wavelengths, allowing for their identification and quantification. Calibration curves may be produced using solutions of known concentrations and plotting the recorded absorbance at a dye's peak maximum (λ_{max}) against concentration. Using these calibration curves, concentrations of dye solutions may be determined using the measured absorbance values. Furthermore, the adsorption kinetics may be monitored using UV-Vis spectroscopy. By taking absorbance measurements at regular intervals, the rate of dye adsorption may be tracked and fitted to kinetic models to understand specific adsorption mechanisms.

Some of the key advantages to using UV-Vis spectroscopy are that it is quick and simple with samples requiring minimal preparation, it is sensitive to very low concentrations of dye and non-destructive to the sample. Furthermore, with respect to this work, it has been successfully demonstrated for in-line analysis.⁶¹

When considering the limitations, it is important to note that the presence of secondary absorbing species will interfere with the measurements even at low concentrations and solvent

effects such as solvatochromism can occur where shifts in the spectra are observed due to differences between the solvation energy of the initial and excited states of a species in different solvents. Through careful selection and consistency within experimental conditions these limitations can be minimised.

5.2 Experimental methods

5.2.1 Materials and methods

All chemicals and reagents were purchased from chemical suppliers with no further purification necessary before use.

$\text{Cu}(\text{NO}_3)_2 \cdot 2.5\text{H}_2\text{O}$ (98 %) and trimesic acid (95 %) were all purchased from Sigma Aldrich. Ethanol solvent was purchased from Sigma Aldrich. Organic dyes: methyl blue, rhodamine B, methylene blue and methyl orange were purchased from Sigma Aldrich. Tubing was obtained from RS components (PTFE, $\varnothing = 1$ mm). Silica capillary was purchased from CM scientific. Syringes (20 mL, BD Plastipak Luer Lock) were purchased from RS components. For all flow syntheses syringe pumps (Harvard Apparatus) controlled *via* computer software (LabView) were used to provide accurate infusion of the reagents.

UV-Vis spectra were collected on Shimadzu UV-2700.

5.2.2 Stock dye solutions and preliminary dye screening

Aqueous and ethanolic solutions for methyl orange ($\lambda_{\text{max}} = 464$ nm), methyl blue ($\lambda_{\text{max}} = 603$ nm), methylene blue ($\lambda_{\text{max}} = 665$ nm) and rhodamine B ($\lambda_{\text{max}} = 545$ nm) (0.025 mM) were made. HKUST-1 and ZIF-8 were synthesised using the methods described in 4.2.2 and 4.2.3, respectively. MOF (5 mg) was weighed out and added to vials containing dye (10 mL) under moderate stirring. After 90 minutes, the solutions were centrifuged (100 rpm, 5 min) and the filtrate decanted into a cuvette for UV-Vis analysis. This was performed for both MOFs for all the organic dyes.

Example: A 0.1 mM stock solution (250 mL) was made with methylene blue (7.99 mg, 0.025 mol) and ethanol. A 0.05 mM solution was made from stock solution (0.1 mM, 5 mL) and DI water (5 mL). A 0.025 mM solution was made from 0.05 mM solution (5 mL) and DI water (5 mL). This was repeated until I had 8 solutions. This was performed for methyl blue, methyl orange and rhodamine B.

5.2.3 Calibration curves

A calibration curve was collected for methylene blue solutions in ethanol for concentrations between 0.0075 and 0.1 mM. The solutions were made *via* a serial dilution from a stock solution of 0.1 mM and collected on a UV-Vis; absorbance of the longer wavelength peak (~665 nm) was plotted.

5.2.4 Control experiments for batch adsorption: pH stability and reagent effect

To methylene blue stock solution (10 mL), 2M HCl was added (0.5 mL). After 30 minutes UV-Vis spectra of the solutions were collected.

In a second control experiment methylene blue solution (10 mL) was separately added to the HKUST-1 reagent stock solutions: copper nitrate hemipentahydrate (10 mL [0.03 M] and trimesic acid (10 mL, [0.06 M]). UV-Vis spectra was taken at different times within a 30 minute range ($t=5, 10, 15, 20$ and 30 minute).

5.2.5 Adsorption kinetics of redispersed HKUST-1 towards methylene blue

HKUST-1 (10 mg) was immersed in methylene blue (0.01 mM, 20 mL, EtOH) and placed under stirring. Aliquots (~1 mL) of the solution were taken at different times ($t= 0, 0.5, 2.5, 5, 10, 15, 30, 60, 90, 120$ min), centrifuged (100 rpm, 1 min) and analysed *via* UV-Vis.

5.2.6 Adsorption kinetics of dispersed HKUST-1

Copper nitrate hemipentahydrate stock solution ([0.03 M], 10 mL) and trimesic acid stock solution ([0.06], 10 mL) were added to a vial under moderate stirring for 10 minutes. Following this 10 mL of reaction mixture was transferred to a second glass vial, also under stirring, and 10 mL of methylene blue solution (0.01 mM) was added. Aliquots (~1 mL) of the solution were taken at different times ($t= 0, 0.5, 2.5, 5, 10, 20, 30, 60$ min), centrifuged (100 rpm, 1 min) and analysed *via* UV-Vis. This was repeated for synthesis times of 20 and 40 minutes.

5.2.7 Adsorption kinetics of dispersed HKUST-1: observing dilution effects

As in 5.2.6, copper nitrate hemipentaydrate stock solution ([0.03 M], 10 mL) and trimesic acid stock solution ([0.06 M], 10 mL) were added to a vial under moderate stirring for 20 minutes. Portions of reaction mixture were transferred to secondary glass vials, also under stirring, and made up to 10 mL total volume using pure ethanol to produce 7 vials of reaction mixture with

varying dilutions of reaction mixture (5, 12.5, 25, 50, 75 and 100 %). 10 mL of methylene blue solution was added to each and aliquots (~1 mL) of the solution were taken at different times ($t = 0, 0.5, 2.5, 5, 10, 20, 30, 60$ min), centrifuged (100 rpm, 1 min) and analysed *via* UV-Vis. This was repeated for synthesis times of 20 and 40 minutes.

5.2.8 Control experiments for flow adsorption

An ethanolic methylene blue solution (0.01 mM) was passed through the different tubing materials: silica capillary ($\varnothing = 700$ μm , 10 m) and PTFE tubing ($\varnothing = 1$ mm, 4 m) using a syringe pump. The fluid output was analysed *via* UV-Vis to assess for any changes in concentration.

5.2.9 Adsorptive kinetics of dispersed HKUST-1 (in flow)

Copper nitrate hemipentahydrate stock solution ([0.03 M], 10 mL) and trimesic acid stock solution ([0.06 M], 10 mL) were added to a vial under moderate stirring for 20 minutes before being loaded into a syringe. A second syringe containing pure ethanol was infused with the first syringe through a T-junction at different flow rates to produce a process fluid with various reaction mixture dilutions and so the total flow rate equalled 384.84 $\mu\text{L}/\text{min}$. 20 cm of PTFE tubing followed this to allow for dispersion of the two streams. A third syringe pump was connected to infuse methylene blue (0.01 mM, 384.84 $\mu\text{L}/\text{min}$) through PTFE tubing ($\varnothing = 1$ mm, 10 cm) to a T-junction with the synthetic section output (total flow rate = 769.68 $\mu\text{L}/\text{min}$). The new stream passed through PTFE tubing ($\varnothing = 1$ mm, 4 m) and was collected in a vial at the outlet. Each collection was centrifuged (100 rpm, 1 min) and analysed *via* UV-Vis. This was repeated for a 40 minute synthesis. The set-up is shown in a simple diagram (Figure 5.4) and example set flow rates are described below. (Table 5.1)

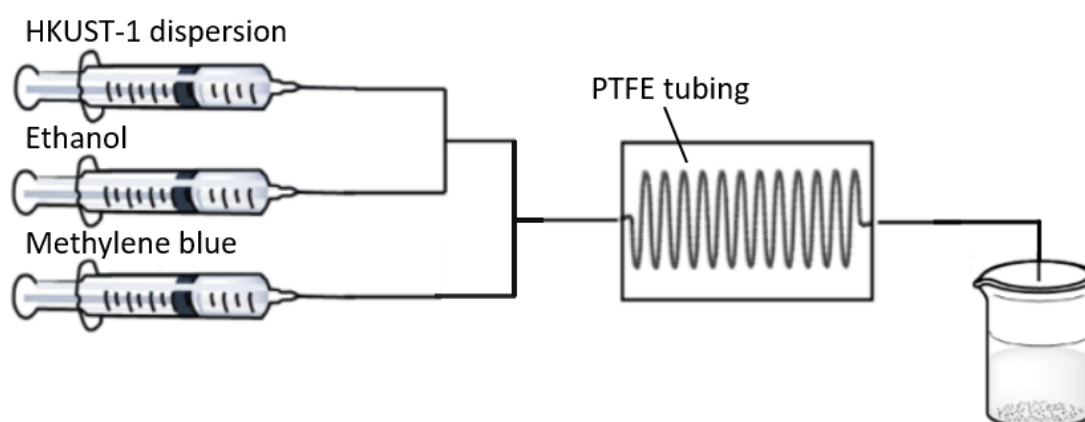


Figure 5.4: Diagram for the set-up used to investigate the adsorptive kinetics of dispersed HKUST-1 in flow for methylene blue.

Table 5.1: Set flow rates for dispersed reaction mixture, ethanol and MB solution (0.01 mM) for dilution experiments looking at how the amount of reaction mixture affects the amount of adsorption. Q = the set volumetric flow rate

HKUST-1 reaction mixture/ %	Q (rxn mixture) / $\mu\text{L}/\text{min}$	Q(EtOH) / $\mu\text{L}/\text{min}$	Q(MB) / $\mu\text{L}/\text{min}$	Total Q / $\mu\text{L}/\text{min}$
5	9.62	182.80	192.42	384.84
12.5	24.05	168.37	192.42	384.84
25	48.11	144.32	192.42	384.84
50	96.21	192.42	192.42	384.84
75	144.32	96.21	192.42	384.84
100	192.42	0	192.42	384.84

5.3 Results and Discussion

5.3.1 Screening of organic dyes for adsorption by HKUST-1

Batch synthesised ZIF-8 and HKUST-1 were screened for their adsorption against several common dyes, these included: methylene blue (MB), rhodamine B (RhB), methyl orange (MO) and methyl blue. They were chosen as examples of cationic and anionic dyes to determine the best pairing of MOF and dye to take forward as a candidate adsorption mechanism for the continuous application-led system. Screening was done by adding a known amount of MOF to the dye which was a set volume and concentration. After a period of time, the MOF was recollected and the filtrate was quantified by UV-Vis (Figure 5.5) and the estimated percentage removal from solution was calculated. (Table 5.2) In the first instance, aqueous solutions were used for adsorption to simulate the environment for the target application; organic dye water adsorption.

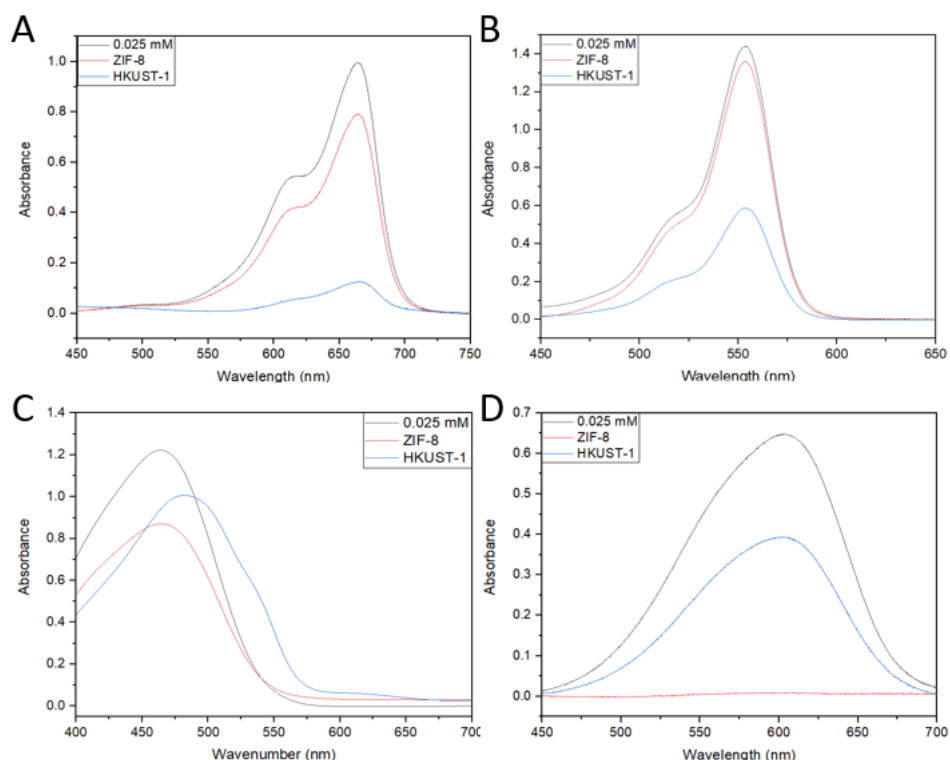


Figure 5.5: Preliminary adsorptive screening results of ZIF-8 and HKUST-1 with A) methylene blue (MB); B) rhodamine B; C) methyl orange and D) methyl blue. In each case the absorbance spectrum at a 0.025 mM solution of the dye is shown, then the same solution after exposure and removal of HKUST-1 and ZIF-8.

Table 5.2: A summary of the adsorption capacities of ZIF-8 and HKUST-1 for various organic dyes (0.025 M) from aqueous environments after 90 min, shown in Figure 5.5.

	Methylene Blue (MB) / mg/g	Rhodamine B (RhB) / mg/g	Methyl Orange (MO) / mg/g	Methyl Blue / mg/g
ZIF-8	3.41	1.25	4.68	39.39
HKUST-1	14.03	14.22	3.03	15.56

ZIF-8 showed excellent uptake of methyl blue ($17 \times 7.6 \times 3.3 \text{ \AA}$) after 90 mins with 98.5 % of the dye being removed from solution. Of the other dyes tested, methyl orange ($13.1 \times 5.5 \times 1.8 \text{ \AA}$) and MB ($17 \times 7.6 \times 33 \text{ \AA}$) also showed fair uptake with no shift in peak wavenumber, removing 28.6 % and 21.3 % of the dye, respectively. Both these dyes have dimensions just larger than the pore aperture of ZIF-8 and could possibly access the internal surface area hence increasing uptake.¹⁴⁰ Removal of RhB ($15.9 \times 11.8 \times 5.6 \text{ \AA}$) was low suggesting that ZIF-8 is not efficient at uptake, despite reports.¹⁴⁰ The difference in findings could be down to the ZIF-8 surface area or zeta potential. RhB is too large to fit into the pores of the framework and hence, adsorption is limited to the exposed outer surface.¹⁴⁰ The obtained characterisation data of ZIF-8 (shown in 4.2.3)

confirmed high crystallinity but gave no indication of the overall surface area, if this was low then inefficient adsorption would be expected. Furthermore, surface charge has a key effect on adsorption in terms of electrostatic interactions. Information on the BET value and zeta potential of the framework would be helpful to identify if these suggestions are the reason for the results compared to literature.

When HKUST-1 was screened against the dyes, methylene blue showed the best adsorption (87.7 %). RhB had a 59.4 % removal from solution, suggesting good uptake. Both dyes are highly conjugated with aromatic rings that can π - π bond to aromatic rings of the organic linker within the framework and promote adsorption. Furthermore, as mentioned, adsorption is enhanced *via* electrostatics; MB and RhB are cationic dyes and showed greater removal than anionic dye MO. HKUST-1 has previously been used in redox reactions where it is oxidised, donating negatively charged electrons¹⁸⁷ which suggests electrostatics could be playing a part in adsorption also. Methyl orange showed low removal from solution (18.5 %) and a red shift in peak wavelength from 462 nm to 482 nm. The reason for the shift is possibly because MO is an indicator, working in the pH range, 3.1-4.4. These results suggest the solution pH has moved within the range for methyl orange and protonation of the framework has occurred, causing a colour change.¹⁸⁸

From these findings, it was decided the adsorption of methyl blue by ZIF-8 and MB by HKUST-1 were to be taken forward for further investigation.

5.3.2 Methyl Blue

Screening results suggested ZIF-8 had a profound ability to remove methyl blue from aqueous environments and was taken forward as a potential candidate. Upon investigation it was recognised that the methyl blue was undergoing a rapid degradation that occurred irrespective of the framework being present. This is shown in Figure 5.6 when a methyl blue solution was left to stand in visible light and UV measurements were taken at different times. In the first 5 minutes, a 31 % decrease in the measured absorbance value was observed which equates to a degradation rate of -0.096 s^{-1} . When solubilised in ethanol, similar results were obtained but to a lesser degree. (data not shown)

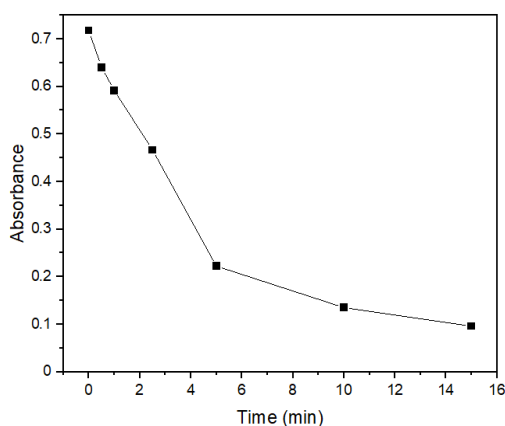


Figure 5.6: A plot of the absorbance of methyl blue (0.025 M) at 603 nm over time when left to stand in visible light, showing the rapid degradation. The data shown represents a single experimental run.

As a result of these findings, methyl blue was excluded from further studies as it was the only dye tested that was appreciably removed by ZIF-8, focus was placed on HKUST-1 and its adsorption of methylene blue.

5.3.3 Methylene Blue

A second blue coloured dye tested for adsorption onto HKUST-1 was methylene blue (MB). MB is an organic, cationic dye commonly used as a staining agent in medical applications and as a general dye but has also previously been used, as a target compound for elucidating a material's adsorptive properties.¹⁸⁹

MB showed the highest adsorption of those tested with HKUST-1. The UV-Vis spectra of MB contains two distinct peaks at 614 nm and 664 nm with the latter showing greater absorbance values. Ethanolic stability was confirmed over 100 minutes (Figure 5.7A) and a calibration curve was collected with good linearity ($R^2 \leq 0.98$) (Figure 5.7B) in line with the findings discussed in 4.3.3.1 where it was determined that HKUST-1 was not stable in aqueous environments and the determined flow synthesis procedure would involve a pure ethanol solvent system in the final setup.

The presence of ethanol in the solvent mixture affects the intensity and position of the spectrum. A 219 % hyperchromic enhancement and a peak shift to 655 nm was seen for concentrations of 0.005 mM MB in ethanol comparative to water. This is due to the lowered polarity of ethanol meaning fewer H-bonds are made to the dye.¹⁹⁰

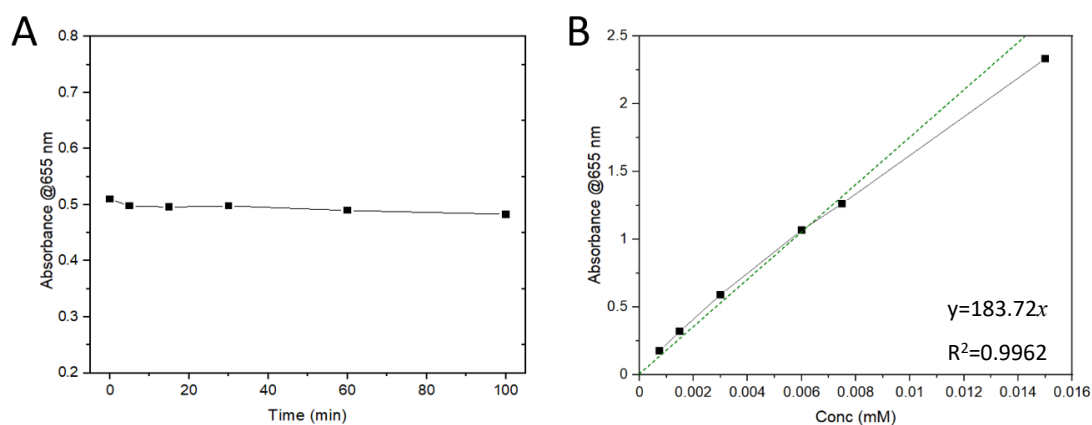


Figure 5.7: A) Dye degradation study of methylene blue in water over 100 minutes showing its stability in visible light and B) A calibration curve for methylene blue in ethanol. The green line shows a linear trendline with an (x,y) intercept of (0,0).

Table 5.3: The solvent mixtures used for MB calibration curves and the peak position and absorbance recorded for 0.005 mM solutions.

Solvent	Peak wavelength / nm	Absorbance ([MB]= 0.005 mM)
Water	665	0.21
Ethanol	655	0.44

The final envisioned process would involve the addition of the methylene blue solution into the synthetic process stream which was expected to contain unreacted reagent and be an acidic environment due to free protons generated during linker deprotonation and coordination. Therefore, MB had to demonstrate stability in the presence of the HKUST-1 reagents and an acidic environment with no change in peak wavelength or intensity in the UV-Vis spectra.

An initial crude control experiment to test this was performed using 2M HCl. Acid (0.5 mL) was added to a 0.01 mM solution of MB in ethanol (10 mL) and the UV-Vis spectrum was taken at different times over 30 minutes to see if there were any observable change in the spectra. No change was observed in the spectra confirming the acidic stability of methylene blue. (data not shown) This opposes some previous reports.¹⁹¹

The second set of control experiments looked individually at the effect of the HKUST-1 reagents: copper nitrate and trimesic acid on methylene blue. (Figure 5.8) In both cases MB showed no observable change in spectra within the 30 min time period tested; peak wavelengths were maintained and absorbance values remained within a 1.2 % range from the initial stock solution.

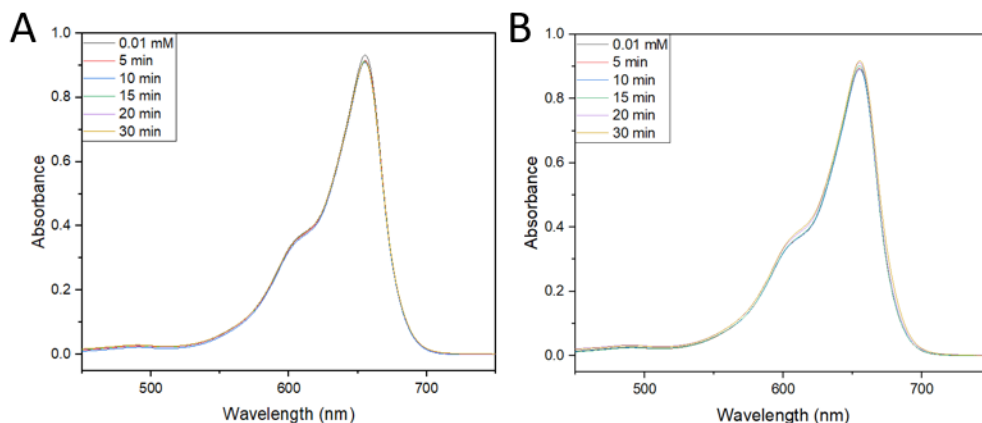


Figure 5.8: UV-Vis spectra collected over time as a part of control tests for the stability of 0.01 mM methylene blue (10 mL) in ethanol with A) copper nitrate hemipentahydrate [0.03 M] and B) trimesic acid [0.06 M].

Following the success of the batch control experiments, methylene blue was deemed an appropriate organic dye for application within the final process and taken forward for further experimentation to characterise its adsorption onto HKUST-1.

5.3.4 Batch adsorption: Adsorptive kinetics of redispersed HKUST-1

To investigate the adsorptive kinetics of methylene blue on HKUST-1 in ethanol, a timed study was undertaken in batch using 20 mg of redispersed HKUST-1, synthesised using a previously described method (4.2.2), in 20 mL of MB ethanolic solution ([0.01 mM]) whereby aliquots of the reaction mixture were taken and measured *via* UV-Vis at set time intervals. (Figure 5.9A) The concentrations and subsequent adsorption capacities were calculated using the calibration curve (Figure 5.7B) and Equation 2, then plotted. (Figure 5.9B)

The adsorption mechanism shows quantifiable and distinct values for each measurement taken and continuous dye removal up to 120 mins. The Q_t vs time plot is shown in Figure 5.9B. A steep initial gradient following by a gradual plateau after just 20 mins indicates rapid and facile uptake of the dye with equilibrium not being reached after 120 mins. After 60 minutes of exposure, 32.7 % of MB was remaining in solution equating to a 10.6 mg/g adsorption capacity. This is comparatively low to literature which reports a maximum adsorption capacity of 250 mg/g in water and using higher adsorbent dosages and different initial MB concentrations.

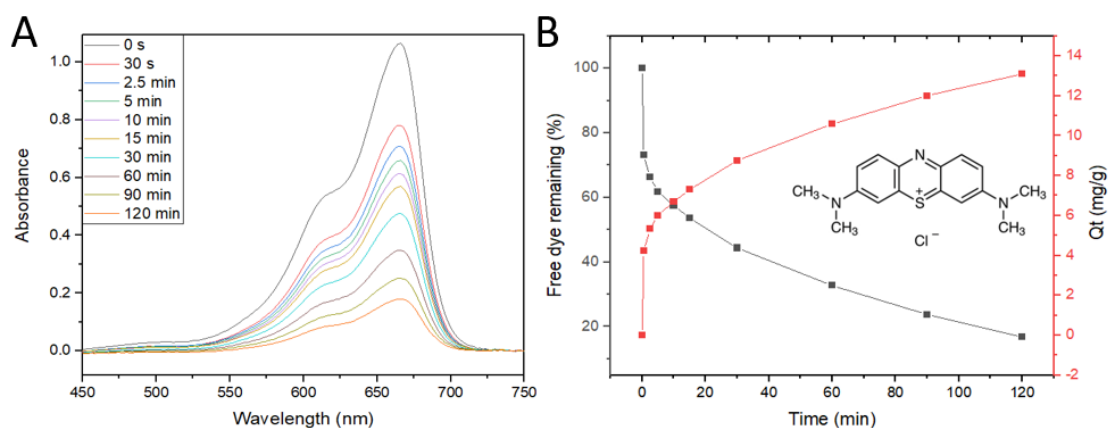


Figure 5.9: A) Measured UV-Vis spectra over time showing the reduction in absorbance as dye is removed and B) a plot showing the calculated free dye remaining (%) and associated adsorption capacities for the time intervals tested when redispersed HKUST-1 (20 mg) is immersed in MB [0.01 mM]. The data shown represents a single experimental run.

5.3.5 Batch adsorption: Adsorptive kinetics of dispersed HKUST-1

Following the success of these results batch experiments were performed to simulate the expected results that would be generated in flow e.g., adsorption of freshly synthesised MOF. The previous experiment featured MOF that was isolated and then redispersed which is not representative of the proposed analysis method. Ethanolic MB solution ([0.01 mM]) was added to a HKUST-1 reaction mixture (RT, M:L= [0.03:0.06 M], ethanol) following different synthetic times in a 1:1 volumetric ratio and adsorption was monitored using UV-Vis spectrometry. (Figure 5.10)

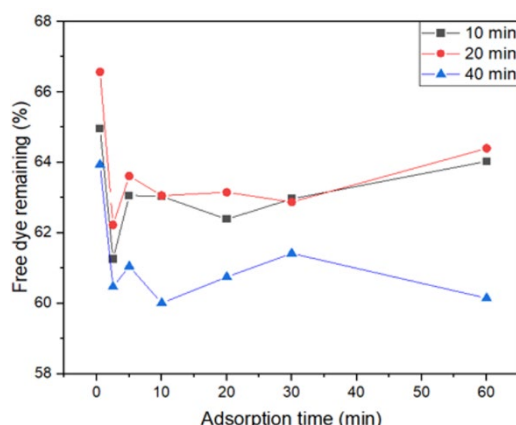


Figure 5.10: The amount of free dye remaining (%) against the time period allowed for MB adsorption in batch with dispersed HKUST-1 in its reaction mixture. The data shown represents a single experimental run.

Synthesis times of 10, 20 and 40 minutes were investigated with adsorption times between 0.5 and 60 minutes. Interestingly, for all synthesis times a similar trend with adsorption time is seen; (Figure 5.10) within the first 30 seconds a large initial uptake followed by a plateauing after just 2 minutes indicating a rapid adsorption mechanism that can be described as independent of time. Despite these experiments being performed in batch and not being directly comparable to flow procedures I can infer from the flow work that doubling the synthesis time from 10 to 20 minutes has little influence on the yield of MOF from these two sets of data. When the synthesis time is increased to 40 minutes, more adsorption is observed as less free dye remains in solution which aligns with data collected in 4.3.4, shown in Figure 4.18, where a higher mass flow rate is expected at the longer reaction time.

Unexpectedly, comparing Figure 5.9 and Figure 5.10, the adsorption behaviour for dispersed and redispersed HKUST-1 is different with a much faster initial uptake for the dispersed sample observed suggesting that HKUST-1 has a stronger ability to adsorb when it is in a dispersed state. Without knowledge of the exact amount of HKUST-1 synthesised due to synthesis occurring in parallel with adsorption once the dye has been added to the mixture it is difficult to compare the amount of dye adsorbed relative to the amount of MOF. However, an explanation for the increased uptake include possible variations in the surface chemistry and the particle sizes. When the HKUST-1 has been dried and redispersed it has been exposed to water in the air and therefore, hydrolysis of the framework could have occurred which slowed the adsorption or a difference in the surface chemistry such as the oxidation state of the copper atoms (Cu^+ and Cu^{2+}) which affects the electrostatic attractions between the framework and MB. It is also possible that some of the framework has agglomerated or collapsed due to being redispersed meaning lower surface area overall and hence a lower adsorption uptake. For dispersed framework, adsorption is rapid with minimal change seen passed 2 minutes but dependent on synthesis time with times of 40 minutes yielding more product and greater adsorption. This presents an interesting perspective of the end purpose of this thesis whereby the system may act as a black box and the amount of dye absorbed could indicate the yield.

5.3.6 Batch adsorption: Effect of the amount of dispersed HKUST-1 on adsorption

To investigate how the amount of MOF affects uptake, a series of dilutions from the dispersed reaction mixture were used for MB adsorption. Extracts of the dispersed reaction mixture following a 20 minute synthesis (5.2.7) were made up to volume (10 mL) with pure ethanol and a further 10 mL of MB solution (0.01 mM) was added to maintain the total volume and initial dye concentration used in the previous experiments (20 mL, 0.005 mM). The data collected is shown in Figure 5.11.

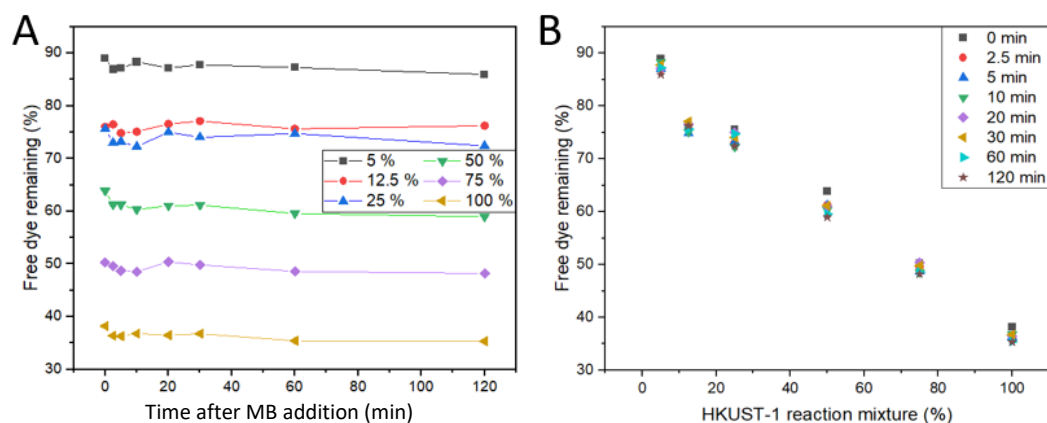


Figure 5.11: Plots showing the effect dilution of a dispersed HKUST-1 reaction mixture has on the adsorption of methylene blue A) against absorbance time and B) percentage of HKUST-1 reaction mixture added. The data represents a single experimental run.

Figure 5.11 illustrates a clear trend between the amount of reaction mixture and adsorption. As the amount of reaction mixture added increases, the amount of free dye remaining in the solution decreases (e.g. after 60 mins the amount of free dye remaining when a 25 % and 75 % solution of HKUST-1 reaction mixture is added to MB is 74 % and 49 %, respectively), which is expected since a greater amount of HKUST-1 introduces more adsorption surface area for the dye. Throughout the measured absorbance time (0.5 to 120 minutes) little change in the amount of dye adsorbed is seen, further evidence of a rapid adsorption mechanism. (Figure 5.11A) When 100 % of the dispersed HKUST-1 reaction mixture (10 mL) is added to the MB stock solution (10 mL, 0.01 mM), the amount of free dye remaining after 60 minutes is 35.4 %. Compared to the redispersed sample (32.7 %) these are similar values indicating their total adsorption was not largely affected by redispersion but the kinetics of it were.

This faster adsorption of methylene blue on dispersed HKUST-1 can be attributed to the more monodisperse nature of the crystals as they nucleate and grow within the reaction mixture. In contrast, when HKUST-1 is redispersed post washing, crystals agglomeration is expected to have occurred, reducing the accessible surface area. Additionally, unreacted reagents are absent within the solution preventing further nucleation or growth of the crystals.

5.3.7 Flow adsorption: control experiment, silica capillary vs PTFE tubing

Alike to designing the synthesis aspect of the process, the adsorption section had to be designed. Application of the dye within the system for adsorption is possible by simply including a T-junction within the process stream for steady infusion through a syringe pump. Control experiments were done to determine an appropriate material for the tubing within which the process fluid would travel during the adsorption section of the system. Fused silica capillary and PTFE tubing were tested by flowing the MB stock solution through each on its own and measuring the UV-Vis absorbance. The desired result was for there to be no change in the spectra from input to output. The results of these experiments are shown in Figure 5.12.

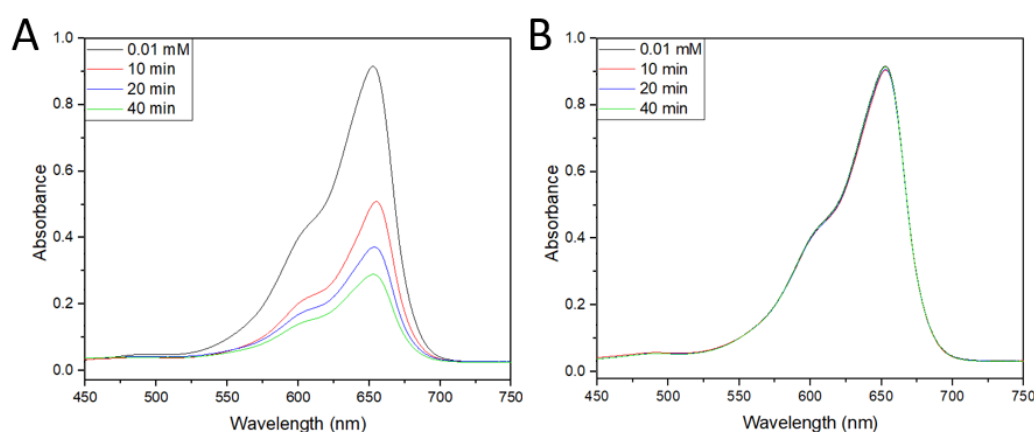


Figure 5.12: UV-Vis spectra when 0.01mM ethanolic methylene blue solution was passed through A) fused silica capillary and B) PTFE tubing.

When fused silica capillary was used (Figure 5.12) a significant lowering of the peak maximum was seen after a 10 minute residence time which was exemplified when increased to 40 minutes indicating a large amount of uptake of the dye onto the surface walls. This is consistent with previous research detailing the use of modified/nano sized silica for adsorptive removal of methylene blue.¹⁹² In contrast, when PTFE tubing was employed, the peak maxima and wavelength remained the same for each residence time, concluding PTFE to be the most appropriate material for the adsorption element of the final envisioned process.

5.3.8 Flow adsorption: effect of dispersed HKUST-1 density on adsorption

To show how the adsorption measurement can be achieved in flow, the batch adsorption experiments discussed in 5.3.6 were replicated in flow. This involved batch synthesis pre-determined earlier in this thesis followed by adsorption which is assessed through a section of PTFE tubing within the flow rig. It was expected that by diluting the reaction mixture process fluid

exiting the synthesis section of the set-up, yield would be diluted and hence upon infusion of the organic dye, less would be adsorbed from solution.

A three syringe system was set-up, including the dispersed batch reaction, pure ethanol and methylene blue ethanolic stock solution (0.01 mM). This is shown in 5.2.9. (Figure 5.4) The dispersed reaction mixture and ethanol were infused through a T-junction at different flow rates totalling either 192.42 and 384.84 $\mu\text{L}/\text{min}$ for the 40 and 20 minute synthesis times, respectively to enable process dilution. By adjusting the flow rates, solutions containing 5, 12.5, 25, 50, 75 and 100 % of the HKUST-1 reaction mixture were infused to meet with the MB solution at the second T-junction. This was followed by a second T-junction infusing the MB solution to start the adsorption section of the overall set-up within the PTFE section of the flow system (2m, $\varnothing=1$ mm). The findings show the effect that HKUST-1 yield has on the adsorption of methylene blue.

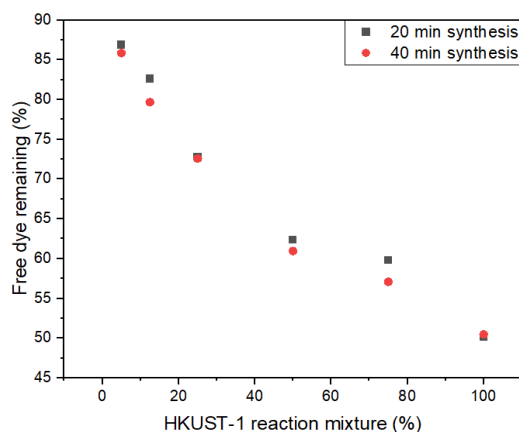


Figure 5.13: Plot showing the percentage of free dye remaining following a 20 and 40 minute synthesis with different amounts of dispersed, continuously synthesised HKUST-1.

Figure 5.13 shows the adsorption results collected when a 20 and 40 minute synthesis were employed with the process fluids containing varying amounts of HKUST-1 reaction mixture. Due to the set length of the fused silica capillary and pre-determined reaction time for synthesis, (4.3.4) flow rate of the process fluid entering the adsorption section of the system was preset ($192.42 \mu\text{Lmin}^{-1}$ and $384.84 \mu\text{Lmin}^{-1}$ for a 20 and 40 minute synthesis, respectively). The total flow rate of the syringes providing the dispersed mixture and ethanol had to equal the set flow rate for the third syringe containing MB for the correct starting concentration for adsorption. Details of these are provided in the experimental.

As expected, when a highly diluted reaction mixture (5 % HKUST-1 reaction mixture) was infused with MB, little dye was adsorbed due to the low mass flow rate (87.19 and 87.26 % of free dye remaining for a 20 and 40 min synthesis, respectively). This followed a strong linear trend as the dilution was reduced and more HKUST-1 reaction mixture was used. Little difference is seen in the

amounts of free dye for when a 20 and 40 minute synthesis was carried out in batch and the amount of free dye remaining is elevated in comparison to the previous experiments (5.3.6) at the lesser diluted ends. However, it is worth noting that this isn't a true representation of the set batch synthesis times as the mixture would have continued to react when placed within the syringe before it was infused with some experiments taking up to 60 minutes post batch synthesis. Furthermore, it was noticed that the reaction mixture was settling within the syringe without a stirrer bar which would inherently affect the mass flow rate and hence adsorption. Nonetheless, this experiment clearly replicates the results seen for the equivalent batch experiment (Figure 5.11) showing that the mass flow rate of HKUST-1 has a direct effect on the amount of MB adsorption seen with little difference between the two reaction durations.

5.4 Conclusions

The synthesised metal-organic frameworks (MOFs), HKUST-1 and ZIF-8, were evaluated for their adsorptive capacities against several common organic dyes to identify a suitable pairing for the final envisioned process. HKUST-1 demonstrated good adsorptive capacity for methylene blue which itself showed good acidic stability with no observable changes when separately tested in the HKUST-1 reagent stock solutions. However, it was strongly adsorbed onto the inner surface area of the fused silica capillary prompting PTFE tubing to be employed for the flow adsorption vessel. No further experiments were carried out using the ZIF-8 following the screening results due to time constraints. However, a system using ZIF-8 for the uptake of Rhodamine B is a possible candidate for the system in the future.

Batch experiments were carried out to assess the adsorptive kinetics of the HKUST-1 adsorption mechanism. Redispersed HKUST-1 showed fast removal of the dye achieving 67.3 % removal within the first 60 minutes, with adsorption slowing but continuing beyond 120 minutes. Further runs in batch simulated a flow system where methylene blue was added to the HKUST-1 reaction mixture at various synthesis and adsorption times. Interestingly, the dispersed reaction mixture showed a faster adsorption mechanism compared to the redispersed sample, with rapid adsorption plateauing in less than 2 minutes.

Of the synthesis times tested for the dispersed sample, 10 and 20 minute synthesis showed similar uptake (64.03 and 64.40 %, respectively), while a 40 minute synthesis resulted in greater uptake (60.15 %), suggesting greater HKUST-1 formation. These findings agree with the work presented in Chapter 4, prompting an investigation into the effect of yield on adsorption. When dilutions of the HKUST-1 reaction mixture were combined with methylene blue solution in batch

experiments, clear and quantifiable dye removal was observed for each dilution showing a strong linear trend: higher amounts of HKUST-1 mixture led to greater removal of dye. For example, when a 5 % and 100 % of HKUST-1 reaction mixture was employed, 87.3 % and 35.4 % of free dye remained in solution, respectively after 60 minutes. This trend was reflected well in flow where a dispersed reaction mixture was loaded into a syringe and infused through PTFE tubing along with the MB solution.

The adsorption behaviour of dispersed HKUST-1 is advantageous in flow when considering potential time delays expected in separation and analysis. The implementation of an in-line system capable of producing varying amounts of HKUST-1 material depending on the initial synthesis parameters set would provide different, quantifiable adsorptions of the dye. This approach could contribute to scalability and consistency within MOF synthesis and enhance the precision or efficiency of MOF adsorption processes, the industrial application and advantages of which can be imagined.

Chapter 6 Separation: Hardware development and testing

In the previous chapters I identified and developed a set of appropriate conditions for flow synthesis for a candidate MOF and looked at its adsorption mechanism for in-line ‘application-led’ analysis. This chapter will look at the next part of the overall planned set-up which involves a downstream separation device that filters remaining free dye from the continuous stream for analysis by UV-Vis spectroscopy. It will discuss the considerations and approaches used, along with results obtained, thus far in the design and fabrication process of the downstream analyser device that will be integrated in-line. The limitations with respect to membrane size and materials, overall device dimensions and sizing have been determined and discussed to give a clear picture of the initial start point for fabrication. Three approaches have been made towards fabrication including a PDMS mould and cast method, a known 3D printing technique termed print-pause-print (PPP), which subsequently facilitated a novel and successful fabrication process to be developed, and finally the purchase of a commercial device to implement for in-line analysis. Successful devices were moved forward for separation runs.

6.1 Functionality of the envisioned analyser device

6.1.1 Separation

In various engineering and industrial processes, separation techniques are crucial for isolating specific components from mixtures. When considering the work described in this thesis, a device must be fabricated to implement in-line that can successfully separate free methylene blue from the process fluid, allowing it to retain the synthesised HKUST-1 with adsorbed methylene blue. The filter medium selected for this device were semi-permeable membrane filters due to their ready availability in various materials and pore sizes allowing for careful selection to favour cationic methylene blue separation with respect to charge and size. This has often been applied in seawater desalination and wastewater remediation. The functionality of the device was dependent on the filtration process selected.

There are several types of filtration processes and arrangements that could be considered for my device. The primary types are discussed below (dead-end and cross-flow filtration, Figure 6.1), focusing on their operational principles and applications.

6.1.1.1 Dead end

Dead-end filtration involves net movement of the solvent through the membrane. It is a batch style processing for solid-liquid separations where solid is retained at the filter surface, while the liquid passes through. Its simple set-up and operation as well as high efficiency separation for low-solid content process fluids are advantageous. However, accumulation of particulate at the membrane surface causes a filter cake to form, reducing the filtration rate and meaning periodic cleaning or filter replacement is required.

6.1.1.2 Cross-flow

Cross-flow filtration utilises tangential flow arrangements whereby the process fluid is flowed across the membrane surface so that small molecules diffuse but no net movement of solvent occurs across the membrane. This method gives a significant reduction in fouling, enables continuous operation, can facilitate fluid streams with higher solid content, has prolonged membrane lifetime and may be used in solid-liquid or liquid-liquid separations. In comparison to dead-end filtration it has a more complex design set-up and greater energy consumption due to the continuous flow.

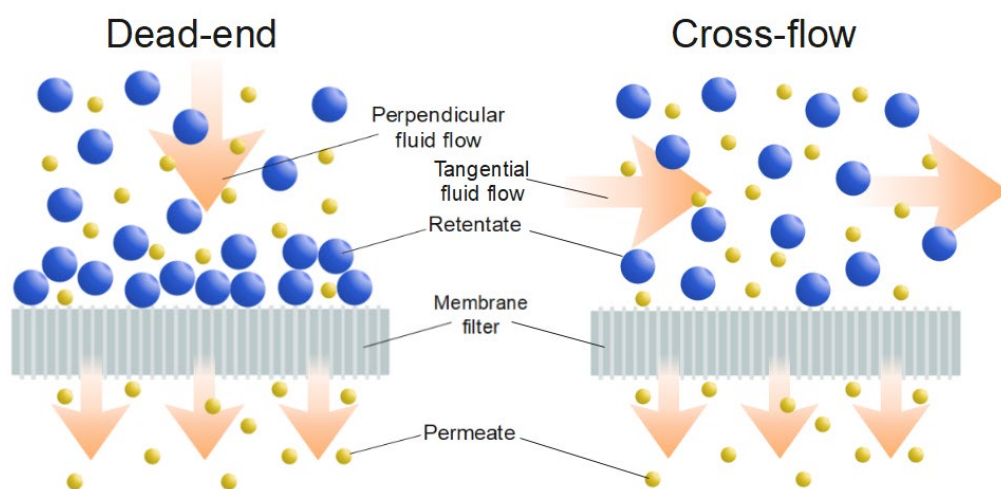


Figure 6.1: Diagram showing the difference between dead-end and cross-flow filtration processes.

Large orange arrows represent the direction of fluid flow and smaller orange arrows represent the permeated small molecules through the membrane filter.

When employing a cross-flow filtration device a second fluid stream containing extracting solvent to carry permeated species may be flowed concurrently on the other side of the membrane filter. This stream may flow in the same or opposite direction to the process stream giving two possible flow arrangements named co-current and counter-current, respectively. These arrangements are discussed below and shown in Figure 6.2.

6.1.1.2.1 Co-current

In a co-current separation, the process fluid and extracting solvent flow in the same direction either side of the semi-permeable membrane. (Figure 6.2, left) This set-up has a simple design and operation with easy control and scale up. However, it has a low separation efficiency, with a maximum separation of 50 % within a single set-up dependent on the device length and initial concentrations.

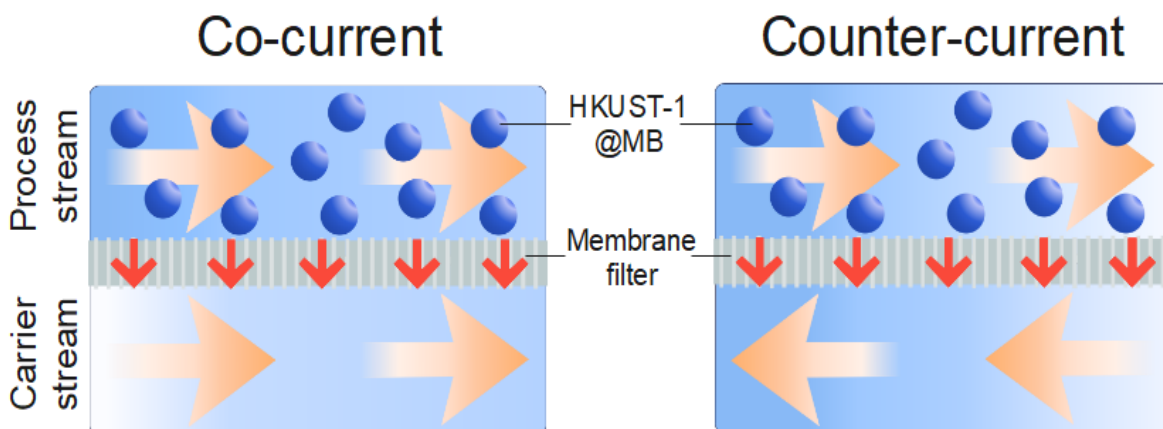


Figure 6.2: Diagrams for a counter and co flow arrangement where orange arrows show the direction of fluid flow for the individual streams and red arrows indicate the direction of diffusion for dye molecules. The colour fill of the streams indicates the concentration of free dye remaining in solution whilst the blue spheres represent HKUST-1.

6.1.1.2.2 Counter-current

In a counter-current separation the process fluid and extracting solvent are flowed in opposite directions either side of the membrane filter. (Figure 6.2, right) This creates a constant concentration gradient across the breadth of the separation surface, enhancing efficiency. The advantages of this technique include high separation efficiencies and lower levels of solvent consumption. In principle, counter-current flow should be able to achieve 100 % removal of dye depending on the set-up. However, operation needs to be carefully controlled, with matched flow rates to prevent transmembrane pressure forming and solvent mass transport across the membrane.

For the purposes of this thesis a solid-liquid continuous filtration was required to remove free MB molecules from the process stream while retaining the synthesised HKUST-1 framework. This excluded the use of dead-end filtration from investigations being as it is a batch style process. On comparing counter and co current flow arrangements, 100 % free dye separation was the most desirable outcome for the device hence a counter arrangement was considered the most

appropriate as it can potentially remove 100 % of dye whereas co-current arrangements may only remove up to ~50 %.

6.2 Experimental methods

Materials and methods

Clear polypropylene filament (2.85 mm, Ultimaker brand) was obtained from RS. Membranes were purchased from Fisherbrand, (mixed cellulose ester and nylon, \varnothing = 47 mm); and VWR (Cytvia, nylon, \varnothing = 90 mm). Methylene blue and ethanol solvent were purchased from Sigma Aldrich. Syringes (20 mL, BD Plastipak Luer Lock) and tubing (PTFE, \varnothing = 1, 1.7 mm) were purchased from RS components. The Spectrum® MicroKros hollow fibre filter modules (41.5 cm, 2 lumen and 65 cm, 9 lumen) were purchased from Repligen. IDEX flangless $\frac{1}{4}$ 28 " fittings and the micrometering valve (IDEX Health and Science, Micro-ming, P-445) were purchased from Cole Parmer.

3D printing was performed on an Ultimaker 3.

6.2.1 Designing of the chips

Chip designs, the 2D drawings used for the microfluidic channels either side of the membrane, were produced on computer-aided design (CAD) software, AutoCAD and 3D parts were designed using SOLIDWORKS.

6.2.2 Membrane filter testing

Nylon and mixed cellulose ester membrane filters (Fisherbrand, \varnothing = 47 mm, pore size= 0.2 and 0.4 μ m, respectively) were tested for their appropriateness within the developed filtration devices with respect to if they allowed MOF to pass through their pores and if they retained the methylene blue dye.

6.2.2.1 MOF filtration

The membrane was folded and placed in a glass funnel. Reaction mixtures for HKUST-1 (10 mL) synthesised used the method described in 4.2.5 that had been combined with a methylene blue ethanolic solution (10 mL, 0.01 mM) were passed through the membrane. Whether the MOF had passed through the membrane or not was determined by centrifugation (2 min, 1000 rpm) of the filtrate to see if a solid was separated.

6.2.2.2 Dye retention

In a crude screening experiment, the membranes were placed in an ethanolic methylene blue solution (0.01 mM) for 30 minutes. The membranes were then removed, rinsed briefly with ethanol within a wash bottle and visually examined for retained dye.

6.2.3 Fabrication methods

The aim was to develop a low-cost device with high functionality that could be constructed rapidly and precisely with commercially available materials and, ideally, easily controlled. Initially, bespoke crossflow filtration devices where dimensions could be adjusted and optimised arbitrarily as required were looked into, before off-the-shelf commercial options were trialled. For the bespoke separation devices, several fabrication methods were explored. A previously reported approach was attempted for fabrication of the devices in the first instance which involved direct printing of the device using a print-pause-print (PPP) technique.

The initial dimensions of the device, considered the sizes of membrane filter available for purchase and the time taken for diffusion at different channel depths. The initial depth of the device design and hence, the channel height was set at 0.1 mm, the smallest possible whilst being easily and reliably manufacturable. Secondly, the extruded design of the device had to be within the constraints of the membrane filter (90 mm), hence, limiting the size of the mould.

6.2.3.1 Print-pause-print (PPP)

The print-pause-print (PPP) technique is a versatile method that exploits the layer-by-layer printing process of additive manufacturing techniques by including processing scripts within the file's G-code that allows a pause or change in conditions.¹⁹³ At any point external materials can be easily incorporated using this approach whereby the print is stopped, the external element is inserted into a pre-designed recess, and then printing resumed to encapsulate it. This enables fully functional, integrated devices to be fabricated with minimal intervention and no post-printing assembly. PPP has been demonstrated using polyjet¹⁹³ and stereolithographic printers,¹⁹⁴ however FDM allows a much greater range of materials to be used meaning extra functionality (e.g. using conductive or flexible materials) and/or high chemical compatibility (e.g. when printing with polypropylene or polyvinylidene difluoride) – essential for synthetic chemistry applications.

Chip designs, the 2D drawings used for the microfluidic channels either side of the membrane, were produced on computer-aided design (CAD) software, AutoCAD and 3D parts were designed using SOLIDWORKS. All designs featured a cavity for the membrane. The height of the cavity was

100 μm and the diameter was set to be 200 μm larger than that of the membrane to accommodate any shrinkage of the material during printing. The 3D design files (.3mf) were prepared for printing using Cura (Ultimaker) and parts were printed using an Ultimaker 3 FDM printer in polypropylene (PP), with an Ultimaker adhesion sheet applied to the print bed to ensure adhesion. Print conditions were set to 100 % infill and the smallest layer height (100 microns). In this method, the print was started and then subsequently paused according to pre-set conditions for a membrane filter or other external object to be added before printing resumption to completion, where the membrane is sealed within.

Several post-processing scripts were entered into the file's G-code. These conditions were adapted from an undergraduate project of a Mech Eng undergrad, Tushar Garg.¹⁹⁵ Initial print conditions had a 120 % flow rate and 100 % print speed. The last printing layer for the membrane cavity was identified using Cura and a pause was added. Upon pausing, the membrane was added to the partial-print, using a glue stick applied around its circumference to hold it in place. Processing of the first layer on resumption used a reduced print speed (25 %) and increased flow rate (200 %) to prevent movement of the membrane and seal it within. Following two printed layers, pre-pause conditions were applied to the remaining layers.

6.2.3.2 PPP: A novel 3D printing fabrication technique

Using the PPP technique a novel technique was developed to produce a functional cross-flow filtration device using direct extrusion of filament onto either side of the membrane filter for a good seal. Two individual parts were printed and the first encapsulated within the second using a pause process added to the print script. Details for the process are described in .6.3.2.1.3

The initial print conditions for both parts were determined through trail and error to be a 120 % flow rate and 90 % print speed. The resume layers for both prints used a 175 % flow rate and 25 % print speed to give a good seal to the membrane filter. All subsequent layers returned to initial print settings.

6.2.4 Device testing methods

6.2.4.1 Preliminary chip testing

One side of a PDMS fabricated device was bonded to a flat sheet of PDMS using plasma activation. In a fume hood with good and clear lighting, a syringe pump was set to a 0.5 mL/min flow rate and loaded with a syringe of diluted food dye. Food dye was used as a less hazardous alternative to organic dyes in the first instance. Tubing with an internal diameter of 1.7 mm led from the

syringe to the inlet of the PDMS device and the pump was started. The device was filmed from a birds eye perspective using a clamped iPhone as the dye passed through. This was repeated several times; alternating with syringes of clear, deionised water and food dye.

6.2.4.1.1 MATLAB: Extraction of RGB data from flow videos

Using a grid to section the video image of the chip, pixel regions (54 pixels) were selected to span each channel at 3 separate positions. Average RGB (red, green, blue) values for each region were indexed from the video file using MATLAB (example of the code is given in the appendix, 10.1) and used to calculate the saturation value which was plotted for each channel against time.

6.2.5 Testing of dye removal using 3D printed filtration devices

Figure 6.3 shows the experimental set-up. A Harvard apparatus syringe pump was loaded with 20 mL BD Plastipak syringes of 0.01mM MB solution in ethanol and pure ethanol solvent. (Figure 6.3A and B) $\frac{1}{4}$ 28" PEEK fittings were applied with PTFE tubing leading to the inlet housing either side of the fabricated device for a counter-current flow arrangement (Figure 6.3C). MB was infused into the top cavity while the carrier ethanol was infused into the bottom cavity. Outlet tubing (PTFE, $\varnothing=1$ mm, 50 cm) came out the opposing sides for the top and bottom channel system at Figure 6.3D and E, respectively. A micrometering valve (IDEX, Micro-ming, P-445) (Figure 6.3F) at the top cavity outlet was adjusted accordingly to match back pressures and provide even flow rates from both outlets. Different flow rates (0.1-0.5 mL/min) were applied and the set-up was left to reach equilibrium. The exiting fluid was collected in vials, weighed and measured using UV-Vis spectroscopy. This was repeated three times for each flow rate tested.

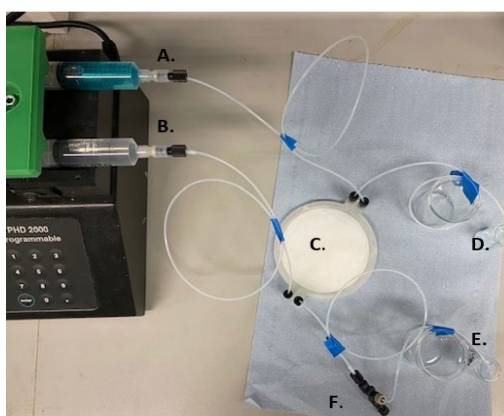


Figure 6.3: The experimental set-up for cross-flow filtration of 0.01 mM methylene blue in ethanol where A is the dye infused into the top cavity; B is the ethanol solvent infused into the bottom cavity for dye removal; C is the 3D printed device; D is the bottom cavity outlet; E is the top cavity outlet and F) is a micrometering valve to apply back pressure across the top cavity and equalise the outlet flow rates.

6.3 Results and Discussion

6.3.1 Designing and testing of microfluidic channels

6.3.1.1 Size and limitations

The first step in design of the separation device was considering the size and limitations. For ideal operation of the proposed analysis system, full diffusion of the dye across the membrane is desired which is dictated by the amount of time spent within the device. The process flow residence time was a key parameter to consider when designing the chip as the dye needed enough time to diffuse from the top of the channel and through the membrane, into the carrier stream. The time required for this to happen directly related to its diffusion coefficient and the chip dimensions. (Equation 3) I looked to determine appropriate channel dimensions (cross section and length) for the process stream of a separator, such that there was sufficient residence time for the dye to enter the carrier stream.

Equation 4: Time taken for diffusion and hence the residence time (t / s). The parameters include: the height of the channel (x / cm) and diffusion coefficient of the dye (D / cm^2/s).

$$t = \frac{x^2}{2D}$$

Equation 5: Volume (V / mL) of the device using the volumetric flow rate (Q / mLmin^{-1}) and residence time (t / min)

$$V = Qt$$

Knowing the primary reaction that will be analysed, the necessary residence time of the dye could be calculated and compared for different channel heights (Table 6.1) using the diffusion coefficient (D) of methylene blue which is reported as $3.34 \times 10^{-6} \text{ cm}^2/\text{s}$ for a 50 % ethanolic solution.¹⁹⁶ As no values have been found for pure ethanol solutions, this will be used in all calculations. Moreover, choosing an appropriate initial flow rate ($200 \mu\text{L}/\text{min}$), the required chip volumes could also be calculated using Equation 4. The initial work for this chapter was done in parallel with that discussed in the previous chapters and as such the actual continuous HKUST-1 synthesis conditions had not yet been determined. The necessary calculated volumes were broad with a 5-fold increase in height requiring a 25-fold increase in volume highlighting how channel depth has a profound effect on the device functionality.

Table 6.1: Calculated diffusion time (expected time for a dye molecule to diffuse to the membrane from the top of the channel and across the membrane) and subsequent volumes necessary for full diffusion with a set flow rate of 200 $\mu\text{L}/\text{min}$ and differing channel height.

Channel height / μm	Max diffusion time / s	Flow rate / $\mu\text{L}/\text{min}$	Volume / mL
100	29.94	200	0.099
150	67.37	200	0.225
200	119.76	200	0.399
250	187.13	200	0.624
300	269.46	200	0.898
500	748.50	200	2.495

The chosen fabrication methods (described below) meant that the channel height was limited to a minimum 100 microns. A smaller channel height means a smaller diffusion path for the organic dye which is desirable to reduce necessary residence times and axial dispersion. In practice, higher channel heights were used in the first instance to initially test the produced device functionality before optimising the dimensions later. Further to this, the (x,y) dimensions of the channel system could also be considered; these values and therefore the overall device size were limited by the membrane filters available for purchase.

6.3.1.2 Membrane filters

Membrane filters of nylon and mixed cellulose esters were purchased based on their hydrophilic properties, good stability and wide availability in terms of diameter and pore size. They were subjected to a series of tests to determine the most suitable material and pore dimensions for application in the device. The ideal membrane will not retain any dye, be chemically inert and remain stable under operational conditions. Furthermore, it will allow facile diffusion of the dye but not the solid framework. Preliminary screening tested the membranes on these criteria.

The nylon membrane did not allow passage of the framework through its pores ($0.2\mu\text{m}$) during filtration experiments and showed no visible dye retention after 30 mins (Figure 6.4A) or 120 mins. (Figure 6.4C) On the other hand, the mixed cellulose ester membrane absorbed a significant amount of dye and allowed partial movement of the smaller crystals of HKUST-1 through its pores ($0.4\mu\text{m}$). (Figure 6.4B) This was identified by slight turbidity of the filtrate and is ascribed to the doubled pore size (This had to be purchased due to commercial availability). By using size-controlled synthesis of the framework, this can be resolved, or simply by ordering filters with a smaller pore size. The results of these tests are summarised in Table 6.2.

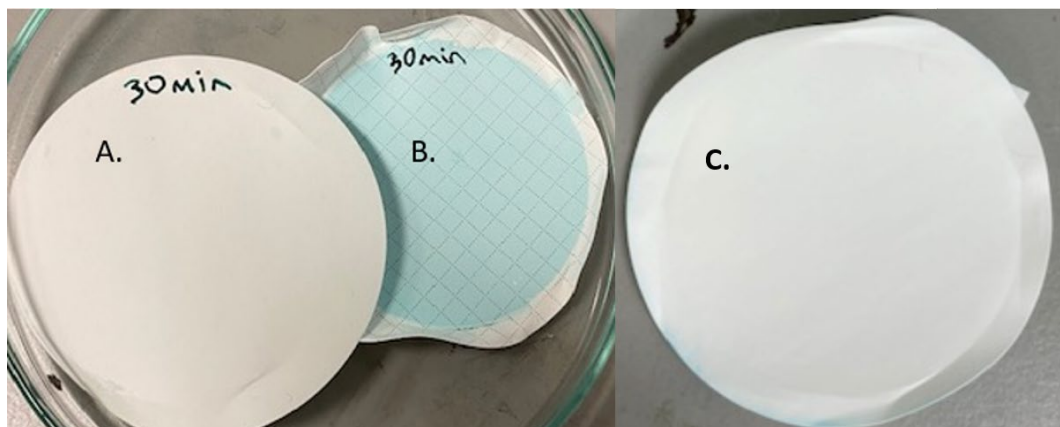


Figure 6.4: Images of A) nylon and B) mixed cellulose esters membranes after 30 mins of soaking in 0.01 mM methylene blue solution. C) Image of the nylon membrane after 120 minutes in methylene blue solution (0.01 mM).

Table 6.2: A table summarising the screening results for the different membrane materials and pore sizes.

Material	Pore/ μm	Any observed dye retention?	MOF diffusion
Nylon	0.2	No	No
Mixed cellulose esters	0.4	Yes	Partial

Stability of the membranes in different pH solutions was also tested *via* a 24 hr soak and assessed using SEM. (Figure 6.5) pH values 3, 7 and 10 were selected to represent a good range of acid to alkali solutions as it is known that the process pH changes during continuous synthesis, converging to pH 4.1. (4.3.3.1) Both membranes showed no change in appearance; porosity remained unchanged and no structural changes were seen between the pre and post soaked membrane. Physical observation of the membranes also showed no evidence of change

e.g. rippling, shrinkage, rigidification. The SEM images for the nylon membrane are shown in Figure 6.5.

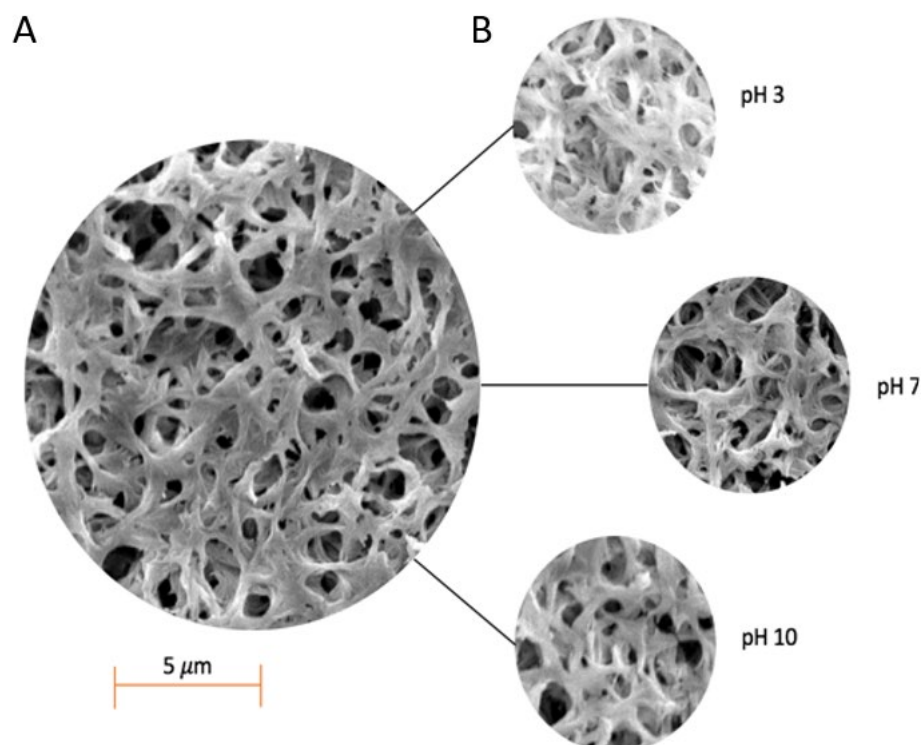


Figure 6.5: Top down SEM images of the nylon membrane filter A) untreated and B) after 24 hr submersion in different pH-adjusted solutions.

Nylon was chosen as the most appropriate membrane for use in the analytical device in the first instance. It showed no change when exposed to various pH solutions and allowed good diffusion of the dye with no absorption. Furthermore, a 0.2 μm was deemed more appropriate than 0.4 μm as it would prevent the passing of smaller crystallites through it. Limitations to what was commercially available at a reasonable cost meant that membrane filters with the smallest pore size and largest diameter had dimensions of 0.2 μm and 90 mm, respectively, hence, all device designs were made and adjusted accordingly.

6.3.1.3 Microfluidic channel design

Several possible designs were proposed for the channels of the chip including a pillar splitting and branched design both of which aimed to split the flow—reducing the flow rate by increasing cross-sectional area and hence increasing residence time. Both drawings went through a series of adjustments and improvements with respect to the detail and sizing during fabrication stages. These are discussed and the most recent drawings are pictured (Figure 6.6) with their dimensions stated. The ideal design will show good and even splitting of the incoming mixture with an even flow rate across its channels and satisfy the residence time criteria described in Table 6.1. Due to

the nature of the envisioned device, a symmetrical design was necessary whereby channel designs above and below the membrane mirrored each other to allow dye transport from process stream to carrier stream.

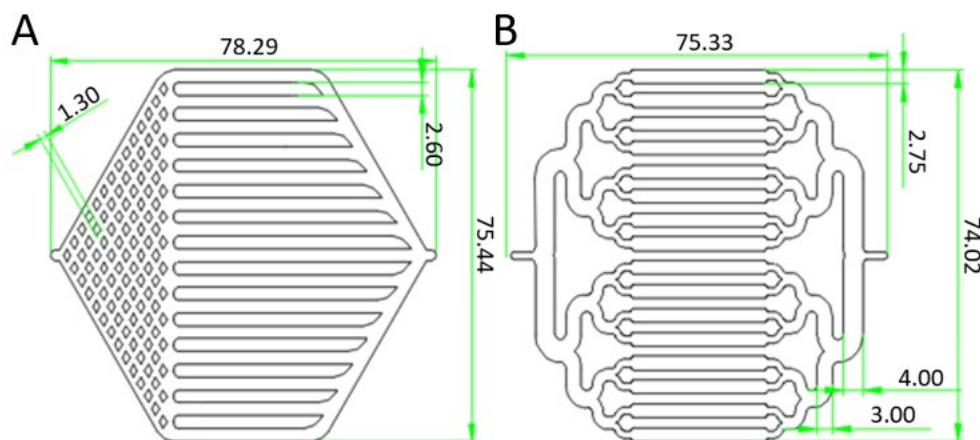


Figure 6.6: Sketches taken from AutoCAD with flow occurring from left to right in each of the geometries A) pillar splitting and B) branched channel designs. All dimensions are given in mm.

6.3.1.3.1 Pillar splitting design

The hexagonal design had diamond shaped pillars to split the incoming mixture at the inlet into 15 channels. These channels stretched for the remainder of the space to the outlet point. Several versions of this design were made and improved upon following observations made during preliminary dye testing (described in 6.2.4.1) to give that shown in Figure 6.6A. These primarily included evidence of dead spots where no dye reached or the opposite where dye accumulated. A main improvement was increasing the level of detail; more splitting levels and channels were introduced with smaller dimensions and thicker supports for structural integrity and edges were smoothed to improve flow and prevent 'dead spots' of gathered liquid. The dimensions for the chip as pictured, included the diamond splitting pillars (1.3 mm) and the channel structures (2.6 mm) to give an overall volume of 0.248 mL and a channel height of 100 μm . This was above the constraints for full diffusion (0.099 mL at $Q = 0.2 \text{ mL/min}$) and was therefore suitable for use. The height dimension was critical, for example if the height was increased to 300 μm , the overall volume would increase to 0.744 mL and would no longer reach the threshold for full diffusion (0.898 mL) at this flow rate. Therefore, a slower flow rate would be required, (0.16 mL/min).

6.3.1.3.2 Branched design

The branched design follows the same splitting principle as the pillared design but with a better defined path. (Figure 6.6B) The incoming fluid was split into two equal channels and repeated a further three times, narrowing each time to give 16 parallel channels with a mirrored rewidening and recombination to the outlet point. The main alterations that were been made within this design from its first proposal included the channel sizes and shapes. In the design pictured, when scaled for a 90 mm diameter membrane filter, the channel sizes were 4 mm, 3 mm, 2.5 mm and 2.0 mm with respect to the branching steps. The central channels expanded to 2.75 mm, to increase the membrane coverage and volume of the device. The calculated volume for this design with a height of 100 μm was 0.225 mL, which exceeded the required (0.099 mL at $Q=0.2$ mL/min) and confirmed that full diffusion could occur. As the volume was slightly reduced compared to the pillar splitting design, full diffusion at a 0.2 mL/min flow rate would not be possible if the channel height was increased to 250 μm (0.562 mL) and a slower flow rate would be required (0.18 mL/min).

Upon comparison, both designs exceeded the required volume needed for full diffusion with a channel height of 100 μm and 0.2 mL/min flow rate (0.099 mL), leaving room for error and deviations such as Taylor axial dispersion which is a property of single phase diffusion and will naturally lead to a residence time distribution under real flow conditions.⁴⁰ The symmetrical nature of the branched design is an advantage from a broader perspective of the chip's later use as the streams of fluid will have the same inlet to outlet path either side of the membrane during cross-flow filtration.

6.3.1.4 Design testing

A series of tests were conducted to assess the fluid transport through the optimised designs. The parts were cast in PDMS from 3D printed moulds and plasma bonded to flat sheets of PDMS for food dye and water to be alternately flowed through *via* syringe and syringe pump. Videos were taken and screenshots from the videos of which are shown in Figure 6.7.

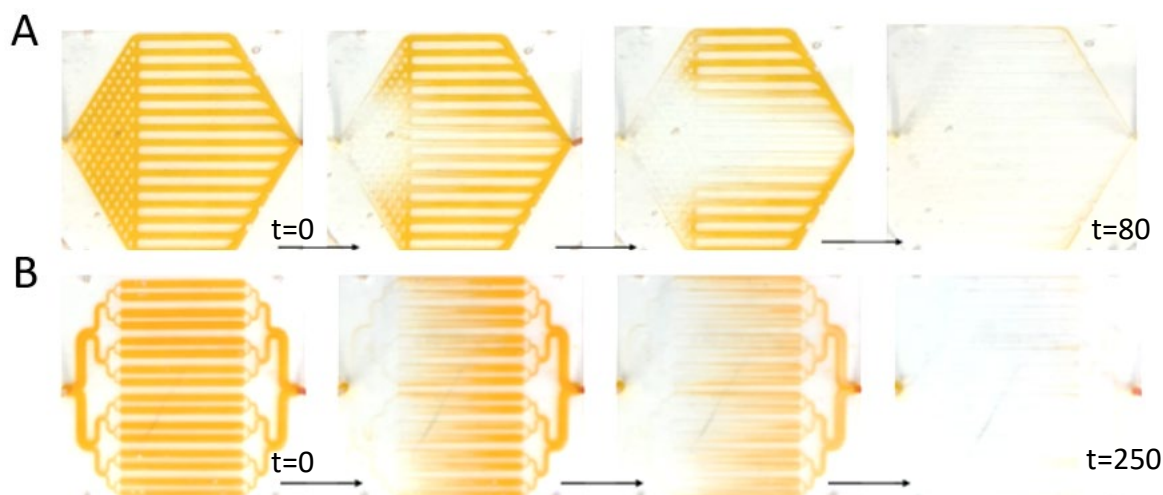


Figure 6.7: Stills of the flow videos taken for the chip designs showing water flushing the dye from the channels. A) Pillar splitting chip; B) Branched chip. All times are measured in secs.

From initial observation, the branched chip (Figure 6.6B) showed dye was cleared approximately equally across the channels. (Figure 6.7A) Moreover, the food dye moved seamlessly through the chip with no dead spots and full clearance. Also, clear in this design was the Taylor axial dispersion within the individual channels where the central area of the channel cleared before the walls, consistent with a gradient of velocities from the centre outwards, across the breadth of the channel. In comparison, the pillar splitting chip (Figure 6.7A) showed a Gaussian distribution of flow rates in the channels with the central one clearing the fastest. The reason for this is that liquid will favour the path with least resistance which in this case is the shortest path. Full clearance of the dye was possible but on a much longer time scale (180 minutes vs 60 minutes).

6.3.1.4.1 Quantification of fluid transport across the chip channels

To quantify these observations, data processing software MATLAB was employed. RGB (red, green, blue) values of selected pixel regions (Figure 6.8A) across the channels were extracted from the videos, saturation values were calculated (Equation 5) and plotted over time to calculate the individual flow rates. (Figure 6.8B)

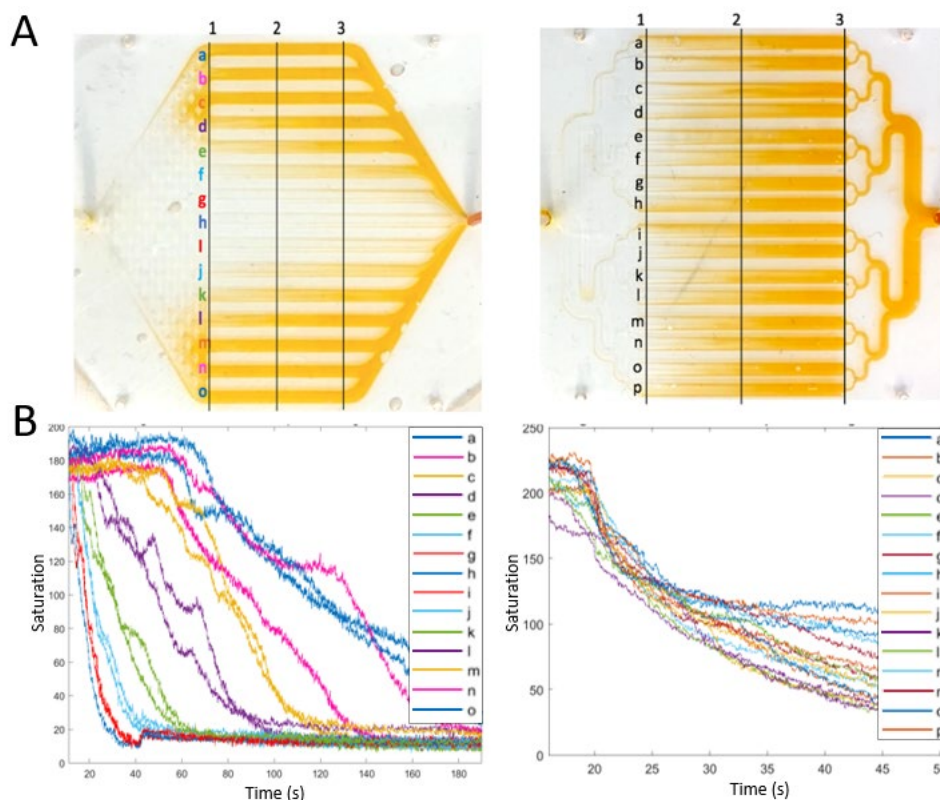


Figure 6.8: A) Diagrams to show the grid sectioning used on the chip designs to identify pixel regions for analysis; B) The change in saturation of each channel at position 3 on the grid.

Equation 6: Calculation for saturation, S . Where (R, G, B) is the (Red, Green, Blue) values.

$$S = \max(R, G, B) - \min(R, G, B)$$

The change in saturation is directly related to the flow rate. The plot in Figure 6.8B, left of the hexagonal chip shows a vast range of rates of change. Channel 'h' shows the fastest drop in saturation with the steepest change as the water passes through the region (30 s) followed by the two channels either side, 'g' and 'i' (40 s), then the next channels 'f' and 'j' (50 s) and so on. These channel couples show almost identical rates of change in saturation and have been colour coded in Figure 6.8B to be the same colour. The outermost channels ('a' and 'o') took over six times as long (>200 s) to clear the dye than the fastest channel ('h'). The notable difference in rate between channels 'b' and 'n' (pink) could be due to the air bubble trapped at the end of

channel 'n' (Figure 6.8A) or a possible blockage/constriction of the channel formed during release of the part from the mould or upon plasma bonding it to the flat piece of PDMS.

On comparison the plot for the equivalent position (3) of the branched chip (Figure 6.8B, right) shows a much closer relationship between the channels. Rate of change is almost equivalent with fluctuations in the starting saturation being attributed to the background light of the fume hood causing reflections off the chip's surface and hence, deviations. It took around 20 seconds for the water to reach the pixel region at position 3 and for the saturation to start to fall. After 30 seconds the rate of change becomes slower and less equal across the channels, evidenced by the shallowed gradient and separating plots, as the final dye is cleared. It is the inner channels, and specifically their middle sections, that are favourably cleared first due to Taylor axial dispersion causing a gradient of flow rates across each channel. Therefore, slower clearance of the outer channels is seen.

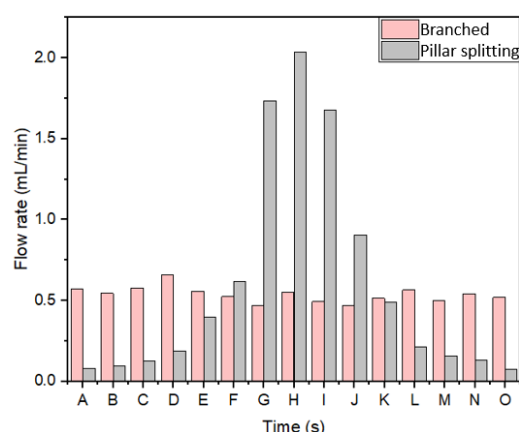


Figure 6.9: A bar chart showing the calculated flow rates for the individual channels in both designs at position 3 of the grid.

Figure 6.9 plots the flow rates for the individual channels in each design and further highlights the disparity between them. The flow rate was calculated by Equation 4 using the time taken for start saturation to half in value. The branched chip shows relatively even flow rate across the channels at the set rate of 0.5 mL/min. On the other hand, the pillar splitting chip shows a clear Gaussian distribution with rapid movement through the central channel, over 4 times the set rate, and very poor flow through the outer channels.

As a result of these findings, and it's non-symmetrical nature, the hexagonal design was no longer considered a viable design for the analysers. The branched chip design was taken forward for device fabrication.

6.3.2 Fabrication of a full cross-flow filtration device

A simplified diagram of the device is shown in Figure 6.10, highlighting its expected function and individual elements. Two channel systems will be separated by a sandwiched membrane material and fluid will flow in opposite directions above and below the membrane enabling the movement of dye molecules from the top to the bottom cavity. The chips discussed in 6.3.1.3 would make up this channel cavity above and below the membrane. The approach made to fabricate this device was 3D printing.

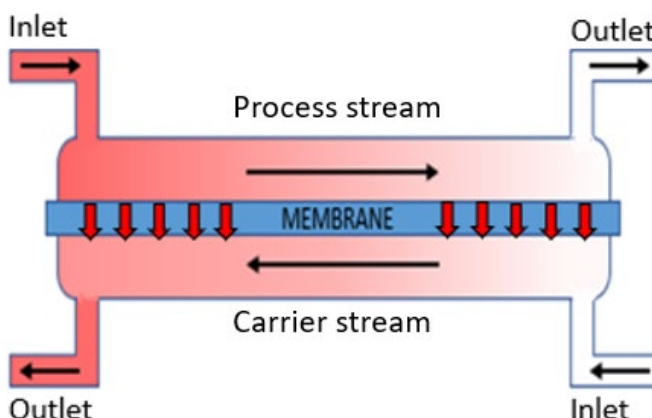


Figure 6.10: A cross-sectional diagram for the envisioned cross-flow filtration device. Red gradient shading indicates the crude concentration of dye within the flowing streams; red arrows indicate the direction of diffusion for the dye molecules from the process to the carrier stream and black arrows represent the expected direction for fluid flow.

6.3.2.1 3D printing

6.3.2.1.1 Print-Pause-Print (PPP)

The print-pause-print (PPP) technique was used for direct printing of the device.^{199,200} The conditions used were taken from an undergraduate project.¹⁹⁵ A pre-set pause layer was added to the g-code script that enabled the addition and encapsulation of the membrane filter. Following resumption, decreased print speeds (25 %) and increase flow rates (200 %) were used for two layers before pre-pause conditions were returned to. Polypropylene was used as the printing material due to its chemical inertness, transparency and low chemical reactivity. Despite some reports that UV-aged polypropylene microplastics have the ability to adsorb methylene blue,²⁰¹ no issues were encountered during my research using the fabricated hardware as determined by control experiments.

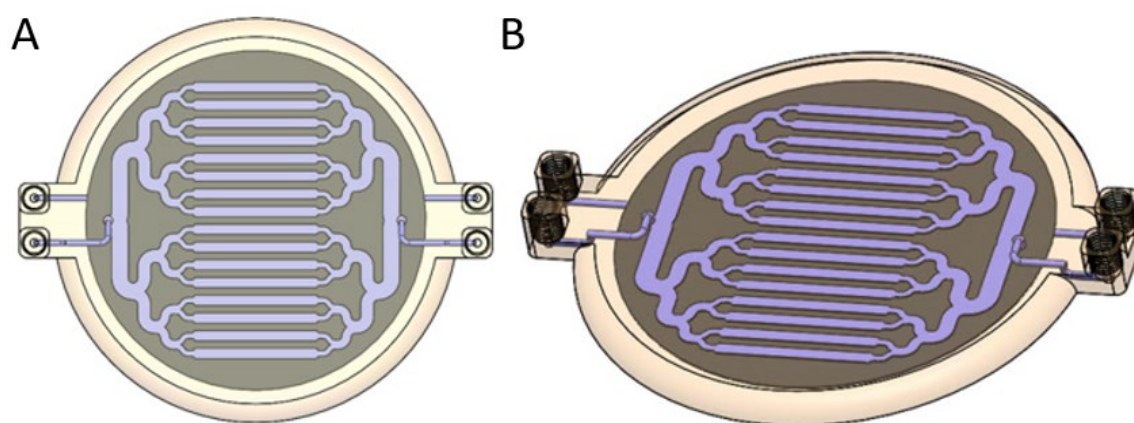


Figure 6.11: A) Birds eye and B) angled view of the first fabricated device on SOLIDWORKS. The channel and pipework design (purple); membrane cavity (dark brown) and remaining housing (orange) are highlighted.

Figure 6.12 shows the first print design on SOLIDWORKS. The anatomy of the print includes $\frac{1}{4}$ 28" PEEK fittings as the inlet/outlet points either side of the device with internal pipework (purple) to direct fluid to the channel design (purple) either side of the membrane. The membrane cavity is 300 μm in depth (dark grey). Finally, the branched design is extruded cut above and below the membrane cavity to provide an aligned channel system 500 μm in depth (purple) for transfer of the organic dye. Overall dimensions of the print are 130 mm x 100 mm.

6.3.2.1.2 Initial flow testing

Food dye was passed through the prints to assess their function and design. In all cases the membrane was successfully encapsulated and a water tight seal was achieved as evidenced by no leaks occurring once liquid was infused within the device.

The first design presented issues with fluid access to the channels above the membrane. Dye was able to flow readily through all channels connecting the $\frac{1}{4}$ - 28" connections to the membrane and immediately below the membrane, but not through the channels above the membrane suggesting a blockage. The connecting channels that delivers dye to the top cavity was widened in diameter (1.1 mm to 1.5 mm) as it was thought that over-extrusion during the resume layer due to its increased flow rate (200 %) and reduced speed (10 %) could be blocking entrance to the connecting channel. In the second print, the increase in diameter did not rectify the issue of flow.

A further expansion to a 2.5 mm diameter showed an improvement, liquid could access the top layer and began to flood the channel system. However, significant pressure was observed and the dye did not travel through the channels as expected. The dye preferentially passed through the membrane and reemerged through the bottom cavity outlet (Figure 6.13) suggesting a blockage remained. Bleeding of the dye around the membrane edge and pooling of the dye in the bottom cavity was also observed indicating an incomplete seal and mobilisation of the membrane within the cavity.



Figure 6.12: The third test print with a pipe diameter of 2.5 mm fabricated using the PPP technique after food dye had been infused, showing how dye infused through the $\frac{1}{4}$ -28" inlet on the right passed through the membrane and exited the let next to it when it should have passed through the channel system to the let on the left side of the device. It also shows how the dye bled throughout the device below the membrane and did not follow the channel system.

During fabrication, it was noticed that for each printed layer, the pathway for the print head would outline the design first before infilling whereby features such as pipe circumferences and channel designs are initially outlined and defined by the printer before infill hence extruding directly onto the channel system with no supporting structures below. (Figure 6.14) It was thought this could be causing blockages within the design.

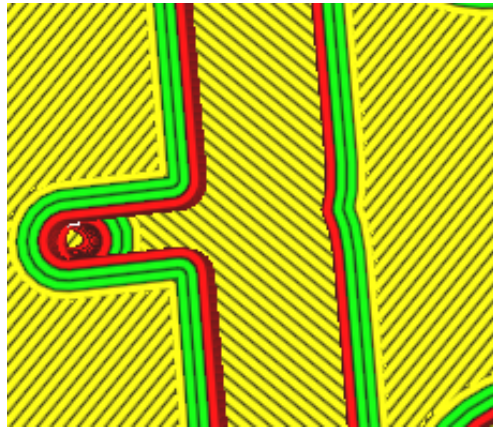


Figure 6.13: A part of the device shown on the Cura software for a print layer within the device that includes the channel system. The layer shown would be printed so the designs are outlined first (red) followed by reinforcement (green) and then the infill (yellow). The outline of the channel for the bottom cavity can be seen below the layers containing the channel system and it can be imagined how when the reciprocal layer is printed above the top layer shown, the extruded filament for the initial outlining of the pipework to the top lets would fall into the channel system of the previous layers.

Therefore, using the same PPP technique, prints were fabricated with an altered branched design and pipework positioning (Figure 6.15). A more direct route for fluid flow from the $\frac{1}{4}$ 28" fittings to the channels was included to minimise print error and distance. Entrance for the fluid *via* the pipes into the cavities was offset and the channel design was thinned to avoid filament extrusion onto the membrane and facilitate the fluid flow. The membrane cavity was also removed with the aim to seal and immobilise the membrane within and isolate the top and bottom channels.

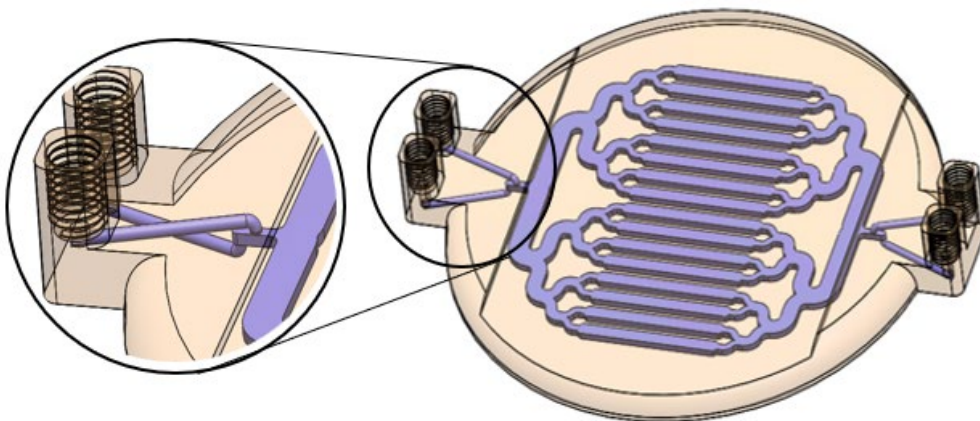


Figure 6.14: The second print design fabricated using PPP with different pipework and inlet/outlet design of the channels.

Food dye tests were repeated on the optimised print. Dye was now able to enter and pass linearly through the top cavity. The channel design was well defined by the dye in the top cavity indicating a good seal was made between the extruded PP and membrane surface. Furthermore, no bleeding of the dye was seen around the membrane perimeter indicating its successful encapsulation and isolation of the top and bottom cavities.

Despite this, the food dye did not follow the printed path of the bottom cavity indicating poor contact between the printed structures and membrane. The difference between the observed flow above and below the membrane was consistent with the membrane only being bonded to the top cavity due to direct extrusion of the material onto it (This is revisited and discussed more deeply in chapter 8). Instead of passing through the bottom cavity, fluid gathered within the unsealed area and caused the device to expand to twice its depth. This is a problem because it means residence time is uncontrolled and diffusion distance is not consistent or known. Repeats of the print were undertaken and all presented the same issue.

To make a robust usable device it was important that the membrane was bonded to the device on both sides to facilitate cross-flow filtration and functionality of the device. This could be achieved using an adhesive at all contact points,¹⁹⁹ however the addition of adhesive is subjective and challenging for reproducible fabrication. It also poses technical challenges due to potential wicking of the adhesive into the membrane. Hence a novel fabrication technique was developed whereby channels were directly patterned (and thus bonded) onto both sides of the membrane.

6.3.2.1.3 A novel 3D printing technique

To achieve a seal between the membrane and extruded material a novel technique was developed combining the ideas of PPP and embedding objects within prints.^{199,200} Previous observations showed that direct printing onto the membrane surface enabled a good seal to be made. Therefore, to produce a cross-flow filtration device with seals above and below the membrane a technique needed to be formulated that enabled the channel design to be printed onto both top and bottom sides of the membrane. This was achieved in a process shown in Figure 6.16.

The diagram in Figure 6.16 shows the 8-step process which involves two individually designed parts whereby one can be placed within a strategically designed cavity of the second for encapsulation to produce a functional device. Part one is shown in orange, (Figure 6.16A-D) part two is shown in purple (Figure 6.16E-H) and the membrane filter is represented in grey. The conditions used are detailed in the experimental (6.2.3.3).

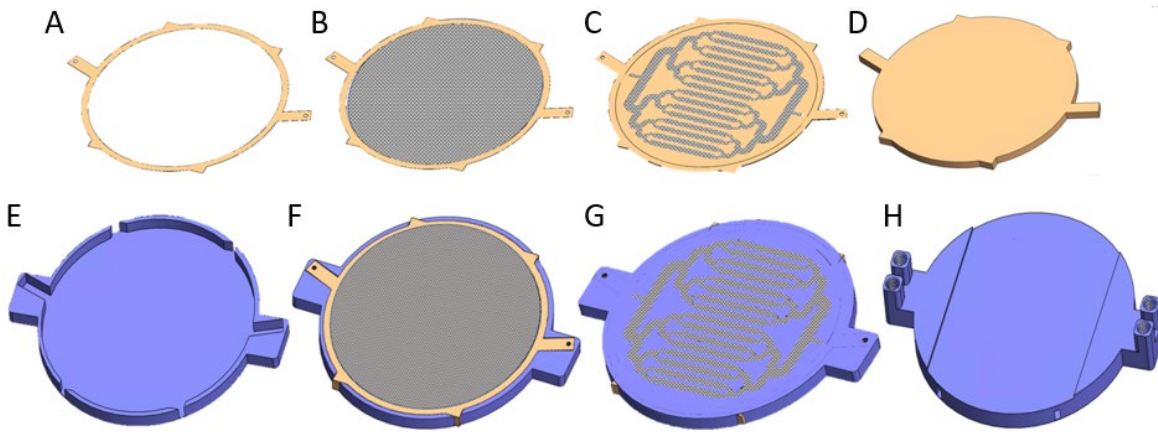


Figure 6.15: Diagram showing the 8-step novel fabrication process for the functioning cross-flow filtration device.

The first layer of part one is printed onto the bed outlining the position for the membrane filter and its cavity. (Figure 6.16A) A pause after this first layer meant the membrane filter could be placed on the print bed (Figure 6.16B) with a very small amount of a weak adhesive applied at the circumference to ensure it didn't move in the subsequent step. The print was resumed, and a channel design directly patterned on the membrane surface (Figure 6.16C) with additional layers enclosing the channels. (Figure 6.16D). This part, which represented the channel network on one side of the membrane, was removed from the print bed and the second phase commenced by printing a hollow receptacle (Figure 6.16E, blue) for the first part. Part one (orange) was placed within the receptacle (Figure 6.16F) with the exposed membrane surface facing upwards and the print resumed. The channel design was once again printed directly onto the exposed surface (Figure 6.16G) until full encapsulation to yield the finished device. (Figure 6.16H)

The complex internal structures for the associated parts including the pipework positioning, channel designs and how the prints aligned to give symmetrical fluid channels above and below the membrane are shown in Figure 6.17. In part one, the connecting channels ($\varnothing = 1.4$ mm) and channel system (depth = 0.5 mm) representing the bottom cavity (dark brown) can be seen showing how fluid can access *via* the $\frac{1}{4}$ 28" fittings printed within part two. Part two shows the receptacle cavity for part one (dark purple) and the symmetrical channel system with associated pipework (grey) for the top channel system. The same pipe diameters and channel depths are retained for the top channel system. The final device (part one + two) shows how part one is encapsulated within part two with the channel systems aligned above and below the membrane and the pipework of part one meets the entrance for the $\frac{1}{4}$ -28" PEEK fitting at the inlet and outlet for the bottom cavity.

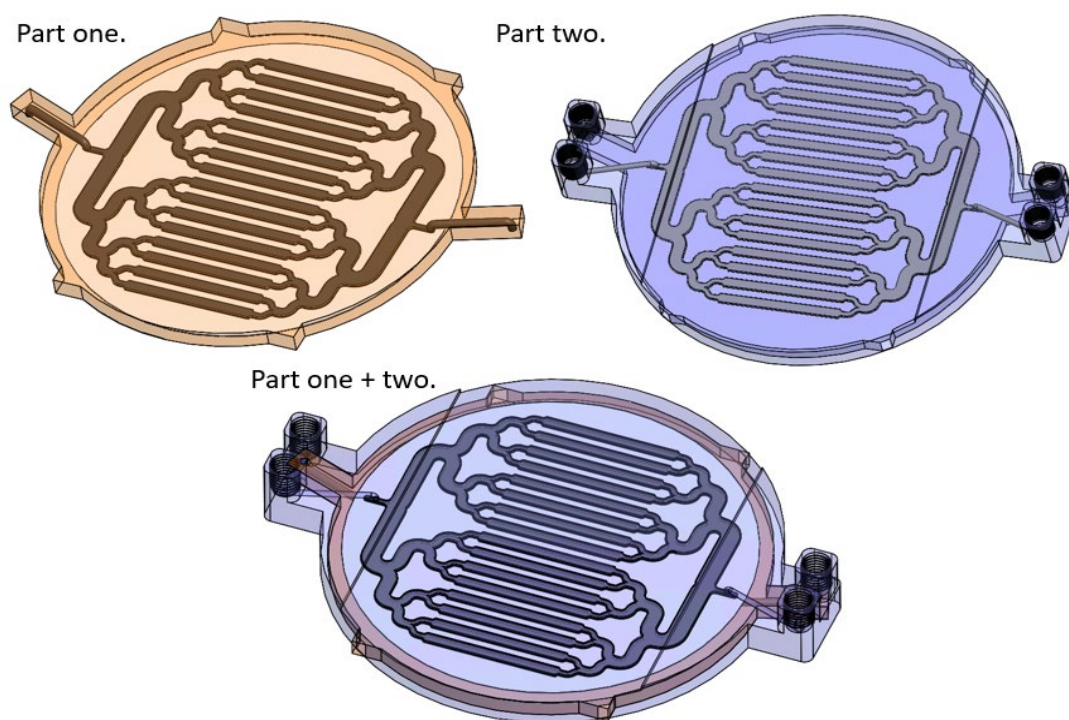


Figure 6.16: Images of the individual parts and full device as seen in SOLIDWORKS software. Part one is encapsulated within part two to produce part one + two.

All prints were monitored at every resume stage of the fabrication process. Small changes to the dimensions of part one were made to ensure placement within the cavity gave a direct seal between the extruded material and the membrane surface. The part had to be placed within the cavity snugly to ensure the channels were well aligned and sat flat for equal extrusion across the membrane surface. Furthermore, the internal connecting channels within the 'arms' of part one had to be accessed through the inlet/outlet fittings of part two. If part one sat proud of the pause cavity, the print cores would cut through the membrane. If the membrane surface of part one sat below the cavity level of the pause, the material was extruded into free air preventing a seal and losing detailing of the channel design.

Table 6.4 summarises the depth dimensions tested for the complete embedded device. The initial depths of 4.2 mm and 4 mm for part 1 and 2, respectively were chosen to account for shrinkage of the first part as it cooled. After several trails, a successful seal was achieved using a depth of 3.9 mm for part one with a cavity depth of 4 mm in part two. This was also repeatable.

Table 6.3: Summary of the print tests performed to get the correct part one depth against the cavity in Part two.

	Part 1 depth / mm	Part 2 cavity depth / mm	Seal to membrane / Yes or No	Comments
1	4.2	4	No	Print core cut through membrane – Too close
2	4	4	No	Print core cut through membrane – Too close
3	3.9	4	Yes	
4	3.9	4	Yes	Repeat of (3)

6.3.3 Functionality

Once a set of print conditions and associated dimensions were successfully established the device was used for cross-flow filtration of organic dye, methylene blue, previously chosen in MOF adsorption studies. The aim was to achieve high levels of dye separation with equal flow rates exiting from the outlets. This required full dispersion of the dye across the channel system and no differences in pressure through the isolated channels. Any air bubbles seen through the transparent polypropylene were removed using small, manually applied surges in flow and by tapping the device on the benchtop.

6.3.3.1 Dye separation

Using the experimental set-up described in 6.2.5, several runs of counter-current, cross-flow filtration were performed with 0.01 mM methylene blue in ethanol at varying flow rates (0.1-1 mL/min) using ethanol as a carrier solvent. The dye removal was calculated along with associated error by averaging the results collected and corresponding residence time of the dye within the device.

Figure 6.18 shows the best results collected by a part fabricated using the novel technique. When a counter-current arrangement was employed with a 0.5 mLmin^{-1} (2.63 min residence time), $74.04 \pm 1.07 \%$ was removed from the process stream and when reduced to 0.1 mLmin^{-1} (13.13 min residence time), $85.85 \pm 0.39 \%$ of the total dye was removed showing a good degree of removal and small associated errors that don't overlap with other data points collected. Under Fick's law it was calculated that a 6.24 min residence time would be required for dye molecules at the top of the channel to diffuse to the membrane surface within the cavity when the channel height was printed to $500 \mu\text{m}$. This is theoretical and would not ensure full diffusion (100%) so the calculated values are respectable in comparison.

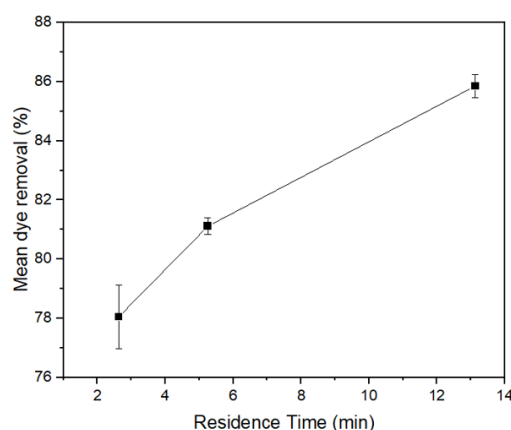


Figure 6.17: Plot showing the mean dye removal (%) and associated error vs residence time by the sixth device fabricated using the novel 3D printing technique.

More data points would be desirable. However, when a 1 mLmin^{-1} flow rate was applied, it was observed that fluid began to gather in the top cavity and the device swelled at the centre of the channel system where the design is most complex and no data point was collected. This could be the consequence of either the polypropylene-membrane seal bursting at weaker points of the design due to the increased flow rate or the presence of volatile solvent, ethanol rupturing the seal as the further data points were collected several days later. Future device testing reduced the flow rate range to $0.1\text{-}0.5 \text{ mLmin}^{-1}$.

6.3.3.2 Reproducibility

A second device was fabricated and tested in the same way starting with the slowest flow rate.

Figure 6.19 shows the results when plotted and compared against the previous device.

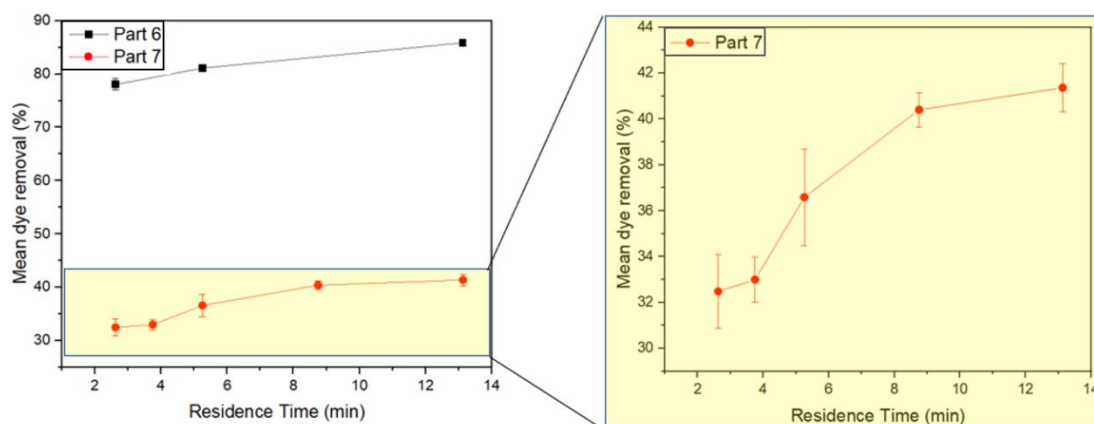


Figure 6.18: Plots showing the results collected for the seventh fabricated device using the novel 3D printing technique against the previous part and magnified for clarity.

Approximately half the dye was removed at all flow rates when compared to the previous device. (Figure 6.19, part 6) During testing it could be seen the dye only accessed half the channel system in the top cavity, reducing the transfer surface area, potentially due to a blockage within the first channel branching, which is consistent with the results. The associated errors were also much larger with some overlap seen. The loss of seal between the membrane and polypropylene was not observed as before even after several days of exposure to the ethanol suggesting the lower flow rate range is more appropriate for the device.

Liquid will preferentially travel down the path of least resistance and despite the symmetrical nature of the designed channel system, it is intricate which statistically gives more room for error during printing. The resolution limit for the 3D printer is 0.1 mm and the dimensions of this device use the very limits of the printers capabilities with some parts of the channel network being as small as 0.2 mm. The volumetric flow rate (Q) is directly proportional to the quartic radius (R^4) of the channels according to the Hagen Poiseuille equation. Therefore, very small differences between prints in terms of varied extrusion rate or littering of the channels with filament will cause detrimental effects on the device functionality at this scale in terms of channel and dimension, hence the need for back pressure. Furthermore, the overall time of print is collectively over 20 hours for the two parts which inherently provides more time for error. Due to these reasons, reproducing the device reliably was a challenge.

When considering the broader applications of this device a reproducible fabrication procedure is required with optimised lifetime, reliable separation of definable amounts of free dye from the process stream and even pressure above and below the membrane for easy integration within the final system. To achieve even flow rates above and below the membrane on the devices discussed, a micrometering valve was required at the process stream outlet. Upon integration within the synthetic process stream this would not be practical as a large degree of pressure would accumulate over time as dispersed framework would back up and foul at the valve. Consequently, it was decided to explore off-the shelf commercial options. While these are only available with set dimensions and materials, they offer increased reproducibility and ease.

6.3.4 Commercial device

Commercial modules designed for cross-flow membrane separation were purchased from Repligen as possible candidates for in-line MOF analysis and to compare data against the fabricated devices.

Spectrum® MicroKros hollow fibre filter modules provide effective microfiltration of small processing volumes (<1 L) using cross-flow technology. Modules may be selected against a range of specifications as ready to use, high surface area, compact modules with the opportunity to apply them alone or in parallel for a series of applications.

6.3.4.1 Function and specification

An image of the device is shown in Figure 6.20. Hollow fibre membranes are encased using a polysulfone housing with ¼ 28" inlet and outlet ports either end. The process fluid is infused through the fibre lumen using a syringe pump to tangentially flow across the membrane surface area. The process stream is collected at the outlet whilst small molecules diffuse across the membrane into the outer annulus for collection at the filtrate outlet. Relating to this project, the process stream corresponds to the synthesised MOF with adsorbed and free methylene blue in ethanol being passed through the fibre lumen. The filtrate contains the free, unadsorbed dye that has diffused through the membrane pores into the carrying solvent stream.



Figure 6.19: Diagram of the Repligen MicroKros Hollow Fibre filtration device. Taken from the Repligen website.

The product specifications for the purchased device were as follows. The total and effective length of the device were 45 cm and 41.5 cm, respectively. Two hollow fibre filter membranes made from hydrophilic polyethersulfone (PES) material and with a 1.0 mm inner diameter were encased within the module housing to give a total membrane surface of 26 cm². These choices were made on account of the large surface area, cost and availability (at the time of purchase a lead time of 3 months was given). PES syringe filters were used prior to purchase to assess their compatibility with methylene blue. No dye was absorbed by the membrane after multiple passes confirming it as a suitable membrane material.

6.3.4.2 Co- vs Counter-current configuration

The removal of dye by a single unit of the commercial device was tested using a 0.01 mM ethanolic methylene blue solution used in previous adsorption studies with the selected MOF systems. (5.2.6) Counter- and co-current configurations were investigated at a range of set equal flow rates (0.05-0.5 mL/min) and the process stream residence times for each flow rate were calculated using the volume of the hollow fibre filters calculated from their radii (0.5 mm) and the effective length (41.5 mm) and plotted. Repligen devices were pre wetted with ethanol to saturate the membrane and device and eliminate air bubbles before each experimental run to prevent any functional issues.

Figure 6.21 presents the mean dye removal from the process stream for the different flow arrangements and the associated errors. At all flow rates tested, a greater amount of dye was removed from the process stream in the counter-current arrangement, as expected. Furthermore, the shape of the curve suggests that further removal is possible at longer residence times whereas the co current flow shows a plateau in removal after 3.26 min. Data collected from a 6.52 min residence time showed that $63.6 \pm 0.5\%$ and $47.9 \pm 1.9\%$ of dye was removed from the process stream during a counter- and co-current arrangement, respectively. A plateau around or

just below 50 % removal is expected for the co-current arrangements due to its maximum possible diffusion of 50 % once the two partially separated streams have reached equilibrium with no concentration gradient between them for methylene blue to move along.

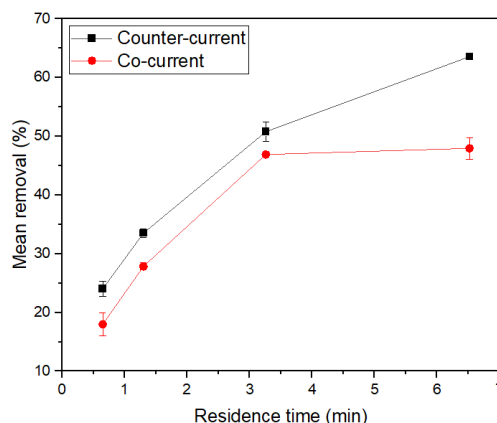


Figure 6.20: Plot of the mean dye removal and associated errors vs residence time for the Repligen device using a co- and counter-current flow arrangement. Errors represent the standard deviation over several experimental repeats.

Using Ficks law, the theoretical time taken for full diffusion of methylene blue across the membrane is 6.24 minutes using the diffusion distance (0.05 cm) and reported diffusion coefficient ($3.34 \times 10^{-6} \text{ cm}^2/\text{s}$ for a 50 % ethanolic solution).¹⁹⁶ In the counter arrangement at $t = 6.52$ mins (approximately the theoretical time) more than half the dye had been removed from the process fluid. Differences in experimental and theoretical are expected as Fick's law is based on an ideal system and the theoretical value represents the maximum time taken for dye molecules positioned at the centre of the fibre filter to diffuse to the membrane surface, e.g. it does not take into account the statistical consideration of Brownian motion of species within a liquid. Furthermore, the reported diffusion coefficient is for a 50 % ethanolic solution whereas the solution used within these experiments are 100 % ethanolic. This is not an ideal assumption to use but without a value for 100 % it is the best that could be made at the time.

The final separation device needs to show reliable and definable removal of dye from the process fluid when integrated within the final set-up. Moreover, it would be optimal if 100 % of the free unadsorbed dye within the process fluid could be separated. Following the successful removal of dye in the counter-flow, and due to the 50 % removal limitations of a co-flow arrangement it was decided that a counter-current arrangement would be the best route to explore.

6.3.4.3 Counter current: concatenated devices

To increase the percentage removal, one strategy was to increase the residence time. The flow rate could not be reduced further so extending the interfacial area by purchasing additional

devices and connecting them in series was explored. A counter- flow arrangement was used according to the results outlined in the previous section and the same carrier fluid was used in series to remove the dye. A micrometering valve was used at the process stream fluid outlet to maintain an equal flow rate between the two fluid streams. It is worth noting that while the results discussed in this section show seemingly good results, it will later be seen (6.3.4.4.1) that they were deceiving.

Figure 6.22 shows the mean dye removal and associated errors for the Repligen devices when used in series. By series it is meant that a single feed of methylene blue solution and fresh ethanol are infused either end and collected for analysis e.g. one process stream outlet and one carrier stream outlet. By doing this, the length of the device has, in essence, been doubled and tripled. The flow rate range tested was $0.1 - 0.5 \text{ mLmin}^{-1}$ corresponding to residence times of $0.13 - 6.52$ mins and $0.19 - 9.77$ mins for the two and three parallel series, respectively.

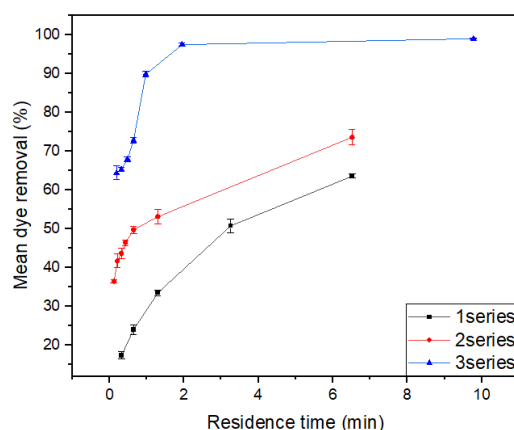


Figure 6.21: Plot of the mean dye removal (%) and associated errors for the Repligen device in a counter-current flow arrangement when used singularly and in a two or three series. Error bars represent the standard deviation over several experimental repeats.

As expected, when more devices were used in parallel, a greater amount of dye was removed from solution. When two are placed in series, no plateau was seen due to the nature of counter-current flow where a constant concentration gradient is maintained across the length of the reactor meaning a plateau would not occur until full diffusion e.g. 100 % dye removal. A lower flow rate could be applied to improve removal. At the longest residence time investigated (6.52 mins), which corresponds to a $100 \mu\text{Lmin}^{-1}$ flow rate, 73.62 ± 1.98 % of the dye was removed.

When a third device was added to the series, a plateau in the plot occurs in under two minutes with 97.49 ± 0.42 % of the dye removed and when the residence time is extended five-fold (9.77 min), this increases slightly to 99.03 ± 0.10 %. UV-Vis of the process stream confirmed that 1.23 ± 0.17 % of the dye remained which is in good agreement with the filtrate.

These results suggest that to remove 100 % of the dye would be difficult due to the almost negligible concentration gradient at the far end of the series and the random motion of species within solution. Also, as discussed, Ficks law calculates that 6.24 minutes are required for full diffusion. The process fluid has a limited flow rate in line with synthesis protocols discussed earlier in this thesis directly influencing the residence time for separation. For a 40 and 20 minute synthesis, the total process fluid flow rate would equal 192.42 and 384.84 $\mu\text{L}/\text{min}$, respectively. These synthesis times were chosen due to synthetic work discussed in 4.3.4 which showed how phase pure HKUST-1 and a mixture of the Cu-BTC complex with the HKUST-1 was synthesised at RT for a 40 and 20 minute synthesis, respectively. The corresponding residence times and expected dye removals for each synthesis when 1, 2 and 3 Repligen devices were used are given in Table 6.5 based off the data shown in Figure 6.21. From this, it is clear that if this set-up was integrated within the system, three Repligen devices would be the most sensible route of action to optimise dye removal.

Table 6.4: Summary of the expected dye removal within the integrated system for a 20 and 40 minute synthesis when 1, 2 and 3 Repligen devices are linked in series with a single carrier stream employed.

Synthesis time / min	No. of Repligen devices in series	Residence time / min	Expected dye removal/ %
20	1	0.85	26.96
20	2	1.69	54.66
20	3	2.54	97.59
40	1	1.69	36.94
40	2	3.39	61.36
40	3	5.08	98.10

Changing the flow rate ratio between the process and carrier stream

The flow rates of the fluid streams are a factor largely affecting dye removal as it directly effects the residence time and concentration gradients across the membrane across the device.

Following the successful dye removal by three Repligen devices connected in series, varying flow rate ratios between the process and carrier stream were investigated to see the effect changes would have. These streams may be defined as a donor and acceptor stream also when being discussed with respect to the dye. For example, the process stream is 'donating' the methylene blue molecules to the 'accepting' carrier stream. The results are shown in Figure 6.23.

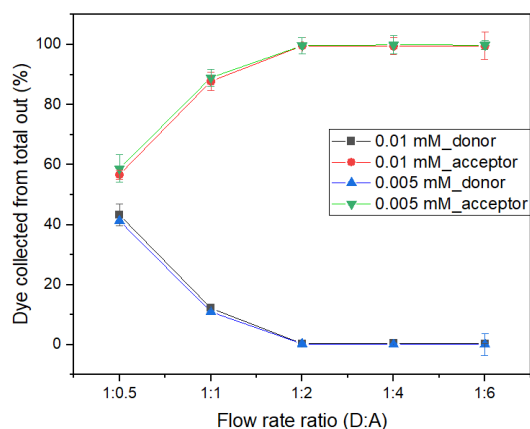


Figure 6.22: A plot showing the amount of dye collected as a percentage of the total for the donor and acceptor stream when a 0.005 and 0.01 mM dye concentration was passed through three Repligen devices connected in series with a single carrier stream at different flow rate ratios. Error bars are defined as the highest and lowest values of several experimental repeats.

The process stream in all cases was set at $384.84 \text{ uLmin}^{-1}$ in line with the flow rate expected for the process stream when a 20 minute synthesis time is employed within the integrated system. As the flow rate for the acceptor stream is increased relative to the process stream, greater removal of dye was observed. When a 1:2 ratio is employed, which corresponds to a $384.84:769.68 \text{ uLmin}^{-1}$ donor to acceptor ratio, $99.65 \pm 2.64 \%$ and $99.72 \pm 2.64 \%$ dye was separated into the acceptor stream for a starting solution of 0.01 and 0.005 mM, respectively. All calculated errors, defined by the highest and lowest values of several experimental repeats, are small suggesting precise and reproducible results. Furthermore, these results show that separation was independent of the starting solution concentration as expected.

6.3.4.3.1 Flow sensors to measure the flow rate between concatenated devices

When measuring the effect of flow rate ratio between the donor and acceptor stream on the dye separation by three Repligen devices connected in series with a single carrier fluid it was observed that connecting PTFE tubing between the devices appeared to show no movement of fluid as air bubbles were seen to form and remain unmoved. Therefore, flow sensors were placed between the first and second device for each fluid stream to measure the fluid flow rate.

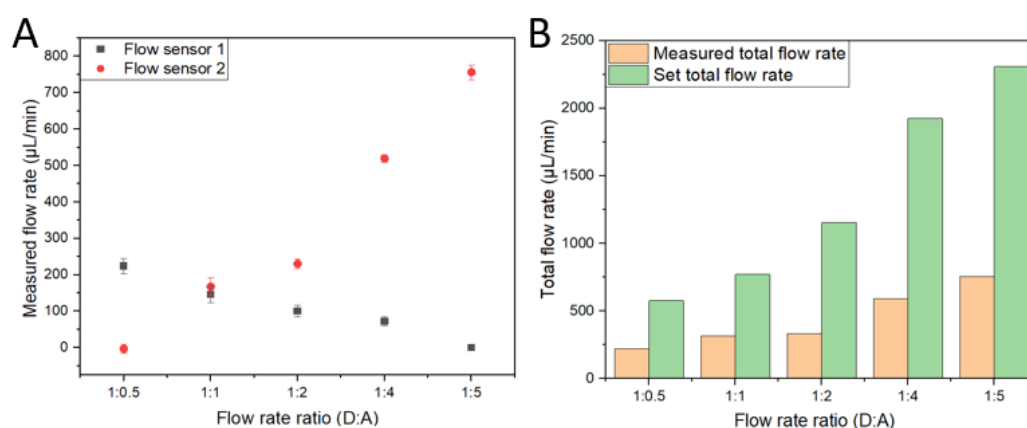


Figure 6.23: A) Plot showing the measured flow rates for each sensor at different flow rate ratios. Error bars errors, represent the highest and lowest values of several experimental repeats, and B) a bar chart showing the difference between the total measured flow rate against the total set flow rate at each flow rate ratio tested.

The flow sensor readings, plotted in Figure 6.24, revealed significant insights into fluid dynamics within the Repligen devices. Flow sensor 1 was placed between the first and second device of the process stream whilst flow sensor 2 was placed in between the first and second device of the carrier stream. At a donor-to-acceptor ratio of 1:0.5, no fluid movement is measured between the first and second Repligen device in the acceptor fluid stream. When the ratio was adjusted to 1:1, the measured flow rates aligned, indicating equal flow rates. As the acceptor ratio increased incrementally up to five times that of the donor stream, fluid movement ceased from the first to the second device within the donor stream with sole movement seen within the acceptor stream. Additionally, when the two flow rate readings were combined and compared to the total set flow rate for both streams, the measured flow rate consistently fell short of the set flow rate even at a 1:1 A:D flow rate when the sensors measured equal flow rates. (Figure 6.24B) The disparity between the total set and measured flow rates grows as the ratio difference increases with the total measured flow rate only 32.75 % of the total set at a 1:5 donor to acceptor flow rate ratio. These observations strongly suggest that net fluid transport was occurring across the membrane, rather than diffusion being the sole process.

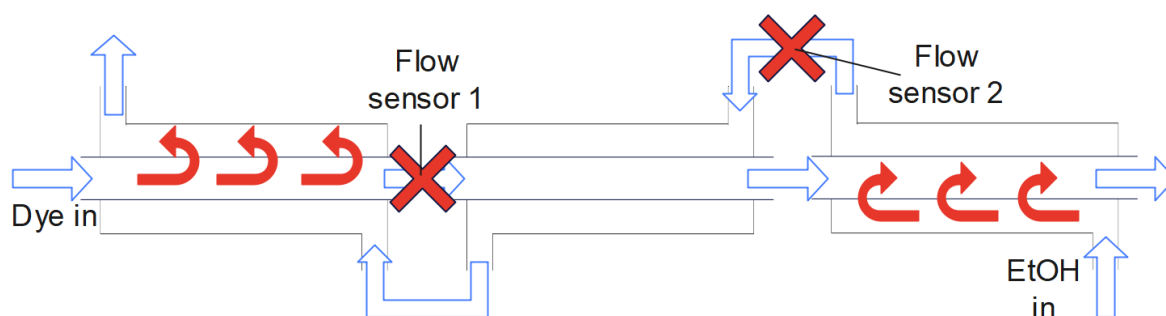


Figure 6.24: A simplified diagram of three Repligen devices in series with a single extracting solvent carrier stream in a counter current flow arrangement. The blue arrows show the expected direction of fluid movements within each stream, red crosses denote how fluid fails to flow according to flow sensor readings and red arrows show how mass fluid transport across the membrane occurs as a result.

In an ideal system, the two fluid streams would flow in a counter current arrangement with no net fluid transport across the membrane and diffusion of the methylene blue dye would occur across the encapsulated hollow fibre filters. This would only occur if the pressure in each stream was equal with no net transmembrane pressure. By changing the flow rate ratios of the two streams a net pressure is generated ceasing fluid movement from inlet to outlet of a singular stream and enabling movement of ethanol across the membrane to be removed out the same side of the device series, as illustrated in Figure 6.25 with red arrows. Moreover, movement between the devices required fluid to pass through PTFE tubing ($\varnothing=1$ mm, 10 cm). The length and diameter of this tubing was the same for each connection but the transfer between devices would exacerbate the pressure increase due to constriction of cross sectional diameter when the acceptor (carrier) stream passes through the PTFE connection and the donor (process) stream moves from two hollow fibre filter lumens to a single PTFE one. The effect of this is an increase in back pressure and a favouring of mass transport across the membrane rather than a device-to-device transfer which is interesting as one would expect partial transport at the limits of the tested periods but not complete ceasing of all movement.

Aside the flow sensor readings, this is also supported by dye removal data shown in Figure 6.23. At a 1:2 donor:acceptor flow rate ratio, almost 100 % of dye is successful removed due to the dye-infused ethanol donor stream entering the first device *via* the donor inlet, passing through the membrane (solvent and solute) and exiting the acceptor stream outlet for collection and analysis as determined by the results of the flow sensors.

As a result of the findings from the flow sensors, it was decided that using multiple Repligen devices in series with a single carrier stream presented inherent pressure problems. This prompted the employment of individual carrier streams for each device to be investigated.

6.3.4.4 Counter current: longer interfacial area with multiple carrier streams

Following the results of the flow sensor experiments, it was decided to explore a set-up which used multiple carrier streams (one per device) to see the amount of dye removal possible with the three concatenated devices and three carrier streams. This means there is a single process stream outlet and three carrier stream outlets.

The experiment series was repeated with the same dye-infused ethanol solutions (0.005 mM and 0.01 mM) but using individual carrier streams of ethanol for each device used. The results are given in Figure 6.26 and show the amount of dye content exiting each outlet.

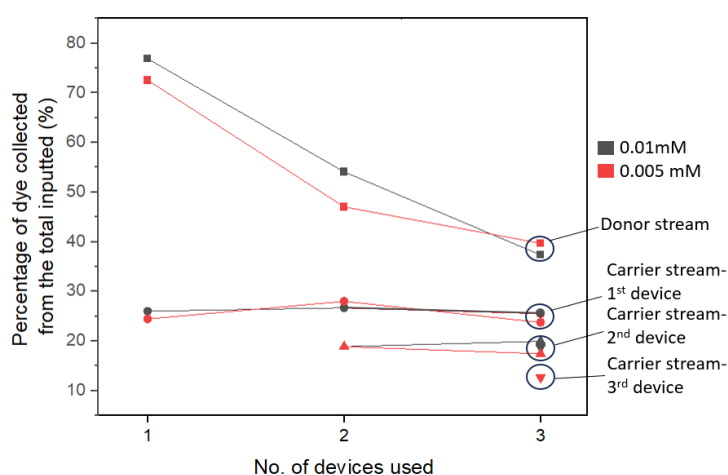


Figure 6.25: A plot showing the amount of dye collected as a percentage of the total for the donor and acceptor streams when a 0.005 and 0.01 mM dye concentration was passed through three Repligen devices connected in series with a single carrier stream and three separate outlets.

Once again, the set-up for this series of experiments demonstrated that separation is independent of the process fluid concentration as a 0.005 and 0.01 mM stream were tested with little difference across the data. The first device removed the highest percentage of total dye inputted into the system followed by the second and then the third device. Each individual device would be expected to remove the same percentage of the incoming donor stream as the concentration gradient is renewed each time. As the incoming donor stream to the second device would have an overall lower dye concentration than that initially flowing into the first device it can be expected that the amount of dye removed would be an equal percentage of the incoming

but a lower percentage of the total initial dye. In the case of a 0.005 mM initial dye concentration for the donor stream when three devices were placed in series with three individual carrier streams the first, second and third device removed 23.76, 17.44 and 12.65 %, respectively with a remaining dye concentration of 39.69 %.

This set-up presents an individual separation per device added. Approximately 24 % of the incoming dye-infused stream was removed per device and after three devices in series there was still between 37.35 and 39.69 % of the total dye remaining in the donor stream for the 0.01 and 0.005 mM runs, respectively. The initial aim for separation was to achieve 100 % removal of the free dye from the donor to the acceptor stream. All efforts possible were made with the equipment available from purchase but this could not be achieved. To achieve 100 % removal of dye from the process stream, a commercial device with a greater surface area would need to be purchased, this is explored in the next chapter following the results and observations of further experiments.

6.4 Conclusion

In this chapter the hardware for separation was investigated. Initially, design and fabrication using common materials was explored before commercially available devices were looked to.

A branched microfluidic channel design incorporated into a part fabricated using FDM 3D printing with the PPP technique for membrane incorporation was determined an appropriate design and fabrication method for the filtration device in the first instances.

During 3D printing, observations made during direct extrusion onto the membrane surface prompted a novel printing strategy to be developed in efforts to alleviate membrane immobilisation issues that were encountered. The strategy involved direct printing onto either side of the membrane surface *via* an 8-stage process involving two printed parts with one being embedded within a receptacle cavity of the other to produce a conformal bond between the extruded filament and membrane surface upon contact. A device with good dye separation (85.85 % @ 13.13 min residence time) was successfully fabricated showing good promise for the method. However, reproducibility of the device was poor despite 3D printing having fantastic capabilities for prototyping with high resolution. Furthermore, the microfluidic dimensions of the device design meant that miniscule changes in channel dimensions had a profound effect on the pressure and functionality according to the Hagen-Poiseuille law and it was decided to move on from this approach within the main body of my research to commercially purchased devices due

to the expectation that its implementation in-line, with HKUST-1 dispersion, would exacerbate issues. However, later on within the research period, this work was returned to as a side project using different channel architecture including a single channel with great success. (8.3.1)

Moving on, commercial devices were purchased from Repligen containing hollow fibre filters as an alternative to the 3D printed devices. Co- and counter- current arrangements demonstrated the typically expected results and a counter flow arrangement was decided on due to its theoretical capability of achieving 100% free dye removal from the process stream which would maximise the measurement sensitivity. A single device was able to remove 63.6 % of dye in the counter flow arrangement after 6.52 min, increasing to 73.6 % and 99.0 %, when a second and third device was added, respectively with a single carrier solvent stream. However, flow sensors showed that the concatenated devices had a net movement of fluid passing through the membrane to the oppositely flowing stream rather than the expected inlet to outlet pathway, possibly a result of transmembrane pressures. These results prevented this set-up to be taken forward as a potential candidate for the final integrated process.

A second approach was taken to use individual carrier streams for each device added to prevent pressure build up across the system and maintain high concentration gradients, promoting diffusion. Results appeared to show that the amount of dye separated as a percentage of the starting total was 23.7 % by the first device, followed by 17.4 % and 12.6 % for the second and third device, respectively when a 0.005 mM starting solution was infused. This was mirrored when the concentration was doubled to 0.01mM, showing that separation is independent of the starting concentration. This set-up alleviated the previous issues, but the donor stream still contained almost 40 % of the starting dye. The nature of this set-up meant that the same percentage of dye from the incoming stream was separated each time and due to limitations in funding, the number of available syringe pumps and system complexity it was apparent that 100 % free dye removal could not be achieved with the three devices.

By removing 100 % of free dye maximum measurement sensitivity could be achieved but it was not fully necessary. As long as quantifiable amounts of dye could be separated reliably, the system could work as imagined for in direct analysis of the HKUST-1 synthesis procedure. Results presented in this chapter do not include any MOF dispersion during separation and suggest that a counter current system for optimal free dye removal using a single device would work well. Therefore, it was decided to use one device only for simplicity in future work and purchase a better Repligen device with the highest surface area available (65 cm effective length, 9 lumen, 92 cm²) to maximise the separation. Taking into account the fact that optimal removal is not

Chapter 6

actually necessary, a co-current arrangement for 50 % removal could also be successfully employed. Both these arrangements are discussed in the next chapter.

Chapter 7 Integrated in-line analysis of Metal Organic Frameworks

7.1 Integration of the system

In the previous chapters, synthesis, adsorption and separation processes have been individually determined and optimised for the continuous synthesis of HKUST-1 and its adsorption for methylene blue. In this chapter, the integration of individual components was achieved to produce a fully operational process involving MOF synthesis, application and in-line UV-Vis analysis to give real time data which is indicative of the initial parameters set in the synthetic part of the process.

7.2 Experimental methods

Materials and methods

All chemicals and reagents were purchased from chemical suppliers with no further purification necessary before use.

$\text{Cu}(\text{NO}_3)_2 \cdot 2.5\text{H}_2\text{O}$ (98 %), trimesic acid (95 %) were all purchased from Sigma Aldrich. Ethanol solvent was purchased from Sigma Aldrich. Methylene blue and ethanol solvent were purchased from Sigma Aldrich. Syringes (20 mL, BD Plastipak Luer Lock) and tubing (PTFE, $\varnothing = 1$) were purchased from RS components. Fused silica capillary was purchased from CM scientific. For all flow syntheses syringe pumps (Harvard apparatus) controlled *via* computer software (LabView) were used to provide accurate infusion of the reagents. The Spectrum® MicroKros hollow fibre filter modules (41.5 cm, 2 lumen and 65 cm, 9 lumen) were purchased from Repligen.

The benchtop UV-Vis spectrometer was a Shimadzu UV-2700 and the in-situ spectrometer was the Ocean Optics FLAME-S-VIS-NIR-ES along with a halogen lamp (Ocean Optics HL-2000) and fibre optics.

7.2.1 The optimised integrated system set-up

A fully integrated set-up including the synthesis, adsorption and separation sections was tested using that determined in the previous chapters. The method described below is the optimised setup following this integration which differs from the initial testing by the device and flow

arrangement used for the separation section only. In the optimised set-up a co-current arrangement with a 65 cm Repligen MicroKros device was used. The optimised set up is shown in Figure 7.1.

Two syringe pumps (Harvard Apparatus) loaded with syringes, computer controlled *via* LabView software, containing copper(II) nitrate hemipentahydrate ($\text{Cu}(\text{NO}_3)_2 \cdot 2.5\text{H}_2\text{O}$, [0.03M], EtOH) and 1,3,5-benzenetricarboxylic acid (H_3BTC , [0.06 M], EtOH) were connected through PTFE tubing (10 cm, $\varnothing=1$ mm) using Luer lock, $\frac{1}{4}$, 28" fittings with flangeless ferrules and a T-junction (IDEX). This was connected to a fused silica capillary (10 m, $\varnothing=0.7$ mm) which acted as the reaction vessel of the system. Following this, a second T-junction was used to infuse methylene blue solution ([0.01 mM], EtOH) into the process stream which was subsequently passed through PTFE tubing (4 m, $\varnothing=1$ mm) as the adsorption phase of the system. The process stream was directed into a Repligen device (effective length= 65 cm, 9 hollow fibre filters, surface area= 92 cm²) that had a carrying ethanol stream flowing in parallel through the hollow fibre filters within the device at an equal flow rate, controlled by a fourth syringe pump. The exiting acceptor/carrier and process/donor stream were collected and analysed ex-situ using a benchtop UV-Vis spectrometer or analysed in-line using an in-situ spectrometer.

Initial synthesis parameters were controlled through different synthesis times ($t= 10, 20, 30, 40$ and 50 minutes) and molar metal to ligand ratios ($\text{M:L}= 1:0.5, 1:1, 1:2, 1:4$ and $1:8$).

7.2.2 In-situ spectrometer

Using the setup described in 7.2.1 an in-situ spectrometer was added to the set-up for system automation and continuous data collection. (Figure 7.1) The acceptor stream outlet tubing was directed through a 3D printed flow cell designed and fabricated by Lyle Oswald.²⁰² A halogen lamp with a 1 mm lens was connected to the flow cell using a fibre optic. A second fibre optic on the other side of the cell directed the light to the Ocean Optics FLAME-S-VIS-NIR-ES in-situ spectrometer which was subsequently connected to a PC. The spectrometer was operated through the OceanView 2.0 software.

A reference was introduced by preparing a batch solution to mimic the process stream flowing through the flow cell minus the free dye. This was done using the copper salt and organic linker solution with an equal volume of ethanol which was left for 60 minutes then centrifuged (1 min, 100 rpm) and filtered. Filtrate was infused through the flow cell using an IDEX shut-off valve *via* 5 mL syringe. A dark spectrum was also taken of the reference by turning off the halogen lamp and removed from the spectrum.

Data collection was set with an integration of 1500 μs and a 'scans to average' setting of 1000 meaning a spectra was collected every 1.5 s. The absorbance value at a wavelength of 654 nm (the peak maxima of the methylene blue UV-Vis spectrum) was recorded after equilibrium of the system was reached. The expected time of equilibrium was calculated using the flow rate and volume of the system to the point of in-situ analysis and confirmed by observing the real-time data which was at equilibrium when no change was observed for 5 minutes.

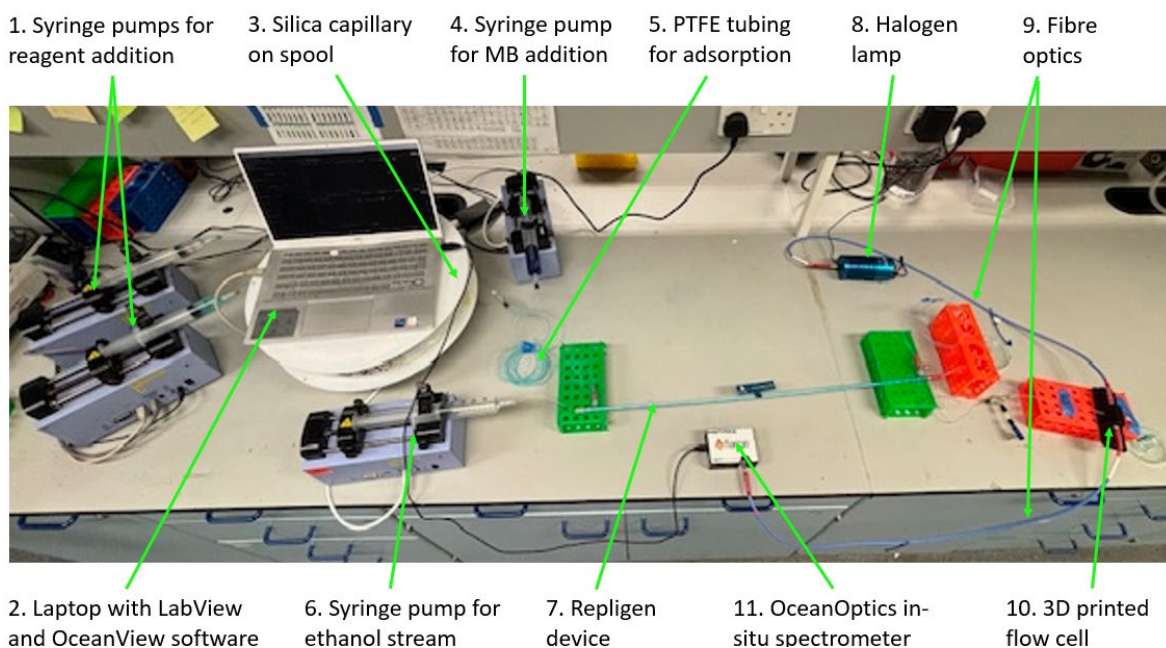


Figure 7.1: Image of the full set-up in operation including continuous synthesis, adsorption, separation and in-situ UV-Vis analysis.

7.2.2.1 Calibration curve

A series of ethanolic methylene blue solutions were produced using sequential dilution and passed through the PTFE tubing ($\varnothing = 1\text{ mm}$) fed through the 3D printed flow cell connected to the in-situ spectrometer. The absorbance value at 654 nm was recorded for each solution. The same solutions were transferred into cuvettes and absorbance values at 654 nm were measured using the benchtop UV-Vis spectrometer. These two calibration curves were plotted on a single absorbance vs concentration and the equation of linear trendlines was calculated.

7.2.2.2 Effect of molar ratio and synthesis duration

A 40 minute synthesis duration was employed (96.21 $\mu\text{L}/\text{min}$) and different molar ratios of the metal and ligand were investigated (M:L= 1:0.5, 1:1, 1:2, 1:4 and 1:8) through adjusting the flow rates of the individual reagents such that the total equalled 96.21 $\mu\text{L}/\text{min}$).

7.3 Results and Discussion

7.3.1 Initial single system integration

All components of the process investigated in the previous chapters with the determined parameters were integrated into a single system. This setup included a flow synthesis section utilising copper(II) nitrate hemipentahydrate ($\text{Cu}(\text{NO}_3)_2 \cdot 2.5\text{H}_2\text{O}$, [0.03M]) and 1,3,5-benzenetricarboxylic acid (H_3BTC , [0.06 M]). These reactants were introduced through PTFE tubing to a T-junction, followed by fused-silica capillary ($\varnothing=0.7$ mm, 10 m) serving as the reaction 'vessel'. Reactant streams were delivered at equal flow rates with a total of 96.21 $\mu\text{L}/\text{min}$ for a 40 minute synthesis (residence) time.

Upon exiting the capillary, the process stream met a second T-junction where an ethanolic solution of methylene blue ([0.01 mM]) was introduced *via* PTFE tubing at an equal flow rate, resulting in a combined total flow rate of 192.42 $\mu\text{L}/\text{min}$. The combined stream travelled through PTFE tubing ($\varnothing=1$ mm, 4 m), corresponding to a residence time of 16.32 min. This second section of the process made up the application phase e.g. adsorption of the methylene blue onto the synthesised HKUST-1.

The resulting HKUST-1 dispersion and unadsorbed dye were directed through the hollow fibre filter lumen of a commercially purchased Repligen MicroKros device (effective length= 41.5 cm, fibre count=2, surface area= 26cm²) for filtration. An ethanol stream flowed counter currently through the outer annulus of the device to separate the free dye from the process stream. Due to results discussed in section 6.3.4.4.1, a 1:1 flow rate ratio between the donor and acceptor fluid streams was initially used. Prior to use, Repligen devices were pre wetted with ethanol to saturate the membrane and device and eliminate air bubbles which could otherwise cause functional issues due to pressure variations within the fibres.

Despite previous experiments covering all bases and controls to enable a simple integration, this setup presented unexpected issues regarding mass flow rate. Where previous testing with Repligen devices excluded the synthesised MOF, this was the first instance this issue was noticed. The mass flow rate at the outlet of the Repligen device did not equal the mass flow rate at the outlet of the adsorption phase of the set-up e.g. the inlet of the Repligen device. Initially, approximately 10 % of the incoming HKUST-1 was collected at the outlet, but this decreased to 0 % after a short period. Upon cleaning the device post-experiment, a buildup of HKUST-1 was flushed from the lumen as shown in Figure 7.2.



Figure 7.2: Image showing HKUST-1 removed from the Repligen device hollow fibre filter lumen after flushing with ethanol post-experiment.

To address these issues, a second Repligen device with different specifications was procured. This device featured 9 hollow fibre filters, an effective length of 65 cm and a total surface area of 92 cm². The membrane material remained the same (PES) but the diameter of the hollow fibre filters was halved to 0.5 mm. This device therefore had a shorter diffusion distance for the free dye within the hollow fibre filters, higher surface area and offered more pathways for the process stream, thereby optimising separation and mitigating clogging problems. However, the issue persisted and no solid was collected at the device outlet. This prompted a reconfiguration, the streams were swapped so that the process stream was passed through the outer annulus and the extracting carrier stream was passed through the hollow fibre filters. This presented a path of less resistance for the process stream while maintaining surface area but a slight drawback of a longer diffusion distance.

Initially the problems were alleviated with HKUST-1 being collected at the outlet, but the MOF mass flow, once again, dwindled until no solid was isolated. An advantage to swapping the streams was the ability to visually observe the HKUST-1 dispersion within the transparent Repligen device. HKUST-1 visibly accumulated over time at the inlet end of the device, as shown in Figure 7.3A and did not reach the outlet of the device. (Figure 7.3B)

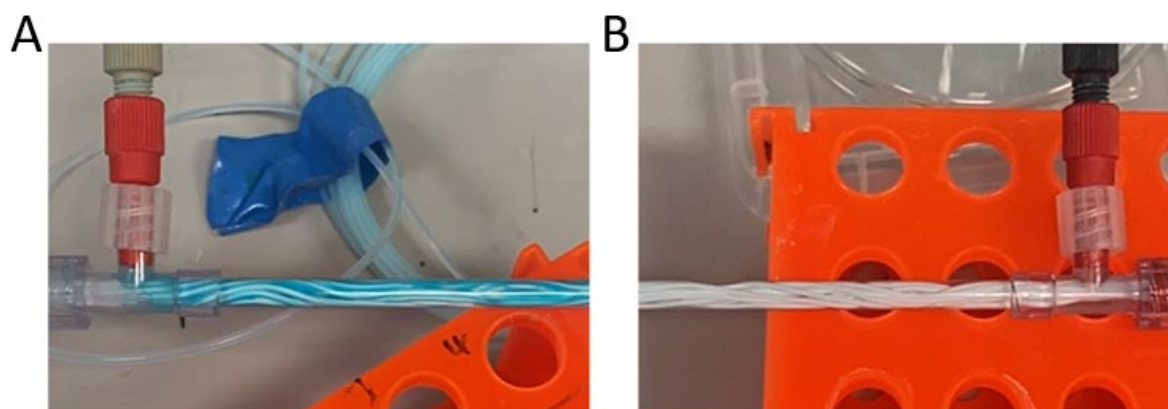


Figure 7.3: Snapshots from videos taken during operation after 15 minutes of the system running showing the A) inlet and B) outlet side of the Repligen device.

It was hypothesised that the cause of this accumulation was transmembrane pressure leading to net mass fluid transport across the membrane. Consequently, the inlet stream passed through the membrane to the opposing outlet, as previously seen when a single extracting carrier stream was investigated for a series of Repligen devices. This was unexpected as one would assume the fluids path of least resistance would be from inlet to outlet of the same stream, not passing through membrane pores. The counter-current arrangement likely caused this effect as with fluids entering from different ends, pressures across the membrane could be comparable to or higher than the capillary pressure of the membrane itself.

For the device to function as an integrated component of a single system, it is imperative that HKUST-1 passes through the device while maintaining a consistent mass flow rate. Without this, the set-up is rendered ineffective due to the lack of collection and limited operational lifespan. Therefore, a set-up had to be determined to facilitate full collection of HKUST-1.

7.3.2 A single system utilising a co-current separation arrangement.

Due to the counter current arrangement not being able to achieve full diffusion of the free dye, as shown in the previous chapter, there was no longer any benefit to using a counter current arrangement over a co current arrangement, so this was adopted with a hypothesis that co-current flow would remove the problems associated with transmembrane pressure and hence, the clogging issue.

A successful run was performed. The system did not show evidence of clogging and the expected mass flow rate was collected at the outlet of the process stream. Moving onto quantifiable testing in the final set of experiments, the amount of dye adsorbed as a percentage of the total dye initially added to the process stream and the associated mass flow rate for the synthesis HKUST-1 was plotted on a double y-axis, for different synthesis times as shown in Figure 7.4. To calculate the total adsorbed dye as a percentage of the total added it is assumed that 50 % of the free dye diffuses across the hollow fibre filter so the total free dye is equal to twice the amount collected at the acceptor outlet (Equation 6), this is then subtracted from the starting total dye. (Equation 7) The equations can also be combined. (Equation 8)

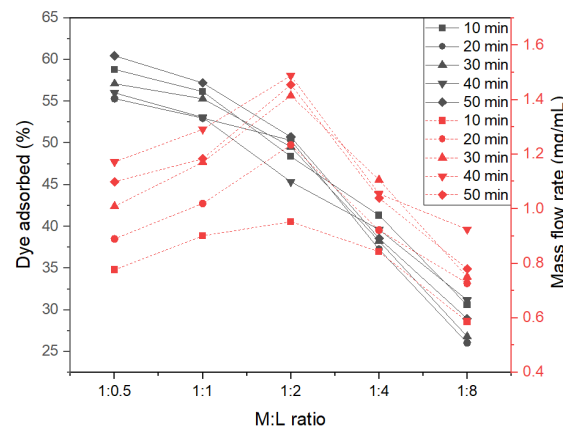


Figure 7.4: A) A double y-axis plot for the amount of dye adsorbed by continuously synthesised HKUST-1 (black) and the associated mass flow rate (red) at different synthesis times (10-50 minutes) when different M:L ratios are employed by adjusting initial flow rates.

Equation 7: Equation for the dye concentration before separation and hence the total free dye in a co-current arrangement ($C_{total\ free\ dye}$) assuming that equilibrium is reached and 50 % of the free dye diffuses across the membrane to the carrying acceptor stream.

Where $C_{acceptor}$ = the amount of dye in the acceptor stream outlet.

$$C_{total\ free\ dye} = 2C_{acceptor}$$

Equation 8: Equation for the percentage concentration of dye adsorbed onto the HKUST-1 surface ($C_{adsorbed}$). Where $C_{total\ dye}$ = The starting dye concentration after addition at the adsorption stage (M) and $C_{total\ free\ dye}$ = the total amount of dye in the process stream before separation (M).

$$\% C_{adsorbed\ dye} = \left(\frac{C_{total\ dye} - C_{total\ free\ dye}}{C_{total\ dye}} \right) \times 100$$

Equation 9: Combining equations 6 and 7 for the percentage concentration of adsorbed dye.

$$\%C_{adsorbed\ dye} = \left(1 - \frac{2C_{acceptor}}{C_{total\ dye}}\right) \times 100$$

Figure 7.3 shows that metal to ligand ratio had a big effect on dye adsorption and both M:L ratio and synthesis time affected the amount of product e.g., mass flow rate. As the M:L ratio was increased from 1:0.5 to 1:8 the amount of adsorbed dye reduced for all synthesis times tested. Meanwhile, the mass flow rates showed similar values and trends to those seen and discussed previously. As the synthesis time increased from 10 to 20 to 30 minutes an increase in the mass flow rate was observed for each synthesis time. When further increased, results were similar for 40 and 50 minutes. Across the ratios from 1:0.5 to 1:8, each continuous synthesis time showed the same trend; a small increase in mass flow rate was seen when the ratio was adjusted from 1:0.5 to 1:2 (M:L) followed by a steady decrease when adjusted to 1:4 and 1:8.

To put these results into context it is worth remembering some of the findings from chapter 4. I have previously determined (4.3.4) that across the parameter range tested (e.g. different synthesis times and reagent molar ratios) there are two crystalline products which typically form; a Cu-BTC complex which was determined by electron diffraction and HKUST-1, the target material, where the Cu-BTC complex is a layered intermediate product with partially formed SBUs containing Cu-O bonds, oriented such that HKUST-1 may easily form through simple bridging. This complex is more prevalent at high molar reagent ratios (e.g. 1:8, M:L) and lower continuous synthesis durations (e.g. 10-20 minutes). A full range of PXRD data was not collected for each individual synthetic time however, it is known that at a 1:2 M:L ratio for a 40 minute synthesis time, no evidence of the Cu-BTC complex was seen compared to a 20 minute synthesis which showed a mixed phase. This does not exclude the possibility that the complex is present but indicates its prevalence is low enough to be considered insignificant compared to HKUST-1.

When correlating this with the observed effect on dye absorbance, it implies that the Cu-BTC complex has a weaker ability to adsorb methylene blue from ethanolic solution than HKUST-1 as the least amount of adsorbed dye was calculated for higher molar ratios. There is also little difference in the amount of dye adsorbed for a 1:0.5 and 1:1 ratio aligning with PXRD (Figure 4.19B) which showed little to no difference in the pattern or crystallinity of the isolated material. This is expected when considering the structural difference between the 3D microporous HKUST-1 structure and 1D-layered Cu-BTC phase.¹⁶⁶ The 3D nature of HKUST-1 has ordered long range order pores which extend through the framework, providing a much larger

surface area for adsorption. It also has a higher Cu:BTC ratio (1:0.66) meaning there is more π - π bonding which increases the adsorption bonding at the surface.

When considering the effect of synthesis duration on dye adsorption, from the data presented, (Figure 7.4) it can be said that the amount of dye adsorbed is independent of the synthesis time within the range tested. Dye adsorbed remains within approximately 5 % range for the entire synthetic time range at each molar ratio tested but no observable trend can be seen. The results show that the mass flow rate does not have a noticeable effect on the amount of dye adsorbed despite earlier findings showing that the adsorption was dependent on yield. (5.3.8) This is possibly due to the range of mass flow rates with relation to the synthesis duration and M:L ratio is small or that the amount of the two crystalline species (HKUST-1 and Cu-BTC) within each sample, which have different adsorption abilities. For example it is known that time and molar ratio effect how much Cu-BTC:HKUST-1 is present within the sample, aside from knowing that Cu-BTC is less efficient at adsorbing dye, I do not have the full set of characterisation data for each run and therefore each data point cannot be fully explained.

From the work presented in this section I have shown that dye removal measurements are very different for different reaction conditions such as time and molar ratio of reagents. This is promising as a method for differentiating products in-line *via* 'application-led' analysis.

7.3.3 In-situ spectrometry: OceanOptics in-situ spectrometer

Following the successful integration of all components of the system: synthesis, adsorption and separation, an in-situ spectrometer was implemented to produce real time data as a final element to complete the system. By collecting in-line data, the performance of the synthesised product can be probed on its ability to adsorb dye and use it as a powerful quality assurance tool for production without the need for manually intensive off-line analysis. All experiments up to now have involved a collection of streams at the outlets followed by a manual measurement of the UV-Vis spectra using a benchtop spectrometer. The aim was to use an in-situ spectrometer, Ocean Optics FLAME-S-VIS-NIR-ES along with a halogen lamp and fibre optics for continuous collection of UV-Vis spectra in real time.

7.3.3.1 Integration and the complete set-up

The full set-up with all elements is shown in Figure 7.5. HKUST-1 reagents were delivered using syringe pumps (Figure 7.5.1), controlled by LabView software by a laptop (Figure 7.5.2), to a spool of fused silica capillary (Figure 7.5.3) as the continuous synthesis section of the setup. Following synthesis, MB was added to the process stream at an flow equal rate *via* a T-junction using a third syringe pump. (Figure 7.5.4) The new process stream, at a now doubled flow rate, was passed through PTFE tubing (Figure 7.5.5) to allow time for the dye to adsorb. The process stream then entered the Repligen device (Figure 7.5.7) along with a carrier stream of ethanol (Figure 7.5.6) in a co-flow arrangement with the process stream flowing through the outer annulus of the device. Free, unadsorbed dye remaining in solution was diffused across the hollow fibre filter membrane, equilibrating with the carrier stream, and the process stream is collected at the outlet of the device. The final section of the process set-up used a halogen lamp (Figure 7.5.8) with an attached fibre optic (Figure 7.5.9) directing light through a 3D printed flow cell (Figure 7.5.10, close up image is seen in Figure 7.6) with which the carrier stream outlet was passed through using PTFE tubing. A second fibre optic took the light to the in-situ spectrometer, Ocean Optics FLAME-S-VIS-NIR-ES (Figure 7.5.11) which delivered its data to the laptop (Figure 7.5.2) to present the absorbance spectra (UV-Vis) of the outlet carrier stream in OceanView software.

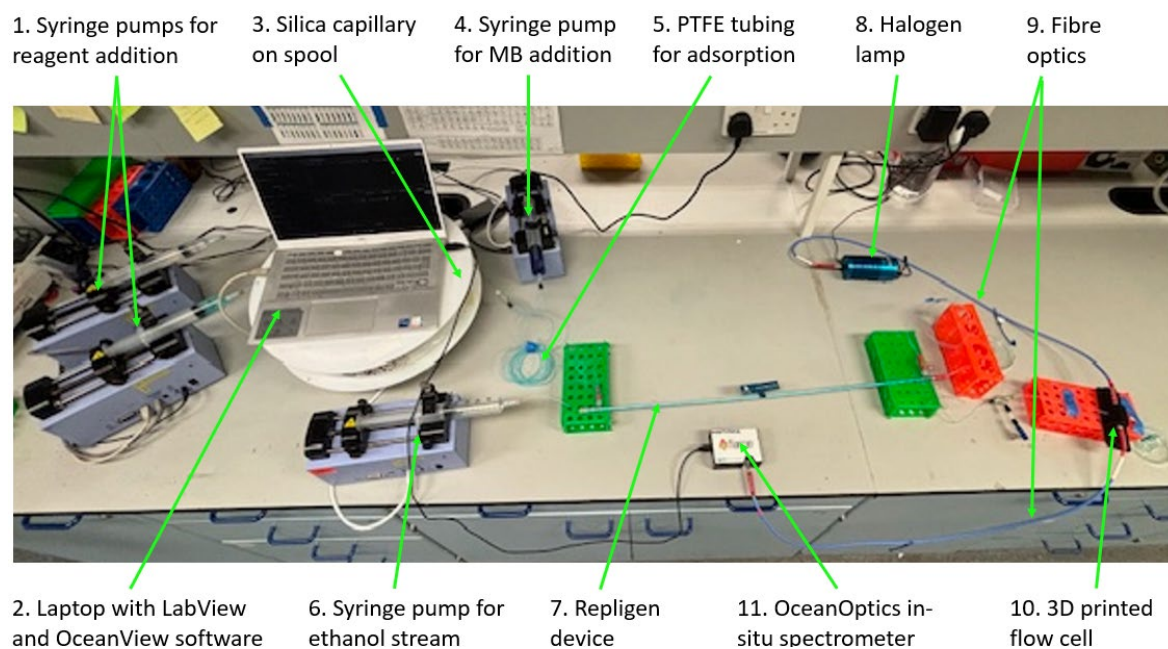


Figure 7.5: Image of the full set-up in operation including continuous synthesis, adsorption, separation and in-situ UV-Vis analysis.

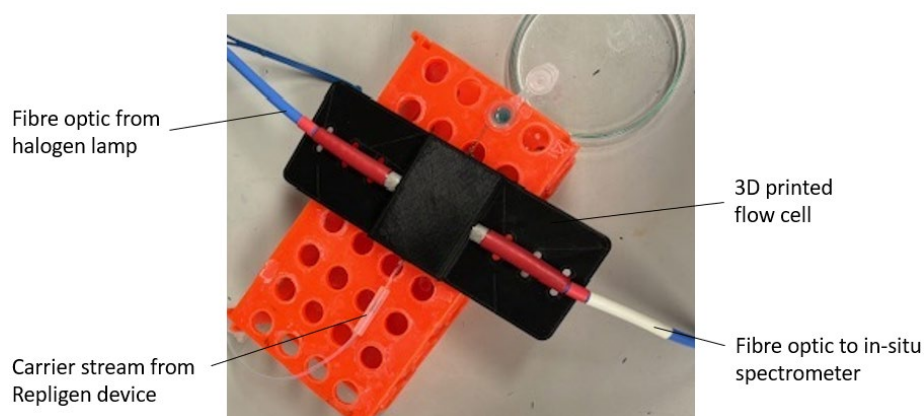


Figure 7.6: A close up of the 3D printed flow cell fabricated by Lyle Oswald.²⁰⁰

7.3.3.2 In-situ vs benchtop spectrometer

To ensure the spectrometer could give quantitative measurements it was first calibrated using the starting MB solution (0.01 mM, EtOH). A calibration curve was produced for the in-situ spectrometer using solutions made from sequential dilutions. The absorbance of each solution was recorded with both the in-line spectrometer and a standard benchtop spectrometer and plotted. (Figure 7.7)

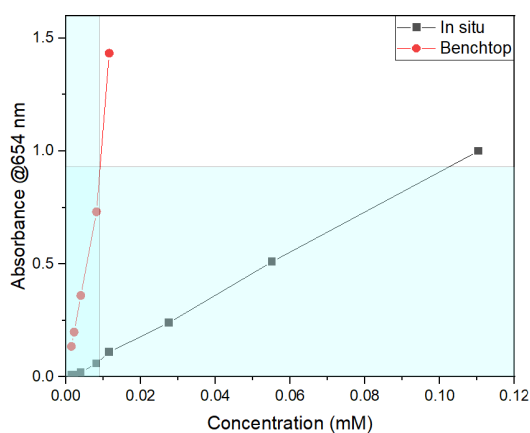


Figure 7.7: Calibration curves for a series of increasingly concentrated methylene blue solutions measured using a benchtop and in-situ spectrometer. The overlapping section of the blue boxes highlight the window of measurement used for all previous measurements with the benchtop spectrometer.

The gradients of linear trendlines with a (0,0) intercept, were calculated with an approximately 10-fold difference; 88.89 and 9.03 for the benchtop and in-situ spectrometer, respectively. This is due to the difference in path length between the two spectrometers (1 cm vs 1 mm), which has a great effect on the absorbance value in accordance with the Beer-Lambert law. (Equation 2)

Moreover, the blue area highlighted within Figure 7.7 shows how the area of measurement for the benchtop spectrometer observed in all previous experiments does not overlap well with the curve for the in-situ spectrometer, indicating that much higher concentrations of methylene blue would need to be initially added to the process stream to give UV-Vis spectra with observable differences in absorbance when the molar ratio of reagents was adjusted at the first stage of the set-up.

Previous findings discussed in this thesis (6.3.4.4 and 6.3.4.5) showed how the adsorption of methylene blue by HKUST-1 was independent of concentration (0.01 mM and 0.005 mM tested) where no difference in the amount of dye separated and hence, adsorbed was observed. Therefore, the starting concentration of methylene blue infused into the process stream was increased by ten times to 0.1 mM.

7.3.3.3 Real time in-situ UV-Vis data for changing molar reagent ratios

Using the integrated set-up shown in Figure 7.5 with a 40 minute synthesis and a 0.1 mM MB ethanolic solution, continuous UV-Vis data was collected in real time by the in-situ spectrometer as the acceptor outlet passed through the flow cell. This synthesis duration was chosen as it was shown to reliably produce phase pure HKUST-1 at low molar concentrations (1:0.5) and mixtures of HKUST-1 and Cu-BTC complex at higher concentrations (1:8) meaning a clear difference in dye adsorption would be observed for 'application-led' analysis. The absorbance at 654 nm (λ_{max}) was recorded over time while the molar ratio of the starting reagents for HKUST-1 were periodically adjusted approximately every 15 minutes. The absorbance value was doubled to indicate the amount of free dye in the process stream before separation and plotted over time. (Figure 7.8)

A stepwise and oscillation style approach was made to the system alterations. A stepwise approach was performed to test that the system was sensitive enough to show clear changes between the smallest system differences e.g. a 1:2 molar ratio of reagents and 1:1 molar ratio of reagents. And an oscillation was performed between the limits of the range tested to assess that the system can return to its initial input without a change in recorded values

Figure 7.8A shows the first plot of collected in-situ UV-Vis data for the fully integrated system. The transparent windows added to this plot were determined using tangent lines of each step and indicate the lengths of time taken between change which agree well with the 15 minute adjustments made except the 1:0.5 to 1:1 transition which took slightly longer (21:10, [mm:ss]) and is shown in orange. This is possibly due to user error. Real time UV-Vis graphs at 1:8, 1:2 and 1:0.5 ratios are shown inset within the graph. An initial molar concentration of 1:8 metal:ligand was employed, and reduced in a stepwise manner to 1:4, 1:2, 1:1 and 1:0.5 before being adjusted, again stepwise, up to 1:4. The ratio was not fully reversed back to 1:8 due to the reagent syringes running out of fluid however, all other repeated ratios had alike absorbance values.

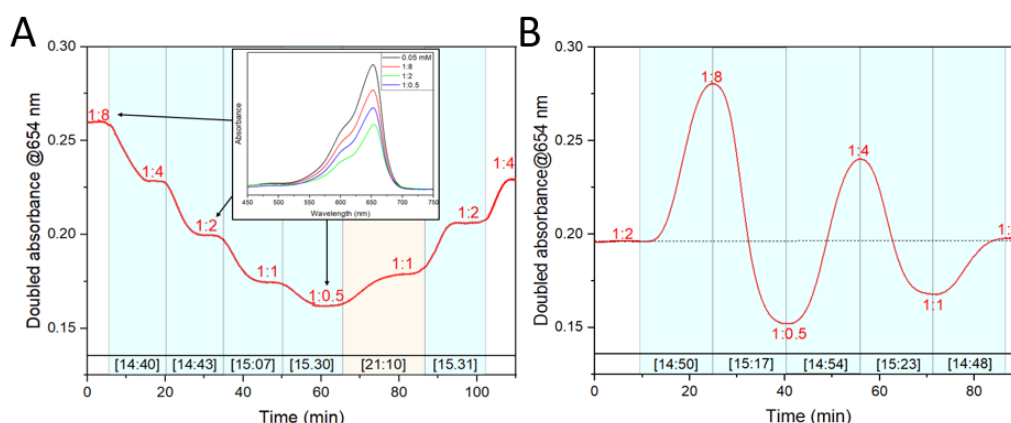


Figure 7.8: Plot showing the change in absorbance at 654 nm as the molar ratio of reagents was adjusted in a A) stepwise and B) oscillating manner at the start of the integrated system. Inlet plot shows the collected UV-Vis spectra against the starting concentration, 0.05mM (0.1 mM is infused at an equal flow rate for adsorption) at selected points and blue/orange windows indicate the time windows between adjustments e.g. the 15 minute periods of change between different molar ratios.

The data showed nice stepwise change in output with time scales aligning to those expected. The y-scale compares well to the previous results (7.3.2) with the absorbance values collected using a 1:0.5 ratio being half that collected when a 1:8 ratio was employed indicating double the amount of dye was adsorbed at the lower ratio (1:0.5). Furthermore, the reproducibility of the results is very good- on the repeated molar ratios absorbance values are within a maximum of 0.007 of each other. For example, when a 1:2 ratio was employed, 0.199 and 0.206 were collected as absorbance values and when a 1:4 ratio was employed absorbance values of 0.228 and 0.229 were collected.

A second experimental run looked at oscillating the graph by adjusting ratios to opposite molar ratios. (Figure 7.8B) Once again, transparent windows were added to indicate the time taken between system changes but this time they were determined by finding peak maxima/minima

points. This was successfully returned to a 1:2 molar ratio with the same double absorbance value. As with the previous experimental run (Figure 7.8A), the time scales aligned with the expected adjustments and the collected values agreed with all previous results. These sets of results indicate a highly effective method for in-line analysis to determine how well the MOF product is at adsorbing methylene blue.

As evidenced by the data presented in Figure 7.8, a clear change in the peak maxima is seen as the molar M:L ratio is adjusted. The trends agree with that previously seen when using the benchtop spectrometer with a 1:8 ratio giving the highest absorbance values ($62.85 \pm 3.42\%$ adsorbed), indicating less dye removal by the product while a 1:0.5 ratio gave the lowest absorbance values ($34.39 \pm 1.61\%$ adsorbed), indicating the greatest dye removal.

The concentration of free dye was calculated for each molar ratio for the data collected using the in-situ spectrometer, averaged with errors bars, and plotted against ex-situ data collected in a previous experiment (7.3.2) where a benchtop spectrometer was used. (Figure 7.9) The trend for both plots are the same with the in-situ data appearing smoother overall than the benchtop. This is possibly due to the delay between adsorption and analysis being diminished and reduction in manual handling. Both are key advantages to this set up. However, the in-situ spectrometer recorded a greater amount of dye being consistently adsorbed at each molar ratio with no overlap of error bars. A 40 minute synthesis was used in both cases along with the same reagent stock solutions for the synthesis phase of the system.

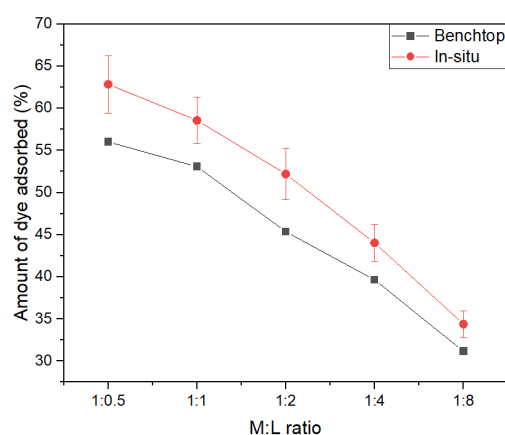


Figure 7.9: A plot showing the amount of dye adsorbed by HKUST-1 for different molar M:L ratios when a manual approach using a benchtop UV-Vis and an in-situ approach using an Ocean View FLAME spectrometer was employed within the system. Error bars represent the data collected in the experimental runs presented in Figure 7.8.

The two operational differences that could have potentially caused this relatively even increase in adsorption at all data points is the MB concentration which was doubled during the in-situ experiment or the spectrometer itself. Furthermore, the difference could be an indication of the system having a finite lifetime/improper cleaning. For example, the full system was cleaned after each experimental run but some product may have adhered and fouled the system or become embedded within the membrane surface of the hollow fibre filter as a result of repeated use, prompting more dye to be adsorbed and slightly elevated but trend-alike dye removal. Finally, there is potential that the calibration of the system from the initial setup is drifted slightly or the walls of the PTFE tubing are causing a drift of results.

Despite a difference between the two data sets, the trend is consistent and highlights how the system could be used to monitor changes in HKUST-1 synthesis. This is preliminary, indicative data and errors bars are produced from only two sets of data which is undesirable but it serves well as a proof of concept for expanding future work. With more time available, many experimental runs would have been performed to produce accurate, averaged data with error bars and explore the reaction parameter space to test the capabilities of the system.

7.4 Conclusions

In conclusion, this chapter successfully integrates the synthesis, adsorption, separation, and analysis components into a single, cohesive system. Initial challenges with commercially purchased Repligen devices, which failed to collect solids at the outlet when placed in a counter current configuration, were addressed by reconfiguration, this included purchasing a better device, swapping the fluid streams and changing to a co-current flow to enable the complete collection of synthesised HKUST-1 at the device's outlet and reliably separate 50 % of free dye into the acceptor stream.

The dye adsorption under varying reaction durations (10, 20, 30, 40, and 50 minutes) and molar metal-to-ligand ratios (1:0.5, 1:1, 1:2, 1:4, and 1:8) was studied. Results indicated lower mass flow rates at shorter synthesis times, stabilising after 30 minutes. Despite variations in mass flow rates, dye adsorption remained relatively consistent across the reaction durations at each molar ratio tested. The 1:0.5 ratio achieved the highest dye adsorption, while the 1:8 ratio resulted in almost half the adsorption (56.0 % and 31.2 % @40 min synthesis duration, respectively).

Characterisation of products at these ratios (isolated after different experiments and presented in Chapter 1, 4.3.4) revealed that a 1:8 M:L ratio with a 40-minute synthesis time yielded a highly crystalline, phase-pure HKUST-1. In contrast, a 1:0.5 ratio produced a mixed phase of HKUST-1

and Cu-BTC, an intermediate species in the HKUST-1 crystallisation mechanism. These findings suggest that HKUST-1 has superior adsorption capabilities compared to Cu-BTC complex, indicating that a 1:8 molar ratio with a 30-50 minute synthesis is necessary for optimal adsorption and yield.

Additionally, an in-situ spectrometer (Ocean Optics FLAME-S-VIS-NIR-ES) was integrated into the system to provide real-time data with quantifiable changes in absorbance for automated operation without manual intervention. Using a 40-minute synthesis, continuous data was collected while the molar ratio of reagents was periodically adjusted in a stepwise and oscillating manner. The temporal graphs of absorbance changes at the 654 nm peak correlated well with previously collected ex-situ data, though variations in determined values were consistently higher at each molar ratio tested. This discrepancy could be due to improper cleaning of the system between uses or differences in spectrometer sensitivity and light source.

The results shown in this chapter serve as a proof of concept that not only is an application-led analytical approach possible for the first time but has been successfully applied during the continuous synthesis of HKUST-1. This integrated system demonstrates a great online analysis method for determining how well a synthesised product is at adsorbing methylene blue. This has advantages with respect to quality assurance within continuous production and high throughput experimentation for example. Further exploration of the parameter space and experimental repeats could produce robust data, enabling informed parameter choices for achieving specific adsorption levels. Additionally, this novel set-up and method could determine unknown products in continuous synthetic lines based on their methylene blue adsorption capabilities, identifying species such as HKUST-1 or the Cu-BTC complex and their mixed phases.

Chapter 8 Application of 'print-pause-print' for new 3D printed chemical processing technology

In chapter 6, the print-pause-print 3D printing technique to embed membranes within 3D printed parts to create cross-flow filtration devices. At the time I found that achieving the desired internal architecture and ultimate end goal, it was not possible within a realistic time frame so I moved on to using commercial devices. However, this 3D printing work was continued in parallel. This chapter describes how I successfully developed a 3D printed cross-flow filtration device and subsequently utilised the 'print-pause-print' technique, honed during the development of the cross-flow filtration device development, to create other technologies for chemical processing.

In this chapter I extend both the standard and novel methods utilising pause functions mid-print to produce fully operational monolithic devices created without post-printing assembly and demonstrate the efficacy of the approach by making and testing three distinct devices: a cross-flow filtration device, which is shown to achieve near full dye removal from an aqueous stream with a residence time of 3.4 minutes; dead-end filters, which can be made in a range of sizes and are shown to fully remove micron-sized particles from a heterogenous mixture; and reactionware for the synthesis of MXenes using a semicontinuous approach which used PVDF filament and involved the incorporation of a stirrer bar and filter membrane. The range of devices showcased in this chapter highlight the versatility of the approach and its potential for use in chemical processing applications that require porous membranes.

The work discussed is the combination of two articles: one published in Reaction Chemistry and Engineering²⁰³ and the second submitted and under peer review to ChemComm in July 2024. Some work discussed within this chapter was undertaken by others: specifically, MXene batch synthesis was performed by Dr Nuno Bimbo and Tom Byrne, a research fellow and previous PhD candidate at the University of Southampton; NMR collection and fitting of the MXenes was performed by Dr Alice Oakley, a postdoctoral researcher with Dr Marinna Carravetta at the University of Southampton; SEM characterisation was performed with the help of Nikolay Zhelev, a specialist research technician within Electrochemistry at the University of Southampton. and the CT scanning of filters was performed by Dr Katy Rankin who works within the μ -vis X-Ray Imaging Centre at the University of Southampton.

8.1 Introduction

8.1.1.1 3D printing

Additive manufacturing, or three-dimensional (3D) printing is a fabrication process that can directly create complex and bespoke parts from computer-aided design (CAD) files.²⁰⁴ Typically used in manufacturing industries for rapid prototyping, it offers precise dimension control with high resolutions and has recently seen significant traction for fabricating fluidic devices²⁰⁵ with recent reports describing devices for synthesis,^{54,206} fluid mixing,²⁰⁷ dialysis,¹⁹³ and analysis.^{204,208} It's continuing development within the flow chemistry and microfluidic communities, is highlighted by various recent reviews on the topic.^{23,204,205,209–211}

Several different methods have been used to make fluidic devices including stereolithographic^{212–214} and polyjet^{215,216} printing, however fused deposition modelling (FDM) is highly attractive for its low cost, wide range of available materials, and the ease with which other elements (actuators, sensors etc.) can be incorporated to enable additional functionality and chemical compatibility of materials.²¹⁷ FDM printers create objects by extruding a thermoplastic through a nozzle moving in a two-dimensional plane, building up the 3D object layer by layer.

8.1.2 MXenes

MXenes are a new family of two-dimensional materials made of transition metal carbides and nitrides. They have shown great promise in many applications, including electrochemical energy storage, catalysis, electromagnetic shielding, and optoelectronics, as they have many desirable features such as high electrical conductivity, robust mechanical properties, and efficient absorption of electromagnetic waves.²¹⁸ MXenes are obtained from precursor MAX phases, (M = early transition metal, A = an A group, mostly a group 13 or 14 element and X = C or N), through the selective etching of the A group layers, which give nanosheet MXene structures with the general formula $M_{n+1}X_nT_z$ ($n = 1–3$, T_z = surface termination).²¹⁹ Etching is typically achieved using caustic fluoride-containing solutions such as hydrofluoric acid, hydrochloric acid and lithium fluoride mixtures, or ammonium bifluoride.²²⁰ However, the use of fluoride-based solutions is highly hazardous, requiring chemically inert process equipment and care during handling. Consequently, scale up is problematic²²¹ and if MXenes are to be used in a wide range of applications as predicted, industry-scale manufacturing strategies must be found.²²² Recently, synthetic methods that are environmentally friendly, safe, efficient, and scalable were identified as the number one challenge for MXene research over the next decade.²²²

Synthesising MXenes using fluoride-free methods has been reported,^{223–225} and other methods have been used, including electrochemical etching^{226–229} or synthesis in molten salts.²³⁰ The synthesis method that is employed significantly affects the resulting MXene, as the composition of the surface functional groups, which highly influence properties, are defined by the method used. Recent methods based on molten salts show that these can also be further modified and a larger range of surface groups, such as imido, sulfur, chlorine, selenium, bromine and tellurium, can be obtained.²³¹ There have also been recent reports of bottom-up synthesis strategies involving chemical vapour deposition,²³² which showed MXenes previously unattainable from MAX phase precursors. So far, all synthesis strategies have been done in batch and, despite some reports of scale-up, such as the one by Shuck et al²³³ where a large reactor was used to synthesise 50 g of MXene, no attempts have been reported of MXene etching using continuous methods.

Continuous processing has many advantages over batch synthesis, such as smaller equipment and space requirements, smaller reactor volumes and hence increased safety and improved space-time yields with lower variation of product quality, simpler process monitoring and control, easier scale-up, and higher productivity.²³⁴ As with much of the work discussed in this thesis, a main motivation is to improve and accelerate continuous production of functional materials. So far, using continuous methods in MXene synthesis has proven elusive, due to harsh operating conditions (HF or HF-forming chemicals) very long reaction times (24 or 48 hours typically for the synthesis of the most researched MXene, $\text{Ti}_3\text{C}_2\text{T}_z$), and handling of solids, which are significant hurdles in the transition from batch to continuous.

8.2 Experimental methods

8.2.1 Materials and methods

Clear polypropylene filament (2.85 mm cross section diameter, Ultimaker brand) was obtained from RS. Polyvinylidene difluoride (PVDF) filament (2.85 mm diameter, “FluorX”) was obtained from 3DXTECH. Membranes were purchased from Thermo Fisher (Whatman, mixed cellulose ester $\varnothing=20$ mm, 30 mm, 125 mm; Fisherbrand, mixed cellulose ester and nylon, $\varnothing=47$ mm); and VWR (Cytvia, nylon, $\varnothing=90$ mm). Where 40 mm membranes were used, these were manually cut from larger filters. PVDF filter membranes ($\varnothing=47$ mm, Millipore) were purchased from Sigma Aldrich and cut into smaller diameters manually ($\varnothing=23.5$ mm). $\text{Zn}(\text{NO}_3)_2 \cdot 6\text{H}_2\text{O}$ (98 %), 2-methyl imidazole (98 %), methylene blue, and ethanol were purchased from Sigma Aldrich. The precursor MAX phase (Ti_3AlC_3) was purchased from Laizhou Kai Kai Ceramic Materials Co., Ltd. Hydrochloric

acid (HCl, 12 M) was purchased from Fisher and lithium fluoride (99.99 %) was purchased from Sigma Aldrich.

ZIF-8 was synthesised from zinc nitrate and 2-methyl imidazole through a simple one pot synthesis at room temperature in deionised water over 48 hrs using a metal to ligand (M:L) molar ratio of 1:12, according to previous reports.²³⁵

8.2.2 Filtration devices

8.2.2.1 Device design and general fabrication protocol: Syringe filter and cross-flow filter

All devices were designed using a combination of AutoCAD (Autodesk) and SOLIDWORKS (Dassault) software. All designs included inlet/outlets that incorporated threads for standard ¼"-28 fittings so that they could be easily interfaced with external tubing. All designs featured a cavity for the membrane. The height of the cavity was 100 µm and the diameter was set to be 200 µm larger than that of the membrane. The 3D design files (.3mf) were prepared for printing using Cura (Ultimaker). They were printed using an Ultimaker 3 FDM printer in polypropylene (PP), with an Ultimaker adhesion sheet applied to the print bed to ensure adhesion. The default print parameters were as follows: layer height, 100 µm; infill, 100 %; print speed, 40 mm/s; flow rate, 110 %; fan speed, 0 %. Post-processing scripts were used in Cura to add a pause at a predefined point so that the membrane could be added. During this pause the membrane was inserted, with a small quantity of adhesive (UHU) lightly applied to the circumference to ensure it did not move when subsequent layers were printed. The next two layers after the print was resumed had altered print parameters (specified in the Cura software using the "ChangeatZ" function) to ensure the membrane was incorporated with a liquid-tight seal: a slower print speed (20 mm/s) and increased flow rate (150 %). After these two layers, all remaining print layers were printed with the original print speed and flowrate (40 mm/s and 110 % respectively) until completion. Using the general protocol, a series of syringe filters (Ø=20 mm, 30 mm, 40 mm) were fabricated using Whatman grade 1 membranes (mixed cellulose ester, pore size= 11 µm, Ø=20 mm, 30 mm, 125 mm) and Fisherbrand membranes (nylon, pore size= 0.45 µm, Ø= 47 mm). The cross-flow filtration device was fabricated incorporating Cytvia membranes (nylon, pore size= 0.2 µm, Ø= 90 mm). Dimensions of individual devices and any changes to this default protocol are described in the results section.

8.2.2.2 Syringe filter testing

Preformed ZIF-8 particles were dispersed in DI water (30 mg, 5 mL) by sonication to yield a cloudy suspension. It was transferred to a syringe with a Luer lock. The 3D printed syringe filter was fitted and the syringe contents passed through it. The quantity of ZIF-8 in the resulting fluid was assessed *via* light transmission measurements using a UV-2700 Shimadzu spectrophotometer.

8.2.2.3 Cross-flow filtration testing

A 0.01 mM methylene blue solution in water was made, collected in a syringe and loaded into a syringe pump. A syringe loaded with DI water was loaded into a second pump. The syringes were directly connected to the 3D printed device *via* PTFE tubing and 1/4"-28 fittings at opposing sides to give counter current flow above and below the membrane with outlet tubing directed to vials for fluid collection. A micrometering valve (IDEX, Micro-ming, P-445) was applied to the top outlet stream to apply a manually adjusted back pressure. Equal flow rates were applied from each syringe (25-2000 $\mu\text{L}/\text{min}$). The system was allowed to equilibrate after each flow rate change, then periodic collection of the outlet fluid was taken and analysed *via* UV-Vis absorption spectrometry (UV-2700, Shimadzu). The amount of dye removed from the process fluid and hence, the separator efficiency could then be quantified.

8.2.2.4 CT scanning

Micro-focus X-ray CT (μCT) scanning was used as a non-destructive analysis tool for volumetric assessment of the internal bond between the 3D printed housing and filter insert within a tested syringe filter. Using a 160 kVp Zeiss Xradia Versa 510 X-ray microscope CT scanner (Carl Zeiss Microscopy GmbH, Germany), the syringe filter was orientated in the sample holder assembly such that the inlet/outlet ports were perpendicular to the axis of rotation and positioned with a source-to-object distance of 25 mm and an object-to-detector distance of 150 mm. A two-stage scanning process was used to focus on the region of interest at the boundary between the 3D print and the edge of the filter material.

The x-ray conditions were set to 110 kVp peak voltage and 10 W power, and the imaging configuration used the 0.4X objective (binning 1) with a 6s exposure time; 3201 projection images were acquired throughout 360 degrees rotation. All associated parameters are summarised in the supplementary information. Projection data was reconstructed into TXM files using the Zeiss XM Reconstructor software (Carl Zeiss Microscopy GmbH, Germany). These were subsequently converted to 16-bit raw volumes for visualisation in ImageJ.

8.2.3 Semi-continuous reaction for MXene synthesis

8.2.3.1 Device design and fabrication: Semi-continuous etching reactionware for MAX phase

The device was designed using Solidworks (Dassault software) and then exported (.3mf format) into Cura (Ultimaker) to generate a g.code file for printing. The device included threaded inlet/outlet recesses to allow watertight connection using PTFE ¼"-28 flangeless fittings (Idex, Cole Parmer). All internal channels had a diameter of 1 mm. The device featured as an open cylindrical chamber subdivided by a recess for the membrane filter included within the design, at a height of 200 µm and a diameter of 23.7 mm (200 µm larger than the membrane diameter). Incorporation of the membrane partitions in the internal volume created a contained chamber (h= 6.97 mm, Ø= 19.2 mm, V= 1.98 mL) below it, where the MAX phase was loaded during etching.

The device was printed using an Ultimaker 3 in PVDF, with an Ultimaker adhesion sheet applied to the print bed. Print parameters were adapted from previous findings and were set as follows: layer height – 200 µm; infill - 60%; print speed – 20 mm/s; flow rate - 100%; fan speed - 0%; wall line count - 3; scaling - 115% (to account for shrinkage of the filament upon cooling); nozzle temperature – 260 °C. The print was paused after the membrane recess was formed to add the stirrer bar (12 mm) and the external membrane before resuming the print with the same settings and sealing the membrane in place. To ensure the membrane didn't move upon resumption, a small amount of all-purpose adhesive (UHU) was applied around the circumference.

8.2.3.2 Standard MXene batch synthesis and neutralisation

The batch sample was obtained using a procedure adapted from Ghidui *et. al.*²³⁶ 6 M of HCl was formulated by dilution from a stock solution of 12 M HCl. This was placed in a HF-resistant beaker under stirring and warmed to 40 °C. Lithium fluoride (1 g) was slowly added to the HCl solution. After 5 min, 1.0 g of Ti₃AlCl₂ was slowly added and the solution was stirred with a magnetic stirrer for 48 hr at 40 °C.

Once the reaction was stopped, the solution was decanted, mixed with deionised water and centrifuged at 5,000 rpm for 10 mins. The supernatant was removed, and the resulting sediment redispersed with deionised water. The procedure was repeated three times and the pH was confirmed to be close to neutral with universal indicator paper. The resulting sediment was then collected and left to dry in air for 24 hr.

8.2.3.3 Semi-continuous MXene synthesis and neutralisation in 3D printed reactionware

The MAX phase (Ti_3AlC_3 , 1.02 g) was loaded into the device as a slurry in DI water using a syringe. A 1:1 solution (50 mL) of lithium fluoride (1 g in 25 mL DI H_2O) and hydrochloric acid (12 M, 25 mL) was prepared and contained within a PTFE beaker. The etchant solution was supplied to the device using a peristaltic pump (Ismatec Reglo ISM834) fitted with Viton fluoroelastomer tubing (WZ-97629-18 Ismatec Pump Tubing, 3-Stop, Viton, $\text{Ø}=0.51$ mm). PTFE tubing was inserted into the Viton pump tubing to take the etchant to the device, being attached to the device using $\frac{1}{4}$ "-28 flangeless fittings. Similarly, the etchant exited the device and was carried back to the beaker reservoir using PTFE tubing attached with $\frac{1}{4}$ "-28 flangeless fittings. To ensure a leak-free seal, gaskets were added to the fittings and were made by punching Viton sheet. The etching solution was continuously flowed through the device for 48 hours at a flow rate of $114\ \mu\text{L}/\text{min}$ under stirring. A diagram of the setup can be found in Figure 8.1.

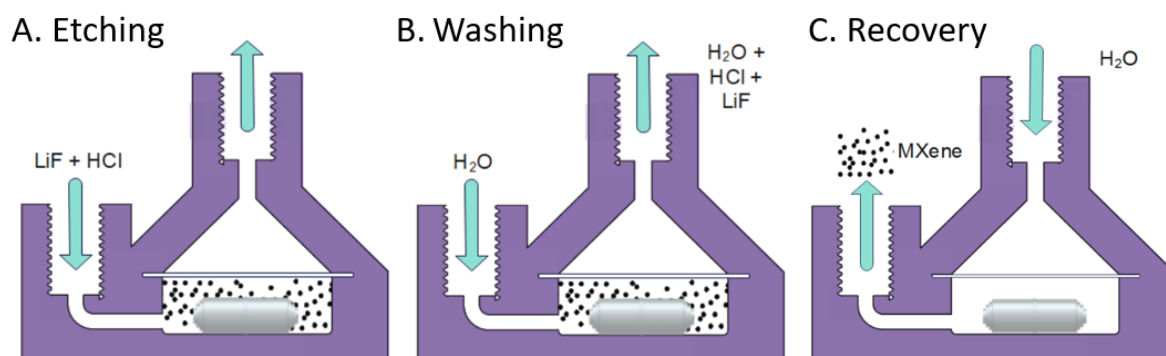


Figure 8.1: Cartoons showing how the reactor was used for etching (A), neutralisation (B) and MXene recovery (C).

Following the 48 hr etching procedure, neutralisation with water was required to remove the etchant and wash the product. The etching solution beaker was removed and replaced with a beaker of DI water to be flowed through the device ($114\ \mu\text{L}/\text{min}$) and a second empty beaker for collection at the outlet. The eluent's pH was monitored with universal indicator paper and neutralisation was established after 11 hrs (75.24 mL) with the flow rate of the wash being the limiting factor. (Figure 8.9) To collect the product the flow direction was reversed, as shown in Figure 8.1C. A syringe loaded with DI water was infused through the previous 'outlet' of the device whilst stirring to collect the product through the previous 'inlet'. The product was filtered and dried overnight in air ($25\ ^\circ\text{C}$).

8.2.3.4 Characterisation of samples

8.2.3.5 SEM

The scanning electron microscopy characterisation involved imaging the sample morphology using a Carl Zeiss Sigma 500 VP field emission electron microscope (FE-SEM), coupled with an Oxford Instruments Ultim Max 170 mm² energy dispersive X-ray spectroscopy detector (EDS) for studying the composition.

8.2.3.6 NMR

Samples were packed into 2.5 mm zirconium oxide rotors with Kel-F[®] caps and acquired at a spinning rate of 6 kHz for ²⁷Al spectra and 10 kHz for ¹H. ¹H and ²⁷Al spectra were acquired in double resonance mode on a Bruker Advance Neo 600 MHz wide bore spectrometer, using a 9.4 T field, in air. The chemical shift axes for the ²⁷Al and ¹H spectra were referenced using yttrium aluminium oxide (YAlO) (0 ppm) and adamantane (1.83 ppm) respectively. Fitting of the ¹H spectra was carried out using a dedicated MATLAB script.

Table 8.1: NMR peak fitting for the ¹H SS NMR for the batch sample.

Amplitude	Position / ppm	Line Width/ ppm	Ratio
4.548	8.082	1.469	0.370
3.571	6.100	0.909	0.280
19.980	5.134	0.743	0.881

Table 8.2: NMR peak fitting for the ¹H SS NMR for the continuous sample.

Region	Binding energy (eV)	FWHM	Fraction
10.730	9.000	29.857	0.0153
2.124	8.423	2.008	9.03E ⁻⁰⁷
5.170	5.800	1.298	0.114
21.887	4.662	0.902	0.786
2.370	2.497	1.595	0.001
0.164	0.499	0.399	0.940

8.3 Results and Discussion

8.3.1 Cross-flow filtration device

In Chapter 6, I found that during testing of FDM fabricated cross-flow filtration devices, liquid would follow the channel architecture above the membrane filter but gather and cause swelling of the part below the membrane. This was evidence a conformal bond can be made between the filament and membrane when it is directly extruded onto its surface. A novel technique was developed to produce 3D printed cross filtration devices that gave a good seal through direct printing onto both sides of the membrane by embedding one part within a receptacle cavity of another.

As was the case for the device described in Chapter 6, this was achieved in a process shown in Figure 8.2, which involved two separate printing phases corresponding to the part areas shown in orange and blue.

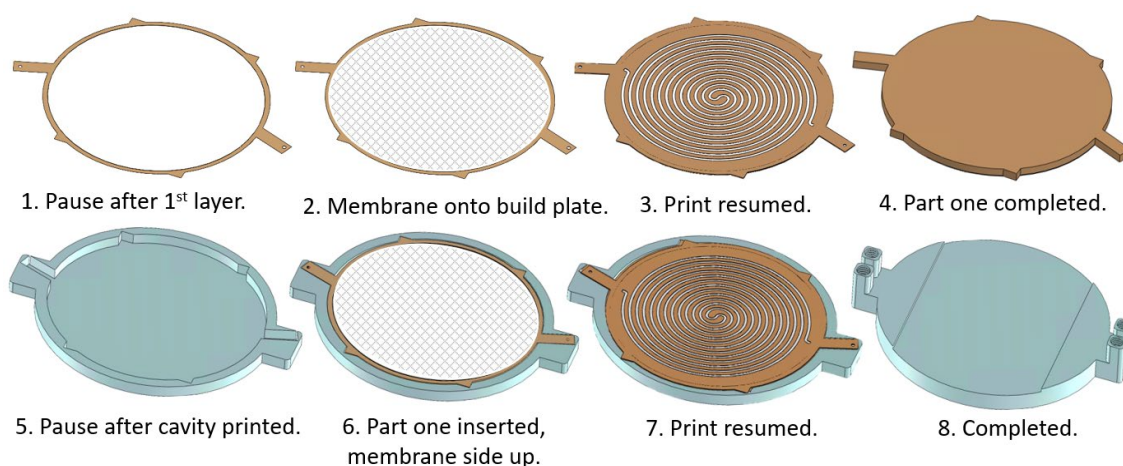


Figure 8.2: Process flow showing the 8-stage process to produce the final device where the first printed part (orange) was embedded within the second printed part (blue).

The first phase started by printing an outline onto the print bed representing the membrane filter cavity (Figure 8.2.1). A pause after this first layer meant the membrane filter could be placed on the print bed (Figure 8.2.2) with a very small amount of a weak adhesive applied at the circumference to ensure it didn't move in the subsequent step. The print was resumed and a channel design directly patterned on the membrane surface (Figure 8.2.3) with additional layers sealing the channels (Figure 8.2.4). This part, which represented the channel network on one side of the membrane, was removed from the print bed and the second phase commenced by printing a hollow receptacle (Figure 8.2.5, blue) for the first part. Part one (orange) was placed within the receptacle (Figure 8.2.6) with the exposed membrane surface facing upwards and the print

resumed. The channel design was once again printed directly onto the exposed surface (Figure 8.2.7) until full encapsulation and completion of the print (Figure 8.2.8) to yield the finished device. (Figure 8.3A-C)

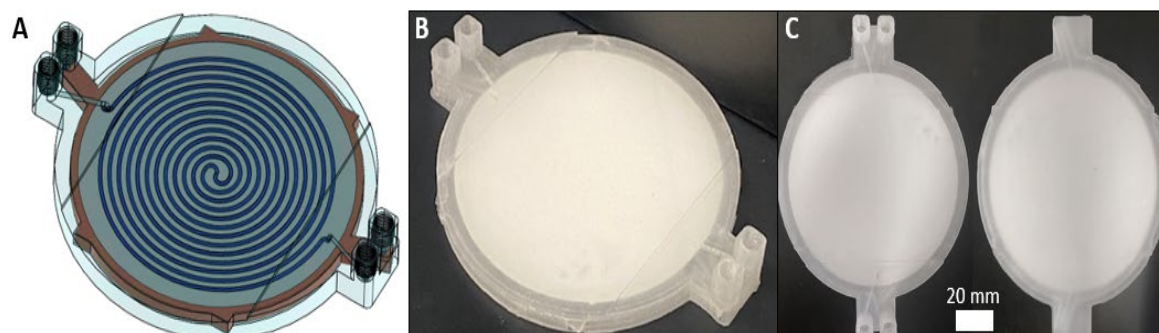


Figure 8.3: A) 3D computer generated image showing the final device with the membrane and channels above the membrane visible. B) Corresponding image of the fabricated device. C) Views of the device from above and below.

To achieve accurate printing, a height for the first part (Figure 8.2.4) and receptacle depth (Figure 8.2.5) of 3.9 mm and 4.0 mm, respectively were used, while the x,y-dimensions of both the first component and receptacle void were identical as determined in Chapter 6. The channels above and below the membrane had an identical concentric pattern (length= 1042.9 mm) but differed slightly in cross-section. The channels above the membrane were slightly wider (1.24 mm vs 1.0 mm) to allow for alignment imperfections. In both cases the channel height was the same (500 μm).

In testing it was found that the backpressure in the channels printed above the membrane were greater than those below the membrane which was determined by observations whereby, fluid was only exiting the hardware from the top cavity and did not pass through the bottom. This was likely due to the over-extrusion to seal the membrane reducing channel dimensions, which resulted in net fluid transport across the membrane. Hence a backpressure was applied at the outlet of the lower channel to compensate. This increase in pressure however had the unexpected effect of causing the device to expand below the membrane, causing separation of the membrane from the structures below it as seen in chapter 6. Consequently, fluid was free to travel along the most direct path from inlet to outlet rather than through the patterned channels, resulting in low residence times and poor dye removal. The expansion of the device below the membrane, with no expansion observed above, is consistent with the observation that while hot filament extruded directly onto the membrane gave a conformal bond, there will be no such bond when the membrane is merely placed on top of a pre-existing printed structure.

To test the device, an aqueous solution of the organic dye methylene blue (0.01 mM) was flowed through the donor channel and deionised water through the bottom channel of the device in a counter current arrangement at varying flow rates (25-2000 $\mu\text{L}/\text{min}$ for each fluid) corresponding to residence times of 0.25 to 20.30 minutes. A micrometering valve was used at the outlet of the top channel cavity and manually tuned to ensure equal flow rates at the device outlets. Both the donor and acceptor fluid were collected at the outlet and analysed *via* UV-Vis absorbance spectroscopy to determine dye concentration.

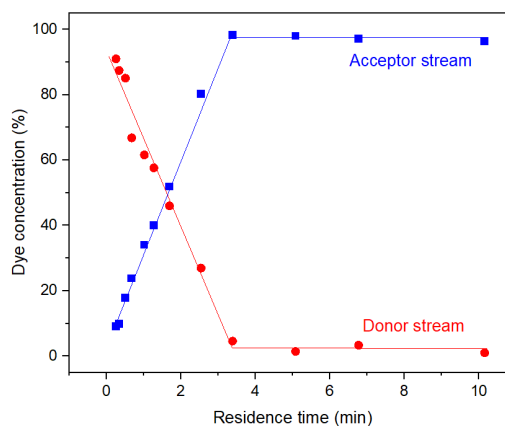


Figure 8.4: Experimental data for the removal of methylene blue from an aqueous flow (0.01 mM) using the cross-flow filtration device.

The device performed as expected: as the residence time was increased (0.25-2.54 mins) there was a steep linear increase in dye removal before plateauing after 3.42 min at near full dye removal (98.2 %). (Figure 8.4) The diffusion coefficient for methylene blue has been reported as $6.74 \times 10^{-6} \text{ cm}^2/\text{s}$ in water.¹⁹⁶ Using this value, and the nominal channel dimensions, a theoretical residence time for 100 % removal was calculated as 3.09 minutes – in good agreement with the experimental findings. Beyond this point, dye removal varied slightly around 98.2 % and not achieving 100 % removal, highlighting the difference of experimental to theoretical values and likely a result of the random motion of dye molecules, a characteristic assumed negligible within Fick's law.

The results show the cross-flow filtration device to be highly effective, and did not encounter any of the problems experienced in the earlier prototypes, even at the highest flow rates. This is consistent with the successful bond between the membrane and the device body using the novel double-sided printing approach. While this was successful, it came too late for the integrated system described in chapter 7 and would have required further testing and optimisation once the process stream containing MOF crystals was used also. Furthermore, considering the findings shown in chapter 7, (7.3.1) it is not known if net transmembrane flow was occurring internally

during the counter-current arrangement making the results seemingly brilliant. Without this knowledge, it can be concluded that the device is likely good for co-current separation or low flow rates with low back pressure. Finally, there is large scope for customisability, both in terms of the 3D printed structure but also the membrane material and size.

8.3.2 Syringe filter

The simplest possible filtration device is a dead-end filter, where the fluid is driven through a filter membrane. Syringe filters – dead-end filters that can be attached to syringes *via* a Luer adaptor – were fabricated as shown in Figure 8.5. The filter design (Figure 8.5A) is shown in the orientation it was printed, with accompanying cross sections showing the fluidic channels (dark blue, height = 500 μm) immediately above and below the membrane. To ensure a watertight seal on the membrane after it was inserted, plastic was extruded with an increased flow rate (ensuring no gaps between the membrane and the 3D printed monolith) and a reduced print speed (ensuring the lateral movement of the printhead did not displace the membrane) as shown inset in Figure 8.5A. A final printed filter using a 30 mm diameter membrane is shown in Figure 8.5B with the incorporated Luer lock feature ensuring an easy leak-free fit to a Luer-tipped syringe.

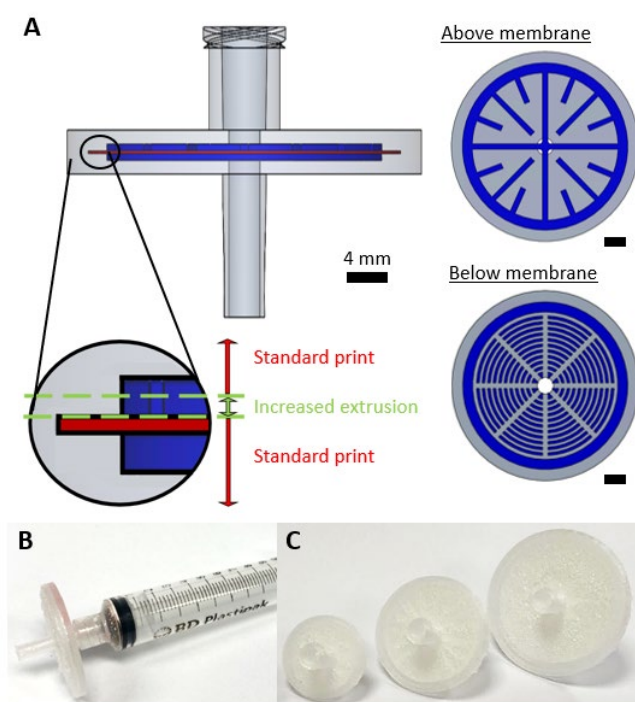


Figure 8.5: A) Computer generated images showing the internal geometry of the syringe filter. The red area represents the membrane cavity, while blue areas represent the channel system above and below the membrane. All scale bars represent 4 mm. B) Image of a finished syringe filter (30 mm) attached to a syringe *via* Luer lock. C) Images of syringe filters of different size ($\varnothing_{\text{mem}} = 20, 30, \text{ and } 40 \text{ mm}$)

The same protocol can be used to make various filters with different membrane materials (e.g. cellulose, mixed cellulose esters, nylon) and sizes (e.g. 20 mm, 30 mm, 40 mm, Figure 8.7C) demonstrating the versatility of the approach.

To show the efficacy of the syringe filter, it was used to separate a heterogeneous dispersion of ZIF-8 crystals in water which featured particle sizes of 0.3 to 15.0 μm . (Figure 8.5A) While the starting dispersion (Figure 8.5B left) was a cloudy white mixture, the resulting filtrate was optically clear (Figure 8.5B right) indicating the solid material had been successfully removed. This was confirmed by examining each solution by spectrophotometry. (Figure 8.5C) The cloudy dispersion prior to filtration reduced light transmission at low wavelengths due to scattering, while the filtrate showed no scattering effects - indicating good removal by the syringe filter in a single pass.

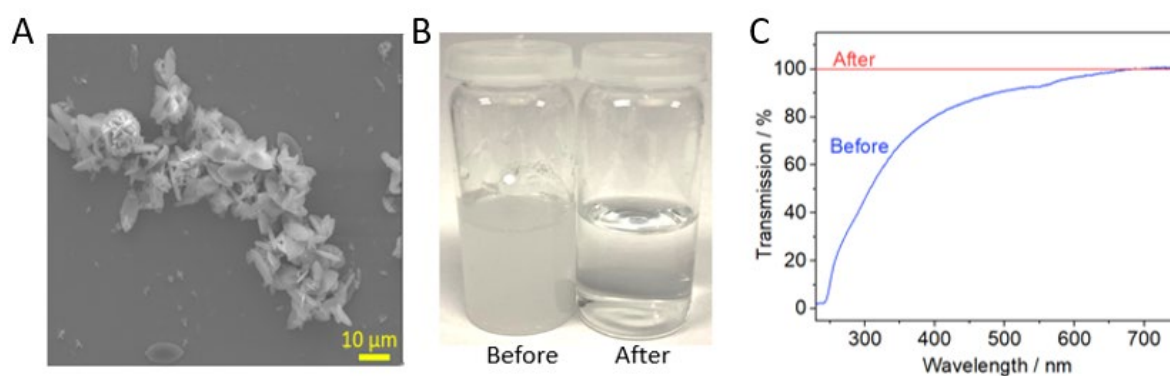


Figure 8.6: A) SEM image of the metal organic framework particles within the sample that was filtered. B) Images of the suspension before and after a single pass through the 3D printed syringe filter. C) The corresponding optical transmission spectra.

Anecdotally, and as previously mentioned, plastic extruded directly onto the membrane forms a close conformal bond such that, upon cooling, the membrane is physically attached to the extruded plastic, as previously reported,²³⁷ and that this bond did not notably differ with membrane material. To investigate the observed bond between the extruded material and membrane fibre, a CT scan of a syringe filter was done to image the bond cross-sectionally. (Figure 8.7)

The fibrous structure of the membrane can be clearly seen bonded to only one side of the device recess with a uniform and complete bond (Figure 8.7B) that is still intact after use. At the plastic/membrane interface, membrane fibres can be seen penetrating the plastic over a few

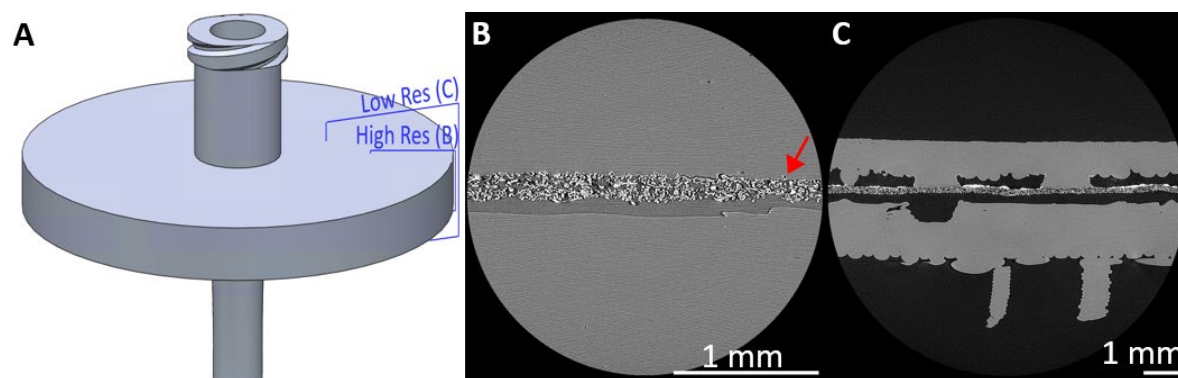


Figure 8.7: A) CAD diagram with planes showing where CT images were taken from; B) high resolution and C) low resolution CT scan showing the membrane conformally bonded to the extruded plastic on one side. The red arrow indicates a singular membrane fibre having been incorporated within the plastic.

microns (Figure 8.7B, red arrow) and solid deposits of MOF leftover from use (Figure 8.7C, white material above the membrane) confirms the membrane remained adhered, evidence of a strong bond. A slight bowing of the membrane between the polypropylene contact points due to shrinkage is evidence of a firm adherence by the membrane. Furthermore, these results preclude the idea that the membrane material is melted during extrusion.

3D printed syringe filters have been previously reported using stereolithographic & inkjet 3D printing,^{238,239} but this is the first 3D printed design printed from a single monolithic structure, meaning no manual assembly and hence fewer potential failure points. Printing on both sides of the membrane filter is not needed in this case as filtrate passes through the membrane but through CT scanning the hypothesised conformal bond between filament and membrane has been proven.

8.3.3 Reactionware: Semi-continuous etching of MAX phase

Motivated by the lack of scalable MXene production methods, a piece of reactionware was developed for a hybrid semi-continuous approach to their synthesis utilising the PPP approach within FDM printing, whereby etchant was continuously flowed through a volume containing an agitated suspension of MAX phase. While this did not allow continuous production of MXene, the continuous flow of etchant meant that HF could be generated in-line (by combining acid and fluoride sources) and then autonomously neutralised in-line, reducing manual handling risks associated with MXene synthesis.

To make the flow reactor, FDM printing was used with a highly inert fluoropolymer, polyvinylidene difluoride (PVDF), compatible with HF-based etchants. While there are many previous reports of 3D printed reactor vessels, this is the first with PVDF to allow use of such aggressive reagents. PVDF filter membranes were incorporated using the PPP method, ensuring the MAX phase remained within the reactor and was not carried out by the etchant flow, as well as a stirrer bar to ensure constant agitation.

During fabrication, it was observed that PVDF experienced a large degree of shrinkage during cooling which caused several difficulties for a successful print. This meant that the print parameters required were much different to previously reported 3D printed microfluidics and what was necessary for the syringe filter and cross-flow filtration device which used PP filament. Firstly, $\frac{1}{4}$ "-28 fittings did not fit the printed thread which was resolved by scaling the print 115% in the Cura software. There were also issues with adhesion of the device to the print bed which were alleviated by reducing the infill density to 60%. Finally, the shrinkage partnered with the molten filament (260 °C) caused warping of the membrane after the print was resumed. This was resolved by using a light adhesive around the membrane circumference and maximising the shelf size of the membrane recess. When designing the device, the aim was to keep the volume for the etching chamber to a minimum to promote complete etching, improve yield, and increase safety.

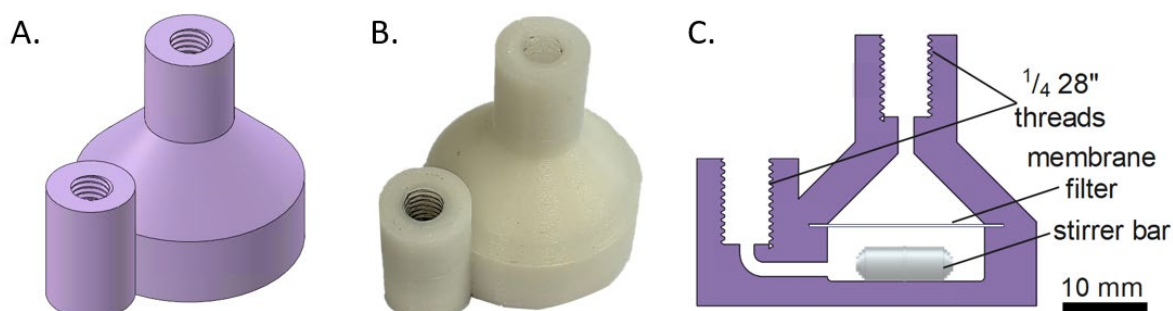


Figure 8.8: A) CAD image of the reactor. B) Corresponding image once fabricated. C) Cross section showing internal geometry and parts.

The device operated as shown in the experimental section. (Figure 8.1) The MAX phase (1 g) was made into a suspension and then loaded into the reactor using a syringe. Etchant was then continuously supplied over 48 hours, followed by neutralisation *via* elution (Figure 8.9) and then recovery by backflowing with water. For the continuous sample, a yield of 671 mg (66.9 %) was retrieved over a 40 minute collection. Losses can be accounted for from initial loading of the MAX phase into the device in the syringe and when filtering the retrieved slurry post-etching. In addition, due to the nanostructure of MXenes, it is possible some smaller MXene particles may have passed through the membrane filter which had a pore size of 0.1 μm .

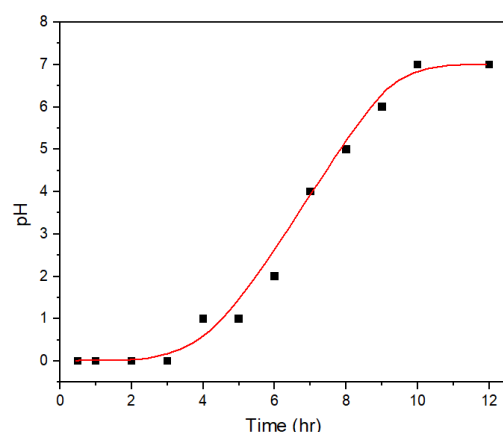


Figure 8.9: A pH vs time graph for the recorded pH at the 3D printed reactionware outlet during the neutralisation stage of the semi-continuous synthesis of MXenes measured using universal indicator paper.

For comparison, an equivalent batch synthesis was performed using the same quantities and concentrations of reagents, the same reaction time, but continuously stirred in a PTFE beaker, and then neutralised by repeated centrifugation, supernatant removal, and resuspension steps.

8.3.3.1 MXene characterisation

To show successful etching of $\text{Ti}_3\text{C}_2\text{T}_z$ and to characterise the surface functional groups, different characterisation methods were applied to both the batch and continuous samples, namely powder X-ray diffraction (PXRD), scanning electron microscopy (SEM) coupled with elemental analysis from energy dispersive spectroscopy (EDS) and solid-state nuclear magnetic resonance (SS-NMR). The aim was to compare the samples, especially successful etching, impurities present, and surface functional group composition.

8.3.3.1.1 PXRD

Powder X-ray diffraction (PXRD) results, shown in Figure 8.10A and B, confirmed that both methods successfully produced crystalline $\text{Ti}_3\text{C}_2\text{T}_z$ with the diffraction pattern matching those previously reported.^{240–242} The characteristic MAX phase (002) peak at 9.5° is almost imperceptible, indicating almost complete removal of the starting material. The higher angle MAX phase peaks are also significantly reduced in size but still present indicating some left-over or unetched MAX phase.

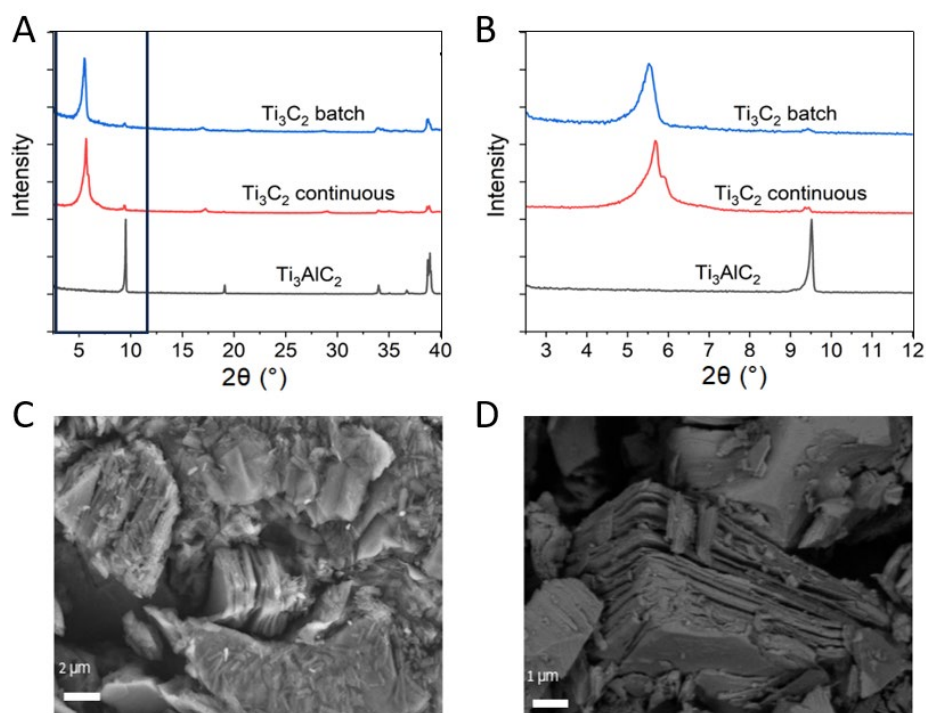


Figure 8.10: PXRD spectra for the precursor MAX phase, the batch sample, and the continuous sample: A) shows 2θ angles up to 40° , while B) shows the 2θ angles up to 12° . C) and D) show SEM images for the batch and continuous samples, respectively. Both images feature the layered morphology of etched $\text{Ti}_3\text{C}_2\text{T}_x$.

Other impurities such as LiF are not present due to peak absences at 39° showing that the neutralisation and washing steps were successful. Comparing the differences between the two MXene products, the flow sample shows better defined peaks compared to the batch sample, most notably the (002) peak located between 5 and 6° . (Figure 8.10B) This peak has a position difference of 0.58° for the two methods - indicative of different interlayer spacings for the 2D nanosheets structures, and probably caused by the re-arrangement of hydrogen-bonded guests such as water molecules between the layers.²⁴³

Scanning electron microscopy (SEM) of the products (Figure 8.10C and D) showed successful exfoliation of the MAX phase, with both samples showing accordion-like structures with clear separation of individual layers, matching those seen in literature.²²⁰ Elemental analysis *via* energy dispersive X-ray spectroscopy (EDS) showed low atomic weight of Al for both samples. This was notably lower for the continuous sample (0.21 %) compared to the batch sample (3.86 %), indicating that better exfoliation and/or washing had occurred. These results were further confirmed by solid-state NMR.

8.3.3.1.2 Nuclear Magnetic Resonance (NMR)

^{27}Al and ^1H solid-state NMR was used to further characterise the MXene surface.²⁴⁴ ^{27}Al solid-state NMR results (Figure 8.11A) confirmed EDS results, with no Al present in the flow-produced sample, but some Al present in the batch sample. The ^1H spectra shown in Figure 8.11B and the corresponding fits (Table 8.1 and 8.2) show that the spectra was dominated by peaks at 5.13 ppm (for the batch sample) and 4.66 ppm (for the continuous sample), indicative of water.^{242,244} The absence of significant peaks above 10 ppm suggest a small proportion of -OH surface functional groups in both samples, consistent with previous results.^{245,246}

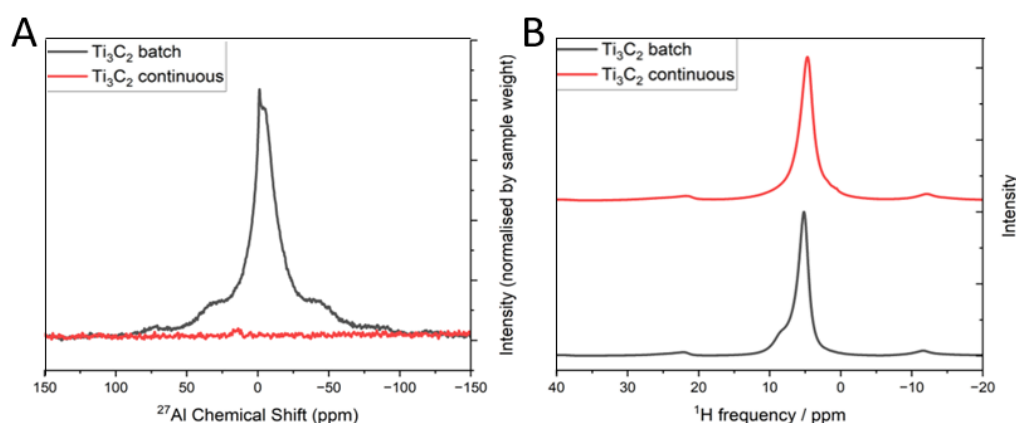


Figure 8.11: A) ^{27}Al and B) ^1H SS NMR Solid-state NMR on the batch and continuous $\text{Ti}_3\text{C}_2\text{T}_x$ MXene samples.

The multiple tools used to characterise the batch and continuous samples show that, for both cases, Ti_3AlC_2 has been successfully etched to yield crystalline $\text{Ti}_3\text{C}_2\text{T}_x$ with morphology and surface properties in keeping with previous literature reports.^{240–242} While all analyses show that no Al is present in the flow-etched sample, which indicates successful etching and washing of the sample, the standard batch sample still contained small levels of Al due to either incomplete etching and/or washing. The reason for this is unknown at present but may be due to better mixing in the printed reactor, something that could be further optimised in subsequent designs e.g., introduction of baffles – taking advantage of the versatility of 3D printing to create almost arbitrary structures.

The successful etching of $\text{Ti}_3\text{C}_2\text{T}_x$ presented in the above results is, to my knowledge, the first obtained using flow methods. It should be noted that there was much less manual handling of the etchant, in particular during the neutralisation stage, which makes for an overall safer production method. Here the etchant was recycled for ease, however safety of the setup could be enhanced by formulating the etchant in-line, by introducing the LiF and HCl separately so that HF is only

generated in the reactor, and immediately neutralising the etchant in-line after contacting with the MAX phase.

8.4 Conclusions

In conclusion, the incorporation of commercial porous membranes into FDM 3D printed fluidic devices using the print-pause-print technique to make functional separation devices and reactionware has been shown. This is the first time that fully-functional membrane-containing devices have been fabricated using 3D printing without needing subsequent post-printing assembly.

Furthermore, the semi-continuous etching of a MAX phase (Ti_3AlC_3) using a bespoke device produced *via* 3D printing has been successfully demonstrated. To my knowledge, this is also the first time that PVDF has been used in 3D-printed reaction vessels, and hence can be used for highly aggressive reagents such as the HF-containing etchant used here. This continuous approach reduces manual intervention and risk associated with typical MXene synthesis, enables easier neutralisation, outputs a product with less impurities and allows for easier standardisation of the synthesis with less room for errors. The versatility of this approach is shown by the fact that three distinct devices, with three different functionalities have been shown and that these can be arbitrarily customised and tailored depending on end user requirements. This could involve optimising mixing, incorporating other functionalities or scaling up potential into larger processes. Furthermore, a new approach to print on both sides of the membrane for instances where it is important that printed structures are firmly attached to both sides of the membrane has also been demonstrated.

Chapter 9 Conclusions and future outlook

9.1 Summary

Review of the literature within chapter 2 discussed how continuous production of MOFs is becoming more prevalent due to its inherent advantages including high productivity, quality assurance and precise multivariate control and how the application of in-situ analysis within batch-style procedures has also become a key field of interest in studying their crystallisation pathways. However, there is currently little crossover between the two e.g. in-situ analysis of MOFs during continuous production which prompted this novel 'application-led' approach. This is due to standard MOF characterisation methods not being suitable for implementation in line and of those that are, the current in-situ methods being mostly inaccessible to the general chemist e.g. synchrotron XRD.

In chapter 3 an initial approach was formulated to produce a fully integrated system from synthesis to online analysis. In chapters 4 to 6 this setup was broken down and each stage was looked at individually. chapter 4 successfully determined a flow synthesis procedure for HKUST-1 in a purely ethanol solvent at room temperature with a fused-silica capillary as a reaction vessel. The synthesis time, concentration and various molar ratio of reagents were investigated also. The adsorption capabilities of HKUST-1 with organic dye, methylene blue was then explored in chapter 5 both in batch and in flow, looking at the effect had when parameters for MOF synthesis were adjusted. Chapter 6 looked at the separation element to the integrated set-up. Attempts to produce cross-flow filtration devices using FDM printing showed good promise and were later explored but, despite attempts, the best obtained results were achieved using commercially purchased devices. Finally, the different aspects of the system were integrated in chapter 7 and an in-situ spectrometer for UV-Vis in-line analysis was added as the final component to produce a complete system and meet the initial aims of this work. Further work that explored the versatility of the PPP approach with FDM fabrication culminated in a published work and submitted paper for chapter 8.

The work presented in this thesis describes an established set-up that can quantifiably assess a products ability to adsorb organic molecules during continuous synthesis. Not only does this prove the concept of 'application-led' analysis for the first time, but it helps to bridge the gap within future MOF production. By producing MOFs in flow while gathering in-situ analytical data on their adsorption ability this setup can act as a quality assurance tool for high throughput experimentation.

Further exploration of the versatile PPP approach within FDM printing led to a publications and a second submitted paper. Within these, the fabrication of monolithic dead-end syringe filters, reactionware for semi-continuous MXene synthesis and, through a novel fabrication procedure that allowed bonding between extruded filament and membrane surfaces on both sides, a cross-flow filtration device, all for the first time. Observations and CT scanning revealed how filament extruded directly onto a membrane surface gives a conformal bond.

9.2 Future work

The developed setup provides a quantitative assessment of a continuously produced product's adsorptive abilities for organic molecules, thereby bridging the gap between laboratory and industrial high-throughput production of metal-organic frameworks (MOFs) with quality assurance. The future potential of this system and its underlying concept is extensive.

Given more time, additional experimental runs would ideally be conducted to generate accurate data with error bars and demonstrate reproducibility. Further exploration of reaction parameters, such as the addition of heat during synthesis and the use of different reaction solvents, would be beneficial to expand the dataset for HKUST-1 adsorption of methylene blue. Implementing alternative frameworks, previously identified as effective organic dye adsorbents, within the system could enhance its versatility. For instance, ZIF-8 could be investigated for Rhodamine B removal, and MIL frameworks -53(Al) and -101(Cr) for methyl orange removal.

The system's application is not limited to adsorption. Other potential MOF applications, such as sensing, luminescent marking, or catalysis, could be integrated in-line and analysed via UV-Vis or other techniques previously applied in-situ using benchtop spectrometers. These applications could be quantified using methods such as fluorescence, UV-Vis, Raman, NMR, or IR spectroscopy.

Prolonged runs to test the system's durability and scalability would be advantageous. To enhance longevity, larger syringes would need to be acquired. For scalability, increasing concentrations to achieve higher outputs should be explored. Adjustments to the setup, such as changing the dimensions of the system (e.g., internal diameters or lengths) or modifying system parameters like reagent concentrations and flow rates, would influence mass flow rates and the efficiency of dye removal.

Compactness is another consideration for improving the system, as the current setup occupies significant bench space. This could be achieved by using microfluidic (MF) glass chips as the

synthetic vessel instead of spooled fused silica capillaries or by employing cross-flow filtration devices, as detailed in Chapter 8.

Further efficiency of the system could be developed by exploring the addition of self optimisation algorithms to autonomise the system. Using an AI-guided approach, high volumes of data can be extracted and collated into a knowledge-base and employed by the algorithm to facilitate process control and achieve user-defined output (e.g. product optimisation, yield, crystal size), further reducing user input and labour for an overall improved outcome. From an industrial perspective, the work presented here would be highly desirable as it enhances quality assurance with minimised delay

With respect to the showcasing of the PPP technique within FDM fabrication device, three distinct devices have been presented here for the first time and demonstrate the type of device that can be made when incorporating membranes into 3D printed structures, there are numerous other types of chemical processing equipment and chemical reactors that could exploit the same approach; for example, applying to reactor technology for combined synthesis and workup in a single device, or as a route for addition or removal of gases during a reaction. The versatility of 3D printing and the increasing maturity of 3D printing technology, means that the incorporation of membranes via PPP will be an enduring tool for fabrication of fluidic devices – not only for separation and filtration, but for chemical processing devices more generally.

Chapter 10 Appendix

10.1 MATLAB code for (R,G,B) value extraction

Example of code used in MATLAB to extract information from Channel A1 in the branched chip.

```
1= 263:266;
```

```
fn1= 400:4500;
```

```
A= 21:39;
```

```
A1r= IMG_4739 (A,X,1,fnX);
```

```
A1b= IMG_4739 (A,X,3,fnX);
```

```
A1r= squeeze(A1r);
```

```
A1b= squeeze (A1b);
```

```
V1_a1= max(max(A1r));
```

```
V2_a1= min(min(A1b));
```

```
sat_A1= V1_a1 - V2_a1;
```

```
sat_A1= squeeze(sat_A1);
```

```
plot(fnX, sat_A1);
```


List of References

1. Yaghi OM, O’Keeffe M, Ockwig NW, Chae HK, Eddaoudi M, Kim J. Reticular synthesis and the design of new materials. *Nature*. 2003;423(6941):705-714. doi:10.1038/nature01650
2. Howarth AJ, Liu Y, Hupp JT, Farha OK. Metal-organic frameworks for applications in remediation of oxyanion/cation-contaminated water. *CrystEngComm*. 2015;17(38):7245-7253. doi:10.1039/c5ce01428j
3. Lin RB, Xiang S, Xing H, Zhou W, Chen B. Exploration of porous metal–organic frameworks for gas separation and purification. *Coord Chem Rev*. 2019;378:87-103. doi:10.1016/j.ccr.2017.09.027
4. Zu DD, Lu L, Liu XQ, Zhang DY, Sun LB. Improving hydrothermal stability and catalytic activity of metal-organic frameworks by graphite oxide incorporation. *J Phys Chem C*. 2014;118(34):19910-19917. doi:10.1021/jp506335x
5. O. M. Yaghi, Guangming Li, Hailian Li. Selective binding and removal of guests in a microporous metal-organic framework. *Nature*. 1995;378:703-706.
6. Chadwick A V., Sherwood JN. Point Defects in Molecular Solids. *Point Defects in Solids*. 1975;85(8):441-475. doi:10.1007/978-1-4684-0904-8_6
7. Raptopoulou CP. Metal-Organic Frameworks : Synthetic Methods and Potential Applications. *Materials*. 2021;14(310). doi:10.3390/ma14020310
8. Furukawa H, Cordova KE, O’Keeffe M, Yaghi OM. The chemistry and applications of metal-organic frameworks. *Science (80-)*. 2013;341(6149). doi:10.1126/science.1230444
9. Wang Q, Gao Q, Al-Enizi AM, Nafady A, Ma S. Recent advances in MOF-based photocatalysis: Environmental remediation under visible light. *Inorg Chem Front*. 2020;7(2):300-339. doi:10.1039/c9qi01120j
10. Kim S, Lee J, Son Y, Yoon M. Study of the Dye Adsorption Kinetics of Metal–Organic Frameworks in Aqueous Media. *Bull Korean Chem Soc*. 2020;41(8):843-850. doi:10.1002/bkcs.12076
11. Hou J, Wang H, Zhang H. Zirconium Metal-Organic Framework Materials for Efficient Ion Adsorption and Sieving. *Ind Eng Chem Res*. 2020;59(29):12907-12923. doi:10.1021/acs.iecr.0c02683

List of References

12. Li H, Wang K, Sun Y, Lollar CT, Li J, Zhou HC. Recent advances in gas storage and separation using metal–organic frameworks. *Mater Today*. 2018;21(2):108-121. doi:10.1016/j.mattod.2017.07.006
13. Abánades Lázaro I, Abánades Lázaro S, Forgan RS. Enhancing anticancer cytotoxicity through bimodal drug delivery from ultrasmall Zr MOF nanoparticles. *Chem Commun*. 2018;54(22):2792-2795. doi:10.1039/c7cc09739e
14. Zhang H, Shi X, Li J, Kumar P, Liu B. Selective dye adsorption by zeolitic imidazolate framework-8 loaded UiO-66-NH₂. *Nanomaterials*. 2019;9(9). doi:10.3390/nano9091283
15. Cheetham AK, Kieslich G, Yeung HH. Thermodynamic and Kinetic Effects in the Crystallization of Metal-Organic Frameworks Thermodynamic and Kinetic Effects in the Crystallization of Metal-Organic Frameworks. *Acc. Chem. Res*. 2018;51(3):659-667. doi:10.1021/acs.accounts.7b00497
16. Lu W, Wei Z, Gu ZY, et al. Tuning the structure and function of metal-organic frameworks via linker design. *Chem Soc Rev*. 2014;43(16):5561-5593. doi:10.1039/c4cs00003j
17. Rubio-Martinez M, Avci-Camur C, Thornton AW, Imaz I, Maspoch D, Hill MR. New synthetic routes towards MOF production at scale. *Chem Soc Rev*. 2017;46(11):3453-3480. doi:10.1039/c7cs00109f
18. Łuczak J, Kroczevska M, Baluk M, Sowik J, Mazierski P, Zaleska-Medynska A. Morphology control through the synthesis of metal-organic frameworks. *Adv Colloid Interface Sci*. 2023;314(February). doi:10.1016/j.cis.2023.102864
19. Mosavi SH, Zare-Dorabei R, Bereyhi M. Microwave-assisted synthesis of metal–organic framework MIL-47 for effective adsorptive removal of dibenzothiophene from model fuel. *J Iran Chem Soc*. 2021;18(3):709-717. doi:10.1007/s13738-020-02057-z
20. Al-Kutubi H, Gascon J, Sudhölter EJR, Rassaei L. Electrosynthesis of Metal-Organic Frameworks: Challenges and Opportunities. *ChemElectroChem*. 2015;2(4):462-474. doi:10.1002/celec.201402429
21. Chen D, Zhao J, Zhang P, Dai S. Mechanochemical synthesis of metal–organic frameworks. *Polyhedron*. 2019;162:59-64. doi:10.1016/j.poly.2019.01.024
22. Young C, Wang J, Kim J, Sugahara Y, Henzie J, Yamauchi Y. Controlled Chemical Vapor Deposition for Synthesis of Nanowire Arrays of Metal-Organic Frameworks and Their

- Thermal Conversion to Carbon/Metal Oxide Hybrid Materials. *Chem Mater*. 2018;30(10):3379-3386. doi:10.1021/acs.chemmater.8b00836
23. Echaide-Górriz C, Clément C, Cacho-Bailo F, Téllez C, Coronas J. New strategies based on microfluidics for the synthesis of metal-organic frameworks and their membranes. *J Mater Chem A*. 2018;6(14):5485-5506. doi:10.1039/c8ta01232f
 24. Stock N, Biswas S. Synthesis of metal-organic frameworks (MOFs): Routes to various MOF topologies, morphologies, and composites. *Chem Rev*. 2012;112(2):933-969. doi:10.1021/cr200304e
 25. Crawford DE, Casaban J. Recent Developments in Mechanochemical Materials Synthesis by Extrusion. *Adv Mater*. 2016;28(27):5747-5754. doi:10.1002/adma.201505352
 26. Bayliss PA, Ibarra IA, Pérez E, et al. Synthesis of metal-organic frameworks by continuous flow. *Green Chem*. 2014;16(8):3796-3802. doi:10.1039/c4gc00313f
 27. Liu Z, Zhu J, Peng C, Wakihara T, Okubo T. Continuous flow synthesis of ordered porous materials: From zeolites to metal-organic frameworks and mesoporous silica. *React Chem Eng*. 2019;4(10):1699-1720. doi:10.1039/c9re00142e
 28. Sebastian V, Khan SA, Kulkarni AA. Perspective Article: Flow Synthesis of Functional Materials. *J Flow Chem*. 2017;7(3-4):96-105. doi:10.1556/1846.2017.00028
 29. Główniak S, Szczęśniak B, Choma J, Jaroniec M. Mechanochemistry: Toward green synthesis of metal-organic frameworks. *Mater Today*. 2021;46(June):109-124. doi:10.1016/j.mattod.2021.01.008
 30. Crawford D, Casaban J, Haydon R, Giri N, McNally T, James SL. Synthesis by extrusion: Continuous, large-scale preparation of MOFs using little or no solvent. *Chem Sci*. 2015;6(3):1645-1649. doi:10.1039/c4sc03217a
 31. Rubio-Martinez M, Hadley TD, Batten MP, et al. Scalability of Continuous Flow Production of Metal-Organic Frameworks. *ChemSusChem*. 2016;9(9):938-941. doi:10.1002/cssc.201501684
 32. Mateos C, Nieves-Remacha MJ, Rincón JA. Automated platforms for reaction self-optimization in flow. *React Chem Eng*. 2019;4(9):1536-1544. doi:10.1039/c9re00116f
 33. Baumann M, Moody TS, Smyth M, Wharry S. A Perspective on Continuous Flow Chemistry

List of References

- in the Pharmaceutical Industry. *Org Process Res Dev.* 2020;24(10):1802-1813.
doi:10.1021/acs.oprd.9b00524
34. Sagmeister P, Lebl R, Castillo I, et al. Advanced Real-Time Process Analytics for Multistep Synthesis in Continuous Flow**. *Angew Chemie - Int Ed.* 2021;60(15):8139-8148.
doi:10.1002/anie.202016007
35. Gutmann B, Cantillo D, Kappe CO. Continuous-flow technology - A tool for the safe manufacturing of active pharmaceutical ingredients. *Angew Chemie - Int Ed.* 2015;54(23):6688-6728. doi:10.1002/anie.201409318
36. Krishnadasan S, Brown RJC, DeMello AJ, DeMello JC. Intelligent routes to the controlled synthesis of nanoparticles. *Lab Chip.* 2007;7(11):1434-1441. doi:10.1039/b711412e
37. Abdel-Latif K, Bateni F, Crouse S, Abolhasani M. Flow Synthesis of Metal Halide Perovskite Quantum Dots: From Rapid Parameter Space Mapping to AI-Guided Modular Manufacturing. *Matter.* 2020;3(4):1053-1086. doi:10.1016/j.matt.2020.07.024
38. Abdel-Latif K, Epps RW, Bateni F, Han S, Reyes KG, Abolhasani M. Self-Driven Multistep Quantum Dot Synthesis Enabled by Autonomous Robotic Experimentation in Flow. *Adv Intell Syst.* 2021;3(2):2000245. doi:10.1002/aisy.202000245
39. Myers RM, Fitzpatrick DE, Turner RM, Ley S V. Flow Chemistry Meets Advanced Functional Materials. *Chem - A Eur J.* 2014;20(39):12348-12366. doi:10.1002/chem.201402801
40. Plutschack MB, Pieber B, Gilmore K, Seeberger PH. The Hitchhiker's Guide to Flow Chemistry â. *Chem Rev.* 2017;117(18):11796-11893. doi:10.1021/acs.chemrev.7b00183
41. Sans V, Cronin L. Towards dial-a-molecule by integrating continuous flow, analytics and self-optimisation. *Chem Soc Rev.* 2016;45(8):2032-2043. doi:10.1039/c5cs00793c
42. Wu KJ, Torrente-Murciano L. Continuous synthesis of tuneable sized silver nanoparticles: Via a tandem seed-mediated method in coiled flow inverter reactors. *React Chem Eng.* 2018;3(3):267-276. doi:10.1039/c7re00194k
43. Taddei M, Casati N, Steitz DA, D mbgen KC, Van Bokhoven JA, Ranocchiari M. In situ high-resolution powder X-ray diffraction study of UiO-66 under synthesis conditions in a continuous-flow microwave reactor. *CrystEngComm.* 2017;19(23):3206-3214.
doi:10.1039/c7ce00867h

44. Gustafsson T, Pontén F, Seeberger PH. Trimethylaluminium mediated amide bond formation in a continuous flow microreactor as key to the synthesis of rimonabant and efaproxiral. *Chem Commun.* 2008;(9):1100-1102. doi:10.1039/b719603b
45. Du Toit H, Macdonald TJ, Huang H, Parkin IP, Gavrilidis A. Continuous flow synthesis of citrate capped gold nanoparticles using UV induced nucleation. *RSC Adv.* 2017;7(16):9632-9638. doi:10.1039/c6ra27173a
46. Bianchi P, Petit G, Monbaliu JCM. Scalable and robust photochemical flow process towards small spherical gold nanoparticles. *React Chem Eng.* 2020;5(7):1224-1236. doi:10.1039/d0re00092b
47. Cardoso FSP, Mickle GE, Da Silva MA, Baraldi PT, Ferreira FB. Application of in Situ FTIR for the Preparation of 17- α -Estradiol via Mitsunobu Reaction. *Org Process Res Dev.* 2016;20(2):306-311. doi:10.1021/acs.oprd.5b00394
48. Qian Z, Baxendale IR, Ley SV. A Continuous Flow Process Using a Sequence of Microreactors with In-line IR Analysis for the Preparation of N,N-Diethyl-4-(3-fluorophenyl)piperidin-4-ylidenemethyl)benzamide as a Potent and Highly Selective d-Opioid. *Chem. Eur. J.* 2010;16:12342-12348. doi: 10.1002/chem.201002147
49. Desai B, Dixon K, Farrant E, et al. Rapid discovery of a novel series of Abl kinase inhibitors by application of an integrated microfluidic synthesis and screening platform. *J Med Chem.* 2013;56(7):3033-3047. doi:10.1021/jm400099d
50. Abécassis B, Bouet C, Garnerio C, et al. Real-Time in Situ Probing of High-Temperature Quantum Dots Solution Synthesis. *Nano Lett.* 2015;15(4):2620-2626. doi:10.1021/acs.nanolett.5b00199
51. Suchan K, Just J, Becker P, Unger EL, Unold T. Optical: In situ monitoring during the synthesis of halide perovskite solar cells reveals formation kinetics and evolution of optoelectronic properties. *J Mater Chem A.* 2020;8(20):10439-10449. doi:10.1039/d0ta01237h
52. Sun Y, Fang H, Lin X, et al. Kinetic Investigation of a Cucurbit[7]uril-Based Pseudo[6]rotaxane System by Microfluidic Nuclear Magnetic Resonance. *CCS Chem.* Published online 2021:948-956. doi:10.31635/ccschem.021.202100773
53. Gomez MV, Verputten HHJ, Díaz-Ortíz A, Moreno A, De La Hoz A, Velders AH. On-line monitoring of a microwave-assisted chemical reaction by nanolitre NMR-spectroscopy.

List of References

- Chem Commun.* 2010;46(25):4514-4516. doi:10.1039/b924936b
54. Kitson PJ, Rosnes MH, Sans V, Dragone V, Cronin L. Configurable 3D-Printed millifluidic and microfluidic “lab on a chip” reactionware devices. *Lab Chip.* 2012;12(18):3267-3271. doi:10.1039/c2lc40761b
55. Carter CF, Lange H, Ley S V, et al. ReactIR Flow Cell : A New Analytical Tool for Continuous Flow Chemical Processing Abstract : A newly developed ReactIR flow cell is reported as a convenient and versatile inline analytical tool for continuous. *Org Process Res Dev.* 2010;14(2):393-404.
56. Lu H, Schmidt MA, Jensen KF. Photochemical reactions and on-line UV detection in microfabricated reactors. *Lab Chip.* 2001;1(1):22-28. doi:10.1039/b104037p
57. Schlindwein W, Bezerra M, Almeida J, Berghaus A, Owen M, Muirhead G. In-line uv-vis spectroscopy as a fast-working process analytical technology (Pat) during early phase product development using hot melt extrusion (hme). *Pharmaceutics.* 2018;10(4):1. - 25. doi:10.3390/pharmaceutics10040166
58. Epps RW, Felton KC, Coley CW, Abolhasani M. Automated microfluidic platform for systematic studies of colloidal perovskite nanocrystals: Towards continuous nano-manufacturing. *Lab Chip.* 2017;17(23):4040-4047. doi:10.1039/c7lc00884h
59. Carter CF, Baxendale IR, O’Brien M, Pavey JBJ, Ley S V. Synthesis of acetal protected building blocks using flow chemistry with flow I.R. analysis: Preparation of butane-2,3-diacetal tartrates. *Org Biomol Chem.* 2009;7(22):4594-4597. doi:10.1039/b917289k
60. Oosthoek-De Vries AJ, Nieuwland PJ, Bart J, et al. Inline Reaction Monitoring of Amine-Catalyzed Acetylation of Benzyl Alcohol Using a Microfluidic Stripline Nuclear Magnetic Resonance Setup. *J Am Chem Soc.* 2019;141(13):5369-5380. doi:10.1021/jacs.9b00039
61. Lauterbach F, Abetz V. Continuous Kinetic Sampling of Flow Polymerizations via Inline UV–Vis Spectroscopy. *Macromol Rapid Commun.* 2020;41(9):1-5. doi:10.1002/marc.202000029
62. Cao E, Sankar M, Firth S, et al. Reaction and Raman spectroscopic studies of alcohol oxidation on gold-palladium catalysts in microstructured reactors. *Chem Eng J.* 2011;167(2-3):734-743. doi:10.1016/j.cej.2010.08.082
63. Bagi S, Wright AM, Oppenheim J, Dincă M, Román-Leshkov Y. Accelerated Synthesis of a Ni₂Cl₂(BTDD) Metal-Organic Framework in a Continuous Flow Reactor for Atmospheric

- Water Capture. *ACS Sustain Chem Eng*. 2021;9(11):3996-4003.
doi:10.1021/acssuschemeng.0c07055
64. Dunne PW, Lester E, Walton RI. Towards scalable and controlled synthesis of metal-organic framework materials using continuous flow reactors. *React Chem Eng*. 2016;1(4):352-360.
doi:10.1039/c6re00107f
 65. Bannock JH, Krishnadasan SH, Heeney M, De Mello JC. A gentle introduction to the noble art of flow chemistry. *Mater Horizons*. 2014;1(4):373-378. doi:10.1039/c4mh00054d
 66. Faustini M, Kim J, Jeong GY, et al. Microfluidic approach toward continuous and ultrafast synthesis of metal-organic framework crystals and hetero structures in confined microdroplets. *J Am Chem Soc*. 2013;135(39):14619-14626. doi:10.1021/ja4039642
 67. He B, Sadiq MM, Batten MP, et al. Continuous Flow Synthesis of a Zr Magnetic Framework Composite for Post-Combustion CO₂ Capture. *Chem - A Eur J*. 2019;25(57):13184-13188.
doi:10.1002/chem.201902560
 68. Polyzoidis A, Altenburg T, Schwarzer M, Loebbecke S, Kaskel S. Continuous microreactor synthesis of ZIF-8 with high space-time-yield and tunable particle size. *Chem Eng J*. 2016;283:971-977. doi:10.1016/j.cej.2015.08.071
 69. Paseta L, Seoane B, Julve D, Sebastián V, Téllez C, Coronas J. Accelerating the controlled synthesis of metal-organic frameworks by a microfluidic approach: A nanoliter continuous reactor. *ACS Appl Mater Interfaces*. 2013;5(19):9405-9410. doi:10.1021/am4029872
 70. Didriksen T, Spjelkavik AI, Blom R. Continuous synthesis of the metal-organic framework cpo-27-ni from aqueous solutions. *J Flow Chem*. 2017;7(1):13-17.
doi:10.1556/1846.2016.00040
 71. Wang Y, Li L, Yan L, et al. Continuous synthesis for zirconium metal-organic frameworks with high quality and productivity via microdroplet flow reaction. *Chinese Chem Lett*. 2018;29(6):849-853. doi:10.1016/j.cclet.2017.09.057
 72. Ameloot R, Vermoortele F, Vanhove W, Roeyers M, Sels BF, De Vos DE. Interfacial synthesis of hollow metal-organic framework capsules demonstrating selective permeability. *Nat Chem*. 2011;3(5):382-387. doi:10.1038/nchem.1026
 73. Zhang Y, Jia Y, Hou L. Synthesis of zeolitic imidazolate framework-8 on polyester fiber for PM_{2.5} removal. *RSC Adv*. 2018;8(55):31471-31477. doi:10.1039/c8ra06414h

List of References

74. D'Arras L, Sassoie C, Rozes L, et al. Fast and continuous processing of a new sub-micronic lanthanide-based metal-organic framework. *New J Chem*. 2014;38(4):1477-1483. doi:10.1039/c3nj01371e
75. Gimeno-Fabra M, Munn AS, Stevens LA, et al. Instant MOFs: Continuous synthesis of metal-organic frameworks by rapid solvent mixing. *Chem Commun*. 2012;48(86):10642-10644. doi:10.1039/c2cc34493a
76. Rubio-Martinez M, Batten MP, Polyzos A, et al. Versatile, high quality and scalable continuous flow production of metal-organic frameworks. *Sci Rep*. 2014;4:1-5. doi:10.1038/srep05443
77. McKinstry C, Cathcart RJ, Cussen EJ, Fletcher AJ, Patwardhan S V., Sefcik J. Scalable continuous solvothermal synthesis of metal organic framework (MOF-5) crystals. *Chem Eng J*. 2016;285:718-725. doi:10.1016/j.cej.2015.10.023
78. Van Vleet MJ, Weng T, Li X, Schmidt JR. In Situ, Time-Resolved, and Mechanistic Studies of Metal-Organic Framework Nucleation and Growth. *Chem Rev*. 2018;118(7):3681-3721. doi:10.1021/acs.chemrev.7b00582
79. Petersen H, Weidenthaler C. A review of recent developments for the in situ/operando characterization of nanoporous materials. *Inorg Chem Front*. Published online 2022. doi:10.1039/d2qi00977c
80. Cerasale DJ, Ward DC, Easun TL. MOFs in the time domain. *Nat Rev Chem*. 2022;6(1):9-30. doi:10.1038/s41570-021-00336-8
81. Goesten MG, Stavitski E, Juan-Alcañiz J, et al. Small-angle X-ray scattering documents the growth of metal-organic frameworks. *Catal Today*. 2013;205:120-127. doi:10.1016/j.cattod.2012.08.044
82. Mundt LE, Schelhas LT. Structural Evolution During Perovskite Crystal Formation and Degradation: In Situ and Operando X-Ray Diffraction Studies. *Adv Energy Mater*. 2020;10(26):1-11. doi:10.1002/aenm.201903074
83. Ming LC, Kim YH, Uchida T, Wang Y, Rivers M. In situ X-ray diffraction study of phase transitions of FeTiO₃ at high pressures and temperatures using a large-volume press and synchrotron radiation. *Am Mineral*. 2006;91(1):120-126. doi:10.2138/am.2006.1930
84. Seoane B, Zamaro JM, Tellez C, Coronas J. Sonocrystallization of zeolitic imidazolate

- frameworks (ZIF-7, ZIF-8, ZIF-11 and ZIF-20). *CrystEngComm*. 2012;14(9):3103-3107. doi:10.1039/c2ce06382d
85. Moh PY, Brenda M, Anderson MW, Attfield MP. Crystallisation of solvothermally synthesised ZIF-8 investigated at the bulk, single crystal and surface level. *CrystEngComm*. 2013;15(45):9672-9678. doi:10.1039/c3ce40943k
 86. Cravillon J, Schröder CA, Bux H, Rothkirch A, Caro J, Wiebcke M. Formate modulated solvothermal synthesis of ZIF-8 investigated using time-resolved in situ X-ray diffraction and scanning electron microscopy. *CrystEngComm*. 2012;14(2):492-498. doi:10.1039/c1ce06002c
 87. Ragon F, Horcajada P, Chevreau H, et al. In situ energy-dispersive x-ray diffraction for the synthesis optimization and scale-up of the porous zirconium terephthalate UiO-66. *Inorg Chem*. 2014;53(5):2491-2500. doi:10.1021/ic402514n
 88. Schoenecker PM, Belancik GA, Grabicka BE, Walton KS, Kinetics study and crystallization process design for scale-up of UiO-66-NH₂ synthesis. *AIChE. J.* 2013;59(4):1255-1262. doi: 10.1002/aic.13901
 89. El Osta R, Feyand M, Stock N, Millange F, Walton RI. Crystallisation kinetics of metal organic frameworks from in situ time-resolved x-ray diffraction. *Powder Diffraction*. 2013;28(SUPPL.2):256-275. doi:10.1017/S0885715613000997
 90. Millange F, El Osta R, Medina ME, Walton RI. A time-resolved diffraction study of a window of stability in the synthesis of a copper carboxylate metal-organic framework. *CrystEngComm*. 2011;13(1):103-108. doi:10.1039/c0ce00530d
 91. Haque E, Khan NA, Park HJ, Jhung SH. Synthesis of a metal-organic framework material, iron terephthalate, by ultrasound, microwave, and conventional electric heating: A kinetic study. *Chem - A Eur J*. 2010;16(3):1046-1052. doi:10.1002/chem.200902382
 92. Haque E, Jeong JH, Jhung SH. Synthesis of isostructural porous metal-benzenedicarboxylates: Effect of metal ions on the kinetics of synthesis. *CrystEngComm*. 2010;12(10):2749-2754. doi:10.1039/b927113a
 93. Haque E, Khan NA, Kim CM, Jhung SH. Syntheses of metal-organic frameworks and aluminophosphates under microwave heating: Quantitative analysis of accelerations. *Cryst Growth Des*. 2011;11(10):4413-4421. doi:10.1021/cg200594e

List of References

94. Wu Y, Breeze MI, Clarkson GJ, Millange F, O'Hare D, Walton RI. Exchange of Coordinated Solvent during Crystallization of a Metal-Organic Framework Observed by in Situ High-Energy X-ray Diffraction. *Angew Chemie - Int Ed.* 2016;55(16):4992-4996. doi:10.1002/anie.201600896
95. Stavitski E, Goesten M, Juan-Alcañiz J, et al. Kinetic control of metal-organic framework crystallization investigated by time-resolved in situ X-ray scattering. *Angew Chemie - Int Ed.* 2011;50(41):9624-9628. doi:10.1002/anie.201101757
96. Cravillon J, Schroder CA, Nayuk R, et al. Fast Nucleation and Growth of ZIF-8 Nanocrystals Monitored by Time-resolved In Situ Small-Angle and Wide-Angle X-Ray Scattering. *Angew. Chem. Int.E.* 2011;50:8067-8071. doi:10.1002/anie.201102071
97. Goesten MG, De Lange MF, Olivos-Suarez AI, et al. Evidence for a chemical clock in oscillatory formation of UiO-66. *Nat Commun.* 2016;7(May):1-8. doi:10.1038/ncomms11832
98. Saha S, Springer S, Schweinefuß ME, Pontoni D, Wiebcke M, Huber K. Insight into Fast Nucleation and Growth of Zeolitic Imidazolate Framework-71 by in Situ Time-Resolved Light and X-ray Scattering Experiments. *Cryst Growth Des.* 2016;16(4):2002-2010. doi:10.1021/acs.cgd.5b01594
99. Carraro F, Williams JD, Linares-Moreau M, et al. Continuous-Flow Synthesis of ZIF-8 Biocomposites with Tunable Particle Size. *Angew Chemie.* 2020;132(21):8200-8204. doi:10.1002/ange.202000678
100. Sang X, Zhang J, Xiang J, et al. Ionic liquid accelerates the crystallisation of Zr-based metal – organic frameworks. *Nat Commun.* 2017;8:1-7. doi:10.1038/s41467-017-00226-y
101. Bugaev AL, Guda AA, Lomachenko KA, et al. Operando study of palladium nanoparticles inside UiO-67 MOF for catalytic hydrogenation of hydrocarbons. *Faraday Discuss.* 2018;208:287-306. doi:10.1039/c7fd00224f
102. Firth FCN, Gaultois MW, Wu Y, et al. Exploring the Solution Formation of UiO Family Hf Metal-Organic Framework clusters with in situ X- Ray Pair Distribution Function Analysis. *J. Am.Chem. Soc.* 2021;143(47):19668-19683. doi:10.1021/jacs.1c06990
103. Batzdorf L, Fischer F, Wilke M, et al. Direct In Situ Investigation of Milling Reactions Using Combined X-ray Diffraction and Raman Spectroscopy. *Angew. Chem. Int. Ed.* 2015;54:1799-1802. doi:10.1002/anie.201409834

104. Weidenthaler C. In Situ Analytical Methods for the Characterization of Mechanochemical Reactions. *Crystals*. 2022;12(3). doi:10.3390/cryst12030345
105. Liu X, Chee SW, Raj S, Sawczyk M, Král P, Mirsaidov U. Three-step nucleation of metal–organic framework nanocrystals. *Proc Natl Acad Sci U S A*. 2021;118(10). doi:10.1073/pnas.2008880118
106. Haouas M, Volkringer C, Loiseau T, Taulelle F. In Situ NMR , Ex Situ XRD and SEM Study of the Hydrothermal Crystallization of Nanoporous Aluminum Trimesates MIL-96 , MIL-. Published online 2012.
107. Worrall SD, Bissett MA, Attfield MP, Dryfe RAW. Anodic dissolution growth of metal – organic framework HKUST-1 monitored via in situ electrochemical atomic force microscopy. Published online 2018:4421-4427. doi:10.1039/c8ce00761f
108. Embrechts H, Kriesten M, Hoffmann K, Peukert W, Hartmann M, Distaso M. Elucidation of the Formation Mechanism of Metal-Organic Frameworks via in-Situ Raman and FTIR Spectroscopy under Solvothermal Conditions. *J Phys Chem C*. 2018;122(23):12267-12278. doi:10.1021/acs.jpcc.8b02484
109. Ren J, Musyoka NM, Langmi HW, et al. In-situ IR monitoring of the formation of Zr-fumarate MOF. *Appl Surf Sci*. 2017;404:263-267. doi:10.1016/j.apsusc.2017.01.271
110. Ren J, Musyoka NM, Langmi HW, Walker J, Mathe M, Liao S. In-situ IR monitoring to probe the formation of structural defects in Zr-fumarate metal–organic framework (MOF). *Polyhedron*. 2018;153:205-212. doi:10.1016/j.poly.2018.07.026
111. Embrechts H, Embrechts H, Kriesten M, et al. Role of Prenucleation Building Units in Determining Metal-Organic Framework MIL-53(Al) Morphology. *Cryst Growth Des*. 2020;20(6):3641-3649. doi:10.1021/acs.cgd.9b01384
112. Embrechts H, Kriesten M, Ermer M, Peukert W, Distaso M. In situ Raman and FTIR spectroscopic study on the. 2020;68:7336-7348. doi:c
113. Sutrisno A, Huang Y. Solid-state NMR: A powerful tool for characterization of metal-organic frameworks. *Solid State Nucl Magn Reson*. 2013;49-50:1-11. doi:10.1016/j.ssnmr.2012.09.003
114. Easun TL, Moreau F, Yan Y, Yang S, Schröder M. Structural and dynamic studies of substrate binding in porous metal-organic frameworks. *Chem Soc Rev*. 2017;46(1):239-274.

List of References

doi:10.1039/c6cs00603e

115. Jones CL, Hughes CE, Yeung HHM, Paul A, Harris KDM, Easun TL. Exploiting in situ NMR to monitor the formation of a metal-organic framework. *Chem Sci.* 2021;12(4):1486-1494. doi:10.1039/d0sc04892e
116. Becker, A., and Schmidt, M. *Makromol. Chem. Macromol. Symp.* 1991;50:249-260
117. Cravillon J, Nayuk R, Springer S, Feldhoff A, Huber K, Wiebcke M. Controlling zeolitic imidazolate framework nano- and microcrystal formation: Insight into crystal growth by time-resolved in situ static light scattering. *Chem Mater.* 2011;23(8):2130-2141. doi:10.1021/cm103571y
118. Hermes S, Witte T, Hikov T, et al. Trapping metal-organic framework nanocrystals: An in-situ time-resolved light scattering study on the crystal growth of MOF-5 in solution. *J Am Chem Soc.* 2007;129(17):5324-5325. doi:10.1021/ja068835i
119. Zacher D, Liu J, Huber K, Fischer RA. Nanocrystals of [Cu₃(btc)₂] (HKUST-1): A combined time-resolved light scattering and scanning electron microscopy study. *Chem Commun.* 2009;3(9):1031-1033. doi:10.1039/b819580c
120. Saha S, Wiebcke M, Huber K. Insight into Fast Nucleation and Growth of Zeolitic Imidazolate Framework-71 by in Situ Static Light Scattering at Variable Temperature and Kinetic Modeling. *Cryst Growth Des.* 2018;18(8):4653-4661. doi:10.1021/acs.cgd.8b00626
121. Yeung HH, Sapnik AF, Massingberd-mundy F, et al. Communications Metal – Organic Frameworks Control of Metal – Organic Framework Crystallization by Metastable Intermediate Pre-equilibrium Species. Published online 2019:566-571. doi:10.1002/anie.201810039
122. Massingberd-Mundy F, Poulston S et al. Use of open source monitoring hardware to improve the production of MOFs: using STA-16(Ni) as a case study. *Scientific Reports.* 2020;10. doi:10.1038/s41598
123. Luo L, Lv G, Wang P, Liu Q, Chen K, Sun W. pH-Dependent cobalt (II) frameworks with mixed structure and sorption property. 2013;3407:9537-9543. doi:10.1039/c3ce41056k
124. Yao Z, Guo J, Wang P, Liu Y, Guo F, Sun W. Controlled synthesis of micro / nanoscale Mg-MOF-74 materials and their adsorption property. *Mater Lett.* 2018;223:174-177. doi:10.1016/j.matlet.2018.04.014

125. Yeung HHM, Sapnik AF, Massingberd-Mundy F, et al. Control of Metal–Organic Framework Crystallization by Metastable Intermediate Pre-equilibrium Species. *Angew Chemie - Int Ed.* 2019;58(2):566-571. doi:10.1002/anie.201810039
126. Yuan N, Church TL, Brandt EG, Hedin N, Zou X, Bernin D. Insights into Functionalization of Metal-Organic Frameworks Using In Situ NMR Spectroscopy. Published online 2018:1-8. doi:10.1038/s41598-018-35842-1
127. Lescouet T, Vitillo JG, Bordiga S, Canivet J, Farrusseng D. An alternative pathway for the synthesis of isocyanato- and urea-functionalised metal-organic frameworks. *Dalt Trans.* 2013;42(23):8249-8258. doi:10.1039/c3dt32714k
128. Plonka AM, Wang Q, Gordon WO, et al. In situ probes of capture and decomposition of chemical warfare agent simulants by Zr-based metal organic frameworks. *J Am Chem Soc.* 2017;139(2):599-602. doi:10.1021/jacs.6b11373
129. Fröhlich D, Henninger SK, Janiak C. Multicycle water vapour stability of microporous breathing MOF aluminium isophthalate CAU-10-H. *Dalt Trans.* 2014;43(41):15300-15304. doi:10.1039/c4dt02264e
130. Dreimann JM, Kohls E, Warmeling HFW, et al. In Situ Infrared Spectroscopy as a Tool for Monitoring Molecular Catalyst for Hydroformylation in Continuous Processes. *ACS Catal.* 2019;9(5):4308-4319. doi:10.1021/acscatal.8b05066
131. Rojas-buzo S, García-garcía P. Catalysis Science & Technology synthesis of polyurethane precursors. Published online 2019:146-156. doi:10.1039/c8cy02235f
132. Polyzoidis A, Etter M, Herrmann M, Loebbecke S, Dinnebier RE. Revealing the Initial Reaction Behavior in the Continuous Synthesis of Metal-Organic Frameworks Using Real-Time Synchrotron X-ray Analysis. *Inorg Chem.* 2017;56(10):5489-5492. doi:10.1021/acs.inorgchem.7b00325
133. Polyzoidis A, Schwarzer M, Loebbecke S, Piscopo CG. Continuous synthesis of UiO-66 in microreactor: Pursuing the optimum between intensified production and structural properties. *Mater Lett.* 2017;197:213-216. doi:10.1016/j.matlet.2017.02.091
134. He B, Macreadie LK, Gardiner J, Telfer SG, Hill MR. In Situ Investigation of Multicomponent MOF Crystallization during Rapid Continuous Flow Synthesis. Published online 2021. doi:10.1021/acsami.1c04920

List of References

135. McKinstry C, Cussen EJ, Fletcher AJ, Patwardhan S V., Sefcik J. Scalable continuous production of high quality HKUST-1 via conventional and microwave heating. *Chem Eng J*. 2017;326:570-577. doi:10.1016/j.cej.2017.05.169
136. Sabouni R, Aidan A, Alobeidli A, et al. Adsorption kinetics and thermodynamics of methylene blue by HKUST-1. *Desalin Water Treat*. 2019;138:301-312. doi:10.5004/dwt.2019.23260
137. Shen J, Wang X, Zhang L, et al. Size-selective adsorption of methyl orange using a novel nano-composite by encapsulating HKUST-1 in hyper-crosslinked polystyrene networks. *J Clean Prod*. 2018;184:949-958. doi:10.1016/j.jclepro.2018.03.015
138. Munn AS, Dunne PW, Tang SVY, Lester EH. Large-scale continuous hydrothermal production and activation of ZIF-8. *Chem Commun*. 2015;51(64):12811-12814. doi:10.1039/c5cc04636j
139. Taddei M, Steitz DA, Van Bokhoven JA, Ranocchiari M. Continuous-Flow Microwave Synthesis of Metal-Organic Frameworks: A Highly Efficient Method for Large-Scale Production. *Chem - A Eur J*. 2016;22(10):3245-3249. doi:10.1002/chem.201505139
140. Luan Tran B, Chin HY, Chang BK, Chiang AST. Dye adsorption in ZIF-8: The importance of external surface area. *Microporous Mesoporous Mater*. 2019;277(August 2018):149-153. doi:10.1016/j.micromeso.2018.10.027
141. Chin M, Cisneros C, Araiza SM, Vargas KM, Ishihara KM, Tian F. Rhodamine B degradation by nanosized zeolitic imidazolate framework-8 (ZIF-8). *RSC Adv*. 2018;8(47):26987-26997. doi:10.1039/c8ra03459a
142. Feng Y, Li Y, Xu M, Liu S, Yao J. Fast adsorption of methyl blue on zeolitic imidazolate framework-8 and its adsorption mechanism. *RSC Adv*. 2016;6(111):109608-109612. doi:10.1039/c6ra23870j
143. Chui SSY, Lo SMF, Charmant JPH, Orpen AG, Williams ID. A chemically functionalizable nanoporous material [Cu₃(TMA)₂(H₂O)₃](n). *Science (80-)*. 1999;283(5405):1148-1150. doi:10.1126/science.283.5405.1148
144. Talin AA, Centrone A, Ford AC, et al. Tunable electrical conductivity in metal-organic framework thin-film devices. *Science (80-)*. 2014;343(6166):66-69. doi:10.1126/science.1246738

145. Bentley J, Foo GS, Rungta M, et al. Effects of open metal site availability on adsorption capacity and olefin/paraffin selectivity in the metal-organic framework Cu₃(BTC)₂. *Ind Eng Chem Res.* 2016;55(17):5043-5053. doi:10.1021/acs.iecr.6b00774
146. Chong KC, Lai SO, Mah SK, et al. A Review of HKUST-1 Metal-Organic Frameworks in Gas Adsorption. *IOP Conf Ser Earth Environ Sci.* 2023;1135(1):0-8. doi:10.1088/1755-1315/1135/1/012030
147. Zhao L, Azhar MR, Li X, et al. Adsorption of cerium (III) by HKUST-1 metal-organic framework from aqueous solution. *J Colloid Interface Sci.* 2019;542:421-428. doi:10.1016/j.jcis.2019.01.117
148. Kalmutzki MJ, Diercks CS, Yaghi OM. Metal–Organic Frameworks for Water Harvesting from Air. *Adv Mater.* 2018;30(37):1-26. doi:10.1002/adma.201704304
149. Logan MW, Langevin S, Xia Z. Reversible Atmospheric Water Harvesting Using Metal-Organic Frameworks. *Sci Rep.* 2020;10(1):1-11. doi:10.1038/s41598-020-58405-9
150. Álvarez JR, Sánchez-González E, Pérez E, et al. Structure stability of HKUST-1 towards water and ethanol and their effect on its CO₂ capture properties. *Dalt Trans.* 2017;46(28):9192-9200. doi:10.1039/c7dt01845b
151. Gong X, Wang Y, Kuang T. ZIF-8-Based Membranes for Carbon Dioxide Capture and Separation. *ACS Sustain Chem Eng.* 2017;5(12):11204-11214. doi:10.1021/acssuschemeng.7b03613
152. Chi WS, Hwang S, Lee SJ, et al. Mixed matrix membranes consisting of SEBS block copolymers and size-controlled ZIF-8 nanoparticles for CO₂ capture. *J Memb Sci.* 2015;495:479-488. doi:10.1016/j.memsci.2015.08.016
153. Hu M, Lou H, Yan X, Hu X, Feng R, Zhou M. In-situ fabrication of ZIF-8 decorated layered double oxides for adsorption and photocatalytic degradation of methylene blue. *Microporous Mesoporous Mater.* 2018;271(April):68-72. doi:10.1016/j.micromeso.2018.05.048
154. Mahmoodi NM, Oveisi M, Taghizadeh A, Taghizadeh M. Synthesis of pearl necklace-like ZIF-8@chitosan/PVA nanofiber with synergistic effect for recycling aqueous dye removal. *Carbohydr Polym.* 2020;227(September 2019):115364. doi:10.1016/j.carbpol.2019.115364
155. Yuan J, Li Q, Shen J, et al. Hydrophobic-functionalized ZIF-8 nanoparticles incorporated

List of References

- PDMS membranes for high-selective separation of propane/nitrogen. *Asia-Pacific J Chem Eng.* 2017;12(1):110-120. doi:10.1002/apj.2058
156. Awadallah-F A, Hillman F, Al-Muhtaseb SA, Jeong HK. On the nanogate-opening pressures of copper-doped zeolitic imidazolate framework ZIF-8 for the adsorption of propane, propylene, isobutane, and n-butane. *J Mater Sci.* 2019;54(7):5513-5527. doi:10.1007/s10853-018-03249-y
157. Jian M, Liu B, Liu R, Qu J, Wang H, Zhang X. Water-based synthesis of zeolitic imidazolate framework-8 with high morphology level at room temperature. *RSC Adv.* 2015;5(60):48433-48441. doi:10.1039/c5ra04033g
158. Abid HR, Azhar MR, Iglauer S, Rada ZH, Al-Yaseri A, Keshavarz A. Physicochemical characterization of metal organic framework materials: A mini review. *Heliyon.* 2024;10(1):e23840. doi:10.1016/j.heliyon.2023.e23840
159. Ediati R, Dewi SK, Hasan MR, Kahardina M, Murwani IK, Nadjib M. Mesoporous HKUST-1 synthesized using solvothermal method. *Rasayan J Chem.* 2019;12(3):1653-1659. doi:10.31788/RJC.2019.1231968
160. Tran T Van, Nguyen DTC, Nguyen TT, Le HTN, Nguyen C Van, Nguyen TD. Metal-organic framework HKUST-1-based Cu/Cu₂O/CuO@C porous composite: Rapid synthesis and uptake application in antibiotics remediation. *J Water Process Eng.* 2020;36(May):101319. doi:10.1016/j.jwpe.2020.101319
161. Cui X, Sun X, Liu L, et al. In-situ fabrication of cellulose foam HKUST-1 and surface modification with polysaccharides for enhanced selective adsorption of toluene and acidic dipeptides. *Chem Eng J.* 2019;369(March):898-907. doi:10.1016/j.cej.2019.03.129
162. Lin KS, Adhikari AK, Ku CN, Chiang CL, Kuo H. Synthesis and characterization of porous HKUST-1 metal organic frameworks for hydrogen storage. *Int J Hydrogen Energy.* 2012;37(18):13865-13871. doi:10.1016/j.ijhydene.2012.04.105
163. Armstrong MR, Senthilnathan S, Balzer CJ, Shan B, Chen L, Mu B. Particle size studies to reveal crystallization mechanisms of the metal organic framework HKUST-1 during sonochemical synthesis. *Ultrason Sonochem.* 2017;34:365-370. doi:10.1016/j.ultsonch.2016.06.011
164. Jian M, Liu B, Liu R, Qu J, Wang H, Zhang X. Water-based synthesis of zeolitic imidazolate framework-8 with high morphology level at room temperature. *RSC Adv.*

- 2015;5(60):48433-48441. doi:10.1039/c5ra04033g
165. Jiang J, Wei F, Yu G, Sui Y. Co₃O₄ electrode prepared by using metal-organic framework as a host for supercapacitors. *J Nanomater.* 2015;2015. doi:10.1155/2015/192174
 166. Majano G, Martin O, Hammes M, Smeets S, Baerlocher C, Pérez-Ramírez J. Solvent-mediated reconstruction of the metal-organic framework HKUST-1 (Cu₃(BTC)₂). *Adv Funct Mater.* 2014;24(25):3855-3865. doi:10.1002/adfm.201303678
 167. Todaro M, Buscarino G, Sciortino L, et al. Decomposition Process of Carboxylate MOF HKUST-1 Unveiled at the Atomic Scale Level. *J Phys Chem C.* 2016;120(23):12879-12889. doi:10.1021/acs.jpcc.6b03237
 168. DeCoste JB, Denny MS, Peterson GW, Mahle JJ, Cohen SM. Enhanced aging properties of HKUST-1 in hydrophobic mixed-matrix membranes for ammonia adsorption. *Chem Sci.* 2016;7(4):2711-2716. doi:10.1039/c5sc04368a
 169. McKinsty C, Cussen EJ, Fletcher AJ, Patwardhan S V., Sefcik J. Effect of synthesis conditions on formation pathways of metal organic framework (MOF-5) crystals. *Cryst Growth Des.* 2013;13(12):5481-5486. doi:10.1021/cg4014619
 170. Agboola OD, Benson NU. Physisorption and Chemisorption Mechanisms Influencing Micro (Nano) Plastics-Organic Chemical Contaminants Interactions : A Review. 2021;9(May):1-27. doi:10.3389/fenvs.2021.678574
 171. Tran Ba Luan. Dye Adsorption on UiO-66: the Importance of Electrostatic Attraction Mechanism. *J Water Chem Technol.* 2020;42(6):441-449. doi:10.3103/s1063455x20060107
 172. Yu CX, Chen J, Zhang Y, et al. Highly efficient and selective removal of anionic dyes from aqueous solution by using a protonated metal-organic framework. *J Alloys Compd.* 2021;853:157383. doi:10.1016/j.jallcom.2020.157383
 173. Tian S, Xu S, Liu J, He C, Xiong Y, Feng P. Highly efficient removal of both cationic and anionic dyes from wastewater with a water-stable and eco-friendly Fe-MOF via host-guest encapsulation. *J Clean Prod.* 2019;239:117767. doi:10.1016/j.jclepro.2019.117767
 174. Razavi SAA, Masoomi MY, Morsali A. Host-Guest Interaction Optimization through Cavity Functionalization for Ultra-Fast and Efficient Water Purification by a Metal-Organic Framework. *Inorg Chem.* 2018;57(18):11578-11587. doi:10.1021/acs.inorgchem.8b01611

List of References

175. Hasan Z, Tong M, Jung BK, Ahmed I, Zhong C, Jhung SH. Adsorption of pyridine over amino-functionalized metal-organic frameworks: Attraction via hydrogen bonding versus base-base repulsion. *J Phys Chem C*. 2014;118(36):21049-21056. doi:10.1021/jp507074x
176. Ahmad K, Shah HUR, Parveen S, et al. Metal Organic Framework (KIUB-MOF-1) as efficient adsorbent for cationic and anionic dyes from brackish water. *J Mol Struct*. 2021;1242:130898. doi:10.1016/j.molstruc.2021.130898
177. Yang JM, Ying RJ, Han CX, et al. Adsorptive removal of organic dyes from aqueous solution by a Zr-based metal-organic framework: Effects of Ce(III) doping. *Dalt Trans*. 2018;47(11):3913-3920. doi:10.1039/c8dt00217g
178. Hasan Z, Jhung SH. Removal of hazardous organics from water using metal-organic frameworks (MOFs): Plausible mechanisms for selective adsorptions. *J Hazard Mater*. 2015;283:329-339. doi:10.1016/j.jhazmat.2014.09.046
179. Haque E, Lee JE, Jang IT, et al. Adsorptive removal of methyl orange from aqueous solution with metal-organic frameworks, porous chromium-benzenedicarboxylates. *J Hazard Mater*. 2010;181(1-3):535-542. doi:10.1016/j.jhazmat.2010.05.047
180. Lin S, Song Z, Che G, et al. Adsorption behavior of metal-organic frameworks for methylene blue from aqueous solution. *Microporous Mesoporous Mater*. 2014;193:27-34. doi:10.1016/j.micromeso.2014.03.004
181. Navarathna CM, Dewage NB, Karunanayake AG, et al. Rhodamine B Adsorptive Removal and Photocatalytic Degradation on MIL-53-Fe MOF/Magnetic Magnetite/Biochar Composites. *J Inorg Organomet Polym Mater*. 2020;30(1):214-229. doi:10.1007/s10904-019-01322-w
182. Jiang C, Fu B, Cai H, Cai T. Efficient adsorptive removal of Congo red from aqueous solution by synthesized zeolitic imidazolate framework-8. *Chem Speciat Bioavailab*. 2016;28(1):199-208. doi:10.1080/09542299.2016.1224983
183. Chi HY, Hung SH, Kan MY, et al. Metal-organic frameworks for dye sorption: Structure-property relationships and scalable deposition of the membrane adsorber. *CrystEngComm*. 2018;20(36):5465-5474. doi:10.1039/c8ce01066h
184. Mohammadi AA, Alinejad A, Kamarehie B, et al. Metal-organic framework Uio-66 for adsorption of methylene blue dye from aqueous solutions. *Int J Environ Sci Technol*. 2017;14(9):1959-1968. doi:10.1007/s13762-017-1289-z

185. Embaby MS, Elwany SD, Setyaningsih W, Saber MR. The adsorptive properties of UiO-66 towards organic dyes: A record adsorption capacity for the anionic dye Alizarin Red S. *Chinese J Chem Eng.* 2018;26(4):731-739. doi:10.1016/j.cjche.2017.07.014
186. Haque E, Jun JW, Jhung SH. Adsorptive removal of methyl orange and methylene blue from aqueous solution with a metal-organic framework material, iron terephthalate (MOF-235). *J Hazard Mater.* 2011;185(1):507-511. doi:10.1016/j.jhazmat.2010.09.035
187. Xia H, Li Z, Zhong X, Li B, Jiang Y, Jiang Y. HKUST-1 catalyzed efficient in situ regeneration of NAD⁺ for dehydrogenase mediated oxidation. *Chem Eng Sci.* 2019;203:43-53. doi:10.1016/j.ces.2019.03.076
188. Acid-Base Indicators. Libre Text Chemistry. Accessed 24 July 2024.
[https://chem.libretexts.org/Bookshelves/General_Chemistry/Map%3A_General_Chemistry_\(Petrucci_et_al.\)/17%3A_Additional_Aspects_of_Acid-Base_Equilibria/17.3%3A_Acid-Base_Indicators#](https://chem.libretexts.org/Bookshelves/General_Chemistry/Map%3A_General_Chemistry_(Petrucci_et_al.)/17%3A_Additional_Aspects_of_Acid-Base_Equilibria/17.3%3A_Acid-Base_Indicators#)
189. Raposo F, De La Rubia MA, Borja R. Methylene blue number as useful indicator to evaluate the adsorptive capacity of granular activated carbon in batch mode: Influence of adsorbate/adsorbent mass ratio and particle size. *J Hazard Mater.* 2009;165(1-3):291-299. doi:10.1016/j.jhazmat.2008.09.106
190. Datta K, Deotare PB. Strain sensitivity of dielectric polarization to doping in a host: guest medium. *Opt Mater Express.* 2020;10(12):3021. doi:10.1364/ome.404468
191. Minamoto C, Fujiwara N, Shigekawa Y, et al. Effect of acidic conditions on decomposition of methylene blue in aqueous solution by air microbubbles. *Chemosphere.* 2021;263:128141. doi:10.1016/j.chemosphere.2020.128141
192. Li Z, Sellaoui L, Gueddida S, et al. Adsorption of methylene blue on silica nanoparticles: Modelling analysis of the adsorption mechanism via a double layer model. *J Mol Liq.* 2020;319. doi:10.1016/j.molliq.2020.114348
193. Pinger CW, Heller AA, Spence DM. A Printed Equilibrium Dialysis Device with Integrated Membranes for Improved Binding Affinity Measurements. *Anal Chem.* 2017;89(14):7302-7306. doi:10.1021/acs.analchem.7b01848
194. Kim YT. A 'print – pause – print' protocol for 3D printing microfluidics using multimaterial stereolithography. doi:10.1038/s41596-022-00792-6

List of References

195. Garg T. Separating fluid mixtures using 3D printed microstructure devices. *Mech Eng. UG Project at University of Aouthampton*. 2021
196. Selifonov AA, Shapoval OG, Mikerov AN, Tuchin V V. Determination of the Diffusion Coefficient of Methylene Blue Solutions in Dentin of a Human Tooth using Reflectance Spectroscopy and Their Antibacterial Activity during Laser Exposure. *Opt Spectrosc*. 2019;126(6):758-768. doi:10.1134/S0030400X19060213
197. Hild F. Surface Energy Of Plastics. Accessed July 8, 2024.
<https://www.tstar.com/blog/bid/33845/surface-energy-of-plastics>
198. Thompson R, Austin D, Wang C, Neville A, Lin L. Low-frequency plasma activation of nylon 6. *Appl Surf Sci*. 2021;544(November 2020):148929. doi:10.1016/j.apsusc.2021.148929
199. Yuen PK. Embedding objects during 3D printing to add new functionalities. *Biomicrofluidics*. 2016;10(4). doi:10.1063/1.4958909
200. Penny MR, Tsui N, Hilton ST. Extending practical flow chemistry into the undergraduate curriculum via the use of a portable low-cost 3D printed continuous flow system. *J Flow Chem*. 2021;11(1):19-29. doi:10.1007/s41981-020-00122-5
201. Liu L, Ma H, Xing B. Chemosphere Aging and characterization of disposable polypropylene plastic cups based microplastics and its adsorption for methylene blue. *Chemosphere*. 2024;349(July 2023):140976. doi:10.1016/j.chemosphere.2023.140976
202. Oswald L. Building a robot chemist : Inline spectrometer design for droplet flows. *Mech. Eng. UG Project at University of Southampton*. 2022
203. Clark MJ, Garg T, Rankin KE, Bradshaw D, Nightingale AM. 3D printed filtration and separation devices with integrated membranes and no post-printing assembly. *React Chem Eng*. 2023;9(2):251-259. doi:10.1039/d3re00245d
204. Li F, MacDonald NP, Guijt RM, Breadmore MC. Multimaterial 3D Printed Fluidic Device for Measuring Pharmaceuticals in Biological Fluids. *Anal Chem*. 2019;91(3):1758-1763. doi:10.1021/acs.analchem.8b03772
205. Balakrishnan HK, Doeven EH, Merenda A, Dumée LF, Guijt RM. 3D printing for the integration of porous materials into miniaturised fluidic devices: A review. *Anal Chim Acta*. 2021;1185. doi:10.1016/j.aca.2021.338796

206. Lederle F, Meyer F, Kaldun C, Namyslo JC, Hübner EG. Sonogashira coupling in 3D-printed NMR cuvettes: synthesis and properties of aryl naphthylalkynes. *New J Chem*. 2017;41(5):1925-1932. doi:10.1039/c6nj03614g
207. Oellers M, Lucklum F, Vellekoop MJ. On-chip mixing of liquids with swap structures written by two-photon polymerization. *Microfluid Nanofluidics*. 2020;24(1):1-8. doi:10.1007/s10404-019-2309-8
208. Scotti G, Nilsson SME, Haapala M, et al. A miniaturised 3D printed polypropylene reactor for online reaction analysis by mass spectrometry. *React Chem Eng*. 2017;2(3):299-303. doi:10.1039/c7re00015d
209. Li F, Ceballos MR, Balavandy SK, et al. 3D Printing in analytical sample preparation. *J Sep Sci*. 2020;43(9-10):1854-1866. doi:10.1002/jssc.202000035
210. Kalsoom U, Nesterenko PN, Paull B. Current and future impact of 3D printing on the separation sciences. *TrAC - Trends Anal Chem*. 2018;105:492-502. doi:10.1016/j.trac.2018.06.006
211. Cocovi-Solberg DJ, Worsfold PJ, Miró M. Opportunities for 3D printed millifluidic platforms incorporating on-line sample handling and separation. *TrAC - Trends Anal Chem*. 2018;108:13-22. doi:10.1016/j.trac.2018.08.007
212. Monaghan T, Harding MJ, Harris RA, Friel RJ, Christie SDR. Customisable 3D printed microfluidics for integrated analysis and optimisation. *Lab Chip*. 2016;16(17):3362-3373. doi:10.1039/c6lc00562d
213. Zhang JM, Li EQ, Aguirre-Pablo AA, Thoroddsen ST. A simple and low-cost fully 3D-printed non-planar emulsion generator. *RSC Adv*. 2016;6(4):2793-2799. doi:10.1039/c5ra23129a
214. Bishop GW, Satterwhite-Warden JE, Bist I, Chen E, Rusling JF. Electrochemiluminescence at Bare and DNA-Coated Graphite Electrodes in 3D-Printed Fluidic Devices. *ACS Sensors*. 2016;1(2):197-202. doi:10.1021/acssensors.5b00156
215. Castiaux AD, Pinger CW, Hayter EA, Bunn ME, Martin RS, Spence DM. PolyJet 3D-Printed Enclosed Microfluidic Channels without Photocurable Supports. *Anal Chem*. 2019;91(10):6910-6917. doi:10.1021/acs.analchem.9b01302
216. Keating SJ, Gariboldi MI, Patrick WG, Sharma S, Kong DS, Oxman N. 3D printed multimaterial microfluidic valve. *PLoS One*. 2016;11(8):1-12.

List of References

doi:10.1371/journal.pone.0160624

217. Li F, Macdonald NP, Guijt RM, Breadmore MC. Increasing the functionalities of 3D printed microchemical devices by single material, multimaterial, and print-pause-print 3D printing. *Lab Chip*. 2019;19(1):35-49. doi:10.1039/c8lc00826d
218. Gogotsi Y, Anasori B. The Rise of MXenes. *ACS Nano*. 2019;13(8):8491-8494. doi:10.1021/acsnano.9b06394
219. Mohammadi AV, Rosen J, Gogotsi Y. The world of two-dimensional carbides and nitrides (MXenes). *Science (80-)*. 2021;372(6547). doi:10.1126/science.abf1581
220. Alhabeb M, Maleski K, Anasori B, et al. Guidelines for Synthesis and Processing of Two-Dimensional Titanium Carbide (Ti₃C₂T_x MXene). *Chem Mater*. 2017;29(18):7633-7644. doi:10.1021/acs.chemmater.7b02847
221. Shuck CE, Ventura-Martinez K, Goad A, Uzun S, Shekhirev M, Gogotsi Y. Safe Synthesis of MAX and MXene: Guidelines to Reduce Risk during Synthesis. *ACS Chem Heal Saf*. 2021;28(5):326-338. doi:10.1021/acs.chas.1c00051
222. Yu M, Feng X. Scalable Manufacturing of MXene Films: Moving toward Industrialization. *Matter*. 2020;3(2):335-336. doi:10.1016/j.matt.2020.07.011
223. Liu H, Chen B, Li C, et al. Fluoride-Free Synthesis of 2D Titanium Carbide MXenes Assisted by scCO₂-Based Ternary Solution. *Adv. Sci. News*. 2024;20:2305321. doi:10.1001/sml.202305321
224. Li T, Yao L, Liu Q, et al. Fluorine-Free Synthesis of High-Purity Ti₃C₂T_x T OH O via Alkali Treatment. *Angew. Chem. Int*. 2018;57:1-6. doi:10.1002/anie.201800887
225. Wang C, Shou H, Chen S, et al. HCl-Based Hydrothermal Etching Strategy toward Fluoride-Free MXenes. *Adv. Mater*. 2021;33:2101015. doi:10.1002/adma.202101015
226. Sun W, Shah SA, Chen Y, et al. Electrochemical etching of Ti₂AlC to Ti₂CT:X (MXene) in low-concentration hydrochloric acid solution. *J Mater Chem A*. 2017;5(41):21663-21668. doi:10.1039/c7ta05574a
227. Yang Y, Zhang P, Wang F, et al. Fluoride-Free Synthesis of Two-Dimensional Titanium Carbide (MXene) Using A Binary Aqueous System. *Angew. Chem. Int*. 2018;57:15491-15495. doi:10.1002/ange.201809662

228. Chen J, Chen M, Zhou W, et al. Simplified Synthesis of Fluoride-Free Ti₃C₂T_x via Electrochemical Etching toward High-Performance Electrochemical Capacitors. *ACS Nano*. 2022;16(2):2461-2470. doi:10.1021/acsnano.1c09004
229. Pang SY, Wong YT, Yuan S, et al. Universal Strategy for HF-Free Facile and Rapid Synthesis of Two-dimensional MXenes as Multifunctional Energy Materials. *J Am Chem Soc*. 2019;141(24):9610-9616. doi:10.1021/jacs.9b02578
230. Li Y, Shao H, Lin Z, et al. A general Lewis acidic etching route for preparing MXenes with enhanced electrochemical performance in non-aqueous electrolyte. *Nat Mater*. 2020;19(8):894-899. doi:10.1038/s41563-020-0657-0
231. Kamysbayev V, Filatov AS, Hu H, et al. Covalent surface modifications and superconductivity of two-dimensional metal carbide MXenes. *Science (80-)*. 2020;369(6506):979-983. doi:10.1126/science.aba8311
232. Wang D, Zhou C, Filatov AS, et al. Direct synthesis and chemical vapor deposition of 2D carbide and nitride MXenes. *Science (80-)*. 2023;379(6638):1242-1247. doi:10.1126/science.add9204
233. Shuck CE, Sarycheva A, Anayee M, et al. Scalable Synthesis of Ti₃C₂T_x MXene. *Adv Eng Mater*. 2020;22(3):1-8. doi:10.1002/adem.201901241
234. Lee SL, O'Connor TF, Yang X, et al. Modernizing Pharmaceutical Manufacturing: from Batch to Continuous Production. *J Pharm Innov*. 2015;10(3):191-199. doi:10.1007/s12247-015-9215-8
235. Lee YR, Jang MS, Cho HY, Kwon HJ, Kim S, Ahn WS. ZIF-8: A comparison of synthesis methods. *Chem Eng J*. 2015;271:276-280. doi:10.1016/j.cej.2015.02.094
236. Ghidui M, Lukatskaya MR, Zhao MQ, Gogotsi Y, Barsoum MW. Conductive two-dimensional titanium carbide "clay" with high volumetric capacitance. *Nature*. 2015;516(7529):78-81. doi:10.1038/nature13970
237. Zargaryan A, Farhoudi N, Haworth G, Ashby JF, Au SH. Hybrid 3D printed-paper microfluidics. *Sci Rep*. 2020;10(1):1-9. doi:10.1038/s41598-020-75489-5
238. Dirkzwager RM, Liang S, Tanner JA. Development of Aptamer-Based Point-of-Care Diagnostic Devices for Malaria Using Three-Dimensional Printing Rapid Prototyping. *ACS Sensors*. 2016;1(4):420-426. doi:10.1021/acssensors.5b00175

239. Castiaux AD, Pinger CW, Spence DM. Ultrafiltration binding analyses of glycated albumin with a 3D-printed syringe attachment. *Anal Bioanal Chem*. 2018;410(29):7565-7573. doi:10.1007/s00216-018-1373-3
240. Maughan PA, Arnold S, Zhang Y, Presser V, Tapia-Ruiz N, Bimbo N. In Situ Investigation of Expansion during the Lithiation of Pillared MXenes with Ultralarge Interlayer Distance. *J Phys Chem C*. 2021;125(38):20791-20797. doi:10.1021/acs.jpcc.1c05092
241. Maughan PA, Tapia-Ruiz N, Bimbo N. In-situ pillared MXene as a viable zinc-ion hybrid capacitor. *Electrochim Acta*. 2020;341:136061. doi:10.1016/j.electacta.2020.136061
242. Maughan PA, Seymour VR, Bernardo-Gavito R, et al. Porous Silica-Pillared MXenes with Controllable Interlayer Distances for Long-Life Na-Ion Batteries. *Langmuir*. 2020;36(16):4370-4382. doi:10.1021/acs.langmuir.0c00462
243. Makaryan T, Okada Y, Kondo H, Kawasaki S, Suzuki K. Removal of Interlayer Water of two Ti₃C₂T_x MXenes as a Versatile Tool for Controlling the Fermi-Level Pinning-Free Schottky Diodes with Nb:SrTiO₃. *Adv Funct Mater*. 2023;33(2):1-13. doi:10.1002/adfm.202209538
244. Hope MA, Forse AC, Griffith KJ, et al. NMR reveals the surface functionalisation of Ti₃C₂ MXene. *Phys Chem Chem Phys*. 2016;18(7):5099-5102. doi:10.1039/c6cp00330c
245. Hu T, Li Z, Hu M, et al. Chemical Origin of Termination-Functionalized MXenes: Ti₃C₂T₂ as a Case Study. *J Phys Chem C*. 2017;121(35):19254-19261. doi:10.1021/acs.jpcc.7b05675
246. Hu T, Hu M, Gao B, Li W, Wang X. Screening Surface Structure of MXenes by High-Throughput Computation and Vibrational Spectroscopic Confirmation. *J Phys Chem C*. 2018;122(32):18501-18509. doi:10.1021/acs.jpcc.8b04427

